DOCTOR OF PHILOSOPHY

Development of a novel pultruded FRP-lightweight concrete hybrid beams

Etim, Offiong Orok

Award date:
2022

Awarding institution:
Coventry University

Development of a Novel Pultruded FRP-Lightweight Concrete Hybrid Beams

By

OFFIONG OROK ETIM

Doctor of Philosophy (PhD)

July 2021

Development of a Novel Pultruded FRP-Lightweight Concrete Hybrid Beams

A thesis submitted in partial fulfilment of the University's requirements for the Degree of Doctor of Philosophy

July 2021

PUBLICATION AND SUBMITTED PAPERS

Below is a list of the author's publications relating to the context of this thesis;

Journal Papers:

Etim, O., Gand, A., Messaoud, S., Fom, P., Ganjian, E., and Okon, E. (2020) 'Shear Characterisation of pultruded superstructural FRP-concrete push-outs'. Institution of Structural Engineers. Structures 23 (2020) 254 – 266.

Conference Papers:

Etim, O., Gand, A., Messaoud, S., Okon, E., and Fom, P. (2019) 'Push-out experimental evaluation of pultruded FRP-concrete composites' in Proceedings of the Fifth International Conference on Sustainable Materials and Technology.

ACKNOWLEDGEMENT

This research has been made successful through tangible contributions from specific persons deserving of my gratitude. Most especially, my supervisory team who inspired and challenged me all through the cause of this journey. I specially want to thank **Mr Alfred Gand** for his mentoring and tutelage over the last five years. **Prof Messaoud Saidani** being my director of studies and former teacher remains one of the most significant members of this team, coordinating the progress of the research and always acting in my best interest. A big thank you to the members of staff including **Dr Pam Fom**, laboratory technicians and the student community. My gratitude to a friend and colleague **Dr Ucheowaji Ogbologugo** for his kind support over the final year of my research.

While the above persons had contributed immensely to the success of this research, I reserve this special gratitude for my wife **Mrs Margaret O. Etim**. This research was self-funded from nothing and could not have been possible without the selfless support from my wife. My wife toiled day and night contributing most of her earnings towards my tuition and while I experienced many ups and downs, she compromised her desires in the interest of family. Words are not enough to thank you **Margaret** but I am certain that the future holds more than promises for us.

Lastly, I want to thank my Father **Chief Orok H. Etim** for his encouragement over the years and early contributions to the start of my research. I remain grateful for the support from my mother **Mrs Offiong Offiong Etim** and siblings who constantly prayed and showed concern over the duration of my studies. A big thank you to all those who had supported me in one way or the other throughout this research.

DEDICATION

This research work is dedicated to God Almighty for his provision and sufficiency throughout the entire programme of study.

…And God is able to bless you abundantly, so that in all things at all times, having all that you need, you will abound in every good work… **2 Corinthians 9:8**

TABLE OF CONTENTS

Contents

LIST OF TABLES

LIST OF FIGURES

ABSTRACT

Fatalities resulting from building collapse are further exacerbated by dead-weights of structural members particularly, in geographical areas easily prone to natural disasters. Beyond these concerns, there is a growing need for lightweight structures aimed at significant reduction to transmissible foundation loads and general savings in materials used for construction and the built environment. The purpose of the current research is to promote the use of lightweight structural elements by publishing experimental findings on the performance of a newly fabricated hybrid composite beam comprising of Glass fibre reinforced polymer (GFRP) material and lightweight aggregate concrete (LWAC). GFRP had been limited to the aerospace industry until recently when it found significant purpose within construction and the built environment. Nevertheless, its application in construction remains limited owing to scarce publications on its performance both as a single structural element and/or a structural composite element.

Locally sourced GFRP wide flange (WF) sections are compositely fastened onto pre-characterised LWA concrete made of Lytag aggregates fashioned after conventional steel-concrete composites. The composite connection is experimentally tested using the push-out test method described Eurocode 4 for determining interfacial shear performance and appropriate configurations for the design of the hybrid composite beam. The developed hybrid beam of an estimated 400kg (about 60% less than the conventional steel-concrete counterpart) was investigated under a four-point loading test. Experimental test results validate numerical results obtained from ANSYS Finite Element (FE) software simulations. Hybrid structural composites involving the use of GFRP and LWAC showed comparable flexural response to that of conventional steel-concrete counterparts but with a deviation in the characteristic lateral shear failure modes

evidencing dominant bearing failures around clearance holes. Shear characterisation of composites reaffirm the single curvature yielding of steel studs for GFRP composites earlier deduced by Hicks (2019) taking the height/diameter characteristics of the stud as a metric for determining their performance. Whereas 19mm studs of equal height showed 22 % (and above) higher capacities over their 16 mm counterpart. The study adopted 12 mm which had 17% lower capacities to the 16 mm studs. The novel hybrid beam can retain up to 66 % reserve capacity against ultimate failure under serviceability state.

CHAPTER 1. INTRODUCTION

1.1 General

Environmental activities either self-occurring (i.e. natural) or activity-induced, have become a focal point of interest in design considerations and these have subsequently influenced the advancement in material research within the development of construction practices. Disasters such as earthquakes, flooding etc. have informed a growing demand on research for lightweight structural materials while issues of temperature change, green-house gas emissions, pollution etc. have generated concerns on material durability and sustainability.

Conventional structural composite practice has been based essentially on welding action to achieve composite connection between two primary structural elements (concrete and steel). This traditional approach adopts a welding action on the shear studs (otherwise known as connectors) through a profiled steel sheeting to the flange of a steel beam while the connector head is embedded in concrete (See Figure 1.1).

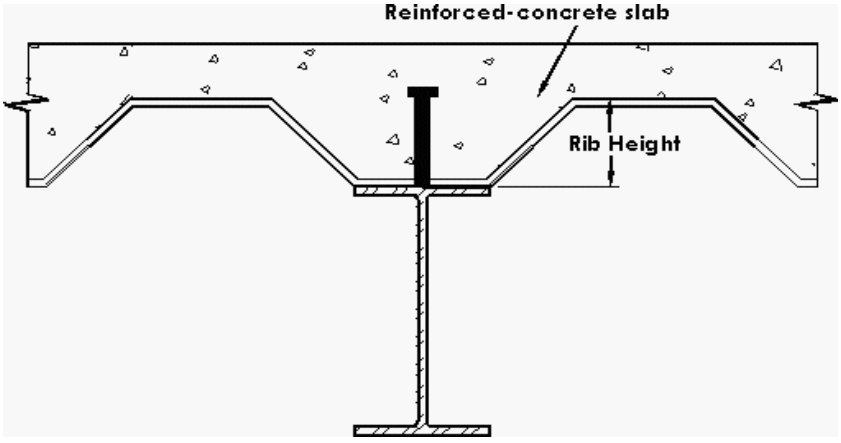

Figure 1.1 Typical cross-section of composite concrete-steel beam

One of the main reasons of these composite structures is to improve on certain weaknesses of conventional construction practice including material conservation, strength and construction efficiency. However, the underlying environmental concerns of weight particularly in regions prone to disasters such as earthquakes, tsunamis etc., remain an area of interest for researchers aiming to improve conditions of safety during such adverse occurrences. Some of the challenges of current practices relying on composite construction include weight, durability and sustainability Another important reason for weight mitigation in composite construction is so that the substructure and soil could be relieved of unnecessary pressure which in turn could mean increased in cost savings. Also, durability remains an ever-growing concern when considering cost of design and maintenance. Steel is considered susceptible to environmental changes in temperature and ionic reactions with water which does result to material degradation in construction lifecycle. The most pressing concern of recent times is the role of construction materials to environmental issues such as climate change due to greenhouse gas emissions. The recycling process is very energy intensive and this does often lead to the release of carbon into the environment (Rehman et al. 2016). Hence, a critical appraisal for alternative replacement in construction is required.

This research has adapted the existing concrete-steel composite practice predominantly responsible for the high demand of construction steel for the alternative fibre reinforced polymer (FRP) material. The study uses two lightweight materials: lightweight aggregate concrete (LWAC) and glass fibre reinforced polymer (GFRP) as a replacement for conventional concrete-steel composite. The major purpose of this research is to advance

the study of composite materials with the aim of fostering their application as alternative construction materials. FRP-concrete composites will benefit from steel bolted shear connections. Bolted or demountable shear connectors have been rarely used in construction apart from rehabilitation work (Rehman et al. 2016). They can be efficient in managing maintenance work as well as promoting sustainability through material re-use at the end of a design life cycle. Demountable shear connectors are rarely used in construction because there is no standard guideline available to promote their usage therefore, this research also aims to contribute to the paucity in knowledge demanding the establishment of standard guidelines to encourage the use of bolted connectors in construction practice.

Although previous studies have investigated the effects of various parameters and configurations for composites however, they have not established optimum limits for these parameters as guidance for proper design and for the recommendations proposed. Most findings have been based on normal weight concrete – steel composites while a few have considered lightweight concrete - steel composites and very scarce literature is available for lightweight-FRP composites in practice.

1.2 Background of Study

The knowledge and principles of material mechanics has led to greater use and adoption of alternative materials including composites in civil engineering construction. Some of these principles include geometric studies stipulating width to thickness ratio as a measure of a material's resistance to fracture relative to its orientation in space. Establishing the appropriateness of use for an engineering material stems from an understanding of the relationship between the property of the material and their corresponding response to the

effect of loads. This understanding is conducted from precise quantitative and qualitative analysis of materials. Hence, the evolution of material use in construction has been largely influenced by studies conducted on optimisation and structural performance under hypothetical principles. Some of these principles centre on the determination of intrinsic properties which accounts for an appropriate classification of the material in terms of their mechanical behaviour, durability and performance in construction. Some of the most successful materials in the last decade include steel, timber and concrete etc. These materials have gained worldwide success on their usage in construction following their flexible conformance to technological advancement. When assessing the appropriateness of materials for construction, some of the performance requirements to consider include geometrical efficiency, enhanced deformation resistance, electrical and thermal resistivity, general material durability etc. Steel and concrete have mostly satisfied the above listed requirements and have been highly susceptible to micro and macro structural optimisation hence, promoting their continuous use in engineering construction. Despite their benefits to construction, they have left a vacuum of concerns which includes issues of environmental impacts, sustainability, and material efficiency. Some of these problems form the motivation for this research.

This study proposes the development of Fibre reinforced polymer and concrete composite (FRP-Concrete Composite) beams for use in construction of lightweight structures. The combination of these two unique materials is in response to the plight of construction under the above-mentioned material deficiencies for steel and normal weight concrete. In this section, the study will explore the motivation and immediate response of the proposed alternative materials of FRP and lightweight concrete under the given concerns.

1.2.1 Shear connectors and associated mechanical problems

Shear connectors refer to mechanical fasteners which are provided to ensure adequate stress transfers between composite materials in service conditions. These conductors may range from standard bolt connectors (Hosseinpour et al., 2021; Rehman et al., 2016; Nguyen et al., 2014) to bespoke stud connectors such as angle connectors (Nguyen et al., 2014; Jiang et al., 2021; Wang et al., 2022) often manufactured using materials such as steel, carbon, and glass fibre plastics etc.

Welded stud connectors widely used on steel beams have significant limitations in ensuring uniform distribution of shear stresses due to difficulty in achieving consistent welding quality across the stud arrangements (Shaochun et al., 2022). The limitations of welded connectors to enable even stress distribution has contributed to the growing use of bolted connectors with a further benefit in promoting ease of assembly and demounting of composites. Steel studs contribute to shear resistance through strength mobilisation often evident in their significant modes of deformation. Hicks (2014) suggest that for full mobilisation to occur, the shear studs must be able to achieve single curvature or double curvature deformations in solid and profiled concrete slabs respectively. Hence, whilst these are mostly observed in steel-concrete composites, limited evidence is reported in literature to support this hypothesis for FRP-concrete composites. Yang et al. (2018) reported reduction of shear connector stiffness due to increase in tolerance for bolt clearance holes. The research reported 50% reduction in stiffness of headless steel bolts against their headed counterparts. Whereas clearance holes are a significant aspect of bolt configuration, it has severe impact on the shear stiffness of connectors. This significant

influence has been reported for FRP-concrete composites (Nguyen et al., 2014) but with limited findings on its contribution to flange failure modes.

Another significant challenge with the performance of shear connectors considers the influence of external factors such as concrete curing and compressive strengths, plate bearing strengths etc on the mechanical properties of connector. The difficulty in accounting for all force interactions during composite shear testing has resulted in further research proposals to improve standard test methods for investigating shear behaviour. These gaps have seen researchers investigate external factors such as concrete confinement strength, slab compressive force, base stability of push specimens etc.

1.2.2 Failure modes of composite connections

A critical aspect of investigation for composite behaviour considers the failure patterns associated with various shear configurations and the corresponding load conditions. The influence of static and cyclic load conditions has been investigated and reported to have significant impact on the performance of composites. FRP-concrete composites utilising similar stud properties and size configurations irrespective of the concrete properties have been reported to mobilise comparable shear strengths of up to 40 kN/stud for 10 mm stud diameters (Correia et al., 2007; Nguyen et al., 2014; Zou et al., 2020) under static load conditions. The associated failure modes of these composites have been stud-bending (Nguyen et al., 2014), stud fracture (Correia et al., 2007, Nguyen et., 2014; Dai et al., 2015; Rehman et al., 2016; Yang et al., 2018) and concrete failures (An & Cedarwall, 1996). Whilst the aforementioned modes of failure are common for steel-concrete composites, flange bearing failures around the bolt holes have been reported by Nguyen et al. (2014) to have significant impact on the shear performance of FRP-concrete

composites. This phenomenon observed on FRP-concrete composites has provided another motivation for the current study due to limited knowledge from existing literature. Limited knowledge exists in current literature to explore the impact of cyclic load conditions on the shear connection performance involving FRP-concrete composites. However, Ataei et al. (2019) investigated shear behaviour of demountable connectors under cyclic loading with conclusions that increase in strength and sizes of bolt connectors result to higher initial stiffnesses and ultimate strength. This phenomenon is necessary under serviceable conditions to determine the fatigue behaviour of composite beams (Hosseini et al., 2020). It remains a relevant aspect of the investigation of FRP-concrete composites informing a key objective of this study.

1.3 Research Significance

The current study investigates shear strength properties of steel bolt connectors for FRP-concrete composites and their corresponding failure modes. The study aims to evaluate moment capacities of the hybrid composite connection between GFRP and LWAC beams under static and cyclic loading. The research study offers an opportunity to build further on the limited knowledge of the application of GFRP structural profiles in construction. It is aimed at facilitating an understanding of the holistic behaviour of GFRP-concrete hybrid composites as flexural structural members. The research explores the significant limitations of traditional composites to proffer alternative solution to material weight issues in a dynamically evolving construction environment. The research will support current publications and promote appropriate principles for the design of novel hybrid composite beams in construction. It is also hoped that the observations and conclusions will provide a fundamental knowledge for further investigations in the future.

1.4 Research Objectives

The following outlines the key objectives of the research.

(a) To explore and review existing knowledge on the mechanical influence of FRP plate properties on the FRP structural composites.
(b) Determine the influence of shear connector arrangement and mechanical properties on the interfacial shear behaviour of the hybrid composite.
(c) Investigate the development and propagation of flexural and interfacial shear failures.
(d) Establish a comparative prediction model of FRP mechanical properties from literature review in order to test the reliability adopted strength and elastic constants in analytical studies.
(e) Design and develop prototype hybrid beams to determine load deflection response, stiffness and failure mechanisms.

1.5 Scope of Study

The study investigates shear connection performance between pultruded FRP I-section profiles and Lytag lightweight concrete beams. Collated data on mechanical properties of FRP profiles will inform further analytical studies on lateral shear and flexural behaviour. In addition, the push-out experimental test method described in Eurocode 4 (EC4) will be adopted for interfacial shear investigation of the composite. The outcome of the test will provide an in-depth knowledge on several parameters on shear connection behaviour utilising steel dowels. The research will involve a comprehensive array of experimental testing, analytical work including non-linear finite element modelling and analyses. Experimental test data will be evaluated against numerically simulated outputs and expected conclusions and recommendations will be contributed to the progressive development of a consensus design guideline for FRP-concrete hybrid composites. The study covers relevant literature on FRP-concrete composites with parallel literature on

steel-concrete composites to illustrate appropriate principles and to derive understanding on various parameters of stud connections for composite structural sections. The literature discusses fabrications of composite components and connections, mechanical properties and their influences on the structural behaviour, theoretical hypothesis for the prediction of structural behaviour and the numerical modelling of FRP-concrete composites using appropriate finite element software.

In further chapters, the research method is expanded to illustrate the adopted experimental design for the current study considering experimental protocols, health and safety considerations, material and setup apparatus availability. The research methodology is intended not only for the outline of appropriate methods but to establish justification for the methods by highlighting the relevance, adequacy, and accuracy of methods.

CHAPTER 2. LITERATURE REVIEW

2.1 Conventional Materials

The demand for steel in European Union (EU) countries is estimated to be about 170 million metric tonnes between 2019 and 2020 with an average total consumption of 159 million metric tonnes. The given data is an overview of the production volume of steel in the United Kingdom (UK) and European Union (EU) and therefore serves as an example of its growing usage globally. In UK, the construction sector is regarded as being the highest consumer of steel at about 50% (and 30% globally) of the total consumption volume (see consumption breakdown in Table 2.1). The significance of steel in construction cannot be overemphasized resulting in high-manufacturing volumes and increased consumption all having severe impact on the environment. The manufacturing of steel involves mining/quarrying, coke production from coal and iron ore smelting all of which have immense effect on the environment such as destruction of landscape, production of unwanted gases and high energy consumption.

From such a significant volume of consumption cited above, it can be concluded that the construction industry is about the most energy intensive sector (D'Amico & Pomponi, 2018). The manufacturing process of steel requires a high volume of water (estimated at about 350,000 litres to produce 1 ton of steel) which results in the generation of an increased volume of wastewater. The construction industry has been reportedly responsible for global waste generations and approximately one-third of the total (global) carbon emission (Giesekem et al., 2014; D'Amico & Pomponi, 2018). The department for business, innovation, and skills in its 2010 IGT supporting materials for low carbon construction report posited that the construction industry was responsible for an estimated

47% of the total CO_2 emissions in the UK (BIS, Estimating the amount of CO_2 emissions that the construction industry can influence, 2010), Allwood et al. (2010) reported that about 2.5Gt of carbon emissions was derived from steel which is at 25% of total global CO_2 emissions. With the knowledge on carbon emissions from steel it will be worrisome to note according to Wang & Muller (2007) reports that nearly half of the manufactured steel is used mainly as profiled members in building construction while UK waste data publication result reported over 100 million tonnes of waste generation from the construction industry in 2008 (UK waste data and management statistics, 2011). Savings from environmental impact of only 1kg of structural steel (see Table 2.2) prove significant in the reduction of CO_2 emissions according to previous studies. Hence, the promotion of the lightweight alternative materials such as FRP becomes relevant in contributing to the UK's legal binding scheme to transition into a low carbon construction industry through an 80% reduction carbon footprint by 2050 (Giesekam et al. 2014).

These environmental concerns have led to the development of low impact processes for steel manufacturing and high demand for steel recycling. While there is a continuous development in steel manufacturing and recycling, there is increase in the environmental burden of steel emanating from its large consumption by the construction industry. Hence, the need for alternative materials with low environmental impacts and carbon footprints. A summary proposition from D'Amico & Pomponi (2018) on possible minimisation of environmental impact from conventional construction practices is presented in Table 2.3. This study serves to validate its relevance and significance by satisfying some of the highlighted recommended approach proposed in Table 2.3 for reducing the significant environmental issues by the promotion of FRP-lightweight concrete composites for construction.

Table 2.1: 2006 allocation of steel products by construction sector for the UK (kt/year) (source: Moynihan et al. 2012)

Sector	***Sections***	***Rebar***	***Sheets***	***Rail***	***Tubes***
Buildings	1600	800	1400	0	500
Utilities	0	400	0	0	300
Rails	0	0	0	200	0
Bridges	0	0	0	0	0
Others	0	200	0	0	100
Total	1600	1400	1400	200	900

Table 2.2: LCA of 1kg of structural steel (Giesekam et al., 2014)

Impact category	**Ref. unit**	**Result**
Acidification potential – average Europe	kg SO_2 eq.	0.071154
Climate change – GWP100	kg CO_2 eq.	11.13592
Depletion of abiotic resources, ultimate reserves	kg antimony eq.	0.000536
Depletion abiotic resources, fossil fuels	MJ	117.9142
Eutrophication	kg PO_4 eq.	0.017546
Human, freshwater and marine toxicity	kg 1,4–$C_6H_4C_{12}$ eq.	16350.53
Ozone layer depletion	kg CFC-11 eq.	4.43E-07
Photochemical oxidation	kg C_2H_4 eq.	0.003533
Terrestrial ecotoxicity	kg 1,4-$C_6H_4C_{12}$ eq.	0.091483

Table 2.3: Summary of options for reducing the options of carbon-intensive materials in the UK (Source: D'Amico & Pomponi, 2018)

Alternative Materials	***Substitution in the production of common materials***	***Minimising excess through design and manufacture***	***Re-use, recycling and leasing of components***	***Adaptive re-use and life extension of existing stock***
Timber (traditional forms, SIPs, Brettstapel and CLT)	Alternative cementitious materials or aggregate substitutes	Optimised carpet/roll-out reinforcements	Increased dismantling and re-use of members	Increased redevelopment and adaptive re-use
Plastic (FRP, ETFE)	GGBS	Mesh reinforcement	Leasing of structural components (e.g. roofs)	Refurbishment of existing structures
Straw-bale (infill, load-bearing or composite panels e.g. Modcell)	Fly Ash	Hollow-core slabs	More use of recycled aggregates	Adaptive design of future structures
Earth (rammed earth, unfired brick, cob, wattle and daub, and adobe)	Agricultural wastes (rice husks, corn cobs, vegetable fibres, nut shells)	Precast sections	Improved recycling practices on site	
Geopolymer concrete	Consumer waste (plastics, glass, ceramics, tyres and carpets)	Modern methods of construction		
Hemp (hemcrete and hem-lime blocks)	Construction and demolition waste	Variable depth structural members		
Limecrete	Industrial waste (pulp and paper mills residuals, coarse steel slag.	Selective use of higher grade materials		
Tyres	Silica fume, cotton waste, sewage sludge ash)			
Bamboo (laminated or unprocessed)	Waste derived fuels			
Cardboard (tubing or panels)	Agricultural wastes (wheat straw, rice husks, nut shells)			

	Non-agricultural biomass (sewage sludge, paper sludge, animal bone and fat) Consumer waste (carpets and textiles, plastics, tyres, municipal solid waste)	

2.1.1 Pultruded Fibre Reinforced Polymer

The study proposes the use of glass fibre reinforced polymer (GFRP) as an alternative to steel for lightweight construction. GFRP composites have the general advantage of addressing material limitations because they are customisable while also being able to satisfy complex engineering requirements due to their enhanced qualities. GFRP is grouped under the class of advanced composites comprising strength criteria (fibre) and durable binder (matrix) phase (Thomas et al., 2012). The constituent materials can be classified as fibre, matrix and interface. Zoghi (2014) notes that most of the materials used for composite reinforcement are found in the first two rows of the periodic table and these materials have high strength, stiffness, and density. The materials include beryllium, boron, carbon, magnesium, aluminium, and silicon. Among these elements, the most commonly used reinforcing materials include glass (silica, SiO_2), carbon (graphite, C), silicon carbide (SiC) etc. The reinforcement fibres can either be continuous or discontinuous (see Figure 2.1). The most common type of fibre used for FRP is glass fibre typically of 5-25μm diameter coated size for improved adhesion to the matrix material.

Figure 2.1: Continuous and discontinuous fibres (source: Middleton, 2016)

2.1.2 Benefits of hybrid composites in construction

Generally, hybridisation is the concept of enhancing the properties of materials to offer optimum performance. The conventional steel-concrete composite has faced several modifications over the years particularly in weight reduction and shape efficiency. Hence, the proposed hybrid GFRP-concrete composite must take these two criteria into relevant account for appropriateness and validity. Some of the unique benefits of the proposed hybrid composite are explored further below.

Established weight-to-strength ratio specifically qualifies FRP as a significant replacement to steel in the promotion of lightweight structures. However, potential advancement in strength properties of FRP has a continuous influence on its marketability

and promotes its application in modern day construction. Apart from the flexibility of the material especially when combined with other structural materials like concrete, the core potential of introducing fibre hybrids within its manufacturing provides certainty on the future of FRP in construction. Fibre hybrids provide the advantage of enhancing strength-ductility relationships by combining both low and high elongated fibres in such a manner that exploits the relevant strength/stiffness properties while minimising the weakness of individual fibres (Middleton, 2016). One of the most enhanced fibre hybrid architecture developed for FRP is the combined use of carbon and glass reinforcement. Middleton (2016) reported an increase in tensile failure strain of 10 – 50% for unidirectional (UD) fibre hybrid composite following the rule of mixtures. Further research improvements on the progression of failure have witnessed the development of pseudo-ductile behaviour to minimise/reduce catastrophic failures typically characterising conventional FRPs hence, reducing the factor of safety to be applied in its design application (Middleton, 2016). Ductility improvement concept has extended to the use of combined HE fibres and natural fibres with higher differences in failure strains (Swolfs et al., 2014).

2.2 Mechanical Properties of the Composite Materials

A knowledge of the properties of the subcomponent will enhance the understanding and analysis of the FRP-concrete hybrid beam. Subcomponents always refer to the dominant compression and tensile materials of the composite beam. Conventionally, these subcomponents are concrete and steel for compression and tensile resistance respectively. However, some of the reported studies referenced in this literature have highlighted that either components can be optimised, modified or replace as the case maybe. For the purposes of this study, lightweight aggregate concrete shall be substituted for the

compression subcomponent while fibre reinforced polymer (FRP) wide flange (WF) section will be substituted for the dominant tensile subcomponent. The literature will explore interchangeably the knowledge from previous findings on the limited behaviour and properties of the materials while also drawing major lessons from the conventional steel-concrete composite.

2.2.1 Strength-density property influence in LWAC

Dilli et al. (2015) presents strength-density relationship plot for concrete ranging between 1640 – 2350 kg/m3 representing LWAC and NWC types (see Figures 2.2 & 2.3). The figures shows a clear relationship between compressive strength and concrete dry density with compressive strength increasing as the dry unit weight increases. Density of concrete is mainly influenced by the unit weight of aggregates (see Figure 2.4); therefore, the characteristic strength of aggregate can significantly contribute to the compressive strengths of concrete. Dilli et al. (2015) highlights the remarkable strength characteristic property of LWAC which does significantly compares with that of conventional concrete (CC). LWAC-2 aggregate properties are characterised according to EC2 with superior strength properties over the LWAC-1 of EC1. With an average strength-increase of between 28-day to 120-day period, LWAC and NWC are reported in Dilli et al. (2015) as being capable of showing 4.9 percent difference between LWAC-1 and LWAC-2 (see Figure 2.3). The fresh-state concrete mortar is said to be the preserve of a sustained compressive strength for concrete which is why as indicated above regarding mix design, most studies have focused on methods leading to an optimisation of cementitious material to ensure sufficient compressive strength. Such methods are principally hinged on water-to-cementitious material ratio with a consensus finding that low cement/water ratio

increases the compressive strength of the matrix phase and dry concrete property (Dilli et al., 2015).

Figure 2.2: Weight and Strength range for concrete (Source: Chandra et al, 2002)

Aggregates do also contribute to the shrinkage and elastic properties of hardened concrete (Neville, 2000; Dilli et al., 2015). In general, LWAC and NWC have similar strength behaviour but with significant differences in the values for other respective performance parameters. A clear relationship between compressive strength and modulus of elasticity (MOE) exists for NWC likewise, prediction models have been developed for the determination of MOE for LWAC following similar relationship between the parameters. Figure 2.5 shows a relationship between MOE and compressive strength for LWAC and NWC. It is significantly clear that increasing compressive strength corresponds to increased MOE for all concrete types and NWC possess higher MOE in comparison to

LWAC. Some of the standard prediction models currently applicable for the estimation of MOE of concrete are given in Table 2.4 below.

Table 2.4: Standard Prediction Equations for Modulus of Elasticity

Model Title	***Equation (MPa)***
ACI 318	$E_c = 0.043 w_c^{1.5} \sqrt{f_c'}$
ACI 363	$E_c = (3320\sqrt{f_c'} + 6900)\left(\frac{w_c}{2320}\right)^{1.5}$
CEB-FIB	$E_c = 21500\alpha \left[{f_c'}/{10} \right]^{1/3}$
TS 500	$E_c = 3250\sqrt{f_c'} + 14000$
Dilli et al., 2015	$E_c = 3000\sqrt{f_c'}\left({w_c}/{2300}\right)^{3.7} + 12500$
Note: $\boldsymbol{E_c = Elastic\ modulus\ of\ concrete}$; $\boldsymbol{f_c' = compressive\ strength\ of\ concrete}$; $\boldsymbol{\alpha = 1.2\ for\ basalt, dense\ limestone\ aggregates}$; $\boldsymbol{1.0\ for\ quartzite\ aggregates}$; $\boldsymbol{0.9\ for\ lim}$; 0.7 for sandstone aggregates	

The density, compressive strength and MOE properties of concrete are quite important in the modelling of concrete response behaviour to loading. However, the combined stress induced effect of the concrete material characteristics is relevant to the overall knowledge of the concrete behaviour. Overli (2017) hypothetically suggest three material characteristics that could generally influence the ultimate response of concrete materials: significant effect of secondary stresses on compressive strength, abrupt increase of transverse concrete expansion close to peak loading (or peak stress) and the rapid unloading of materials at the peak stress level respectively. This principle is in contrast with the conventional hypothesis of the reliability of strength and ductility development

on stress-redistributions from post peak material characteristics. It is mainly centred on the suggestion that strength and ductility of concrete structures depend significantly on local triaxial stress conditions emanating from within the compressive zone prior to

Figure 2.3: Compressive strength-unit density curve representation for 28-day and 120-day old concretes (Dilli et al., 2015)

failure with evidence of applicability in the behaviour prediction for NWC at ultimate limit state (Kotsovos and Pavlovic, 1995; Engen et al., 2015).

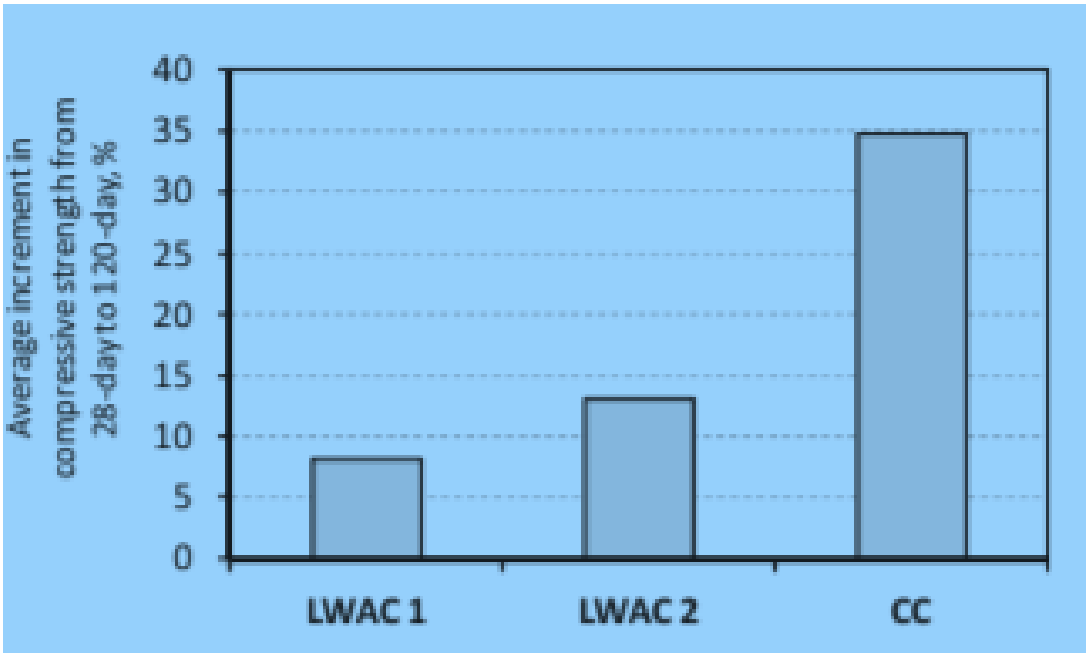

Figure 2.4: Relationship between Compressive strength

Figure 2.5: Average compressive strength-increase for LWAC-1, LWAC-2 and CC mixtures from 28-day -120day period (Dilli et al., 2015)

The overall compressive strength of the LWAC can be understood from previous findings reported above on the comparative effect of mortar strength to the overall LWAC strength implying that to a certain limit, LWAC strength will be dependent on mortar strength (Overli, 2017; Dilli et al., 2015). Within the limit governed by the mortar strength, LWAC behaves like NWC while above the limit, stiffness characteristics does set in with the mortar eventually sustaining a significant part of the load. This limit defines the transition between class 1 to class 2 concrete. Hence, the class 1 phase is characterised by stronger and stiffer particles embedded in a weaker and softer matrix while class 2 phase refers to the transformed concrete phase where softer and weaker particles become embedded in stronger and stiffer matrix. This knowledge clearly describes the final failure of the class two concrete as being propagated from the initial splitting of the aggregate as a result of their lower strength and tensile stress concentrations around the aggregate (see Figure 2.6). Overli (2017) highlights that the splitting failure is initiated from microcracks which propagate into the mortar when the tensile stress concentration around the aggregate exceeds the strain energy capacity. This failure mechanism for concrete can be exacerbated if a redistribution of these stresses does not occur or if the bond between the aggregates and the cement-mortar is weak. The failure mechanism described above provides an understanding of the tensile failure of concrete and informs the principle behind improved or optimised mortar strength in the design and development of LWAC.

Overli (2017), opposes the uniaxial compressive stress-strain model for LWAC against NWC published in EC 2 which suggest a sharp distinction between the two types of concrete. He argues that the linear stress-strain profile for the LWAC does not represent the microcracking behaviour discussed above whereas, the steep drop in profile assumes a very brittle failure for LWAC against NWC. He emphasises that such illustration

generates a limiting barrier in the development of LWAC of considerable strength using significantly stiff lightweight aggregates.

Figure 2.6: Internal stress transfer in concrete under a compressive load (source: Bardhan-Roy and Crozier, 1983)

2.2.2 Strength Properties of FRP

Manufacturers of pultruded GFRP profiles would typically provide information on mechanical properties for the full section as a guidance to aid design. However, studies do often demand verification of these properties to determine the actual behaviour of pultruded profiles subject to loading. One of the major studies relevant for assessing the performance of a beam section is the investigation of lateral-torsional buckling. The two most relevant properties of elasticity modulus E and shear modulus G are determined as necessary in predicting the Lateral-Torsional Buckling (LTB) resistance of a beam.

The orientation of fibres within pultruded FRP material has an influence on the behavioural properties of the composite Zhang et al. (2018). The GFRP composite is considered to have a uniaxial fibre strength of 2350 - 4830 MPa with tensile modulus of 72 – 88 GPa and corresponding resin strength of 65 - 90 MPa with modulus of 3 - 4 GPa respectively (Bank 2006; Gibson, 2011; Zhang et al., 2018). Three dominant properties are necessary for the evaluation of FRP performance in the current study. These properties include tensile, shear and bearing properties of the FRP profile.

Zhang et al. (2018) proposed a modified formula for determining the off-axis strength of FRP plates. The proposed formula was modified from the Hankinson expression for the strength property of wood as in equation 2.1.

$$\sigma_\theta = \frac{\sigma_0 \sigma_{90}}{\sigma_0 Sin^n\theta + \sigma_{90} Cos^n\theta}$$

Equation 2.1

Where σ_θ = off-axis strength of plate;

σ_0 = plate longitudinal strength;

σ_{90}= plate transverse strength;

θ = off-axis angle;

n= empirical coefficient.

Hankinson's formula has been accurately applied to orthotropic wood materials but with limited success to other orthotropic materials (Zhang et al., 2018). The results of unsuccessful application of Hankinson's formula to FRP led to the proposed modified expression by Zhang et al. (2018). Zhang estimates the exponential coefficient on the

Hankinson's formula to derive a modified equation tailored to FRP materials with a predetermined correlation efficiency.

Modified equation given in equation 2.2:

$$\sigma_\theta = \frac{\sigma_0 \sigma_{90}}{\sigma_0 Sin^{1.284}\theta + \sigma_{90} Cos^{1.284}\theta}$$

Equation 2.2

The value of exponential coefficient for FRP is estimated to be 1.284 ± 0.045 which is below the value range of 1.5 – 2 estimated for compressive and tensile strength of wood. Zhang proposed an equation for the prediction of corresponding elastic modulus of FRP as given in equation 2.3.

$$E_\theta = \frac{E_0 E_{90}}{E_0 Sin^{1.386}\theta + E_{90} Cos^{1.386}\theta}$$

Equation 2.3

2.2.2.1 10 Degree (10^0) Off-axis tensile test method

The 10^0 off-axis test has become more practical due to continuous research on the need to establish test methods capable of producing pure shear in thin-narrow material as well as providing time efficiency and material conservation. Previous test includes the three-point-bend short-beam-shear test (ASTM D-2344-72) which is profitable for material control. Chamis (1976) opposed the reliability on the test data by citing the non-uniformity of shear stress generated through the specimen thickness and the inability of the test to generate total stresses of shear-stress shear-strain rather than limiting fracture stress.

Following the activities of several researchers, recommendations for the use of the 10^0 off-axis test has become widely accepted due to the benefits below.

- Simplicity of test method and specimen
- Time efficiency
- Material conservation
- Commonness of test equipment setup
- Conservativeness of results and correlation to theoretical predictions

The background governing the equations for predicting shear stress and shear strain are developed from the studies of relative stress magnitude at 10^0 plane using the equilibrium of forces theory to assess the combined stress and strength of the material. When a 10^0 off-axis specimen is subjected to an axial load, a bi-axial stress state is induced consisting of three stress units, longitudinal stress σ_{11}, transverse stress σ_{22} and intralaminar shear σ_{12} at the 10^0 plane. For the biaxial stress state to satisfy the conditions for shear, the fracture of the specimen must occur at the 10^0 plane when the intralaminar shear σ_{12} reaches it critical value before the other two stresses.

Chamis and Sinclair (1976) adopted the force equilibrium theory to find the relative stress magnitude of a ply with fibres oriented at an angle (θ) from the load direction (see Figure 2.7). The derived equations are presented in the corresponding equations below:

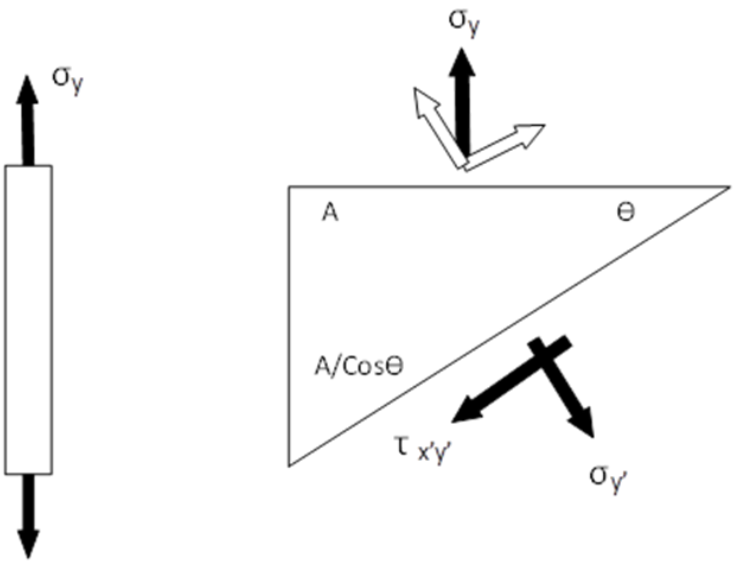

Figure 2.7: Stress Resolution from Equilibrium Theory

$$\sigma_y A Cos\theta = \sigma_{y'}\left({}^{A}/_{Cos\theta}\right)$$

Equation 2.4

$$\sigma_{y'} = \sigma_y Cos^2\theta$$

Equation 2.5

As $\sigma_{y'} \rightarrow \sigma_{11}$ and $\sigma_y \rightarrow \sigma_{xx}$

$$\sigma_{11'} = \sigma_{xx} Cos^2\theta$$

Equation 2.6

Also using the same equilibrium of forces theory, we can derive,

$$\sigma_{22'} = \sigma_{yy} Sin^2\theta$$

Equation 2.7

$$\sigma_{12'} = \sigma_{xy} Sin^2\theta$$

Equation 2.8

A fully developed form of the equation above into a matrix representation common in studies is given below.

$$\begin{matrix} \sigma_{11'} \\ \sigma_{22'} \\ \sigma_{12'} \end{matrix} = \begin{matrix} Cos^2\theta & Sin^2\theta & 2Cos\theta Sin\theta \\ Sin^2\theta & Cos^2\theta & -2Cos\theta Sin\theta \\ -Cos^2\theta Sin^2\theta & Cos\theta Sin\theta & Cos^2\theta - Sin^2\theta \end{matrix} \times \begin{matrix} \sigma_{xx} \\ \sigma_{yy} \\ \sigma_{xy} \end{matrix}$$

Equation 2.9

Substituting 10^0 into Equations 2.6 – 2.8

$$\sigma_{11'} = 0.97\sigma_{yy}$$

Equation 2.10

$$\sigma_{22'} = 0.03\sigma_{xx}$$

Equation 2.11

$$\sigma_{12'} = 0.17\sigma_{xy}$$

Equation 2.12

Equations (2.11) and (2.12) represent the magnitudes for transverse and intralaminar shear stresses. As could be observed from the equation, the intralaminar shear is about six times greater than the transverse stress. The σ_{yy} and σ_{xx} denotes the ply strength in the longitudinal and transverse axes measured from the test.

From the strain transformation equation, we have

$$\begin{matrix} \varepsilon_{11'} \\ \varepsilon_{22'} \\ 0.5\gamma_{12'} \end{matrix} = \begin{matrix} Cos^2\theta & Sin^2\theta & 2Cos\theta Sin\theta \\ Sin^2\theta & Cos^2\theta & -2Cos\theta Sin\theta \\ -Cos^2\theta Sin^2\theta & Cos\theta Sin\theta & Cos^2\theta - Sin^2\theta \end{matrix} \times \begin{matrix} \varepsilon_{xx} \\ \varepsilon_{yy} \\ 0.5\gamma_{xy} \end{matrix}$$

Equation 2.13

Substituting for $\theta = 10^0$ in Eq. 2.13, the principal shear strain is given by Eq. 2.14

$$\gamma_{12} = -0.34(\varepsilon_{xx} - \varepsilon_{yy}) + 0.94\gamma_{xy}$$

Equation 2.14

Stacked "rosette" strain gauge can be used to measure the three strain components of ε_{xx}, ε_{yy} and γ_{xy} representative of 0^0, 45^0 and 90^0 loaded in the tensile direction.

Substituting these strain gauges with directions into Eq. 2.13:

$$\begin{matrix} \varepsilon_0 \\ \varepsilon_{90} \\ \varepsilon_{45} \end{matrix} = \begin{matrix} Cos^2\theta_1 & Sin^2\theta_1 & 2Cos\theta_1 Sin\theta_1 \\ Sin^2\theta_2 & Cos^2\theta_2 & 2Cos\theta_2 Sin\theta_2 \\ -Cos^2\theta_3 & Sin^2\theta_3 & 2Cos\theta_3 Sin\theta_3 \end{matrix} \times \begin{matrix} \varepsilon_{xx} \\ \varepsilon_{yy} \\ 0.5\gamma_{xy} \end{matrix}$$

Equation 2.15

θ_1, θ_2 and θ_3 are the angles subtended between the loading axis x with the strain gauges measuringε_0, ε_{90} and ε_{45}. Substituting θ_1= 0^o, θ_2= 90^o and θ_3= 45^o in Eq. (2.15), we can then evaluate the matrix above:

$$\varepsilon_0 = \varepsilon_{xx}$$

Equation 2.16

$$\varepsilon_{90} = \varepsilon_{yy}$$

Equation 2.17

$$\varepsilon_{45} = 0.5\varepsilon_{xx} + 0.5\varepsilon_{yy} + 0.5\gamma_{xy}$$

Equation 2.18

Resolving Eq. (2.18), we have;

γ_{xy}=2ε_{45} - ε_{xx} - ε_{yy} then Substituting ε_{xx} = ε_0 and ε_{yy} = ε_{90} in the equation

$$\gamma_{xy} = 2\varepsilon_{45} - \varepsilon_{90} - \varepsilon_0$$

Equation 2.19

To obtain the required shear strain from the measured strain, we substitute equation (2.19) into (2.14):

$$\gamma_{12} = 1.88\varepsilon_{45} - 1.28\varepsilon_0 - 0.60\varepsilon_{90}$$

Equation 2.20

Therefore, the expression for the in-plane shear modulus is thus given by equation 2.21:

$$G_{12} = \frac{\sigma_{12}}{\gamma_{12}} = \frac{Eq.2.7}{Eq.2.13} = \frac{0.17\sigma_{xy}}{1.88\varepsilon_{45} - 1.28\varepsilon_0 - 0.60\varepsilon_{90}}$$

Equation 2.21

In the absence of reliable experimental setup for the determination of compressive and tensile strength of off-axis fibre-oriented profiles, the equation presented above can be applied as a reliability test for an approximate prediction of the strength values of the profiles with an adoption of the lowest conservative value based on Zhang et al. (2018) findings that the experimental test reported significantly lower values.

2.3 Interfacial Slip Behaviour

Transverse shear forces are usually initiated in beams subjected to bending although the effect of these shear forces cannot be observed easily on plane uniform sections. However, the effect of the forces can become quite conspicuous in structural composite beam sections consisting of parallel subcomponents. The forces are derived from the

horizontal bending of the beam section such that a shear plane exist at the interface between the concrete and FRP section. As the bending action intensifies, the action of forces at the shear interface increases resulting in a sliding action of one subcomponent over the other. This sliding effect between the two subcomponents of conventional steel and concrete (or FRP and LWAC as in the case of the current study) is referred to as the transverse shear interaction, (see Figure 2.8). The transverse shear force is maximum at the horizontal interface between the subcomponents when the peak flexural capacity of the composite structural beam is reached. Experimental studies have developed companion models to adequately study and describe the interfacial slip behaviour of steel-concrete composites with a standard experimental test procedure outlined in Eurocode 4 (2004) commonly referred to as the push-out test. The test is designed for the prediction of shear capacity and related parameters of a typical steel-concrete composite (see Figure 2.9). The test comprises of two vertical concrete slabs of effective width and a vertically positioned steel profiled section. The steel section flange (positioned in the longitudinal direction to the vertical) is connected to a pair of vertically positioned concrete slab by means of shear connectors either welded or bolted on the flanges of the steel section. The steel-concrete push-out test is a modified version of an earlier standard shear test detailed in BS 5900 (1996). The revised test accommodates the effect of longitudinal spacing of studs and has been reported to influence shear capacity (Qureshi et al., 2011a). Researchers have adopted the push-out test for investigations of modified steel-concrete connections, including novel and standard shear connectors. The flexibility and adaptability of the push-out test to predict interfacial shear behaviour and evaluate associated parameters cannot be overemphasized. Jin et al. (2018) investigated the performance of perfobond connectors in steel-concrete joints and reported significant

performance of connectors under push-out experimental testing for improved shearing capacity. Emad *et al*. (2018) carried out push-out experimental studies on the shear opening of steel beam for slim-floor systems. Their investigations successfully proposed

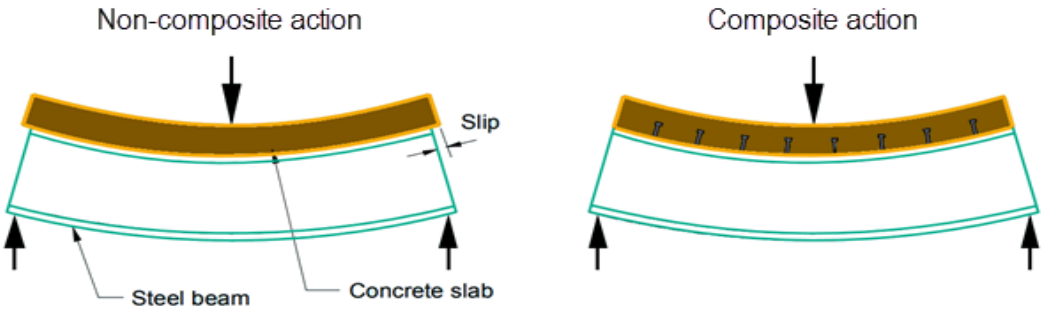

Figure 2.8: Interfacial slip between subcomponents

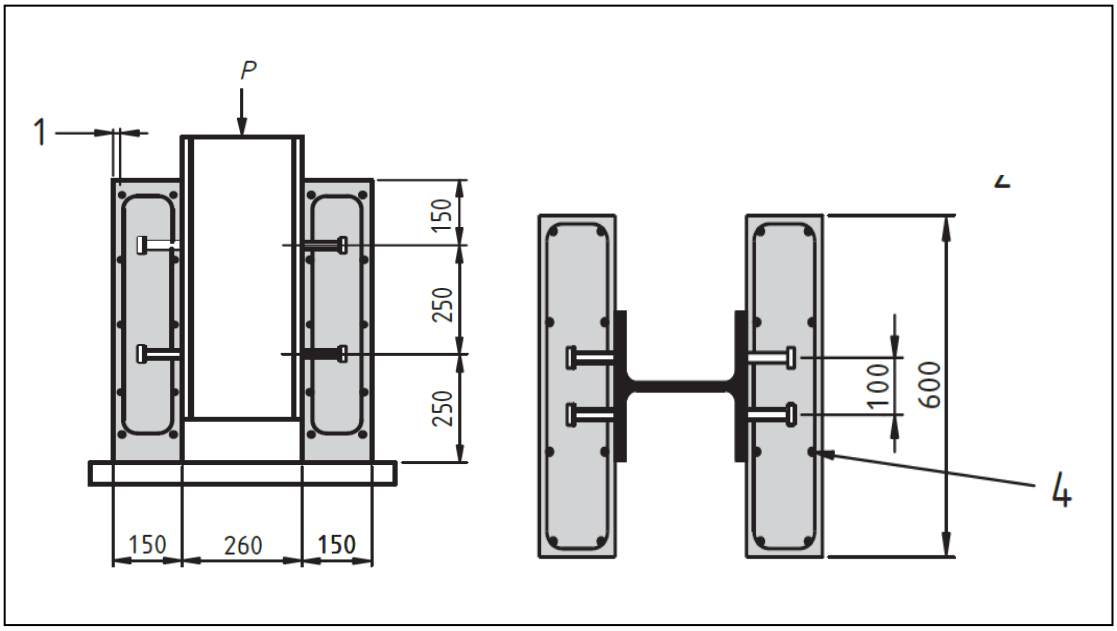

Figure 2.9: Standard Push-Out test specimen (EC4)

effective spacing for various shapes of openings to attain maximum shear strength. Their

research adopted the push-out experimental set-up for evaluation of performance and reliable data analysis was derived from this test method.

Despite the reported success of the test in closely predicting shear behaviour and capacity of steel-concrete composites, various studies have continued to highlight some of the test deficiencies in predicting the actual shear performance of steel-concrete composite beams (Ollgaard et al., 1971; Hicks, 2014; Rehman et al., 2016; Odenbreit and Nellinger, 2017). Hicks (2014) observed a significant difference in results obtained from companion push-out test and composite beam test. His investigations suggested that the observed difference in results were due to the absence of compression force at the concrete-flange interface exerted by floor loading. Odenbreit and Nellinger (2017) observed that the magnitude of the tension force F_{ten} is affected by frictional forces developing at the base of the slab at the interface between the test slabs and the strong floor. Odenbreit and Nellinger (2017) reported that the influence of frictional forces causes sliding bearings, which may underestimate the real shear resistance of the connection. However, all these investigations have not deterred or undermined the growing dependence on push-out test experiments for the investigation of novel composite materials including timber-concrete, timber-steel, and more recently FRP-concrete composites respectively. The need for experimental testing to be carried out on novel composite beams remain a factor for the growing dependence on push-out test experiments. This forms the basis of the method employed to investigate the performance of the novel composite connection between pultruded fibre reinforced polymer (PFRP) and concrete.

2.3.1 Push-out Model

Hicks (2014) illustrates how shear interaction can occur between steel and concrete composite by using a force-interaction model (see Figure 2.10) to demonstrate an understanding of the push-out experimental test design. The significance of the model was developed to highlight a critical omission of the push-out design outlined in EC4 and to further evaluate the effect of such omission on the shear capacity of studs. The force-interaction model outlines relevant forces generated at the shear interface of the composite beam due to increase bending of the section. The forces together with the shear studs were used to derive the required shear resistance capacity for the composite section.

The force-interaction model highlights two sets of equilibrium within the embedded stud and at the interface of the connection. The first equilibrium exists between the longitudinal shear forces (F_1) and concrete compressive forces (F_c) and transverse tensile

Figure 2.10: Push-out force-interaction model (Source: Hicks, 2014)

forces from the rebars (F_{sf}) as shown in Figure 2.10(a). Hicks (2014) highlights a second equilibrium from the inclination of the embedded stud in the concrete and the uplift reaction force due to increased bending (see Figure 2.10b). Based on Hicks illustrated model, an understanding of the push-out test can be captured for further investigations.

Some of these studies are discussed in subsections under the expected performance criteria established by engineering design. The performance criteria include stud shear capacity, stiffness, ductility and failure modes. Subsequent discussions will explore the findings of steel-concrete components to substantiate the limited knowledge and findings on FRP-concrete composites. This is necessary and feasible because most of the limited research have not highlighted many significant deviations in the pattern or behaviour observed in steel structural composite hence, the knowledge of steel-concrete composite is relevant in the understanding of FRP-concrete composite behaviour. Nevertheless, FRP-concrete composites do deviate from steel in other aspects of their mechanism and performance to which the purpose of the current research is based. Such deviations result in unfamiliar composite behaviours including failure modes and variable shear capacities. Sections 2.3.2 and 2.3.3 will discuss some of the findings under these behaviours for steel-concrete and FRP-concrete structural composites.

2.3.2 Shear capacity and stiffness

Shear capacity and stiffness are a direct functions of stud capacity therefore, the type of stud used for the shear connection is vital in the design and development of composite beams. Ollgaard et al. (1971) outlined the historical evolution of shear connectors for structural composites beginning with an early use of spiral connectors for bridge construction. Historical changes in the use of connectors have witnessed series of changes

in the use of connectors for over 50 years with more rapid use of flexible channels and stud connectors in recent years. Today, shear connection in conventional steel-concrete composites is achieved by welding or bolted action although recent studies have attempted the use of bonding action by using high strength adhesives (Jayajothi et al., 2013).

Shear connection techniques can influence the shear behaviour and capacity of these structural composites. The shear capacity of demountable shear connectors is reported to be slightly higher than that of their welded counterparts (Jayas et al. 1988; Nguyen et al., 2014; Rehman et al. 2016; Yang et al., 2018), ductility of demountable (bolted) connections is reported to be higher than that of welded shear connectors even though the initial stiffness is typically much lower. Yang et al. (2018) observed a closed range in the shear capacities of M22 bolted connectors against their welded counterpart and reported that M27 bolted connectors mobilised shear strength up to 1.6 times that of their welded counterpart with a predicted capacity of 0.8 times the bolt tensile strength which agrees with predictive equation (see table 2.4) outlined in EC4. Also, shear capacity, ductility and stiffness behaviour of profiled metal decking slabs compare evenly to that of solid slabs with an exception that the ultimate strength of demountable connectors in solid slabs are typically higher than profiled metal deck slabs (Rehman et al., 2016; Odenbreit, 2017). Odenbreit describes the lower shear capacity to be due to a reducing effect of the trapezoidal profiled deck. Rehman et al. (2016) explained that such difference may be attributed to higher concrete confinement strength around the connectors whereas the profiled metal deck provides less confinement owing to its trough but however, reported that shear slip was relatively lower for the solid slab compared to profiled metal slabs.

Unlike conventional steel-concrete composites, FRP-concrete composites can only be connected as demountable members using bolts or bond adhesives. Nguyen et al. (2014) reported findings for both stud connections and adhesive bonded connections. Bonded shear connections were characterised as brittle following high initial stiffness and shear capacities but with sudden fall from peak strength. Nguyen (2014) further observed that when shear studs were used along with bond adhesives, the load-slip curve exhibited early linear progression with sudden drop into a nonlinear propagation up until failure. The study suggested that shear resistance is solely sustained by the adhesive until debonding fully occurs and the shear load is then transferred to the connectors. If the bond adhesive strength is higher than the shear connector strength, then the load-slip curve will be characterised by only the sustained linear plot until failure occurs with a sudden drop in strength. Nguyen's investigation promotes the use of combined bond adhesive and shear connectors as hybrid connections suggesting that shear studs can provide reserve strength and ductility required for FRP-concrete composites. Nguyen et al. established that with the use of shear connectors with h_{ef}/d ratios of 2.4 and above, ductile connections can be achieved from both epoxy bonded and non-epoxy bonded UHPFRC-FRP composites to achieve reserve capacity.

In general, researchers have reported unanimous findings on the influence of concrete confinement strength and/or stud collar diameter on the shear capacity for demountable shear connections (Dai et al., 2015; Rehman et al., 2016). These influences are discussed further below.

2.3.2.1 Influence of stud geometry

An and Cederwall (1996) characterises the strength performance of a shear stud as a function of its geometrical design such as stud height, diameter and shape design. In addition, the stud tensile property and the embedded concrete environment contributes to the effective performance of the shear connection (Dai et al., 2015). Published findings for composites have provided significant evidence on the influence of stud diameter on the resistance capacity for shear connections. Yang et al. (2018) reported higher slip values corresponding to increase in bolt diameters. He also observed some correlation between shear stiffness or strength and bolt diameter suggesting that shear stiffness of bolted connector decreases with increase of bolt clearance holes. The differences in initial stiffness can be attributed to clearance holes for bolted connections and can be subsequently improved by reduction in clearance hole allowance or through pre-tension of bolts (Qureshi et al., 2011; Yang et al., 2018). The drop in initial stiffness during a push-out test was also observed by Nguyen et al. (2014) who suggested that it was due to a gradual slippage of the bolt connector into a bearing region around the clearance holes. Higher diameter sizes of stud have shown significantly higher shear capacities and stiffnesses for both steel-concrete and FRP-concrete composites. Some of the reported values of strength against the stud diameters are presented in Table 2.5 below.

The concept of h_{ef}/d ratios were adopted by Nguyen et al. (2014) as a descriptive criterion to evaluate the performance of shear studs and their typical failure modes in UHPFRC – FRP composites. The method adopted a ratio of the stud height to its diameter to formulate design criteria for characterising stud performance and corresponding behaviour for FRP-concrete composites. Smaller values of h_{ef}/d ratios were used to describe typically short

and stiff shear connectors which are capable of bending in a single curvature mode under direct shear force while higher values of h_{ef}/d ratio depicted longer and less stiff shear connectors capable of bending in a double curvature mode with the embedded head portion of the connector constantly fixed in the concrete slab. Nguyen (2014) highlighted that the area of concrete failure was directly proportional to the h_{ef}/d ratios and as such smaller h_{ef}/d ratios may result in more severe cracks than larger h_{ef}/d ratios. Nguyen (2014) established three h_{ef}/d boundary values for characterising shear failure; a) h_{ef}/d values between 1.3 – 1.6 for concrete cracking of slabs, bearing failure of HFRP/GFRP flanges and shearing failure of the bolt connectors, b) h_{ef}/d values between 1.6 - 2.4 characterized bearing failure of FRP girder and/or shearing failure of connectors, c) h_{ef}/d values between 2.4 - 2.9 were governed by shearing failure of the connectors. However, the findings did not account for failure modes for a range of h_{ef}/d values less than 1.3 or greater than 2.9. This review presents a summary of some of the failure modes reported from literature based on Nguyen's h_{ef}/d value criteria of stud geometry for both steel-concrete and FRP-concrete composites under shear evaluation.

Table 2.5: Load capacity for various stud diameters from literature findings

S/N	*Authors*	*Stud diameter size (mm)*	*Load per stud (kN)*	*Stud strength (MPa)*	*Compression subcomponent strength (MPa)*	*Tension subcomponent type*	*Failure modes*
1	An & Cedarwall	19	120		NWC	steel	Stud fracture/concrete failures
2	Correia et al	8	17	480/D	43/NWC	GFRP	Stud fracture
3	Correia et al.	10	39	480/D	40/NWC	GFRP	Stud fracture
4	Dai et al.	16	75	Demountable	NWC	steel	Stud fracture
5	Dai et al.	17	94	Demountable	NWC	steel	Stud fracture
6	Dai et al.	18	108	Demountable	NWC	steel	Stud fracture
7	Hicks, S.	19	53	Welded	NWC	steel	-
8	Lowe, D.			-	NWC	steel	-
9	Nguyen	10	31	Demountable	UHPFRC	HFRP	Stud fracture
10	Nguyen	16	97	Demountable	UHPFRC	HFRP	Stud bending/HFRP bearing failures
11	Odenbreit & Nellinger	19	37	-	NWC	steel	-
12	Ollgaard	16	92	-	NWC	steel	-
13	Ollgaard	19	136	-	NWC	steel	-
14	Prakash	20	132	-	NWC	steel	-
15	Qureshi	-	-	-	NWC	steel	-
16	Rehman	16	80	-	NWC	steel	-
17	Rehman	20	66	-	NWC	steel	-
18	Shen, H.	19	121	Welded	NWC	steel	-
19	Shen, H.	19	58	Welded	*NWC	steel	-
20	Yang	18	170	-	NWC	steel	Stud failures

21	Yang	22	229	-	NWC	steel	-
22	Yang	27	346	-	NWC	steel	-
23	Zou	10	25	Demountable	NWC	GFRP	-
24	Zou	10	38	Demountable	HSC	GFRP	-

(*) – profiled slabs

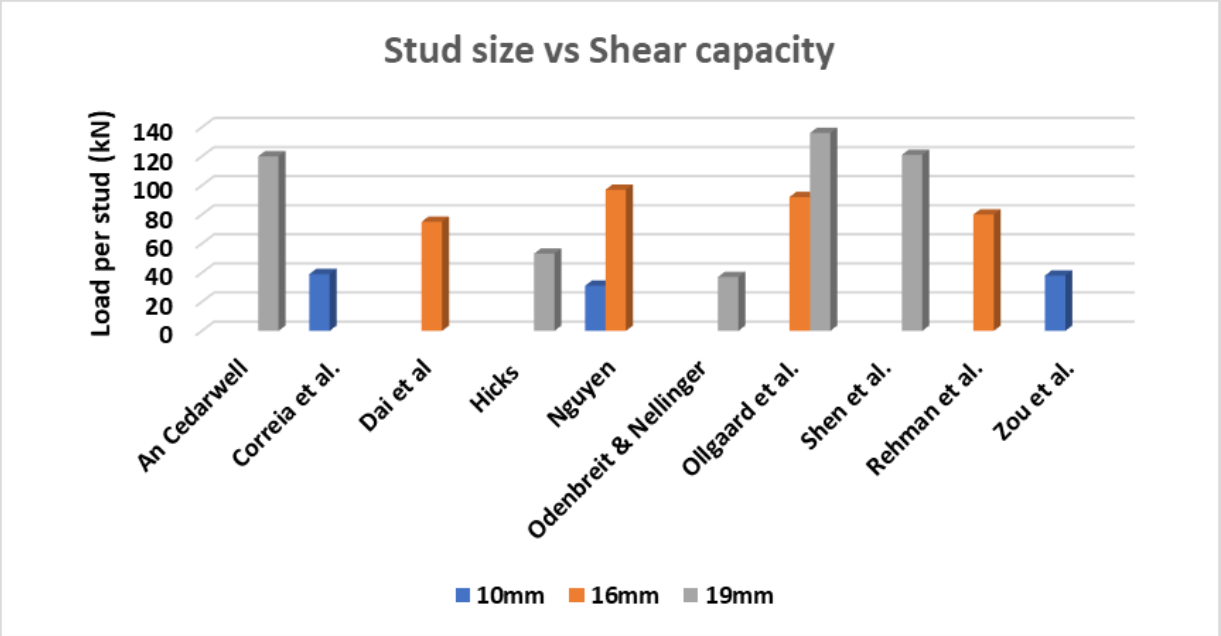

Figure 2.11: Stud size influence on shear strength

To get a better understanding of the findings from literature, a summary chart is presented in Figure 2.11 to show the size influence of studs on shear strength. The chart represents some of the reported values from literature provided in table 2.5 and clearly show the collar size relationship with shear strength while also corroborating findings among researchers. However, variability in shear strength is a direct result of the multivariate parameters that characterise various experimental studies in literature. These parameters include variable concrete strength properties, stud strength, tensile subcomponent, loading rates and experimental modifications.

Spacing between connectors have also been reported to have direct effect on the shear strength of connections (Qureshi et al. 2011). However, an important property of a connection notably termed as ductility is highly attainable in the two shear (pair) connector per trough compared to the single connector per trough (Rehman et al 2016, Qureshi et al. 2011). Nguyen et al. (2014) also reported that inclined bolts attained up to 1.8 times the shear strength of straight bolt shear connectors of same geometric and material identities. He attributed these to the inclination of the bolts which allowed it to bend and slip inside the slabs to resist additional shear force after cracking of the concrete slabs. This is evident from the zigzag behaviour observed on a load-slip graph indicating multiple cracks inside the ultra-high-performance fibre reinforced concrete (UHPFRC) which is not visible on the surface.

Several researchers (Shen et al., 2020; Ollgaard et al., 1971; Odenbreit and Nellinger, 2017) have reported that 19mm diameter shear studs show very ductile behaviour. Rehman et al. (2016) reports a slip of 6-10mm observed for 19mm diameter connectors which fulfils the ductile limit of 6mm in Eurocode 4 (BS EN 1994-1-1: 2004). Rehman et al. concluded that stiffness increased relatively with increase in concrete strength. Studies on reinforcement modification also carried out by Rehman et al. (2016) demonstrated that reinforcement contributed to an improvement in shear capacity. Increased stiffness can be observed with increased shear connector diameter as demonstrated by Rehman et al. (2016). Nguyen et al. (2014) investigation compared three bolt types; stainless headed steel bolt, high corrosion resistant headed steel bolt and stainless steel inclined bolt connectors. However, load slip plots for straight and inclined bolt were similar but with conspicuous wave-like plots suggesting increased concrete cracking resulting from stud resistance.

Nguyen et al. (2014) noted that the compressive strength was insignificant for GFRP bolts because of the relatively low stiffness and brittle behaviour which limited their ability to slip under resistance to further forces of shear. Nguyen et al. (2014) determined a minimum stud embedment depth of 30mm as practicable for lightweight concrete – FRP composites. However, the depth was determined from a slab minimum thickness of 35mm which therefore begs the question; if the slab thickness was greater, can a minimum depth lower than 30mm be achieved? This could have been easily concluded from his investigation but the studies on end distance was carried out with inclined bolt which already established higher shear strength over straight bolt connectors. Inclined bolt connectors were reported to exceed their shear strength during investigation and were reportedly concluded to bear load by shearing and bending. This further requires the investigation on the effect of end distance relative to effective depth for straight headed shear connectors.

2.3.2.2 Concrete strength Influences

Early knowledge on the influence of concrete strength was promoted by Driscoll and Slutter (1961) who established a relationship between shear connector strength and concrete compressive strength. Further experimental investigations have sort to determine the influence of other concrete properties on the shear strength of composite connections. Some of the investigations include; influence of concrete density, tensile strength, and modulus of elasticity. Ollgaard et al. (1971) began early investigation of the effect of concrete density on shear strength by comparing lightweight aggregate concrete (LWAC) and normal weight concrete (NWC). The istudy observed a decreasing shear connection capacity with decrease concrete density. There has been no significant reports on the influence of concrete tensile strength on the shear capacity although a good correlation has been reported for concrete modulus of elasticity taken from compressive strength behaviour between LWAC and NWC (Ollgaard et al., 1971).

Rehman et al. (2016) reported brittle failure in concrete of high strength at a slip of 6 – 7mm corresponding to the maximum load (slip fulfilled ductility limit provided in Eurocode 4). This observation suggests a full mobilization of stud deformation therefore, with a relatively high concrete strength, shear connector fracture shall be conspicuous with no significant concrete crushing. However, slip is reported to be more significant in specimens with lower concrete strength because the concrete allows the shear connectors to move within its surrounding (Rehman et al. 2016; Nguyen et al., 2014; An and Cederwall 1996). Hence, concrete failure becomes more apparent in specimens with lower concrete strength. Although Rehman et al. (2016) noted that with a single shear connector per trough, concrete strength has no significant effect on shear capacity however, failure mode remains affected by concrete strength. An and Cederwall (1996) reports that the number of reinforcement contained in a normal strength concrete does contributes to shear strength improvements but becomes insignificant in high strength concrete. A review from Ollgaard's study suggest that studs embedded in LWAC have 5 - 40% lower shear capacities compared to their NWC counterparts. The study reported about 15 – 25 % lower strength for studs embedded in LWAC. Ollgaard (1971) observed higher shear capacities in specimens of LWAC having part replacement of lightweight aggregates with normal weight sand in comparison to LWAC with 100% lightweight aggregates. There is reported evidence of good correlation between increased stiffness and increased concrete strength (Rehman et al., 2016; Nguyen et al., 2014; An and Cederwall, 1996). Researchers compared the experimental values for the shear strength of connectors to the manufacturers estimated values. It was reported that the experimental values of the shear strength were higher, and these outcomes are attributed to the high compressive strength of concrete (Nguyen et al. 2014, An and Cederwall 1996).

Rehman et al. (2016) observed that shear connectors with pair connectors per trough recorded 13% lesser shear strength compared to single shear stud per trough of lesser concrete strength

specimen suggesting that shear strength of connectors cannot be fully mobilised with pair connectors when compared to single connectors per trough. High shear capacities can be obtained from connectors provided their concrete resistances are fully mobilised (Rehman et al., 2016).

2.3.2.3 Flange influences

There has been little or no reports on the flange influences of steel sections to shear capacity as most theoretical studies have assumed steel flanges as being rigid members with minimal contribution to the shear capacity of connectors. However, this has not been the case for FRP-concrete composites as flange deformations have been observed in experimental testing. The adoption of standard theoretical equations for the prediction of shear capacity has shown a deviation in the estimated values for FRP-concrete composites against their steel-concrete counterparts. This deviation may be evidence of the significant influence of flange bearing strength for FRP-concrete composites in the overall behaviour and capacity of the structural composite. Typically, steel members are easily perforated for many reasons including service utilities within construction and/or structural connections (such as the current study for FRP). Discontinuities in cross-sectional members (such as cellular beams) pose medium to significant effect on the integrity of connections. Materials of steel have higher tensile and bearing strengths when compared to FRP counterparts hence, flange bearing strength becomes an important consideration in the design of FRP-concrete composites. Nguyen et al. (2014) observed severe fibre delamination failures of the GFRP in his push-out experimental investigation of FRP-concrete shear capacities. Correia et al. (2007) reported web-flange shearing failure from flexural test of FRP-concrete hybrid beams. Matharu & Mottram (2017) had reported that increased bolt clearance holes resulted in decreased bearing strength of FRP flange plates. It should be noted that for PRFP connections, lateral unrestrained pin-bearing failures are characterised by fibre

delamination and material crushing (Mottram & Turvey, 2003; Turvey, 2013; Matharu & Mottram, 2017). The knowledge of pin-bearing strength is necessary in fully understanding the bearing influence of FRP flanges on shear performance and capacity of FRP-concrete composites hence, it has been suggested by Matharu (2017) that pin-baring strength is a function of bolt diameter, material thickness, fibre architecture and orientation, clearance hole size and general boundary conditions. Also, there is reported evidence on bearing strength reduction for FRP plates connected with threaded pins against their plain pins counterparts. American Load and Resistance Factor Design (LRFD) has outlined in its pre-standard for design, the consideration of pin-bearing strength as a mandatory bearing strength per bolts for bearing resistance of pultruded profiles. Accordingly, the following equation was proposed:

$$R_{br} = tdF_0^{br}$$

Equation 2.22

Where t and d represent the thickness of the pultruded flange material and diameter of the bolt connector. R_{br} and F_0^{br} represents the FRP flange bearing strength and pin-bearing strengths respectively. FRP systems of connection may exist either as parallel connections along the longitudinal axis of the profiles (as in the case of the current study) or as transverse connections at perpendicular angles (Matharu & Mottram, 2017). Hence, angle of connection is considered in the determination of pin-bearing strength for FRP pultruded profiles. The current study may attempt to adapt the knowledge of pin-bearing strength to the prediction of FRP-concrete shear capacity.

2.3.3 Failure mechanism at shear interface

Similar failure modes have been reported for both steel-concrete composites and FRP-concrete composites. Steel-concrete composites have been dominated by either steel fracture, concrete sprawling and concrete tensile cracks. Most of the failure behaviour is attributed to the overbearing effect of the above discussed material and geometric influences. In addition to the established failure modes observed in steel-concrete composites, other failure modes have been reported for FRP-concrete composites including FRP flange failures. Nguyen et al. (2014) reported that while straight bolts used in high performing concrete tend to fail majorly by shear connector fracture with minor bearing failure around the connector holes, the failure mode of their inclined counterparts were rather bearing failure of girders, a behaviour observed when using Glass Fibre Reinforced Polymer (GFRP) and Hybrid Fibre reinforced Polymer (HFRP) girders as alternative to conventional steel. Some of these failure modes are discussed in subsections below.

2.3.3.1 Concrete cone failure

The concrete cone failure typically associated with concrete crushing and cracks is one typical failure mode observed in steel-concrete push-out test as well as FRP-concrete composites and may be independent of shear connector failure or occur as a combined failure along with shear connector failure. This type of failure occurs when the concrete around the shear connector fails in compression producing a crack propagation while also forming a cone-like boundary of concrete through its depth bearing against the concrete surrounding (see Figure 2.12). During compression loading, transverse cracks can be typically observed at the outer surfaces of concrete and can proliferate with loading intensity but may be controlled or mitigated using steel reinforcement or anti-crack mesh which ensures the propagation does not extend into the depth of the concrete. Rehman et al (2016) reports that damage patterns in concrete specimen from push-

out test are very similar irrespective of the shear connector arrangement or the concrete strength. However, Rehman (2016) emphasizes that concrete cone failure is less severe in concrete specimens with single shear connector per trough compared to concrete specimens with pair shear connectors per trough. The severity of concrete failure is further influenced by the size diameter of the stud hence, the failure exacerbation is attributed to an induced higher shear resistance and compression on the concrete around the shear connectors as reported in previous sections. Combined concrete cone failure, shear connector fracture and concrete crushing have been reported by several researchers (see Table 2.5). Typical failures observed on profile metal decking slabs also include longitudinal crack propagation across slab causing concrete rib failure, profile metal connector hole deformation etc.

Figure 2.12: Concrete sprawling and cone failure

2.3.3.2 Shear connector failure

This type of failure is observed when the stud connector attains its maximum yield stress before the concrete ultimate compressive strength is reached. It is characterized by some bending of the stud connector showing its yielding process and a fracture at the collar end of the shear connector for failure (see Figure 2.13). Rehman et al. (2016) reports that shear connector failure is mostly significant with high concrete strength and observed that the deformation of shear connectors was less significant in concrete specimens of higher strength compared to those of lower strength. Yang et al. (2018) investigated the performance of various types of demountable stud connectors and reported that failure modes of demountable studs were slightly different from their welded counterpart and that the clearance between stud holes and stud shanks had a significant effect on the shear stiffness of stud connectors.

The stud failure mode can be understood from the simplified failure model illustrated by Odenbreit and Nellinger (2017) for single and double plastic hinge formations (see Figure 2.14). The model explains that the number of plastic hinges that may form is dependent on shaft anchorage length above the top flange of steel sheeting for a profiled slab. Hicks (2014) hypothetically reports that single curvature deformations (plastic hinges) are common for solid slabs while double curvature deformations (plastic hinges) were common for profiled slabs. Nellinger (2015) proposes

equations for the prediction of stud plastic yield suggesting that complete formation of hinges (double curvature) can occur if $h_A \geq 2d\sqrt{n_r}$ and only one hinge may form if the $h_A \leq 2d\sqrt{n_r}$.

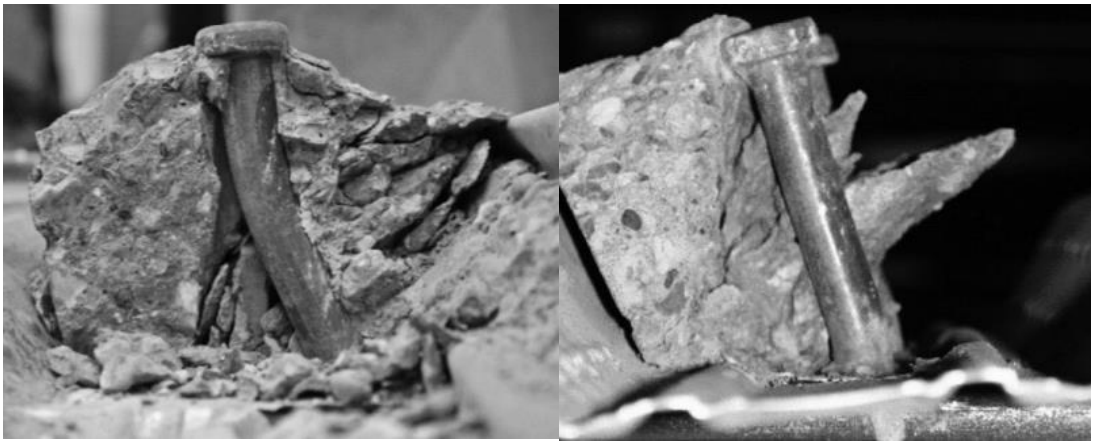

(a) Double curvature (b) Single Curvature

(c) Stud fracture

Figure 2.13(a-c); Plastic yielding and fracture failures of stud connectors

Figure 2.14: Plastic yielding mechanism of studs (Source: Odenbreit & Nellinger, 2017)

The discussions above on the influence of subcomponent properties and failure modes for shear capacity and stiffness of structural composites have led to the development of theoretical principles and equations to predict shear properties of these structural composites. The equations were earlier established for steel-concrete composites but has been modified over the years for accurate predictions and adapted for other materials such as FRP-concrete composites. Most of the equations are founded on similar fundamental principles reflecting failure components or subcomponent strength influences.

2.3.3.3 Flange fibre delamination

Fibre reinforced polymers (FRP) have been reported to have inherent imperfections owing to the fibre architecture inconsistencies from the manufacturing process. Cintra et al. (2021) correlated material imperfections examined from optical microscopic analysis against crack formation and propagation of web flange junctions of GFRP sections. The investigation noted differences in fibre architecture imperfections for channel and I-sections and reported that all sections have manufacturing imperfections at the jointed regions. Notably, three types of manufacturing

imperfections exist: mat wrinkling due to fibre pultrusion, intralaminar pre-cracks from matrix and incidence of void respectively. Although the research investigation (Cintra et al., 2021) studied the rotational stiffness of PFRP web flange joints (WBJ), further research studies have reported web flange joint failures under compression and shear load experimentation of GFRP profiles. Zou et al. (2020) reported horizontal shear fractures which propagated close to the WBJ at support of an FRP-concrete composite during experimental testing. While the investigation did not report on possible causes for the failure, it is important to note that the position of the failures were initiated around WBJ located close to the shear interface between concrete slabs and PFRP profile. Nguyen et al (2010) reported brittle failures of FRP compressive flanges for small and wide flange sections. The investigation observed delamination failures at the interfacial layers of the compressive flange for small flange sections and nonlinear unstable behaviour leading to severe delamination failures for wide flange sections. The report noted that stress concentrations at loading points on the flange typically lead to compressive crushing failures thus implying the need for stress distribution at the loading points to prevent premature failures during experimental testing.

The most significantly reported flange failures of FRP sections in composite connections are delamination and bearing failures. Bearing failures occurring around stud/bolt clearance holes due to possible stress concentrations. Nguyen et al. (2014) reported flange failures from bearing stresses which built up around the slipped bolts region on the clearance holes. Matharu and Mottram (2017) describe this failure mode as occurring due to pressure contact between threaded/unthreaded bolts and PFRP materials directly underneath the bolts resulting in delamination fractures and crushing failures of the PFRP fibres. Research investigations have reported that bolt diameters, PFRP thickness, clearance hole size and fibre architecture contribute to strength response of bolted connections to bearing failure (ASCE, 2010; Mottram & Turvey,

2003; Turvey, 1998). Matharu & Mottram (2017) highlights the difficulty to account for all practical influences on bearing strength response of bolted connections but suggest that delamination failures are a result of localised bulging deformations which induces tensile stress fields that dissipate through the thickness of the PFRP layers. The investigation reported increased cracking failures from PRFP plates with threaded bolts compared to their plain counterparts. The study reported that the variation in crack indicated uneven fracturing induced by the embedded bolt threads on the PFRP though thickness. The research findings suggest that cracks are minimised when loading is applied along the direction of the fibre orientation. The current study must consider potential influence of this contributing factors to minimise premature failures of the test specimens.

2.3.4 Theoretical prediction of shear capacity

The existing equations for predicting ultimate shear resistance has been established on the concept of failure modes for steel-concrete composites. Hence, these equations account for either the maximum tensile strength of the shear studs and/or the compressive strength of concrete (reaffirming the influence of compressive strength in stud shear resistance) in combination with reduction factors. The establishment of these equations have come from detailed experimental analysis of the behaviour of these shear studs in composite connections. Several standard equations have been developed from parametric and sensitivity analysis on influencing factors reported by researchers. However, the underlying principle is validly set on observed failure mechanisms of the stud connections under shear actions. Since most of the equations are established from steel-concrete shear relationships, their applicability becomes limited when alternative replacement materials such as FRP are used for composites. This concept of failure mechanisms in the establishment of shear equations for stud connections which does establishes a knowledge gap

because FRP-concrete composites have been reported to exhibit peculiar failure mechanism different from steel-concrete counterparts. Hence, this has become a motivation for recent studies on the use of various types of connectors, girders and concrete materials to fully develop predictive equations and modify experimental test methods for shear composites subjected to bending stresses. Accordingly, many researchers have provided comparative analysis between predictive models and experimental results with diverse outcomes ranging between low-high correlative margins. Nguyen et al. (2014) reported that standard code equations for predicting ultimate resistance of shear connectors for shear failure mode compared relatively well with the experimental results; ACI318-11, AISC 2011, AASHTO LRFD 2010 and PCI 2004 were fairly comparative for stud fracture failures and Eurocode 4 (EC4) closely comparable for concrete failure mode. ACI 318 was reported to be too conservative and Nguyen concluded that the outcome may be attributed to the equation from the code's assumption of a concrete breakout failure. This further emphasizes the gap in knowledge earlier stated and such inconsistency established from findings provides motivation for the current research. Another finding from Nguyen et al. (2014) in his investigation showed that despite the rule of adoption for the governing failure mode which specified smaller values out of the two values for shear connector failure and concrete failure for design, a combined failure was observed in some of the tested specimens. This further illustrates the insufficiency of the present governing standard predictive models. Table 2.6 highlights some of the theoretical equations specified in standard codes for the prediction of ultimate shear resistance. The equations are either suggesting stud fracture failure or concrete sprawling failures. This is representative for most of the existing standard equations from national and international standard specifications for steel-concrete composites. There is a lack of consensus for the establishment of a theoretical equation for the prediction of shear resistance of FRP-concrete composites. From the table, Nguyen (2014) establishes a modified equation from Oehler and

Johnson's equation considering the combine influence of concrete, stud and girder flanges in the failure of FRP-concrete composites (see Table 2.6). This study will review the premise for which Oehler and Johnson formulated the theoretical equation and the modifications adapted for FRP-concrete composites by Nguyen et al (2014).

Table 2.6: Existing equations for the prediction of ultimate shear resistance (source: Adapted from Nquyen et. al. (2014)

S/N	Standard codes	Predictive Equations based of failures		Remarks
		Stud failure	**Concrete failure**	
1	ACI 318-11	$A_{SC}F_u$	$k_{cp}24\lambda\sqrt{f_c'}(h_{ef})^{1.5}$ $k_{cp} = 1\ for\ h_{ef} < 2.5inch$ $k_{cp} = 2\ for\ h_{ef} > 2.5inch\ and\ \lambda = 1\ for\ NWC$	Stud failure is purely as a result of stud strength and diameter. Considers the reduced property of lightweight concrete based on concrete failure
2	AISC, 2011 & AASHTO LRFD, 2010	$A_{SC}F_u$	$0.5A_{SC}\sqrt{f_c'E_c}$	Stud failure is purely as a result of stud strength and diameter. Concrete failure may result from combined stud interaction around embedded area
3	PCI, 2004	$A_{SC}F_u$	$215\lambda\sqrt{f_c'}d^{1.5}(h_{ef})^{0.5}$	Stud failure is purely as a result of stud strength and diameter.
4	Eurocode-4 2004 (EC-4, 2004)	$0.8A_{SC}F_u$	$0.29\alpha d^2\sqrt{f_{ck}E_{cm}}$ where $\alpha = 0.2\left(\frac{h_{cm}}{d}+1\right)$ $for\ 3 \le {}^{h_{cm}}/_{d} \le 4$ and $\alpha = 1\ for\ {}^{h_{cm}}/_{d} > 4$	Provides a reduction factor to account for stud mobilisation effects
5	Oehlers and Johnson (1987)	$P_{R-OJ} = K_{ch}A_{SC}F_u\left(\frac{f_c'}{F_u}\right)^{0.35}\left(\frac{E_c}{E_{sc}}\right)^{0.4}$ $K_{ch} = 4.7 - \frac{1.2}{\sqrt{N_{gr}}}$		Unified influence of stud and concrete interaction. Taking ratios of strength and elastic ratios of components.
6	Nguyen et. al (2014)	$P_{R-MOJ} = A_{SC}F_u\left(\frac{f_c'}{F_u}\right)^{0.7}\left(\frac{E_c}{E_{sc}}\right)^{0.5}\left(\frac{t_f d\sigma_b E_f}{E_{sc}}\right)^{0.15}$		Factors flange properties including thickness along with stud and concrete mechanical influence on the failure mode of the connections.

Note: $\boldsymbol{P_{Rs} = ultimate\ shear\ connector\ resistance\ for\ shear\ connector\ failure}$; $\boldsymbol{P_{Rc} = ultimate\ shear\ connector\ resistance\ for\ concrete\ failure}$; $\boldsymbol{A_{SC} = cross\ sectional\ area\ of\ s\ ashear\ connector}$; $\boldsymbol{F_u = specified\ mimimum\ tensile\ strength\ of\ a\ shear\ connector}$; $\boldsymbol{d = nominal\ diameter\ of\ a\ shear\ connector}$; $\boldsymbol{k_{cp} = coefficient\ for\ pry - out\ strength}$; $\boldsymbol{\lambda = modification\ factor\ reflecting\ the\ reduced\ mechanical\ properties\ of\ lightweight\ concrete}$; $\boldsymbol{f_c' = specified\ compressive\ strength\ of\ concrete}$; $\boldsymbol{E_c = modulus\ of\ elasticity\ of\ concrete}$; $\boldsymbol{h_{ef} = effective\ embedment\ depth\ of\ shear\ connector}$; $\boldsymbol{h_{cm} = embedment\ depth\ of\ headed\ stud\ shear\ connectors}$; $\boldsymbol{f_{ck} = characteristic\ value\ of\ the\ cylinder\ compressive\ strength\ of\ concrete\ at\ 28days}$; $\boldsymbol{E_{cm} = secant\ modulus\ of\ elsticity\ of\ concrete}$; $\boldsymbol{P_{R-OJ} = ultimate\ shear\ connector\ resistance\ derived\ from\ Oehlers\ and\ Johnson\ equation}$; $\boldsymbol{E_{sc} =}$

$\boldsymbol{modulus\ of\ elasticity\ of\ shear\ connectors}$; $\boldsymbol{N_{gr} = number\ of\ shear\ connectors\ that\ can\ be\ assumed\ to\ fail\ as\ a\ group}$; $\boldsymbol{P_{R-MOJ} = modified\ Oehlers\ and\ Johnsons\ equation\ for\ ultimate\ shear\ resistance\ derived\ from\ Nguyen\ (2014)}$; $\boldsymbol{t_f = thichness\ of\ girder\ flanges}$; $\boldsymbol{\sigma_b = bearing\ strength\ of\ girder\ flanges}$; $\boldsymbol{E_f = equivalent\ modulus\ of\ elasticity\ of\ flanges}$; *NWC = normal weight concrete.*

2.3.4.1 Modified equations for predicting shear strength of connectors

To account for the contribution of both failure modes, Oehlers a,nd Johnson (1987) carried out an investigation on static strength prediction of shear studs in composite connections by varying the compressive strength and stiffness of concrete as well as the tensile strength of shear studs. He outlined a functional equation using a unified relationship for all relevant parameters governing shear behaviour of the steel-concrete composites.

$$P_p = f(A, E_c, E_s, f_{cu}, f_u)$$

Equation 2.23

P_p is the shear strength of the connection which depends of the size of the stud specified in terms of cross-sectional area of the shank A, and on the stiffness and strength of the material components (f_{cu} and E_c are the compressive strength and modulus of concrete while f_u and E_s are the tensile strength and modulus of the shear stud) of the connection.

Eq. (2.23) was adopted to reflect the effect of changes in material strength and stiffness. The equation further established a ratio in the relationship between the moduli of steel E_s and concrete E_c as directly proportional to P_p. Whereas these relationships tend to affect the behaviour of the beam such that an increase or reduction in modulus of one of the materials relative to the other can further increase or reduce the bending moment of the beam. The assumption allows for consideration between the strengths of the concrete and steel suggesting that an increase in the concrete strength will reduce the flexural forces on the stud and allow a greater shear load before fracture of the stud. Similarly, increasing the stud strength will allow the concrete to resist a greater

shear load as the interface pressure can be distributed along a larger surface area before fracture of the stud.

The proportionality relationship between E_c and E_s proposes an exponential relationship for f_{cu} and f_u. See Eq. (2.24)

$$P_p = KA\left(\frac{E_c}{E_s}\right)^{\alpha} f_{cu}^{\beta} f_u^{\gamma}$$

Equation 2.24

Oehler and Johnson attempts to validate this assumption, by suggesting that the sum of the components of the material properties must be 1. Therefore, Oehlers and Johnson equated the stud strength (Af_u) against the variation of concrete strength properties $\left(\frac{f_{cu}}{f_s}\right)$ and modulus $\left(\frac{E_c}{E_s}\right)$ relative to steel.

$$\frac{P_p}{Af_u} = K\left(\frac{E_c}{E_s}\right)^{\alpha}\left(\frac{f_{cu}}{f_s}\right)^{\beta}$$

Equation 2.25

The values for the exponents were derived from statistical regression analysis of the results obtained from various tests with a consideration of existing variations within the test occurring due to a number of conditions including differences between the restraints to specimen, differences between the method of testing and materials and between the geometries and stud positions of the specimen. The values for the exponents were derived as 0.4 for α and 0.35 for β. This investigation

led Oehlers and Johnson to propose an equation to predict the ultimate shear resistance by an inclusive consideration of both failure modes established as Eq. 2.26.

$$P_p = KAf_u \left(\frac{E_c}{E_s}\right)^{0.40} \left(\frac{f_{cu}}{f_s}\right)^{0.35}$$

Equation 2.26

Where $K = 4.1 - \frac{1}{\sqrt{n}}$

Equation 2.27

n = number of studs.

Nguyen et al. proposed a modification from Oehlers and Johnson's model stating that the material boundary from Oehlers equation did not account for higher concrete strength therefore limiting the application of the formula in making accurate predictions. He reported that the average E_c and f_{cu} obtained from his experimental investigation was about 33.3% and 107.4% higher considering the maximum material bounds of the concrete suggested by Oehler. Therefore, Nguyen proposed a modified equation from the Oehlers equation where the exponents where increased to 0.5 and 0.7 and introduced another parameter accounting for the girder effect observed from his investigation using FRP I - girders.

$$P_{R-MOJ} = A_{sc}F_u \left(\frac{E_c}{E_{sc}}\right)^{0.5} \left(\frac{f_c}{f_u}\right)^{0.7} \left(\frac{t_{fd}\sigma_b E_f}{E_{sc}}\right)^{0.15}$$

Equation 2.28

Where t_f = thickness of the girder flanges, d = diameter of the bolt shear connectors,

σ_b = bearing strength of the girder flanges, E_f = equivalent modulus of elasticity of the flanges and E_s = modulus of elasticity of the shear connectors. The power of the expression for girder effect $\left(\frac{t_f d \sigma_b E_f}{E_{sc}}\right)$ was empirically determined by Nguyen et al. (2014).

The effect of girder may be neglected for steel-concrete push-out test because steel possesses a very high compressive strength however, applicable when FRP becomes the alternative replacement for steel due to its lower compressive strength when compared to steel. Eq. 2.28 is adopted in this study as a predictive model although will be further compared against standard models and if any inconsistency exists, a proposed equation may be derived for FRP-concrete ultimate shear resistance.

2.4 Composite Beam Behaviour

The behaviour of composite beams may not fully deviate from the traditional performance of horizontal structural members subjected to bending. Horizontal members subjected to the combined effect of gravity and bending forces will undergo a bending deformation (deflection) causing stresses and strains along the longitudinal and transverse profile of the cross-sectional member. However, composite beams will undergo lateral deformations in addition to flexural deformation when subjected to bending and these lateral deformations must be resisted hence, all forces within the composite must be at equilibrium for stability to occur. The nature and behaviour of composite beams emanates from an understanding of the bending effect of traditional horizontal beams which are

characterised by compression and tension forces propagating away from the centroid of the beam cross section. In addition to the bending deformation, lateral shear deformations occur at the composite interface between the concrete and steel capable of undermining the flexural performance of the composite. This interfacial shear behaviour is already discussed in detail under section 2.3. The performance characteristics of composite beams is discussed under subsections below comparatively against traditional steel and reinforced concrete beam structures.

2.4.1 Moment & shear capacities

Conventional steel-concrete composites are typically designed to deal directly with the compression-tension relationship of the bending cross-section thereby enhancing the flexural capacity of the composites over singular structural beams. Flexural phenomenon in composite beams is not only limited to steel-concrete composites but includes composites of similar nature such as FRP-concrete composites. The shear connector, tensile and compressive subcomponents (e.g., steel and concrete) also contribute to the overall performance of the beam. Suwaed and Karavasilis (2020) investigated the performance of demountable friction-based shear connector (FBSC) in steel-concrete composite beams. The study contrasted EC4 recommendations for partial shear connections suggesting that though FSBC achieved 32% degree of shear connection which was lower than the recommended 57% minimum specified in EC4 for welded studs in partial shear connection, the corresponding slip capacity was higher. It further reported that the elastic theoretical prediction of deflection deviated by 29 % from the experimental findings resulting in the underestimation of deflection at serviceability limit state (SLS). Slip capacity was estimated to be about 1.7 times that of welded studs. Suwaed &

Karavasilis (2020) reported peak moment capacity of 1259kNm at full shear and 1069kNm at partial shear. Due to the increased flexural capacities of composite section, corresponding moment and shear capacities are expected to be higher for sections with decreased centroidal axis and shape property. As a direct consequence of bending, deflecting curvature, stiffness and angular slopes fully describes the characteristic performance of the beam irrespective of its composite make-up. Correia et al. (2007) investigated the flexural capacity of GFRP-concrete hybrid beams on a three-point and four-point bending test. The study reported significant structural improvements and enhancement of the hybrid section over traditional GFRP section including 350% increased stiffness, 300% increased flexural capacity and GFRP longitudinal peak stress of 386MPa at beam failure. Experimental test findings showed a consistent strain profile depicting interfacial slip activity proportional to the values of moment. Correia's study also observed that GFRP profile absorbed between 50 – 70% of the total shear force. Neagoe et al. (2015) carried out a comparative investigation of FRP-concrete hybrid beams using two significant composite fabrications; one modelled as a replica of the conventional steel-concrete structural beams and the other took a step further to encase the GFRP profile section in the same batch of concrete slab (see Figure 2.15). The models were compared against traditional GFRP profiles and equivalent reinforced concrete (RC) sections. It was reported that GFRP profiles failed traditionally from lateral-torsional buckling resulting from loss of global stability. The study characterised the flexural behaviour of GFRP profiles as linear elastic with reported higher flexural capacities for the profile with reinforced stiffeners. When web-section profiles are used as flexural members, their flexural capacity can be effectively improved with the use of web-plate stiffeners. Neagoe et al. (2015) reported that the equivalent RC-section showed higher

flexural rigidity with increased capacity of about 17% over the web-stiffened GFRP profile. The study observed improved flexural capacities of the encased GFRP-concrete and hybrid GFRP-concrete composites up to 90% over the RC-sections and GFRP profiles. The hybrid sections (both encased and conventional FRP-concrete composite) are characterised by a bilinear response depicting the stress transfer mechanism between the subcomponents (Neagoe et al., 2015). Encased FRP-concrete composite sections are characterised by early tensile cracks at the bottom of the beam, concrete crushing at the top and possible plate delamination failures from severe bending (Neagoe et al., 2015). However, hybrid FRP-concrete composites are characterised alike in their failure modes but with variations in deformability due to boundary conditions and related parameters. The deformations are mainly located along the connector axis and propagate towards the support from the mid-section of the beam (Neagoe et al., 2015). Neagoe's experimental reports showed that 4-point bending test result in excessive deformation with lower flexural capacities in comparison to their 3-point counterparts.

Figure 2.15: Forms of GFRP hybrid connection (Source: Neagoe et al., 2015)

However, physical parameters such as deflection does not provide the full detail of the composite behaviour hence, the knowledge of internal reactions to the bending effects are required for full understanding of the composite behaviour. The internal response of the beam may be explored from research findings and reports on shear and moment capacities as discussed in the subsections below.

2.4.2 Stress-strain deformation

The stress-strain deformation of composite beams is of three characteristic modes determined mainly from the depth of neutral axis orientation. The stress-strain deformation can be considered for partial shear and/or full shear interaction between the FRP (or steel)-concrete composite (see Figure 2.16 & 2.17). When composite beam

sections are subjected to bending, the concrete slab tends to initiate a linear elastic behaviour from initial loading and as the magnitude of the loading intensifies, tensile strains gradually creep unto the bottom face of the slab at the shear interface (Suwaed & Karavasilis, 2020). These tensile strains initiate as tiny cracks referred to as hairline cracks (Suwaed & Karavasilis, 2020) and propagate from the bottom towards the top face of the beam. If appropriate reinforcement is in place, the tensile cracks can be kept under control without compromising the integrity of the flexural behaviour.

Strain profiles can be obtained with proper gauging through the cross-section to determine the shear interaction of the subcomponents (Neagoe et al., 2015; Suwaed & Karavasilis, 2020). Suwaed & Karavasilis (2020) reported yielding failure of the steel subcomponent in their investigation resulting from large tensile strains at the bottom flange which exceeded the elastic limit of the steel section. Hence, strain profiles can be effective in determining the failure mode associated with structural composites.

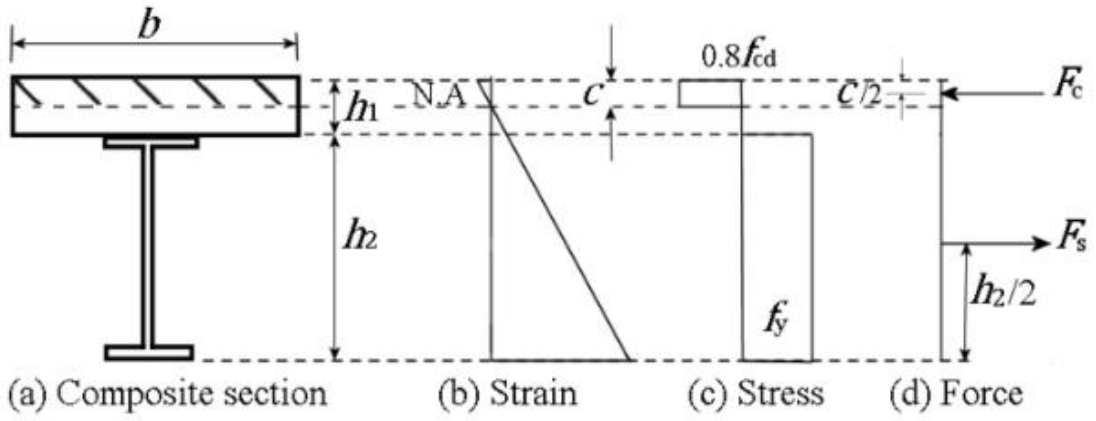

Figure 2.16 Full shear interaction

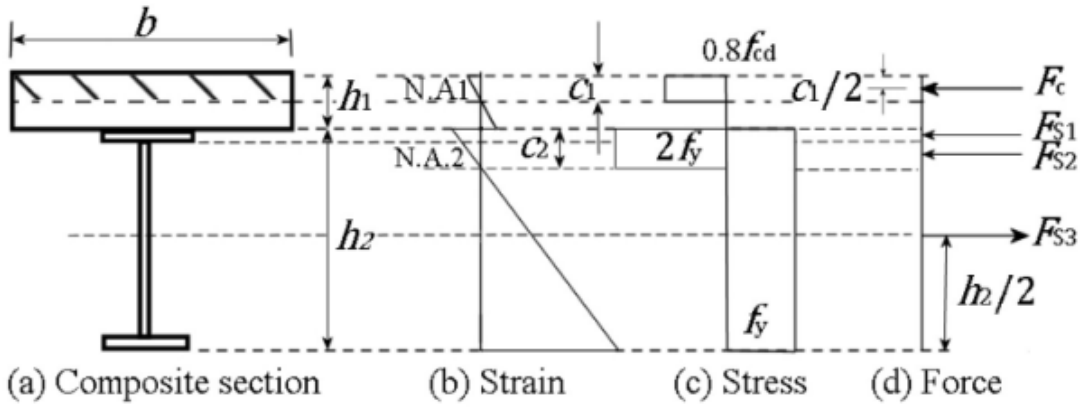

Figure 2.17: Partial shear interaction

2.4.3 Theoretical Analysis of FRP-concrete beams

The analysis of an FRP-concrete composite structure requires a fundamental theoretical reasoning which was earlier developed for steel-concrete sections. However, due to the material peculiarity of FRP with respect to bending, analysis of sections assumes elastic behaviour. Hence, most theoretical predictions of the composite behaviour have adapted the linear elastic model. Girhammer (1993) began an analytic prediction of the steel-concrete composite behaviour by exploring basic assumptions for the composite section and illustrating the combined effect of axial and bending forces on a composite beam (see Figure 2.18). Neagoe & Gil (2015) suggest that evaluation of deflection for bybrid beams can be carried out within the elastic region.

From the model, we have that the sum of forces and moments from the components (i.e steel and concrete) of the composite equal the applied effect of the external loading effect.

$$F = N_1 + N_2$$

Equation 2.29

$$V = V_1 + V_2$$

Equation 2.30

$$M = M_1 + M_2 - N_1 r + F\left(r - Z_{cg,\infty}\right)$$

Equation 2.31

The horizontal displacement component for the beam can be deduced from the equation below:

$$\Delta x = x_2 - x_1 + w'' r$$

Equation 2.32

Using $w'' = -\frac{M_1}{E_1 I_1}$

Equation 2.33

And $w'' = -\frac{M_2}{E_2 I_2}$

Equation 2.34

Substituting eq. 2.33 or 2.34 into eq. 2.3;

$$M_1 = \frac{E_1 I_1}{E I_0}\left[M - F\left(r - Z_{cg,\infty}\right) + N_1 r\right]$$

Equation 2.35

Figure 2.18: Combined Effects of Axial and Bending Forces on a Composite Section (source: Girhammar, 1993)

$$M_2 = \frac{E_2 I_2}{E I_0}\left[M - F\left(r - Z_{cg,\infty}\right) + N_2 r\right]$$

Equation 2.36

Where the bending stiffness of the noncomposite section is given as:

$$EI_0 = E_1 I_1 + E_2 I_2$$

Equation 2.37

Hence, equation for the beam deflection is given as:

$$w'' = -\frac{M - F\left(r - Z_{cg,\infty}\right) + N_1 r}{EI_0}$$

Equation 2.38

$$w^{IV} = -\frac{q - N_1'' r}{EI_0}$$

Equation 2.39

2.5 Numerical Modelling of Composites

The finite element method is a computational approach to the analysis of physical entities by means of general-purpose nonlinear finite element analysis packages which has become available to practicing engineers and academic researchers. Some of the most current FE software packages include ABAQUS, ANSYS, DYNA etc with ANSYS and ABAQUS gaining prominent use in the area of structural research and analysis.

An appropriate description of the FE method of structural analysis by Overli (2017) states that the method involves a breakdown of a whole structure into finite number of elements where mathematical equations can be applied to the individual elements to determine their deformation and strength response for arbitrary boundary conditions. The definition implies that a defining equation can be applied on any given representative element to ascertain the overall response under a well-defined state of stress.

The advantage of numerical modelling includes its inexpensive ability to simulate experimental setups in the development of innovative and efficient building materials with a closed form solution towards predicting the behaviour and performance of materials. However, its limited application can be attributed to common variations in results obtained by various analyst despite adopting the same FE code on similar structures following the uncertainty with many of the materials parameters during the analysis (Overli, 2017). Some of the problems associated with this inaccuracy are a general lack of objectivity when the FE method is applied in the study of materials like concrete. A key to enhancing the modelling accuracy is to employ realistic hypothesis in the description of the material.

2.5.1 Modelling assumptions and hypothesis

Dai et al. (2015) adopts a three dimensional eight-node solid element for concrete slabs, steel beam and stud connector for material element under the ABAQUS FE software. Surface-to-surface contacts were outlined for all interacting material surfaces. Contact frictions was adopted for bonded action between concrete core and steel hollow section with friction coefficients of 0.2 – 0.3 under sensitivity studies. One of the key challenges in the modelling of subcomponents Is the selection of appropriate damage model to closely depict the failure of materials. The concrete plasticity damage model is typically selected to simulate tensile stress cracking of concrete (Dai et al., 2015; Qureshi et al., 2011). Dai et al., assumed a maximum tensile strength concrete before cracking as 10% of the concrete compressive strength. One significant problem with concrete modelling involves the appropriate simulation of cracking behaviour which can often lead to numerical instabilities in the analysis if a uniaxial model is adopted (Overli, 2017).

Uniaxial models typically represent a post peak material behaviour resulting from a gradual loss of load-carrying capacity hence, Overli (2017) suggest the adoption of triaxial material model with a realistic identity to capture the abrupt transverse expansion of the concrete prior to failure responsible for the triaxial stress conditions in structures. It is important to consider the brittle nature of concrete due to the increased transverse expansion behaviour prior to failure (Vidosa et al., 1991).

2.5.2 Material model and geometry

Qureshi et al. (2011a) highlights the advantage of using dynamic nonlinear explicit analysis over nonlinear static implicit method in modelling complex nonlinear problems involving large deformations, complex interactions and material damage. Qureshi et al. (2011a) adopts a combined three-dimensional ABAQUS 8-node brick (C3D8R) and 6-node wedge (C3D6R) as reduced integration elements for modelling of shear stud, steel beam and concrete slabs. Qureshi mentioned that explicit models adopt first order elements for stress/displacement analysis which reduces computational time and eliminates shear locking in solid elements capable of undermining bending behaviour. Most researchers using the ABAQUS FE software have reported significant success in the use of the concrete damaged plasticity model (CDP) which ideally simulates concrete damage behaviour because of tensile cracking and compressive crushing (Qureshi et al., 2011a; Mirza, 2010; Dai et al., 2015).

Researchers using the ANSYS software have typically adopted the SOLID65 elements for modelling concrete and steel owing to the unique 8-nodal structure of the element with a three degree of freedom capability at each node (Queiroz et al., 2007; Luo et al., 2012; Jayajothi et al., 2013) (see Figure 2.20). The SOLID65 is capable of simulating

three orthogonal cracking of concrete including crushing, creep and plastic deformations (Queiroz et al., 2007). Whereas Queiroz et al. (2007) adopted the elastic plastic SHELL43 element for modelling steel elements and nonlinear springs COMBIN39 for shear connectors. The SHELL43 is characterised by four nodes with six degrees of freedom at each node. The element is capable of simulating plasticity, creep, stress stiffening, large deflections and strain deformations (Queiroz et al., 2007). However, BEAM188 3D element has been used by Luo et al. (2012) to model steel reinforcing bars. COMBIN 39 is a uniaxial tension-compression element of three degrees of freedom defined at each of its two nodal points with a force-deflection curve and longitudinal or torsional capability (Queiroz et al., 2007). COMBIN39 has also been used for the simulation of shear debonding behaviour of steel-concrete bonded composite by Luo et al. (2012). The nodal element is meant to capture either the steel-concrete debonding behaviour resulting from specimen fabrication technique or typical adhesive debonding from concrete (see Figure 2.19). An eight-node solid element, Solid 65, was used to model the concrete. The solid element has eight nodes with three degrees of freedom at each node – translations in the nodal x, y, and z directions. The element is capable of plastic deformation, cracking in three orthogonal directions, and crushing. The geometry and node locations for this element type are shown in Figure 2.20.

A Link 8 element was used to model the steel reinforcement. Two nodes are required for this element. Each node has three degrees of freedom, – translations in the nodal x, y, and z directions. The element is also capable of plastic deformation. The geometry and node

(a) adhesive debonding (Luo et al., 2012) (b) steel-concrete debonding (Queiroz et al. 2007)

Figure 2.19: Illustration of Nonlinear Springs

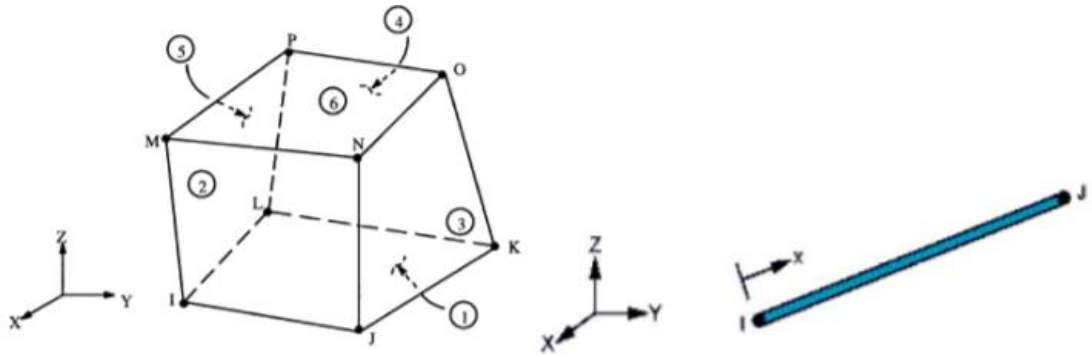

(a) 3D SOLID65 element (b) 3D LINK8 element

Figure 2.20: Element Structures

locations for this element type are shown in Figure 2.20 (b)

Steel beam behaviour has been analysed by Queiroz (2007) who used the von mises yield criterion with isotropic hardening rule (multi-linear work hardening material). The von mises stress-strain criterion is also used for steel reinforcement considering the elastic-linear-work hardening material behaviour with tangent modulus estimated as 1/10,000 of the elastic modulus of the material to minimise computational problems (Queiroz et al., 2007). Concrete slab behaviour is modelled as multi-linear isotropic hardening materials using von mises yield criterion in addition. Post cracking behaviour of concrete can be modelled by trial adjustment of concrete material property for the adopted element (SOLID65) due to the shear stiffness behaviour of concrete cracking such that shear stiffness of the cracked area is reduced to γ_t times that of the uncracked concrete area (Luo et al., 2012). Hence, if concrete normal stress around the cracked region becomes compressive then the cracked gap closes and regains its ability to transfer shear forces across the cracked face. Concrete element shear transfers are typically considered within the ranges of 0 – 1 depicting crack behaviour such that zero depicts a smooth crack (fully loss of shear transfer) and one depicts a rough crack (no loss of shear transfer) respectively (Queiroz et al., 2007; Luo et al., 2012). Luo et al. (2012) proposes $0 \leq \gamma_t \leq \gamma_c \leq 1$ condition to be satisfied under a trial and error procedure for the shear transfer coefficients 0.35 and 0.75 for γ_t and γ_c respectively where $\gamma_t = shear\ transfer\ coefficient\ under\ open\ condition$ and $\gamma_c = shear\ transfer\ coefficent\ under\ closed\ condition.$ Queiroz (2007) defines the stress relaxation coefficient as a function which accelerates convergence when cracking is imminent therefore proposing a value of 0.6 with a default omission of the crushing capacity of concrete to improve convergence and computational efficiency of the model.

2.6 Summary

In summary of the above literature on research works published on conventional structural composites, the current study has explored developments in shear composite connections and review opportunities for the current study. The literature explores existing concerns on the environmental impact of steel owing to its carbon footprint to emphasize on the growing demand for alternative materials for construction. The study reviews current benefits of PFRP for use as alternative structural composite in practice in view of opportunities for the use of GFRP materials within construction. To fully understand the research investigation on new materials, the study explores relevant properties of GFRP and LWAC which may influence the performance of composite shear connections. The review adopts Hicks (2014) force-interaction model to establish the stress-states and equilibrium of forces which characterises the conventional structural composite behaviour. Further review identifies inherent material properties of studs, and concrete slabs as major influences on shear capacity and stiffness. Most research studies (An & Cedarwall, 1996; Nguyen et a., 2014; Dai et al., 2015; Nellinger S., 2015; Jin et al., 2018) reported that higher stud diameters, tensile strength and embedment depth increases shear capacity and stiffness. Nguyen et al. (2014) characterises this influence as a proportional influence between (h_{ef}/d) ratios and shear capacities. Apart from conventional stud fracture and concrete failures, the review highlights flange bearing failures as a significant characteristic failure mode for FRP-concrete composites. This failure suggest plate bearing strengths of PFRP's play a significant role on the mobility of shear resistance for FRP-concrete connections. Although these factors influence shear resistance and stiffness, they remain scarce knowledge on the behaviour of shear connections for PFRP-concrete composites. Also, the rapid development of these

independent materials such as hybrid PFRP's and concretes highlights a gap in knowledge which fails to establish parameters that deviate the behaviour and performance of FRP-concrete connections against their steel counterparts. Limited research has explored shear connections of GFRP and their hybrids against a range of high performing lightweight concretes thus leading to multivariate impacts or factors of influence. Hence, the current study will aim to build on existing findings in the fabrication, curing, control, and testing of FRP-concrete connections to bridge knowledge gaps and contribute to the development of prototype PFRP-concrete hybrid beams.

CHAPTER 3. RESEARCH METHODOLOGY

3.1 General

This chapter outlines the methodology adopted for the current study. It illustrates the design and analytical tools employed in the development of the novel hybrid beam. The research utilises a quantitative approach combining experimental and numerical methods in the development and analysis of the beam. Hence, the research investigation is carried out under two broad studies namely, experimental and numerical design studies. Each study is carefully analysed complementarily to validate the expected research findings. This section expounds the method and procedures of the experimental test programme and subsequent development of the numerical model (see Figure 3.1).

3.2 Experimental Test Methods

The study will embark on sets of experimental testing building up towards the development of the hybrid beam. Experimental investigations involved characterisation of the major components GFRP and LWAC with follow up push-out test for shear connection characterisation and the development of the hybrid composite beam for the determination of moment capacity. Subsections will expound on justifications for the selected test methods for these experimental activities.

3.2.1 Test Methods for GFRP & Limitations

PFRP materials may be subjected to standard or non-standard test to determine their relevant mechanical characteristics. The GFRP material for the current study was pre-characterised by Matharu (2014) and validated against material data provided by the manufacturers (Creative Pultrusions). Due to the limited capacity of Coventry

University's light-structure's laboratory to perform complex PFRP plate characterisation test, the study adopted experimental test results presented by Matharu (2014) which was conducted in Warwick University laboratory. The selected test methods for the determination of material properties were dependent mostly on the capacity of the laboratory and availability of equipment. Thus, the methods adopted for testing as reported by Matharu (2014) and outlined in table 3.1.

Table 3.1: Test Methods for PFRP Characterisation

S/N	***Mechanical Property***	***Standard/Non-standard Test***	***Test Author***
1	Compressive strength	Non-standard test	Mottram (1994)
2	In-plane Shear Strength	Standard test	ASTM D5379
3	Tensile strength	Standard test	ASTM D3039
4	Open hole tensile strength	Non-standard test	Mottram (2010)

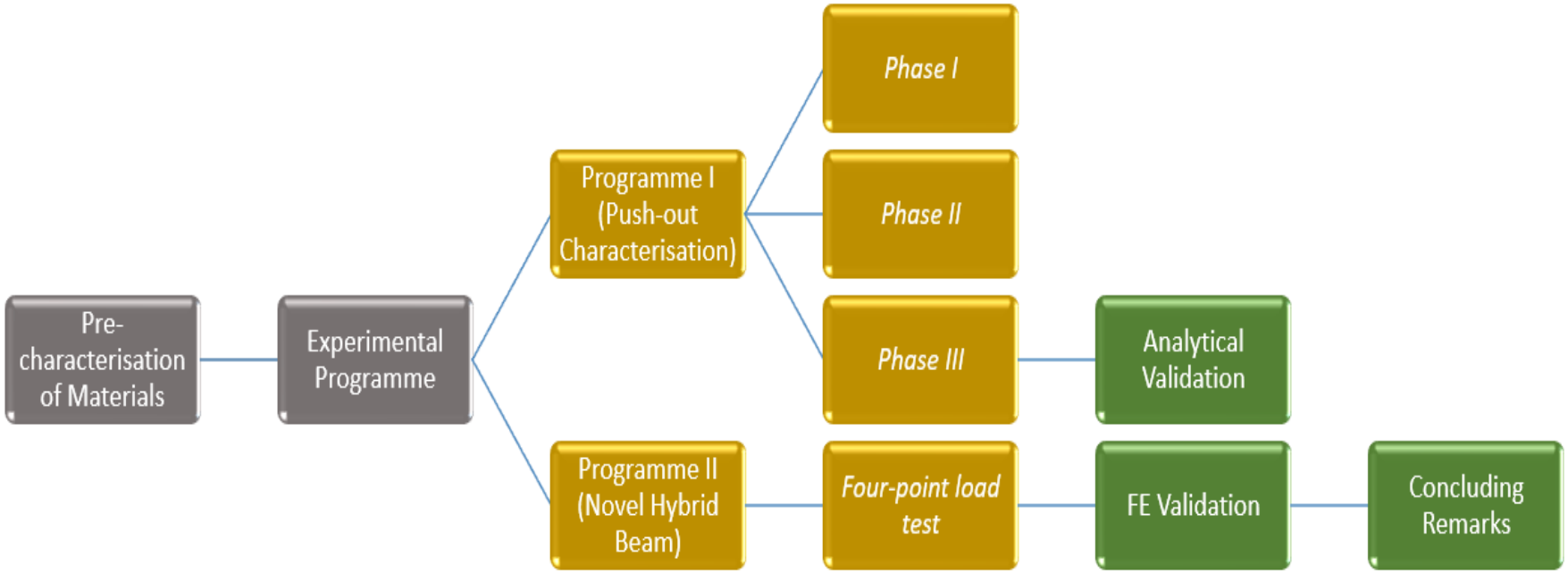

Figure 3.1: Design Methodology for the Research Study

3.2.2 Test Methods for LWAC & Limitations

Characterisation of LWAC for the determination of material properties adopted widely acceptable methods detailed from standards and summarised in table 3.2. The selection of Lytag material as the lightweight aggregate for the concrete is primarily due to its structural benefits including good compressive strength and low porosity. The test methods comply with British standards for the determination of mechanical properties of structural aggregates. One of the significant benefits of using standardised test methods for experimental investigations is the wide acceptance and ability to produce uniformly consistent results with limited errors. However, their limitations include difficulty in controlling laboratory temperatures for appropriate curing, calibration errors from manual setups, effects of finished surface conditions on the estimation strength properties. One significant limitation of the test results includes the material defects from inconsistent curing which may affect the pattern and rate of crack propagation in concrete during testing.

3.2.3 Companion Shear test method

The companion shear test is aimed at characterising shear connections between composites to determine shear capacity, stiffness and related parameters. The standard test method is specified in BS5400-5 (2005) for single row connectors and BS EN 1994-1-1 (2004) for double row connectors. However, they have been significant deviations from these standard methods by researchers to account for concrete slab compressive forces on the FRP-section. None of these modified test methods have received wide acceptance and reported deviations in results from composite beam test has not been

consistently significant. Following the above and capacity of the laboratory, the current study adopts method specified in BS EN 1994-1-1 (2004) for the push-out test.

3.2.3.1 Limitations & Challenges of the test method

Test results may be compromised if uniform loading is not achieved either due to uneven floors or cut variations of the GFRP-section. This could lead to unlikely failure modes such as tensile tear-out failures and/or slab splitting failures. Test frames require appropriate strength to resist the upward reactions from the test specimen. Measurement errors may be encountered from non-uniform loading or inconsistent loading rates. Concrete curing around the bolt holes may present point of weakness due to collated moisture dripping through the bolts. This may lead to poor strength mobilisation and/or concrete cracking during testing.

3.2.3.2 Control measures

Specimens are plumbed to ensure flatness at the top and on the sides. Where ground is uneven, metal plates are provided to ensure flatness. Automated loading and measurement systems are deployed for testing to ensure uniform loading rates. While it is difficult to control accumulated moisture around bolt areas, the specimens can be placed flat on the ground after the first 3 days of curing to ensure direct exposure of these areas to the atmosphere.

3.2.4 Four-point load/deflection test of the hybrid Beam

The standard four-point bending test which is the widely accepted test method for determining the bending capacity of beams and slabs was adopted for testing the moment capacity of the hybrid beam. This method closely depicts real-life behaviour of beams

under load. This test was carried out on a full-scale composite beam measuring 3.3m in length and 400mm in width. The test enabled measurements of increase loading and corresponding deflections with appropriate observations on crack initiation, propagation, and final failure modes to be recorded.

3.2.4.1 Limitations & Challenges of the test method

One of the key challenges of this method is the effect of loading reactions at the support which can cause premature buckling failure of the FRP-section underneath the concrete slab. Another vital issue is the concentration of stresses on the slab at the point of loading which may lead to concrete sprawling or premature buckling failures of the FRP-section at points directly under the applied load. Another significant challenge was the need for test frames to resists upward reactions during loading. All these issues have the combined impact to present false failures and undermine the moment capacities of the hybrid beam. Load measurement and corresponding deflections may contain error if there is difficulty to maintain loading rate.

3.2.4.2 Control measures

To prevent premature buckling failures of the FRP-section, the web section was reinforced with steel stiffeners at support and points of loading. At the point of load application on the concrete slab, rubber pads were placed underneath the loading clamps to prevent localised stress build-up by redistributing the stress over a wider transverse area. Additional steel I-sections were added to the test rig to provide resistance to upward reactions from the test specimen. Appropriate calibrations of loading cells and the use of automated loading systems and digital recordings are ensured to minimise errors in measurement.

3.3 Fabrication and Setup Technique

Design techniques are an integral part of construction planning often carried out to reduce as much as possible any defect that would have undermined the integrity of the structure. Significant consideration must be given to the design technique employed in the fabrication of components as it could significantly improve the service-use performance of the structure. The two major fabrication techniques discussed herein for conventional structural composites are also very much applicable to FRP-concrete composites.

3.3.1 In-situ fabrication techniques

To achieve the push-out arrangement, clearance holes are drilled through both flanges of the GFRP section. The LWAC slabs are cured through bespoke mould comprising open-steel cuboid and timber infill for accommodating the bolt arrangement. The bolts are pre-positioned on the mould with clamps at appropriate embedment depths before concreting is carried out.

Although the in-situ fabrication technique is common with welded shear connections of steel-concrete composites, FRP-concrete composites tend to use demountable shear connections following the difficulty with welding action on FRP sections. Apart from demountable connections, further research studies have combined epoxy-adhesives with demountable connections to achieve increase shear capacity. The current study uses steel bolts to achieve demountable connections between FRP sections and concrete slabs. The selection of demountable shear connection technique for GFRP-LWAC composites is based on industry practice and the current capacity of the structure's laboratory.

The fabrication involves two stages: arrangement of bolts into perforated clearance holes on the GFRP flange section and concreting of the LWAC slab with the inverted bolts as an integral part of the form work. Steel reinforcement rods are mainly inserted into the mould to ensure tensile reinforcement to prevent against slab failures during lifting. Further details of the fabrication of the hybrid composite beam are presented under experimental programme section 4.4.2.

3.3.2 Limitations & Challenges of fabrications

One of the significant limitations of curing the concrete in an upright position is the tendency to create weakness directly beneath the bolt area due to accumulation of water dripping from the concrete. Also, there is significant challenge with the effects of concrete vibrations around the bolt area offsetting the embedment depth hence, leading to uneven stress distribution during shear loading of the specimen.

One of the key challenges of the fabricating the composite hybrid beam is the need to achieve appropriate curing of concrete with limited access for vibration. This is because of the availability of only single vibratory technique using a hand-held vibrator. Another significant challenge with the hybrid composite was to ensure the shear connection would be demountable by applying emulsion oil to the flange surface bearing the bolts.

3.3.3 Control Measures

One of the most important aspects of fabrication is capacity to demould without damage to specimen or mould. Hence, this becomes a significant aspect in the pre-fabrication design to determine the functionality of the moulds. Three key control was considered for the design of the moulds as follows:

i) Using viscous oil to create a barrier between the mould and the concrete specimen during curing to prevent adhesion which may lead to difficulty in demoulding or damage to specimen.

ii) Another vital approach was to ensure that all moulds were demountable to achieve specimen demoulding after curing. This is possible where joints are bolted together. Hence, the choice of an open cuboid as a basic design for all moulds using steel material for the push-out specimen and timber planks for the hybrid beam.

iii) Mould design must embed access to meet handling requirements of the specimen or else it may pose a safety risk in the laboratory.

3.4 Numerical Design

The numerical design is intended as an effective approach to predict the shear performance and failure of the FRP-LWAC composite. The criteria for selecting appropriate software for the study was based on knowledge and skills competency, availability of software and support, software capabilities to model complex materials and deliver non-linear simulations etc. Hence, the selected ANSYS APDL software satisfied the listed criteria and was considered within a range of software from published literature capable of predicting nonlinear behaviour of FRP-concrete materials.

3.4.1 Limitations and Challenges of the Numerical design

Apart from demand in skill to cope with the developments in the software throughout the time of study, modelling material complexities can be time consuming and difficult when using Finite Element (FE) software. However, the accuracy of the solution is mostly dependent on the material calibration, model assumptions and simulation competence. There are two key influences which may impact on the accuracy of the model: model

calibration (factor dependent of experimental characterisation) and model development (factor dependent user skill and experience).

3.4.2 Control Measures

Control measures are adopted for the current study to reduce numerical errors in the prediction of the model. A calibration model is designed using Normal Weight Concrete (NWC) to characterise a simple beam model for the study. Further to the development of a prototype model, will require a discretisation test to ensure an acceptable solution accuracy.

3.5 Result Analysis

The research analysis will follow a quantitative approach using graphs and tables to analyse the data derived from experimental testing. All test data obtained from experimental programmes will be collated on a table for abrupt determination of key values in respect of test performance. Graphical representation of data will be developed to determine behavioural patterns, trends, and deviations among test specimens. Quantitative representation of data allows for appropriate comparisons of results against published data and theoretical principles. Graphical illustration of results enables further discussion on the behaviour of the novel beam including a holistic assessment of the primary objectives of the research.

3.6 Research Validation

The pilot study for the research carried out on characterising lateral interfacial shear behaviour of the composites embarked on three phases of testing progressively validating one another and generating significant data for the analysis of the study (see section 6.2). The initial phase of testing was conducted on NWC slabs following availability of aggregate materials in the light structures laboratory with the need to have a control test specimen for parallel comparison and subsequent validation. Hence, three phases of testing involving LWAC and NWC specimens provided adequate number of samples to generate significant data which were analysed to determine relevant and valid conclusions on the lateral shear behaviour of the FRP-concrete composites.

Numerical studies involving FE analysis aimed at predicting the moment capacity and failure mode of a prototype hybrid beam should provide insights into the behaviour of the model and corroborate literature reports. A prototype half-model beam was developed using the ANSYS FE software for the aforementioned and validated using from experimental testing of a full scale developed hybrid beam (see section 6.3).

CHAPTER 4. EXPERIMENTAL PROGRAMME: MATERIALS & TEST METHODS

4.1 Introduction

The novel hybrid beam investigated in this research consist of two distinct material components highlighted in previous chapters hence, experimental studies must consider intrinsic properties of these components to fully determine and interpret the behaviour of the hybrid beam. Previous research from Nguyen et al. (2014) investigated the performance of hybrid composite materials such as hybrid Fibre reinforced polymer (HFRP) and Ultra-high performing lightweight concrete (UHPLWC) with pre-enhanced mechanical properties whereas the current study considered practicality and affordability to characterise basic hybrid composites of GFRP and LWAC to determine shear performance. Also, Nguyen et al. (2014) in his research characterised the behaviour of a variety of studs including headed steel studs, headless inclined steel studs and GFRP studs all in combination with/without epoxy adhesives. Some of the reported findings from Nguyen et al. (2014) on the shear capacity of these various types of studs have contributed to validate current findings in this research. A key difference is that the current research investigated single/double curvature hypothesis propounded by Smith (2014) for headed steel studs in solid slabs for shear mobility. Hence, this study determined the contribution of stud deformation to increase shear capacity. Following the above, this chapter outlines three significant stages in the development of the beam including material characterisation, push-out characterisation, and hybrid beam performance. The experimental characterisation for both LWAC and GFRP provide fundamental details which will aid numerical calibration and offer further interpretation to the performance

of the hybrid beam. The push-out characterisation informed subsequent configuration of the hybrid beam. Subsections provided in this chapter will elaborate further on the above-mentioned stages of the development.

4.2 Material Characterisation

Characterisation of material is a necessary preamble in experimental research involving the study of materials. The significance of material characterisation serves as a quality control measure which ensures that test performances conform to standard specifications and promote the reliability of results. However, it is very important to bear in mind that prefabricated industrial materials such as steel and FRP are usually characterised by manufacturers and information on physical, chemical and mechanical properties are often made available to end users. Research publications have reported significantly higher properties for materials against property data published by manufacturers. Such relative variation in the degree of mechanical property may impact on research findings hence, material characterisation must be carried out or deduced from available research data. The current study adopts a combination of both characterisation and an estimation of material property for the experimental studies.

4.2.1 Concrete Materials & Composition of Samples

Two types of concretes are used in this research: normal weight concrete (NWC) and lightweight aggregate concrete (LWAC). The NWC was required as a control mix for pre-characterisation studies of the shear behaviour of the hybrid composite whereas the LWAC is the adopted concrete material for the current hybrid beam. The concrete slabs were fabricated from predetermined mix designs for NWC and LWAC following

standard design procedures detailed on Appendix A. The design of experimental method is adopted for the formulation of mix proportions for normal weight concrete (NWC).

Four distinct constituents were carefully proportioned together to develop the lightweight concrete (LWAC) referred as Lytag concrete. The constituents included cement, sand, coarse aggregate and water. The cement used refers to Portland Cement CEM1 52.5N which conforms to BS EN 197-1(2011) manufactured by Hanson Heidelberg Cement Group (see Figure 4.1a).

a) Portland cement for binder material

b) River sand for fine aggregate

c) Lytag aggregate (LWA)

Figure 4.1:Constituent materials for concrete

The fine aggregate which was used for all concrete mixes is sourced from a natural river with a nominal size finer than 2.36 mm. The sand is taken from regular supply available at the Coventry University light-structures laboratory (see Figure 4.1b). Potable water supplied at Coventry University light-structures laboratory was used for all mixes and curing in accordance with BS EN 1008 (2002). Trial mixes were carried out on percentage proportions for aggregates (sand and lytag aggregates) including cement/water ratios (see Appendix A1). However, mix proportions of trial mixes were compared against design mix using the design of experiments method (see Appendix A2) to determine final mix proportions for Lytag concrete. In addition, details of constituent for the control mix targeting normal density concrete is presented in Table 4.1.

Table 4.1 Mass (in kg) of Constituent materials per cubic metre.

Concrete Type	***Target Density (kg/m^3)***	***Cement (kg)***	***Water (kg)***	***Aggregates***	
				Sand (kg)	***Lytag*/Gravel** (kg)***
LWAC	1800	429.78	202.00	392.75	855.36*
NWC	2400	46.28	21.32	85.8	93.08**

The design of mix proportions for LWAC concrete is carried out in accordance with ASTM C 211. Standard test techniques are applied to determine the mechanical properties of the LWA and to ensure conformity to standard specifications (see Table 4.2). Table 4.3 shows the required standard test methods applied for the determination of their mechanical properties.

Table 4.2: Standards for LWA Characterisation

S/N	*Standard Title*	*Code*
1	Standard specification for lightweight aggregates for structural concrete	C330/C330M
2	Practice for reducing samples of aggregates to testing size	C702/C702M
3	Practice for sampling aggregates	D75/D75M
4	Test method for sieve analysis of fine and coarse aggregates	C136/C136M
5	Test method for bulk density (unit weight) and voids in aggregates	C29/C29M
6	Test method for relative density (specific gravity) and absorption of coarse aggregates	C127

Table 4.3: Test Standards for Concrete Properties

Test Description	*Test Standard*	*Equations*
Cube/Cylinder Compressive Strength, (Mpa)	BS EN 12390-3 (2011)	$f_c = {}^{F}/_{A}$
Split Tensile Strength (Mpa)	BS EN 12390-6 (2009)	$f_{ct} = {}^{2F}/_{\pi dL}$
Flexural Strength, (Mpa)	BS EN 12390-5 (2009)	$f_{cf} = {}^{Fl}\big/_{b_{fr}h_{fr}^2}$
Elastic Modulus (Mpa)	BS EN 12390-13 (2013)	$f_{ck,cyl} = 0.8 f_{ck,cube}$
Density, (kg/m^3)	BS EN 12390-7 (2009)	$\rho = \frac{Dry\ weight\ \times density\ of\ water}{Dry\ weight - Wet\ weight}$

4.2.2 GFRP Properties

This section focuses on the physical and mechanical properties of pultruded glass fibre-reinforced polymer otherwise referred in this study as GFRP. Some of the material properties reported in this section are obtained from the manufacturers. However, certain

significant properties of the materials have been derived from experimental testing's conducted at Warwick University by Matharu (2014) and calibrated against the manufacturers data. The calibration exercise aims to provide control over further experimental results and subsequent analysis of the hybrid beam section.

GFRP material used for pre-characterisation of shear behaviour involving GFRP-NWC push-out specimens was procured from engineering composites with material properties published by the manufacturers. Follow-up characterisation and hybrid beam test adopted wide flange (Pultex superstructural 1525 WF) sections previously domiciled at Warwick University and manufactured by Creative Pultrusions (CP). The geometrical dimensions

Figure 4.2: Wide Flange (WF) Profile Section (Matharu, 2014)

of the WF-section given in Figure 4.2 represents a symmetrical wide flange (WF) profile of equal thickness in web and flange sections. WF-profile sections are manufactured from continuous fibre pultrusion process (Bank, 2006) subjected to resin injection (closed

mould resin injection). Further information on material properties for the WF sections are provided in Appendix B of this research.

4.3 Experimental Design

The experimental study is broadly divided into two major parts to carefully study the interdependent components that fully describe the behaviour of the novel hybrid composite beam. The first part of the push-out experimental programme was designed to test the interfacial shear behaviour of the composite beam using standard test methods and industry-based practice (see section 4.3.1 and 4.4.1). The test was designed to investigate the various parameters that influence the interfacial shear behaviour of the hybrid composite.

The second part of the experimental programme focused on the fabrication and testing of the hybrid composite beam. The fabrication of the hybrid composite is based on the knowledge of steel-concrete composite developed from industry practice. The key concept of the fabrication is centred on a technique required to ensure composite action without compromising the flexural integrity of the beam. The design, fabrication and instrumentation of the beam is detailed in section 4.4.2.

4.3.1 Push-Out Characterisation

The experimental design for the pushout test aims to investigate various aspects of the shear connection, which influences composite shear behaviour. Composite action in all specimens are achieved using steel shear studs in establishing a complete connection between concrete slabs and the flanges of FRP WF sections. The choice of connection adopted to resist lateral shear forces in the composite is due to the limited choices

available for sustaining composite connection between pultruded FRP sections and concrete slabs. FRP sections can either be bolted or bonded to other elements to form composites. From these two available methods, shear connection can be achieved by a combined and/or independent method as the case maybe. The current method of stud connection is carefully adopted to replicate the traditional stud connection for steel-concrete composite in an attempt to proffer the FRP WF section as an alternative lightweight material to steel in composite structures. It is therefore necessary, that the steel stud satisfies the relevant characteristic requirement to ensure optimal shear capacity for the connection and to prevent premature failures of the composite beam under serviceability and ultimate limit performance. Eligibility aspects of the stud considered in the design includes the cross-sectional geometry and corresponding strength properties. From the selection of appropriate studs to the above conformity criteria, other parameters of the connection are determined subject to the experimental test capacity. These parameters include the shear resistance and corresponding optimal stud arrangement (configuration) for the GFRP-concrete composites. The experimental design is implemented under three distinct phases to investigate preceding characteristics of the shear connections (see Figure 4.3). These phases represent the key investigations carried out under each set of experimental tests to derive relevant details of the connection which

will build integrity and reliability for the proposed novel hybrid beam. Descriptions and illustrations for the activities within the phases are detailed in subsequent sections below.

4.3.1.1 Phase I: Stud configuration

This phase is designed to study the effect of stud arrangement (configuration) on the shear performance of the composite section. The bolt arrangement for composite connection is based on two standard formats and an industry practice format; single-row (2 number of studs per row), double-row (four number of bolts of two per each row) and staggered stud (three number of bolts of one stud per row) configurations respectively (see Figure 4.4 a, b & c). The single-row and double-row configuration represents the geometric specification obtained from standards; BS5400-5 (2005) and BS EN 1994-1-1 (2004) respectively. The staggered stud arrangement represents common practice obtained in

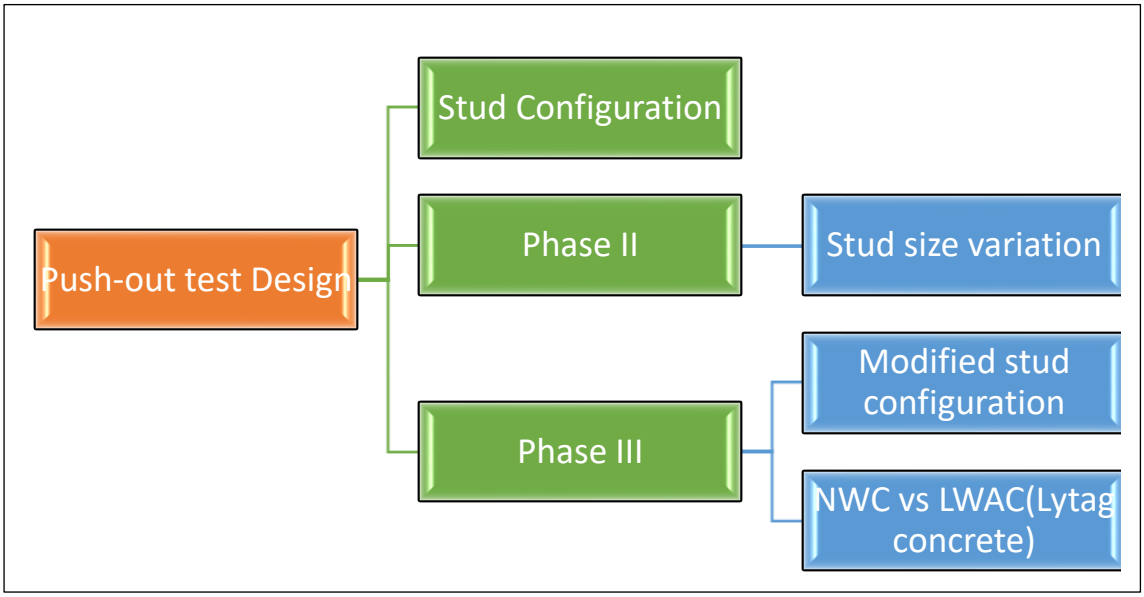

Figure 4.3: Experimental Characterisation Plan

industry. A stud cross-sectional diameter of 19 mm was adopted within this phase for the characterization study. The choice of using this single size stud diameter was to enable appropriate characterisation of the arrangements which may produce significant shear

resistance with minimum number of studs. Specimen geometry consist of two normal weight concrete (NWC) slabs of cross-sectional area 550 x 500 mm and slab thickness of 150 mm respectively. GFRP WF-section of 200 x 200 mm cross-section with constant thickness of 10 mm and 600 mm axial length. Identification of specimens is necessary to ensure a distinct identity for the purpose of analysis. Hence, specimens are labelled to reflect key characteristic features such as stud size, configurations, concrete type and serial number etc. Specimen labelling for the three specimens include PO-SR-S1, PO-DR-S2 and PO-SG-S3 respectively (see Figure 4.4 a, b & c). Label notation details are PO to indicate Push-out; SR, DR, SG to represent single-row, double-row and staggered arrangements (configurations) respectively; and S1 represent test specimen serial number 1, 2 or 3 (Expanded description of variables are presented in Table 4.4). All concrete slabs are from a single batch of concrete mix under a 28-day curing period. All concrete slabs were cured from the fabricated mould described in section 3.3 with details of the concrete mix design and properties outlined in Appendix A1.

Table 4.4: Variable Description for Phase I Test Specimens

Specimen ID	**Stud diameter (mm)**	**Stud arrangement (SR, DR, SG)**	**Stud Embedment depth (mm)**	**Concrete cylinder /cube strength (MPa)**	**Concrete Elastic Modulus (GPa)**
PO-SR-S1	19	SR	100	47.2/49.9	31.3
PO-SG-S2	19	SG	100	47.2/49.9	31.3
PO-DR-S3	19	DR	100	47.2/49.9	31.3

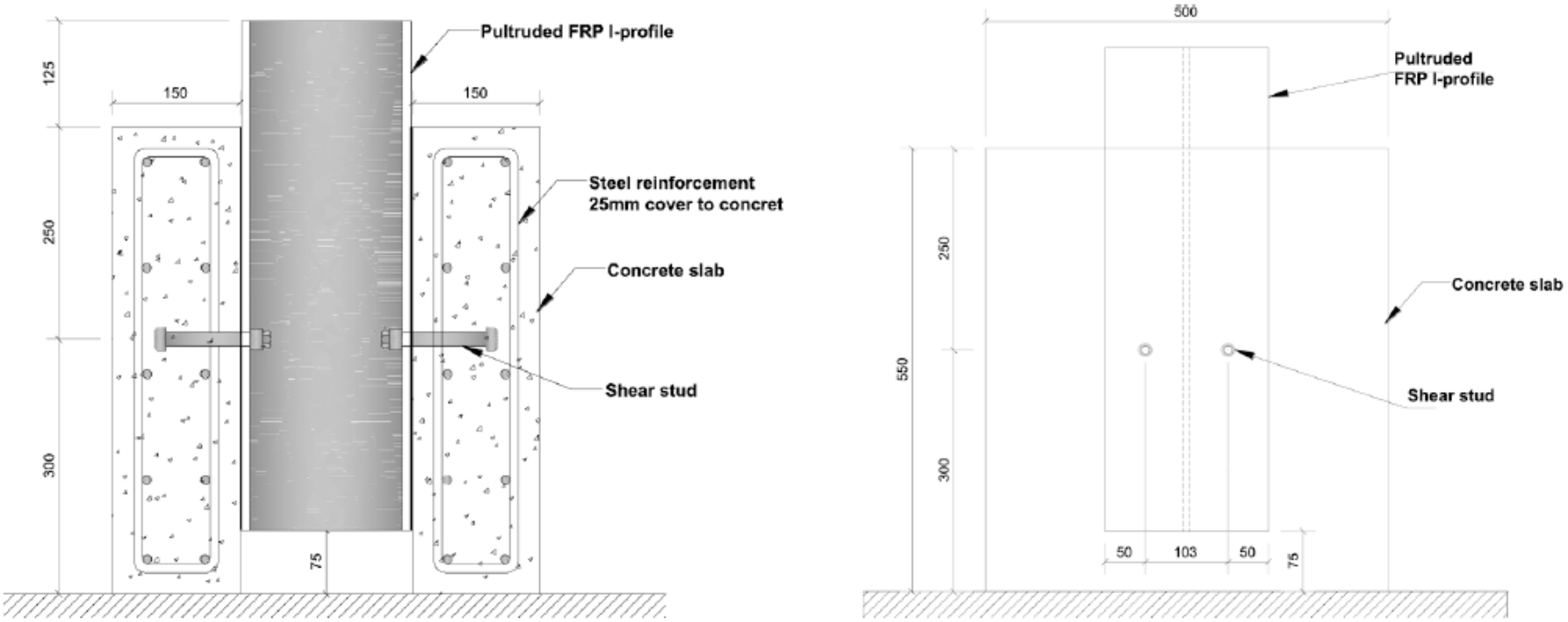

a) Single row stud arrangement (PO-SR-S1)

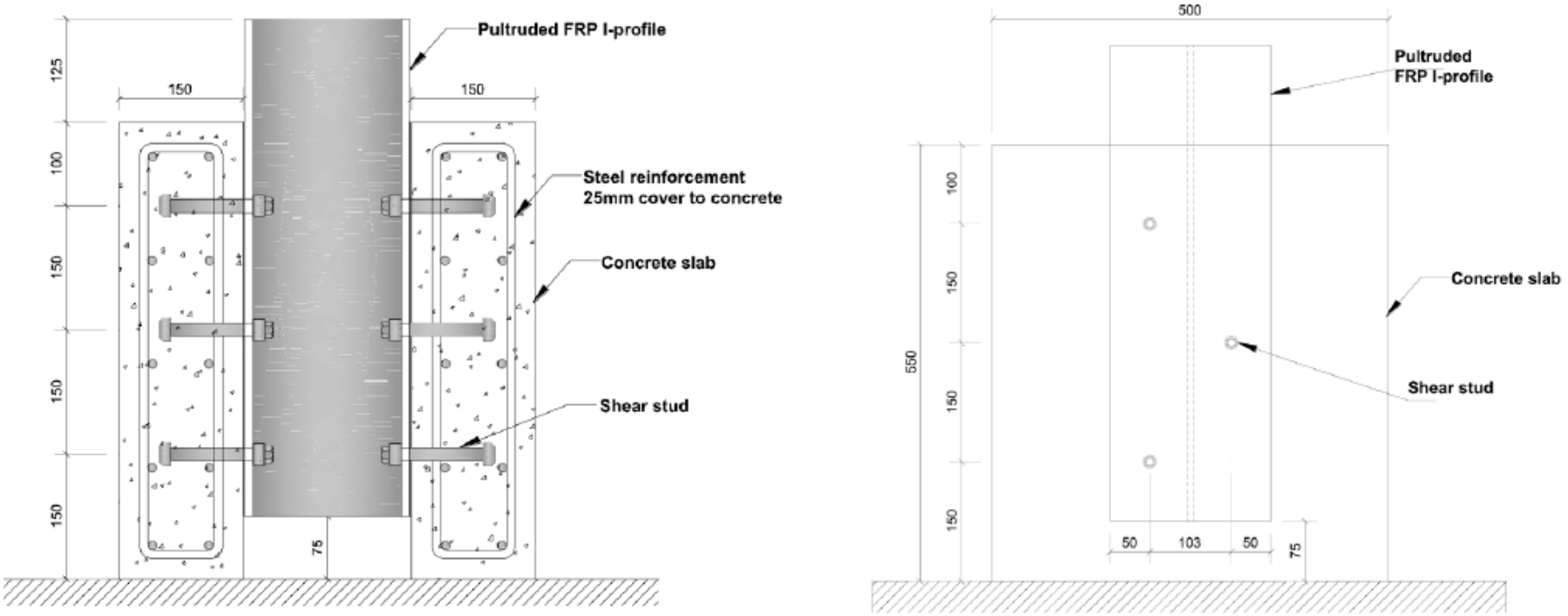

b) Staggered stud arrangement (PO-SG-S2)

Figure 4.4: Specimen Configuration (Etim et al., 2020)

4.3.1.2 Phase II: Stud size variations

Result findings from phase I determined the stud configuration for the hybrid GFRP-concrete beam using the two-row stud arrangements. Phase II focused on developing specimens under this double-row stud arrangement to determine an optimum size of stud for the composite connection. Two stud cross-sectional sizes of 12- and 16-mm diameters respectively are adopted for this phase of experimental testing on a constant double-row configuration (see Figure 4.4c). Apart from the stud sizes, all other parameters are kept constant including the geometric dimensions of the specimens and stud embedment depth. Specimen label in the phase captured the variation in stud sizes and serial numbers of specimen in continuance of phase I. Three specimens are considered including; PO-12B-S4, PO-12B-S5 and PO-16B-S6 respectively. Designated labels are as follows; PO for push-out, 12B or 16B for 12- or 16-mm stud diameter and S4 for specimen serial number 4. Normal weight concrete (NWC) was deployed for the development of the concrete slabs under a 28-day curing period in connection to the FRP WF-section of similar geometrical identity to that of phase I.

Table 4.5: Variable Description for Phase II Test Specimens

Specimen ID	**Stud diameter (mm)**	**Stud arrangement (SR, DR, SG)**	**Stud Embedment depth (mm)**	**Concrete cylinder /cube strength (MPa)**	**Concrete Elastic Modulus (GPa)**
PO-12B-S4	12	DR	90	28.2/46.0	30.1
PO-12B-S5	12	DR	90	27.8/45.3	29.9

PO-16B-S6	16	DR	90	25.8/40.0	28.1

4.3.1.3 Phase III: Bolt modification in Lytag concrete

Two specimens are developed within this phase comprising of LWAC (Lytag) concrete slabs. The key difference between the specimens of this phase was in the nature of the embedded studs. Summary findings from the previous phases resulted in the adoption of double-row configuration for the Lytag (actual) push-out specimens from Phase I and the 12 mm stud size diameter from Phase II as appropriate characteristic features of the LWAC (Lytag) companion specimens to the novel hybrid beam. Another significant change was the introduction of a collar stud (see Figure 4.5) to reflect the developed stud configuration of the hybrid beam due to tolerance and fabrication limitations. Phase II specimen configuration is replicated for lytag specimens of phase III with a reduction in the slab thickness from 150 mm to 120 mm to ensure significant conservation of the concrete materials. GFRP WF-section (Creative Pultrusion) of 200 x 200 mm cross-section with 10 mm thickness is adopted at a longitudinal length of 450mm. The shear studs used for the pushout specimen in this phase consist of 12 mm diameter steel studs

of 130 mm length. Both specimens are labelled as PO-12B-LS7 and PO-12Bm-LS8 respectively with B_m representing the collar stud. See Table

Table 4.6: Variable Description for Phase III Test Specimen

Specimen ID	**Stud diameter (mm)**	**Stud arrangement (SR, DR, SG)**	**Stud Embedment depth (mm)**	**Concrete cube strength (MPa)**	**Concrete Elastic Modulus (GPa)**
PO – 12B – LS7	12	DR	90	40	18.7
PO -12Bm – LS8	12	DR	90	40	18.7

Figure 4.5: Collar steel stud

4.3.2 Hybrid Composite Beam

The development of the hybrid beam is informed from series of characterised push-out test involving stud sizing and configuration. The most feasible arrangement is adopted in the design of the hybrid beam to outline lateral spacing of studs. The concrete (LWAC) is prepared from similar mix proportions adopted for the push-out and cured for a 28-day period and compositely connected to GFRP WF-section as detailed in subsection 4.4.

4.4 Fabrication Methods & Setup

This section will provide information on the design methods, fabrication processes and test setups for both the push-out specimens and hybrid beam specimen.

4.4.1 Push-out specimen fabrication

The experimental test is carried out following detailed methodological plan involving prefabrication of moulds (formwork), drilling, coupling and specimen setup. The materials adopted for the mould fabrication of the precast concrete slabs comprised of steel plates (6 mm thick) carefully welded together into an open sided cuboid and timber infill of 10 mm thickness to cover the open sided cuboid (see Figure 4.6). The timber infill was carefully designed for flexibility to provide an adjustable control to the thickness of concrete as a significant variable in the push-out experimental study. See Table 4.4 for details of the inner dimensions of the mould.

Table 4.7: Geometric dimensions (Internal) of Mould

Material type	***Geometric detail***	***Dimension (mm)***	***Adjustability***
Steel/timber	Height	550	Rigid
Steel/timber	width	500	Rigid
Steel/timber	thickness	0-200	Adjustable

Figure 4.6: Concrete Slab Mould with Adjustable Timber In-Ply

The choice of timber adopted to provide adjustable control of the slab thickness became necessary to ensure sustainability of the mould from frequent use and potential modification of stud arrangements in the slab considering edge distances and spacing (longitudinal and transverse spacing). Hence, the timber infill was drilled to create clearance openings to accommodate the size of bolts with slip tolerances of 2mm providing temporary support to the embedded stud fixtures (stud embedment) in concrete during the curing period.

4.4.1.1 Curing of concrete slabs:

The precast concrete slabs were formed into shape using the prefabricated bespoke steel mould described in section 4.4.1 (see Figure 4.7a). The timber infill permitted a temporary insertion of the steel studs through the pre-drilled clearance holes into the concrete allowing for the adjustment of stud embedment depth. The concrete was compacted in four equal layers using the handheld concrete vibrator to ensure efficient compaction and reduction of air voids in the resulting concrete mixture. The curing process was carefully controlled using wet sack bag to provide moisture intermittently thus enabling appropriate hydration and strength mobilisation for a curing period of 28 days. The final precast cured slabs reflected the inner dimensions of the mould that was used for the concrete casting

(a) Concrete infilled into Fabricated Mould

(b) Cured Concrete Slabs

Figure 4.7: Precast Concrete Slabs

(see Figure 4.7b). Companion samples of the concrete were set aside for the determination of concrete mechanical properties as reported in Appendix A.

4.4.1.2 Fabrication of GFRP specimen:

The GFRP WF-section was cut into 600 mm heights and holes drilled on the flange for stud allowance holes (clearance holes) to specific arrangement described in section 4.4.2. The clearance holes were drilled in excess of 1 mm to the stud size (shank diameter) onto both flanges of the section. The drilled clearance holes were configured into three major arrangements; single row (SR), double row (DR) and staggered arrangements for Phase I of the push-out experimental programme (see Figure 4.8 a-c).

(a) Single-row arrangement

(b) Double-row arrangement

(c) Staggered arrangement

Figure 4.8: Fabricated push-out specimens

4.4.1.3 Specimen configuration, instrumentation, and test setup

The slab specimen was assembled to an FRP-section using a bolt configuration that ensured composite action between the two distinct materials. The precast slabs with protruding studs (bolts) were fastened to both flanges of the pultruded fibre reinforced polymer (GFRP) WF-section using nuts and washers to establish a demountable connection. The need for a robust parametric evaluation of shear performance resulted in the segmentation of experimental activities to study the variability effect of stud configuration on shear performance. Hence, experimental activities are carried out in phases to reflect stud arrangements and parameters (see section 4.2 for details on push-out experimental design).

The test rig shown in Figure 4.9 illustrates the test mechanism and setup for loading the specimens. The specimen loading was carried out to a degree capable of deforming the shear studs or until physical failure was observed where no further load was permissible. Loading unto the specimen was practicable at a rate of 10kN/min using a manually operated hydraulic jack with a 500kN load cell. A spreader steel plate of 10 mm thickness was adopted to ensure uniformity of load distribution across the geometric surface of the composite section. The loading data was received through a data logger system which was used to read and record the incremental loading deduced from the load cell. Two displacement transducers were positioned on opposite sides of spreader steel plate to measure the longitudinal slip during loading of the FRP WF-section against the reinforced concrete slabs.

Strain gauges were instrumented on the flanges of the GFRP I-section and the embedded stud specimens (see Figure 4.10 & 4.11). The strain gauge was placed longitudinally at

25 mm distance above the clearance holes of the FRP flanges where composite connection was established to determine the strain response of the flanges to shear load (see Figure 4.10). A set of strain gauges were attached to the shanks of the embedded studs before concrete curing for measurement of deformation responses to shear forces. The positions of the strains on the stud are illustrated in the schematic diagram below (see Figure 4.11 a-b).

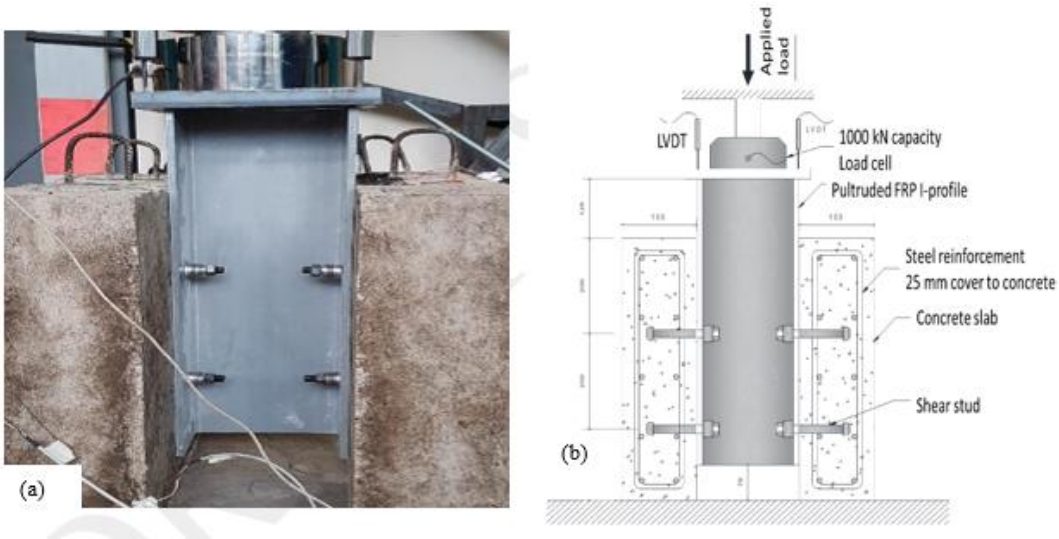

Figure 4.9: Push-out test setup

Figure 4.10: Representation of strain gauge on GFRP flanges (Etim et al., 2020)

Figure 4.11: Representation of strain gauge on shear studs (Etim et al., 2020)

4.4.2 Composite beam fabrication

The novel hybrid composite beam was developed from prefabricated moulds designed to generate the required geometric details of the hybrid composite. One of the key challenges of the fabricated composite is the arrangement and alignment of the shear studs within

the concrete to accommodate the clearance holes on the flange of the FRP section. The principal consideration of design for the beam can be summarised under the following:

- ✓ The fabricated mould must ensure appropriate vibration and curing of the concrete (LWAC) material.
- ✓ Shear studs must be embedded at required depth with an arrangement to accommodate the transverse and longitudinal spacing of the clearance holes on the FRP flange section.
- ✓ The mould must enhance the compaction of concrete around the embedded studs for the mobilisation of adequate compression forces during the flexural test.

The above principles will be illustrated under the subsections below to demonstrate the efficiency of the fabricated sections and the general reliability of the experimental setup.

4.4.2.1 Design & fabrication concept

The need for a prefabricated mould to ensure concrete slab curing for the concrete component of the hybrid GFRP-LWAC becomes mandatory in the experimental preparation of the specimen. However, the challenge for the design of the mould is centred on achieving accuracy of bolt configuration and alignment to enable composite fitness or compatibility with the GFRP WF-section. Therefore, a simple rectangular mould was designed using timber boards of 10 mm thickness to establish an open sided rectangular cuboid with inner geometric dimensions of 400 x 3500 x 120 mm for width, length and depth respectively (see Figure 4.12). The inner dimensions represent the geometric size of the concrete slab to be cured. The challenge of ensuring a reasonable and accurate configuration of the embedded bolt arrangement in the concrete was achieved by making the FRP WF-section a permanent integral member of the mould (see Figure 4.13). The concrete mould comprised of five wooden plates: bottom plates (with

an underneath clearance for steel handles to ease lifting) and two pairs of sides to achieve the width and length of the concrete slab. The internal height of the sides was limited to 120mm to reflect the thickness of the cured concrete slab.

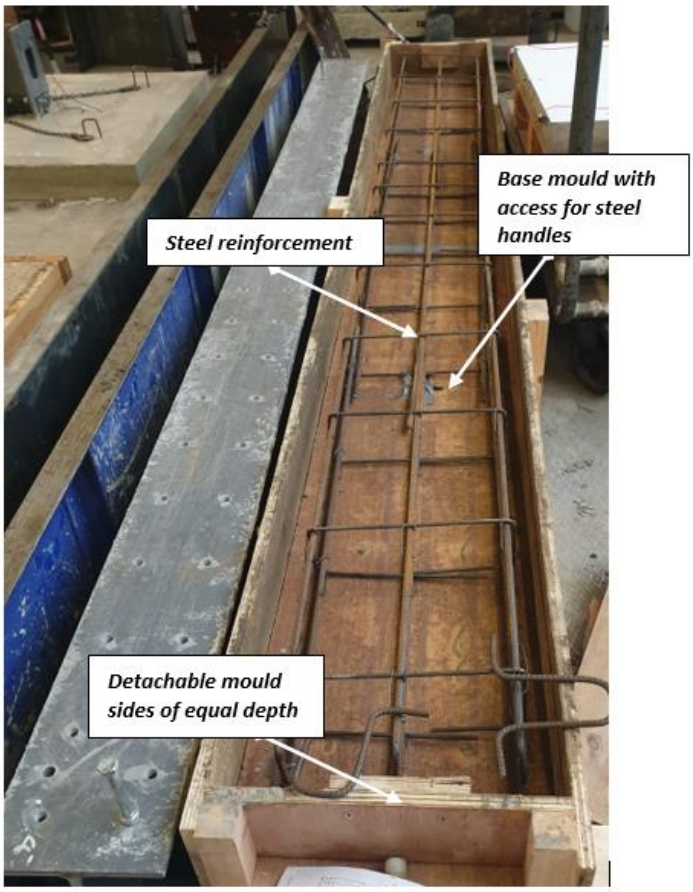

Figure 4.12: Concrete mould with steel reinforcement

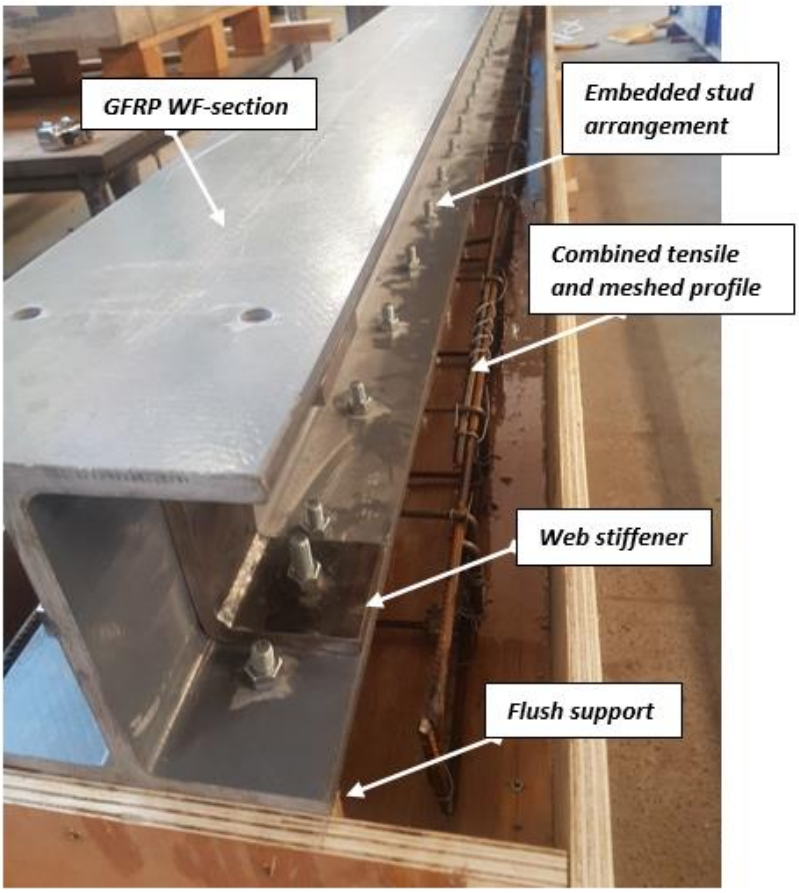

Figure 4.13: GFRP-Integrated-Concrete Mould

4.4.2.2 Fabrication of GFRP subcomponent

The GFRP WF-section was cut to a length of 3.5 m in equal alignment to compliment the span of the concrete slab. The cross-sectional dimensions of the WF-section is provided in Figure 4.2. Clearance holes drilled into the top flange of the FRP-section were made using an industrial drilling machine for bolt installation at a specified stud spacing taking

into account the longitudinal, transverse and edge spacing respectively (see Figure 4.14). Two pairs of bolted C-shaped web stiffeners of 75 mm width and 6 mm thickness were provided on the web at the ends of the girder directly above the proposed area for end supports. The stiffeners accounted for web strengthening against premature failures at the supports of the FRP-section due to the anticipated support reactions against the applied flexural load.

4.4.2.3 Fabrication of concrete subcomponent

The bolts, GFRP-section and concrete mould became an integral system for concreting and curing activities. However, before the mould assemblage, concerns of concrete slab handling was accounted for through the provision of a unified reinforcement system combining tensile reinforcement and anti-crack meshing functions simultaneously. The schematic design proposed an anti-crack mesh to minimize concrete cracking during loading and this consideration was merged with the tensile reinforcement concerns for ease of handling. The longitudinal reinforcement bars adopted was Y10 bars at 100 mm spacing with transverse confinement links using M8 bars at 300 mm spacing. The embedded bolt was modified to ensure stiffness and rigidity unto the girder. This was necessary in achieving accuracy of the hybrid composite demountable connection also, to ensure accurate embedment depth for the bolt arrangement.

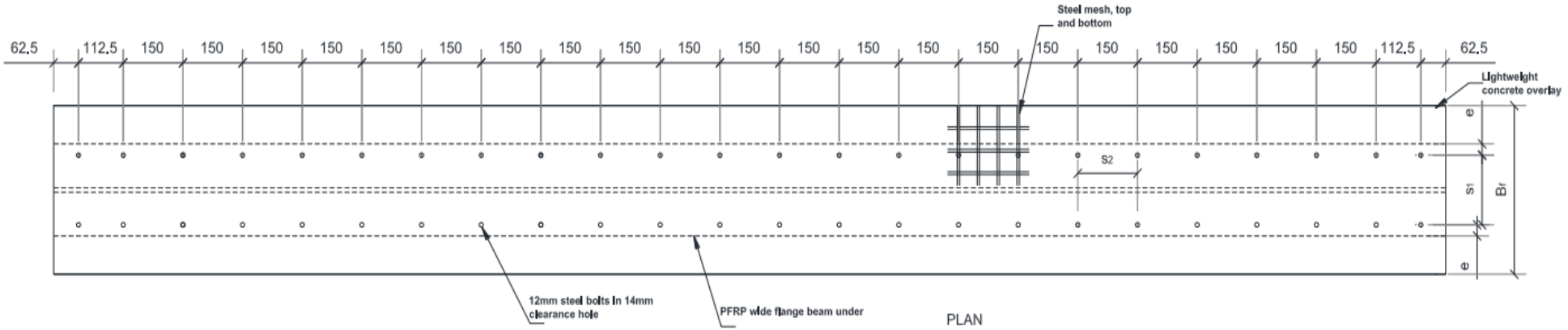

Figure 4.14: Representation of bolt spacing

4.4.2.4 Specimen configuration

The bolt assemblage process was carried out with the bolt (stud) already pre-fixed into the clearance holes on the flange of the FRP-section at an embedment depth of 100 mm. The pre-bolted GFRP profile section was placed on the concrete mould with the pre-bolted flanges inverted to allow for the suspension of bolts downwards into the mould at the specified embedment depth of 100 mm. The reinforcement cage was placed beforehand, allowing a 15 mm concrete cover at the top and bottom of the mould. The finished mould already replicated an inverted composite section ready for concrete placement (see Figure 4.15). After curing, a torque of 30 Nmm was applied to all bolts to ensure an evenly distributed pretension force across all connection. See Figure 4.15 for the cured concrete assembled novel beam.

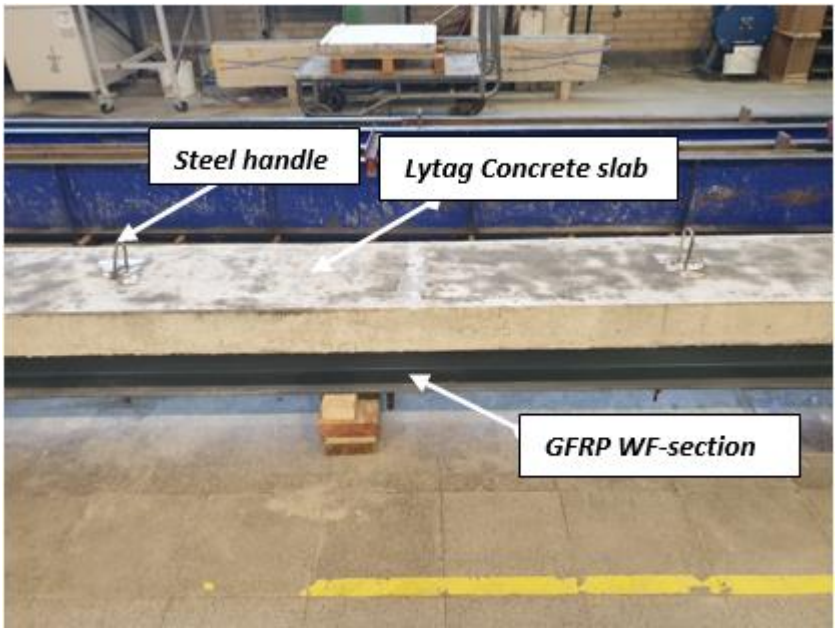

a) Front view

b) Cross sectional view

Figure 4.15: Sectional Views of Precast Composite Beam

4.4.2.5 Composite Specimen Instrumentation

The curing process was completed in 28 days in conformance to standard practice. During the curing process, concrete slab was constantly wetted with water to control the hydration process. The specimen was instrumented with strain gauges as a significant component of the test setup to achieve careful monitoring and evaluation of the specimen behaviour during the test.

Instrumentation is a mandatory index for carrying out experimental testing involving mechanical performance of materials. Therefore, it becomes necessary to prepare an instrumentation plan (see Figure 4.16) with the aim of fulfilling the experimental which is one of this study's objectives (see Section 1.4). Summary of instrumentation details is presented in Table 4.5 below.

Table 4.8 Specimen Instrumentation Details

Objectives	Parameter	Instrumentation	Positions
Flexural strength	Load/stress	Load cell	Central load spreader on the slab surface
Vertical Deflection	Rotation/displacement	Load displacement transducers (LVDT)	Vertically positioned LVDTs on slab surface
Lateral Deflection	Torsion	Load displacement transducers (LVDT)	laterally positioned LVDTs on FRP web
Bolt Deformation	Strain distribution	Strain gauges	Strain gauges placed on steel bolts embedded in concrete
Stress distribution	Strain distribution	Strain gauges	Strain gauges placed on FRP flanges, web and concrete surfaces.

The summary table associates the experimental objectives with instrumentation plan/design carried out to obtain relevant data for interpretation and further. The summarized description is not exhaustive of the objectives presented as further relationships detailed in subsequent sections could become possible due to the carefully designed and implemented instrumentation activity.

4.4.2.6 Test Setup and Procedure

The experimental setup was designed to replicate the traditional four-point bending test setup for the flexural determination of flexural properties of materials. The test required simple supports at the ends of the longitudinal composite sections for reactions to counter the applied loads and a spreader beam of pre-specified length to apply two symmetrical point loads at equal distance from the end supports of the composite beam section (see Figure 4.16 & 4.17). The four-point test setup was constructed on a test frame to ensure proportional and controlled distribution of forces (load transfer pathway) throughout the setup and to minimize health and safety concerns. The test setup was loaded incrementally using an automated hydraulic mechanical device at a rate of 10kN/min using a device

connected to a 1000KN load cell with output to a data logger for obtaining load data and corresponding time. Data loggers for all instrumentation devices were connected to system router for obtaining corresponding readings of the changes (external and internal) on the composite section.

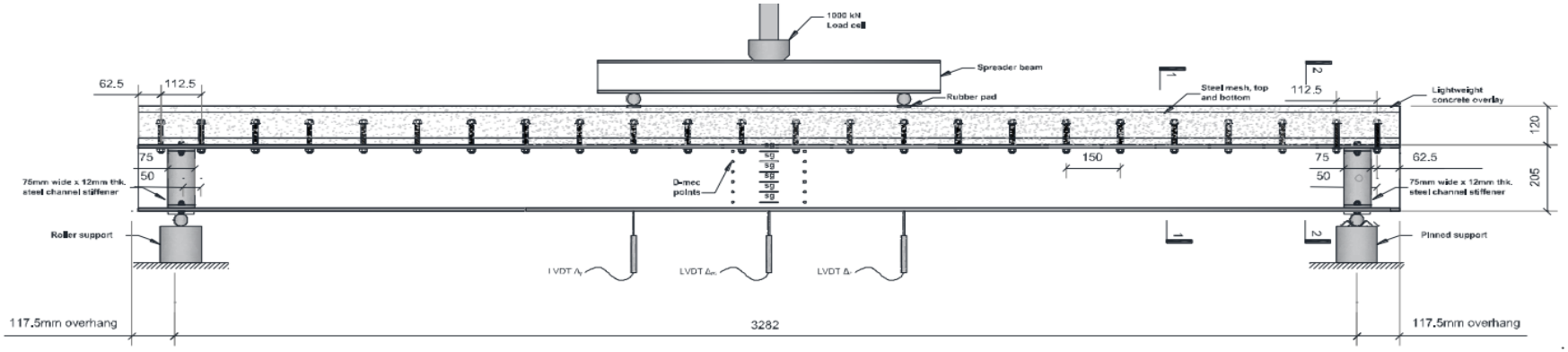

(a) Font elevation view

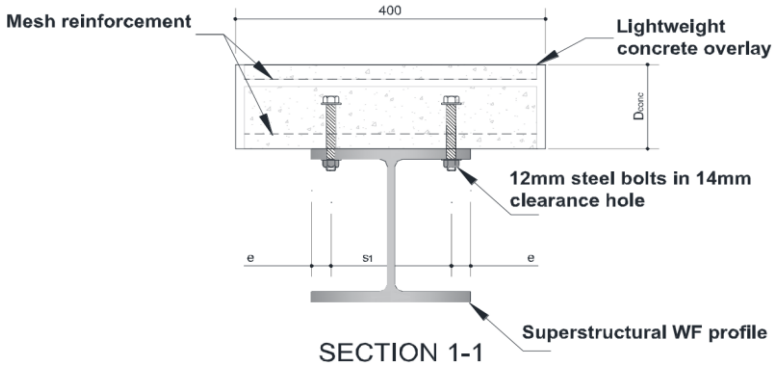

(b) Cross-sectional view

Figure 4.16: Schematic setup of novel beam

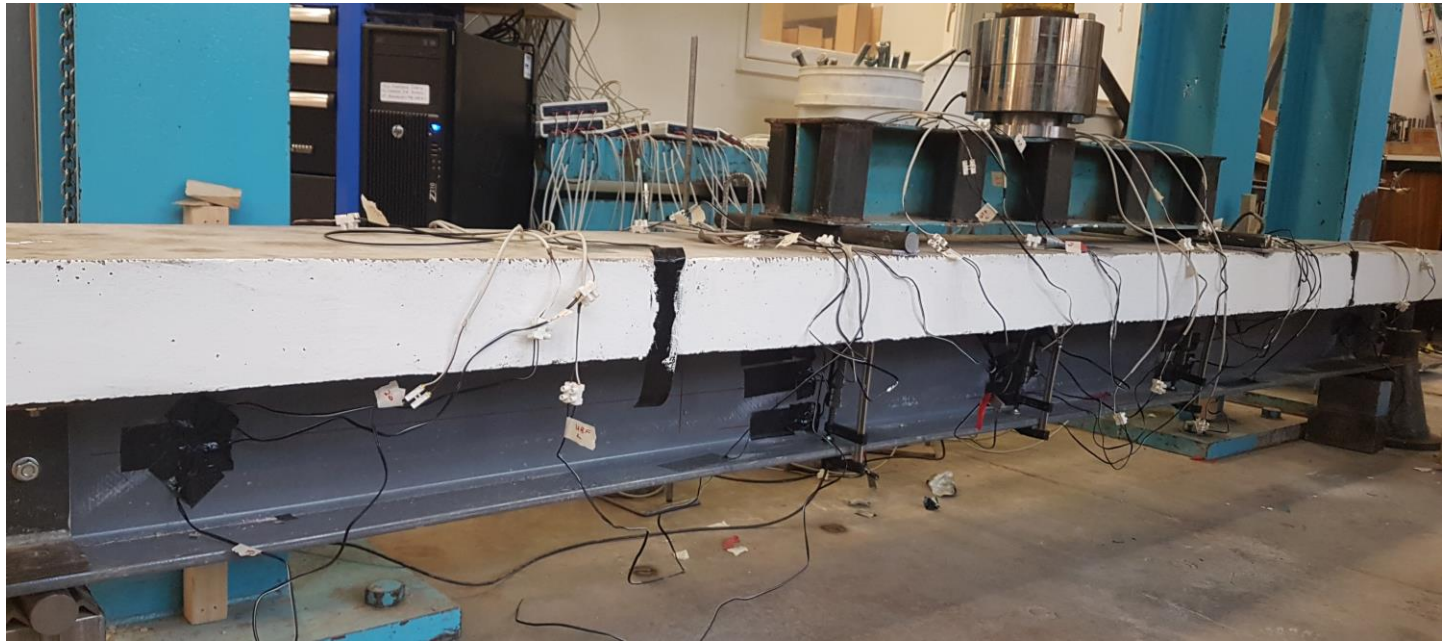

Figure 4.17: Experimental setup of novel hybrid beam

CHAPTER 5. NUMERICAL DESIGN & METHODS

5.1 General.

The aim of this chapter is to describe the computational settings required to develop a numerical model which will predict the behaviour of the hybrid composite beam. The numerical model is intended to establish solutions which closely describes the behaviour and performance of the physical composite beam and aid the derivation of appropriate conclusions for the study.

The objectives of the numerical study include:

- ✓ Replicate the four-point test on the ANSYS APDL software developing a finite element model with similar geometric properties and assigned material data, simulating all boundary and loading conditions to derive composite behaviour, deformations and failure modes.
- ✓ Produce a direct comparison to the actual experimental loading setup setting up boundary restraints and applied load against virtual nodal restraints and applied nodal displacement-loads.
- ✓ Provide a parallel result against literature, experimental and analytical results.
- ✓ To generate pilot reference data for future research studies on GFRP-concrete composites. In addition, to offer a basis of the numerical results to establish safe design criteria for GFRP-concrete hybrid beams.

5.2 Numerical design.

Finite element analysis was adopted to develop a virtual model to simulate the novel hybrid beam under the action of forces and the corresponding effect in terms of physical deformations and internal stresses within its component members. Subramani et al.

(2014b) describes the finite element method as a numerical approach which can be adopted to simulate the behaviour of materials and evaluate their corresponding responses under a given loading condition. The method disintegrates the model into elemental fragments which can be evaluated using iterative equations to determine an approximate solution for the model. This disintegration approach for the model ensures its effectiveness for nonlinear solutions involving varied stress-strain behaviour of materials. In order to properly represent the model, certain assumptions are made from hypothetical theorems and principles including boundary conditions, determinacies and equilibrium theorems.

The current numerical study is carried out on ANSYS finite element analysis (FEA) software (ANSYS APDL R19.1) due to its ability to design and adapt models from other CAD software's into its application. The ANSYS APDL allows for the development of geometry using keypoints, lines, areas and volumes etc. to generate 1D, 2D and 3D geometry with semblance to realistic physical matter representing engineering components. Any developed geometry can be assigned a material element to give description and enable simulation of physical material behaviour.

One of the reasons for the choice of ANSYS APDL FE software is mainly to overcome the vast limitation of experimental testing usually associated with large consumption of materials, increasing cost of research and material waste. In addition, FE software packages offer the benefit of time efficiency and extended analysis resulting from parametric and sensitivity studies. The low-cost advantage of numerical analysis makes it a crucial component of current research methods. A model can be validated against experimentally or theoretically obtained results for reliability and in furtherance to

simulate complex test-setups which predict material behaviour. This section expounds on the procedure for setting up the finite element model using the ANSYS APDL software.

5.3 Numerical Modelling

Elements refer to solid model fragments assigned to a space geometry which enables model discretisation for finite analysis. Element formulations in ANSYS may be classified under two categories (Thompson & Thompson, 2017). The first category is based on technology (current technology or legacy technology) while the second class is based on usage (general purpose or special-purpose use). The common elements used for static structural simulations include SOLID, BEAM and SHELL elements. Studies have proposed the use of SHELL elements in comparison to SOLID elements in analysing thin-to-moderately thick beams or structures for computational efficiency (Zhu et al., 2014). SHELL181 element characterised by four nodes on the first order-shear-deformation theory are often used in modelling steel structural plates or beams in ANSYS FE software (*Zhang et al.*, 2013; Queiroz et al., 2007). This element is capable of simulating boundary conditions which consist of three translational and rotational displacements represented as U_X, U_Y and U_Z for translational and ROT_X, ROT_Y and ROT_Z for rotational freedoms respectively. Whereas the SOLID185 and SOLID65 of 3D 8-node element are characterized by three degrees of freedom (U_X, U_Y, U_Z) at each node is commonly used for 3D modelling of concrete structures (Queiroz et al., 2007; Luo et al., 2012; Jayajothi et al., 2013; Satasivam and Bai, 2014, Ibrahim, 2016, Pakala and Kodur, 2016). However, SOLID 185 (see Figure 5.1a) elements have plasticity, hyper-elasticity, stress stiffening, creep, large deflection, and large strain capabilities. Due to its mixed formulation capability for simulating deformations of both nearly incompressible

elastoplastic and fully incompressible hyper-elastic materials, it can be applied to simulate GFRP materials. The most important distinction between SOLID185 and SOLID65 is the ability of SOLID65 element to treat nonlinear properties of concrete. The SOLID 65 legacy element does simulate nonlinear concrete behaviour (cracking under tension and crushing under compression) making it quite relevant for the current study. However, the Solid185 element was adopted for modelling GFRP section due to the limitation of simulating tension cracking or compression crushing of concrete. Hence, the SOLID65 legacy element (see Figure 5.1a) remains the most efficient element for modelling reinforced concrete and promotes the use of ANSYS ADPL over its user-friendly counterpart ANSYS workbench.

SOLID185 remains relevant as an element deployed for modelling the GFRP composite. The element is reportedly flexible to accommodate material stack-up comprising of multiple orientations and orthotropic material properties within each layer. This is applicable to steel plates or web stiffeners used in the model. The LINK 180 element type (see Figure 5.1b) was adopted for the studs and all steel components due to its ability to simulate compression and tension under the discretisation approach. LINK 180 element is a uniaxial element possessing three degrees of freedom at each node for translational motion in the x, y and z directions. Some key limitations of the element include materials must be straight, axially loaded, and contain uniform properties end-to-end. A displacement shape function may imply a uniform stress in the spar.

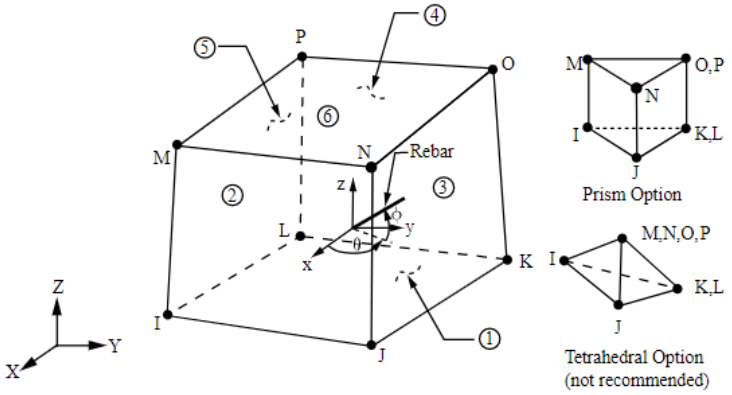

(a) SOLID65 or SOLID185 element

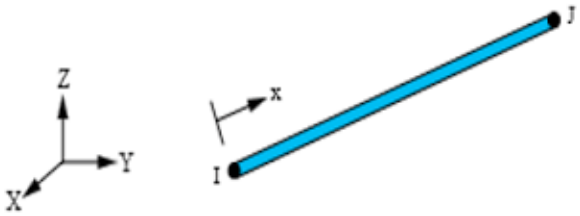

(b) LINK180

Figure 5.1: Element types used for the current study

5.3.1 Material Model

The constitutive material to be assigned to the solid model will be defined by the inherent mechanical properties predetermined from experimental testing or obtained from other reliable sources (including manufacturers guide, research publications etc.). In this study, linear and nonlinear properties of concrete were determined from laboratory experiments. Due to major limitations in the characterisation of the GFRP and stud materials at the

structure's laboratory (Coventry University), data for material properties of these components were obtained from other reliable sources: mechanical properties of studs were obtained from manufacturers raw data and GFRP mechanical properties were adopted from previously characterised data of similar batch of profiles (carried out at Warwick University) and published by Matharu (2017).

5.3.1.1 Concrete Material

Concrete has been described by Vacev et al. (2015) as a material which exhibits a linear elastic quasi-brittle behaviour under low compression (until about one third of its compressive strength). The tensile strength of concrete has been reported to be about 8 – 15% its compressive strength (shah, et al. 1995). Elastic modulus and poisons ratio are both inherent properties which describe the linear elastic isotropic behaviour of materials like concrete. The values for elastic modulus and Poisson's ratio are obtained from concrete characterisation of both Normal Weight Concrete (NWC) and Lightweight Aggregate Concrete (LWAC) tabulated in Table 5.1.

Table 5.1 Linear Isotropic Properties of Concrete

Linear Isotropic Properties of Concrete and steel		
NWC concrete	Elastic Modulus (EX)	27650 MPa
	Poisson's ratio (PRXY)	0.2
LWAC – 1 (D1810)	Elastic Modulus (EX)	11264 MPa
	Poisson's ratio (PRXY)	0.2
LWAC – 2 (D1865)	Elastic Modulus (EX)	18790 MPa
	Poisson's ratio (PRXY)	0.2
Reinforcement Bar	Elastic Modulus (EX)	210000 MPa

	Poisson's ratio (PRXY)	0.3

Concrete exhibits nonlinear behaviour under increased compression and some ductility may be expected as published by Vacev et al. (2015). The flexural behaviour of the prismatic beams tested in the laboratory for flexural properties were consistent with Vacev's report. Concrete cracking is a result of tensile yielding after exceeding the linear elastic maximum tensile strength of the concrete. Crushing behaviour is exhibited at concrete softening point beyond the maximum compressive strength. Nonlinear properties for all concrete components are defined under the multilinear isotropic hardening curve, which is an inelastic, rate-dependent property of concrete materials. Table 5.2 outlines the stress-strain values obtained from concrete crushing test carried out in the laboratory and inserted into the model for both NWC and LWAC. Beyond the concrete linear properties (elastic modulus and Poisson's ratio) outlined in Table 5.1, the nonlinear properties for simulating the cracking and crushing behaviour is outlined in Table 5.2 & 5.4, respectively. The steel component was marked into the nonlinear material model using bilinear isotropic hardening inputting the yield stress and tangent modulus for the steel material (see Table 5.3). These values were adopted from manufacturers and compared against the standard steel table in Cambridge University Engineering Department (2003).

Table 5.2 Stress-strain values for NWC and LWAC

NWC Specimen		**D1810**		**D1865**	
Stress (MPa)	**Strain**	**Stress (MPa)**	**Strain**	**Stress (MPa)**	**Strain**
2.765	0.0001	1.1264	0.0001	1.879	0.0001
3.288	0.0006	3.8291	0.00064	3.017	0.0009
4.313	0.0012	4.323	0.0011	3.926	0.0022
7.923	0.0021	6.196	0.00205	6.447	0.0031
14.161	0.0032	8.5567	0.00305	8.038	0.0043
19.676	0.0043	9.1753	0.00411	9.852	0.00504
26.075	0.0052	13.8258	0.00485	13.476	0.00611
31.003	0.0062	16.522	0.0062	16.911	0.00712

33.422	0.0073	20.032	0.00701	21.033	0.0084
35.716	0.0081	23.254	0.008	24.143	0.009
35.8	0.0090	30.212	0.00902	30.003	0.0107
35.8	0.0110	32.413	0.01011	32.021	0.01112
35.8	0.0120	33.523	0.01107	34.873	0.01233
-	-	33.875	0.01234	35.4	0.012
-	-	34.001	0.013	35.4	0.013
-	-	34.001	0.014	35.4	0.014

Table 5.3 Bilinear properties of steel

Bilinear Isotropic Hardening for steel Material	
Yield Stress (MPa)	460
Tangent Modulus (MPa)	20

Table 5.4 Nonlinear isotropic properties of concrete

	NWC	**D1810**	**D1865**
Open shear transfer coefficient	0.4	0.3	0.3
Closed shear transfer coefficient	1	1	1
Uniaxial cracking stress	3.8	3.33	3.36
Uniaxial crushing stress	35.8	40	40
Biaxial crushing stress	-	-	-
Hydrostatic pressure	-	-	-
Hydrostatic biaxial crushing stress	-	-	-
Tensile crack factor	-	-	-

5.3.1.2 GFRP Material

GFRP material properties were computed into the Engineering data interface of ANSYS Workbench. GFRP materials are orthotropic materials with distinct properties in the longitudinal and transverse orientations. GFRP profiles are expressed using three

mutually orthogonal planes referred to as the principal material coordinates. The principal material coordinates as defined in relation to the X-direction (fibre direction) includes XY, XZ and YZ planes (see Figure 5.2). Hence, the material properties are defined in these coordinates with reports from research showing that XY and XZ have near properties leaving YZ (transverse plane) exclusively isotropic (Kachlakev & Miller, 2001). The material data was obtained from manufacturers (Engineering Composites) for the wide flange (WF) profiles used in Phase I of the push-out test and compared against published standard values reported in literature for GFRP structural profiles. The GFRP WF profile used for the novel hybrid beam was obtained from Warwick University's civil engineering laboratory and this was previously characterised by Matharu (2017). All values for the GFRP WF-section are detailed in Table 5.5 and associated steel material properties outlined in Table 5.6. Matharu (2017) reported high coefficient of variation up to 10% (CoV≈10%), it was concluded that the values lay within acceptable range as established by Chauvenet criteria (Kennedy and Neville, 1986). The chart of comparison presented in Appendix B for GFRP mechanical strength properties show close agreement between Matharu's (2017) characteristic values and data published by Creative Pultrusions. Hence, justification for the adopted values from manufacturers for the purpose of numerical study.

Table 5.5 Orthotropic material data for WF-profile sections

Orthotropic Material Data for WF- Profile Sections		
Description	**Engineering Composite**	**Creative Pultrusions**
Elastic Modulus, E_X (MPa)	23000	28600
Elastic Modulus, E_{YZ} (MPa)	7000	9600
Elastic Modulus, E_{ZX} (MPa)	23000	28600

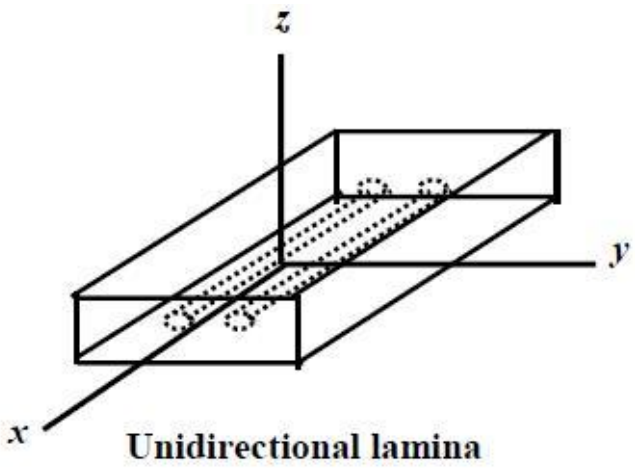

Figure 5.2: Material Orientation

Shear Modulus, G_{XY} (MPa)	25	23.4
Shear Modulus, G_{YZ} (MPa)	25	23.4
Shear Modulus, G_{ZX} (MPa)	25	23.4
Poisson's Ratio, V_{XY} (MPa)	0.32	0.32
Poisson's Ratio, V_{YZ} (MPa)	0.15	0.12
Poisson's Ratio, V_{ZX} (MPa)	0.15	0.12

Table 5.6: Associated steel properties

Isotropic Material Data – Steel Plate & Roller		
	Elastic Modulus, E_{LT} (MPa)	***Poisson's Ratio, V_{LT}***
Steel Plate	205000	0.3
Steel Rollers	205000	0.3

5.3.2 Mesh Control

The mesh discretisation process is the most vital aspect of numerical analysis owing to the ability of the FEA software to decompose an entire geometry representative of a structural body into fragmental volumes subjected to predefined iterative algorithms and subsequent interpolations. Due to the infinite nature of continuous bodies in terms of degrees of freedom, the mesh control process reduces these infinite boundaries to several finite degrees of freedom with the help of nodal elements. 3D volume elements are adopted for the FEA models capable of decomposing into tetrahedral, pentahedral and hexahedral shapes.

5.3.2.1 Mesh configurations

The determination of appropriate elemental property will depend on a number of factors including the type of loading (static or dynamic loading), type of analysis (linear and nonlinear analysis), solution run time, geometry size and shape factor (Mappable or non-mappable complex geometry) etc. The mesh commands are accessible under the ANSYS Mechanical Main menu (Proprocessor<Meshing) with the following applicable options including mesh attributes, mesh tool, size control, mesh, modify mesh, check mesh and clear options respectively. The mesh attributes action (Preprocessor<Meshing<Mesh Attributes<All Volumes) was used to assign appropriate properties (including material number, real constants, element type, element coordinate system) to the plotted volume intended for meshing. Also, the sweep options (Preprocessor<Meshing<Mesh<Volume Sweep<Sweep Opt) dialog box was accessed to enable possible tetrahedral meshes around non-sweepable areas/volumes by selecting the Tet mesh in nonsweepable volumes option. The meshing action was completed through the mesh tool dialog box

(Preprocessor<Meshing<Mesh Tool). The mesh attributes was set to global (default) with the set button enabling the input for element size. The concrete slabs are geometrically formulated into three subcomponents to ensure efficient meshing of elements due to shape (curvature) complexity at stud clearance holes and embedded cap. Hence, the bodies are plane split at stud shank and stud cap respectively to enable face meshing for uniformity of element distribution (see Figure 5.3a-c).

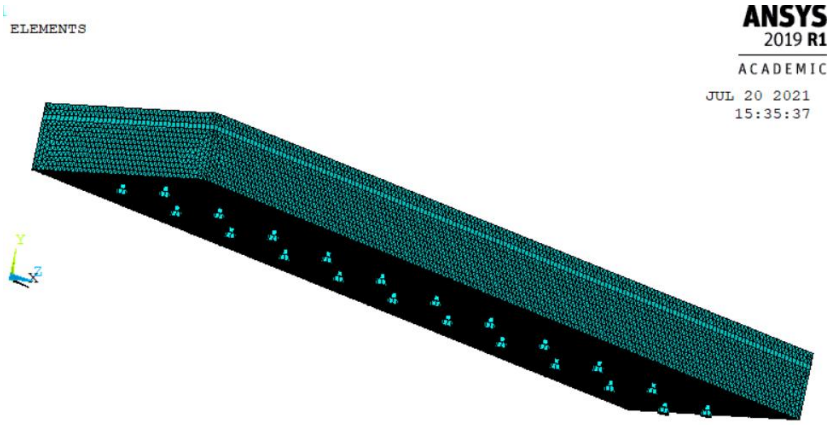

(a) Meshed Concrete Slab

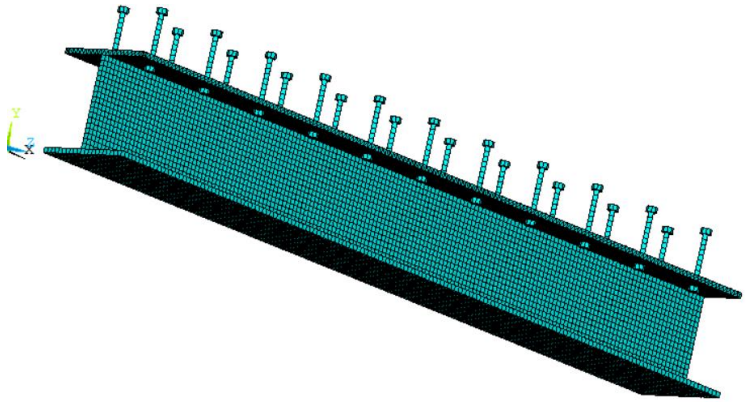

(b) Meshed Configuration for WF-Section & Stud Arrangement

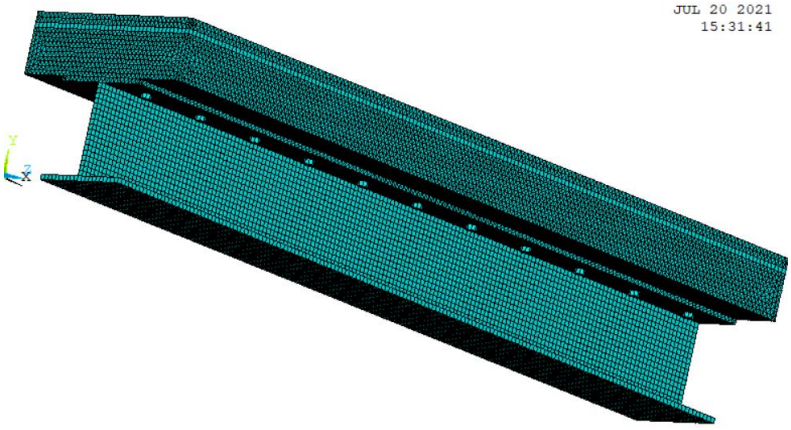

c) Meshed Arrangement for the Assembly

Figure 5.3 Meshed Assembly of the FE Model

5.3.2.2 Mesh reliability

To ensure appropriate reliability for mesh discretisation, basic quality checks are establish under mesh control settings on ANSYS. Further reliability is established through convergence analysis to derive optimum element sizing for result accuracy. In addition, mesh refinement on complex geometrically configured areas which may require specific stress probe assessment are mandatorily analysed. Convergence test is performed to develop suitable element discretisation for predicting closely a global behaviour for the novel composite beam. Multiple element mesh sizes are varied to assess the convergence of results for reliability. This multivariate analysis of element mesh sizes is carried out on two beam models devoid of shear connections to study flexural behaviour of non-shear contact composite beam.

The element mesh size of 12.5 – 15 mm showed lower solution time corresponding with fewer discretisation elements hence, as expected with such characteristics the shape effect and deviation values were significantly erroneous suggesting potentially higher marginal errors compared with smaller element sizes of 10mm and below.

5.3.3 Component Interaction

All components assembled to form the experimental model can be defined on ANSYS FE as linear or non-linear connections. Hence, component interactions are established as contacts and target bodies with the former referring to non-penetrable surfaces capable of transferring normal compressive and tangential frictional forces under variable system stiffness's. Table 5.7 summarises five key contact types applicable to our model characterised by directional and mechanical behaviours. The adopted contact type used

for the various component interactions of our assemblies and corresponding settings relevant to the predicted realistic behaviour of the model is detailed in Table 5.8. The interface treatment option available for nonlinear contacts is set for frictional contacts between the bolts and the GFRP clearance holes as “add offset, ramping effects” with an offset value of 1mm in excess of the bolt diameter while all other nonlinear contacts were set as “adjust to touch” to take care of any CAD modelling inaccuracies. Trimmed contacts are adjusted off for large nonlinear models due to unpredictable directional behaviours resulting from possible contact/target offsets. Normal stiffness calculated by the system’s algorithm for contact surfaces are allowed under program-controlled settings as ANSYS sets default factors of 10 for bonded/ No-separation contacts and 1.0 for other contact types.

Table 5.7: Summary of Linear and Nonlinear Contacts

Contact type	**Directional Behaviour**		**Mechanical Behaviour**
	Normal (Separation)	**Tangential (Sliding)**	
Frictionless	Allowed	Allowed (without resistance)	Non-Linear behaviour (Multiple iterations)
Frictional	Allowed	Allowed (with resistance)	
Rough contact	Allowed	Not allowed	
No separation	Not allowed	Allowed (without resistance)	Linear behaviour (Single iterations)
Bonded	Not allowed	Not allowed	

Table 5.8:Contact setting for body interactions

Contact	*Target*	*Contact type*	*Friction coefficient*	*Scope mode*	*Behaviour*	*Trim contact*	*Trim tolerance*
GFRP clearance	Stud shank	Frictionless	-	Auto	Program controlled	Program controlled	-
Stud shank	Nut	Bonded	-	Auto	Program controlled	Program controlled	4.2315
Stud shank	Concrete clearance	Bonded	-	Auto	Program controlled	Program controlled	4.2315
Stud cap	Concrete clearance	Bonded	-	Auto	Program controlled	Program controlled	-
GFRP B_Flange	Nut Surface	Frictional	-	Auto	Program controlled	Program controlled	-
GFRP T_Flange	Concrete interface	Frictional	-	Auto	Program controlled	Program controlled	-

5.3.4 Loading & Boundary Conditions

The FE Models are constrained at boundaries that depict the experimental conditions for the test setup. Due to complexity of equations and solving time, symmetry was applied to the half model at mid-span for the composite beam. The symmetry condition applied on the model constrained the nodes on the cut section about the z-direction (UZ = 0).

Boundary conditions are applied to selected elements of the base model for restraint conditioning. These applied restraints are defined by six degrees of freedom for displacement and rotation vectors within the global axis x-y-z. Figure 5.4 shows positions

Figure 5.4: Loading and Boundary Conditions for the Numerical Model

of typical boundary conditions applied on the various models within the numerical study. The values of 1 or 0 are entered for displacement and rotations to define admissible freedom or restraint for displacement and rotation in the global coordinate system (see Table 5.9). Significant application of displacement-loading is defined an assumption which takes advantage of the FE virtual space to apply displacement-load (-Y axis) along the mesh nodes at similar position to the experimentally located points. The need for modelling a roller is not of much significance if a named selection of nodes (element) is created for applying a nodal finite element analysis.

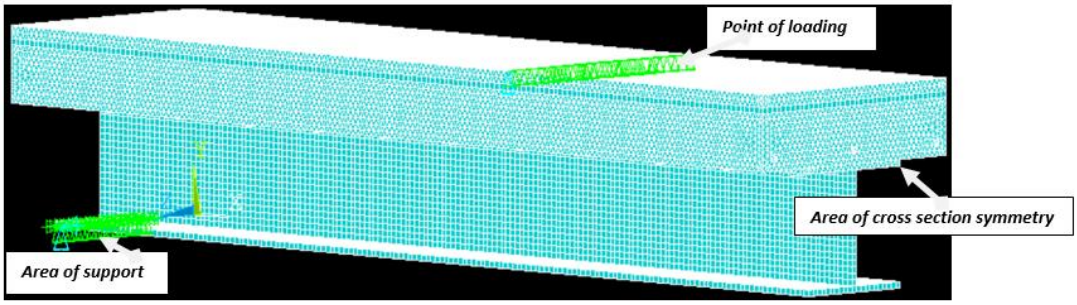

Table 5.9: Restraint Conditions for Models

Model	Boundary	Element Positions	U_X	U_Y	U_Z
Novel Beam	Support	Roller Support	Free	Lock	Lock
	Loading	Steel Roller Pad	Lock	Free	Lock

The mechanical properties of concrete and GFRP are sensitive to loading rates hence, load application for the model is rate dependent and must simulate laboratory practice using the time stepping settings on ANSYS APDL.

5.4 Analysis Settings

The analysis for the novel beam model under the static structural analysis setup of ANSYS APDL. The nonlinear solutions are defined under the solution controls of APDL with typical values for the settings shown in Table 5.10.

Table 5.10: Basic Control Settings for Nonlinear Analysis

Analysis Options	Large Displacement static
Calculate Prestress Effects	No
Time at End of Load step	30
Automatic Time Stepping	On
Number of Substeps	150
Max no. of Substeps	500
Min no. of Substeps	100
Write Items to Result File	All Solution Items
Frequency	Write Every Substep

Large displacement static option is defined to enable the nonlinear solution by accounting for element deformations of the components at severe flexure. The end of load step time is set to reflect the value of displacement applied per load step. Substeps refer to the displacement load increments of the program analysis in relation to number of substeps

achieved before total convergence is reached. Program solver option was left in default to determine the solver programme for the problem. The Nonlinear algorithm was not adjusted but left to default settings as preset by the programme while the settings for force and displacement convergence criteria is outlined in Table 5.11. Displacement criteria were chosen to govern the simulation due to convergence challenges resulting from material yielding. The maximum and minimum tolerance value was set to 5 and 1.0 for both force and displacement criteria as published by Attiyah et al. (2013) and other settings left as default.

Table 5.11 Convergence Criteria Settings for the Models

Set Convergence Criteria		
Label	F	U
Ref. Value	Calculated	Calculated
Tolerance	-	0.05
Norm	-	L2
Min Ref	-	1.0

In general, the analysis settings are carefully carried out to ensure an extraction of the results with higher levels of accuracy. Time history post-processing command is used for result extraction from the converged solution to enable graph plotting. Essential behaviours are obtained from the analysis including strength capacity, concrete cracking (where possible), slip values, failure modes and corresponding yielding of materials. The nonlinear material properties predetermined from experimental testing of concrete was inputted using command prompts with codes generated from the ANSYS Mechanical APDL interface.

5.5 Reliability of Numerical Modelling

Numerical models are said to be reliable if certain principles are considered during the development of the model. Details including material properties, boundary conditions, geometrical elemental properties and mathematical formulation are necessary to ensure reliability of numerical models. Numerical models must be in close agreement with experimental models and theoretical prediction. Reliability of numerical models will have to conform firstly to numerical design principles stated in section 2. Further to hypothetical conformity, parametric and sensitivity studies are carried out to establish validity of results as predicted behaviour can be adjusted to closely match obtained experimental results.

Primary data derived from both experimental and numerical study will be analysed quantitatively using mathematical tools including tables, graphs and equations. Independent data analysis will be carried out on each class of data such as experimental or numerical data etc. Reliability test can be conducted on research data by carrying out statistical comparisons on all classes of data including findings from literature. Test data and analysis are reliable if the following conditions are satisfied:

- ✓ Plotted data from all classes show similar trend and pattern between data classes and literature.
- ✓ The quantitative data obtained from results compare relatively within an acceptable range of values established either from literature or hypothetical principles.
- ✓ Derived data and analysis correlate with theoretical and numerical findings in line with stated engineering principles.

5.6 Summary of Chapter

The numerical model is assigned material models using selected elements capable of simulating linear and nonlinear behaviours under specified boundary conditions. The selected elements based on simulation capabilities include SOLID65 (concrete), SOLID185 (GFRP), LINK180 (Bolts & Reinforcement) etc. Material properties from experimental characterisation is assigned to each constitutive model to define inherent behaviour for the model. Model is discretised using mesh capabilities to enable finite analysis of elemental fragmentation. To fully define the component connection, the FE system requires appropriate identification of components to establish accurate mechanical behaviours (linear and/or nonlinear penetrations) for the model. The final design to run a prototype simulation requires the definition of loads and boundary conditions for the given model.

CHAPTER 6. RESULTS & ANALYSIS

6.1 General

In the design of flexural composite beams, it is necessary to ensure a controlled behaviour and performance of the hybrid beam through a parametric characterisation of its shear connections. The parametric characterisation involves the determinacy of the shear behaviour of composite connections subject to the stud configuration. This process deploys the traditional push-out test setup detailed in EC4 for steel-concrete composites. This chapter outlines the design and setup of the test aimed to investigate the characteristic shear behaviour and subsequent performance of the composite beam.

6.2 Push-out test results

The results obtained from all three phases of the experimental test involving a total number of eight push-out specimens is presented and analysed to illustrate the implication of shear connections comparatively against existing standard guidelines for steel-concrete composites. The study attempts to analyse the influence of certain parameters such as stud geometry, concrete properties, and stud configuration on the shear behaviour of the composite. The evaluation of the composite is to determine the failure mode, shear capacity, ductility, and other performance criteria for the composite connections. Summary of test results is presented in Table 6.1. The reported results illustrate significant difference in load capacities per stud for the 8-stud double-row configuration specimen in Phase 1 with an ultimate load of 552.6kN. The high load capacity is mainly due to higher number of studs which can redistribute stresses while providing significant resistance to the shear load. The ultimate load is representative of 69.1kN load per stud which is approximately 7.9% less than the load capacities per stud of specimen 1 (PO-

SR-S1) and 2 (PO-SG-S2) respectively. However, bolt arrangements may sometimes influence shear capacity as observed in the results for specimen 1 and 2. Also test data shows that reduction in bolt sizes under similar stud arrangement can result in lower load capacities per stud of about 30% (for 12mm bolt sizes) and about 22% (for 16mm bolt sizes) respectively. All specimens reportedly showed extreme fibre failures and stud deformations with the 19mm bolt showing net tensile failures. Further analysis of the results presented in table 6.1 are carried out in subsections of section 6.2.

Table 6.1: Summary of test results and observation

Specimen ID (1)	**Ultimate load, P_u (kN) (2)**	**Peak Slip, S_u (mm) (3)**	**Experimental Strength/stud P_{Exp} (kN) (4)**	**Shear Stiffness of connection, K (kN/mm) (5)**	**Failure mode (6)**
PO – SR – S1	300.5	10.7	75.1	48.3	*Bearing failure of FRP flanges/bending of shear stud/severe delamination of FRP flanges*
PO – SG – S2	443.7	10.8	74.0	105.2	*Bearing failure of FRP flanges/bending of shear stud/severe delamination of FRP flanges*
PO – DR – S3	552.6	11.5	69.1	75.5	*Bending of flanges/tension/bearing failures (FRP)*
PO – 12B – S4	333.0	8.0	41.6	62.5	*Bearing failure of FRP flanges/bending of shear stud/severe delamination of FRP flanges*
PO – 12B – S5	385.0	8.9	48.1	96.4	*Bearing failure of FRP flanges/bending of shear stud/severe delamination of FRP flanges*
PO – 16B – S6	431.0	10.9	53.8	110.0	*Bearing failure of FRP flanges/bending of shear stud/severe delamination of FRP flanges*
PO – 12B – LS7	384.7	12.2	48.1	95.2	*Bearing failure of FRP flanges/bending of shear stud/severe delamination of FRP flanges*
PO -12Bm – LS8	270.2	10.7	33.8	42.3	*Bearing failure of FRP flanges/bending of shear stud/severe delamination of FRP flanges*

6.2.1 Failure mechanisms

Steel-concrete composites are typically associated with concrete pull-out, sprawling and stud fracture failure, respectively. However, when the component materials are altered, other failure modes can be expected as reported in literature. Nguyen (2014) has reported the failure mode observed from research investigations on pultruded fibre reinforced polymer (PFRP) concrete as dominantly bearing failure around the holes on the flanges of both HFRP (hybrid fibre reinforced polymer) and PFRP, respectively. The use of 10 mm and 16 mm sizes of various types of steel stud was used alongside a combination with epoxy adhesive for several specimens, but the failure observation was never without the inclusion of bearing failure for the FRP material, which indicated a low bearing strength of the PFRP flanges comparatively against their steel counterpart. This primary observation reemphasises the importance of the push-out experimental testing as highlighted in EC 4 for the investigation of composite connection consisting of non-traditional components (i.e., alternative materials to concrete and steel). Figure 6.1 & 6.2 illustrates the general failure mode observed in the current study. It corroborates the previous study undertaken by Nguyen (2014) on the predominant bearing failures of the PFRP flanges. Another vital failure observation was the single curvature bending of the studs as described and reported by Odenbreit (2017) for shear studs in solid slabs. However, the single curvature bending was more evident in stud size diameters less than 19 mm diameter stud, as shown in Figure 6.2. A combined shear-out and bearing failures were observed on the PFRP flanges for stud size diameters of 19 mm. The depth of the shear-out failures was higher for 19 mm stud size specimen (PO-DR-S3). Fibre delamination was severe around the bolt holes. Fibre failure noise increasingly characterising experimental test involving fibre materials due to the fibre matrix

Figure 6.1: Flange bearing failures at stud clearance holes (Etim et al., 2020)

Figure 6.2: Stud curvature deformation (Etim et al., 2020)

relationship depicting stress levels within fibres as well as energy loss from the breakdown of the fibres. Therefore, fibre failure sound was anticipated during the experiment and observed mildly at about 45 – 74% of ultimate load with louder fibre failure sounds observed between 85% of peak load until failure for all test specimens. Another predominant failure mode, the shear-out failure occurred on the flange panel of specimen PO-DR-S3, utilising the 19 mm bolt. As outlined earlier, the 19 mm stud hardly deformed and with the double row configuration (PO-DR-S3), it provided more resistance

to the shear load allowing for significant damage to occur around the flange panel. The specimens tested in phase 2 (PO-12B-S4, PO-12B-S5) and PO-16B-S6) and phase 3 (PO-12B-LS7 and PO-12Bm-LS8) proceeded on a simultaneous deformation of shear stud during loading at an almost non-significant disparity among stud members. The eventual failure of stud showed that almost all stud members deformed at similar angles with a visually insignificant difference, which may be due to varied differences in concrete strength mobility or non-homogeneity in the concrete mix, as outlined in Table 6.2. The mean value for the deformation angle was marginally similar. The variance in the deformation angle becomes more significant with higher stud sizes. Following the single-curvature phenomenon of embedded shear studs, it may appear that the bearing of the stud and nuts on the PFRP initiated the second type of failure, which dominated the overall failure of the connection. Even though, stud fracture had been reported by Nguyen (2014) in his experimental investigations, it may appear that fracture failures are a characteristic of hybrid FRP sections of improved mechanical strength properties. The flange bearing failure seems to govern the PFRP-concrete connection against the conventional stud fracture and concrete pull-out failures typical of steel-concrete composites. This phenomenon is common among structural materials with geometric discontinuities along the section therefore, an important criterion to be considered in the design of FRP connection members. The transition from a linear zone of the stud deformation unto the combine nonlinear bending and bearing on the FRP occurred at 78% of an ultimate failure load of 333 kN with a corresponding slip of 3.9 mm for PO-12B-S4. The transition for PO-12BS5 was at 83% of the ultimate load of 385 kN at a corresponding slip of 3.2 mm. Specimens PO-12B-S4 and PO-12B-S5 showed a similar pattern of failure without any significant variation in behaviour. The shear studs were all

deformed at similar angles simultaneously (see Table 6.2) during the test until the initiation of bearing failure on the PFRP girder gradually became conspicuous up until ultimate failure, where no further load was reasonable. The longitudinal depth of bearing failure was measured to be approximately 4 – 4.5 mm at single curvature deformation of the studs. The extent of the damage to the flange panel is presented in Figure 6.1. The 16 mm stud diameter specimen of an exact stud arrangement reaffirmed the mechanical behaviour of the composite connection bearing the same stud configuration. The deformation of the stud was observed to be simultaneous and a gradual transition from linear response to the single curvature bending of the 16 mm shear stud unto the bearing failure of the PFRP material propagated around the clearance holes. However, unlike the first phase of testing for specimens PO-DRS3 (utilising 19 mm stud), net tension failures of the PFRP plates did not occur. The initiation of bearing failure was observed at approximately 348 kN loading, and ultimate failure was recorded at 430 kN. Specimen PO-DR-S3 recorded an ultimate load of 552.7 kN with a corresponding slip of 11.5 mm. The predominant modes of failure observed on this specimen included a clear tensile tear out of the PFRP flanges with the tension line passing right above the bolt holes and extending out to the edge of the PFRP on one end, and the web-flange junction on the other end. The failure line followed a straight longitudinal shear line down to the bottom end of the flange. This type of failure has been reported by Mottram (2009). The consistency of the double-row configuration specimens in all three phases with reports from Nguyen (2014) will imply the contribution of FRP flange properties in predicting the shear resistance of PFRP-concrete composites. The failure mode reported between specimens of NWC and LWAC deduces that PFRP-concrete specimen irrespective of

concrete density and other geometrical properties will typically be dominated by flange bearing failures.

Table 6.2: Degree of stud curvature deformation (Etim et al., 2020)

6.2.2 Load Slip Relationships

The incremental load applied on the push-out specimen is plotted against the corresponding interfacial slip between the concrete slabs and GFRP flanges. Load–slip relationships for all specimens are presented in Figure 6.3 - 6.5 for all three phases of testing, respectively.

6.2.2.1 Phase 1 load-slip plots

Presented in Figure 6.3b is the load-slip plot for all three specimens tested under phase I. The slip response is taken as the average slip plot for the two LVDTS on the left-hand-side (LHS) and right-hand-side (RHS). The LHS and RHS plots evidently showed an even response to load suggesting appropriate stress distributions between the two slabs hence, corresponding average slip demonstrates significant reliability (see Figure 6.4). The load-slip curve for PO-SR-S1 (a single row or four-bolt configuration) showed a reasonable linear behaviour before reaching an ultimate load of 300.5 kN at an average longitudinal slip of 10.71 mm. The curve exhibits a distorted (zigzag) behaviour from

when the load was increased from 128 kN till the failure load and post-failure. From the observation of the concrete slabs after the experiment, there were no visible cracks on either of the slabs that might have been suggestive of the observed irregular distorted profile. However, it was common with all specimens and more suggestive of inner fibre delamination response to loading. After the ultimate resistance is reached, the curve exhibits a non-linear and gradual drop in resistance up until failure. A pseudo-ductile behaviour is exhibited in the non-elastic zone, mainly because of the steel bolts. PO-SG-S2 (staggered or six-bolt configuration) exhibits a similar behavioural response to PO-SR-S1 with an initial stiffness at loading up to 25 kN. Redistribution of loading with the shear studs seemed a likely occurrence in this setup as the shear response at yielding was slower before attending its peak at 443.7 kN with a corresponding slip of 11 mm. PO-DR-S3 (double row or eight bolt configuration) provided the highest shear resistance and became the adopted configuration for phase two testing. The ultimate load was obtained at 552.7 kN with a corresponding slip of 11.5 mm. The curve exhibits a more sustained linear zone than the other specimens with corresponding nonlinear zone beyond yielding and a sudden drop in load which might describe the net tension failure reported in Section 6.4.1. Hypothetically, higher number of bolts would result in greater shear resistance as illustrated in the results from the double-row stud configuration. However, the Phase I study aimed to characterise the configurations to determine conservative ways of achieving shear resistance by possibly reducing the number of studs. Specimen 1 (PO-SR-S1) and 2 (PO-SG-S2) show that bolt arrangements can contribute to shear performance and may impact the shear resistance of the connection.

Figure 6.3: Load-slip plots for Phase I & II (Etim et al., 2020)

Figure 6.4: Slip response for LHS & RHS concrete slabs (Etim et al., 2020)

6.2.2.2 ***Phase 2 load-slip plots***

Presented in Figure 6.3a is the load-slip plot for the three specimens investigated under phase II. PO-12B-S5 specimen showed evidence of slip movement at a load of about 33 kN then provided a conspicuous slip at a load of about 88 kN which might have been due to the stud bearing unto the clearance hole. The specimen behaved linearly transitioning at yielding unto a nonlinear behaviour until failure occurred. The specimen recorded an ultimate load of about 380 kN at which time the bearing failure was already initiated on the PFRP and sustained a combined bearing and stud deformation until failure where no further load was admissible. PO-12B-S4 (similar configuration and stud size to PO-12B-S5) also behaved linearly until yielding occurred then behaved nonlinearly until failure occurred. The ultimate load recorded was 13.5% less than PO-12B-S5 at 385 kN. Slip values for PO-12B-S4 and PO-12B-S5 were approximately 8 mm and 8.9 mm, respectively. The reason for the difference in failure load may be due to a combine non-homogenous weakness in the PFRP and a non-consistency in the concrete mix around the stud area for the various specimens. Specimen PO-16B-S6 had similar behaviour to the PO-12B-S4 and PO12B-S5 as all three samples failed in a ductile manner depicting a combined and simultaneous deformation of both stud and bearing failure of the PFRP flange. However, the 16 mm stud peaked at a higher load of 430 kN about 10.5% greater than PO-12B-S5. The slip of 10 mm was obtained at the point of yield to avoid the contribution of the PFRP flange bearing to ductility forming a pseudo-ductile behaviour in the nonlinear zone. The plot in Figure 6.4 represents the load slip curve for both left and right load-displacement-transducers (LVDTs), and it can be seen that the loading was fairly distributed on the specimen as well as the resistance and slip throughout the

connection. This is equally evident from the stud deformation and depth of bearing failure captured.

6.2.2.3 ***Phase 3 load-slip plots***

The load-slip plot for specimen PO-12B-LS (see Figure 6.5b) shows linear progression of the plot as it extends into a curve at an ultimate load of 357.1kN. The linear plot shows a constant resistance of load until about 267kN at corresponding slip of about 8.5mm. At yielding, a transition into the inelastic zone is extended to an approximate ultimate load of 357.1kN at which the amplitude of the curve maintains an inconsistent peak load until 384.7kN at a slip of 24.4mm. A steep decline in load occurs and failure becomes conspicuous due to the excessive bearing and severe delamination of the GFRP flange.

Figure 6.5a illustrates the load-slip plot for specimen PO-12B_m-LS at which an initial slip occurred at an approximate load of 10kN. The plot is very similar to the plot for specimen PO-12B-LS. Clear linear progression with greater steepness suggesting higher stiffness but with a more sustained peak at yielding up until failure. The linear progression of the curve attains a maximum yield at 270.2kN with a corresponding slip of 10.7mm. The linear zone transitions into a nonlinear curve at an approximate load of 190kN with an early slip of 4mm at which the physical deformation of studs becomes visible with increase loading. The nonlinear zone subtends a fairly consistent flat peak in comparison to specimen PO-12B-LS plot, which is sustained up until failure at a peak failure load of 278.8kN with corresponding slip of 13.1mm. The peak load and slip values for PO-12B_m-LS is about 24.33% and 29.14% less than the peak value for PO-12B-LS respectively. The significant difference in peak values is attributed to the bolt collar configuration in specimen PO-12B_M-LS compromising the single curvature deformation of the bolt as a

requirement in ensuring full shear strength mobilization. However, studies from phase I and II observed lower percentage differences between composites of similar geometry, material properties and configuration suggesting that such differences are due mainly to the combined non-homogeneity of PFRP materials and non-consistency in the concrete mix. It is practical to have variances in results from similar specimen configurations due to the general non-linearity of materials. With the modification of the embedded bolt, a significant variance in the peak load and subsequent slip of the two composite specimen is expected. Failures of GFRP-LWAC composite generally depict ductile propagations of combined and simultaneous deformation of stud with corresponding bearing failures of the GFRP flange (Nguyen, 2014). Peak load values are obtained around the yield area of the plot before the contribution of the flange bearing failures to avoid a pseudo ductile representation of results. The plots in Figures 6.5 (a) and (b) illustrates two LVDTS placed on opposite sides to measure the differences in slip. The plot also shows a corresponding trend of both LVDT's with an almost negligible difference in values with the average slip plot lying very closely between the two obtained slip values of the LVDTs.

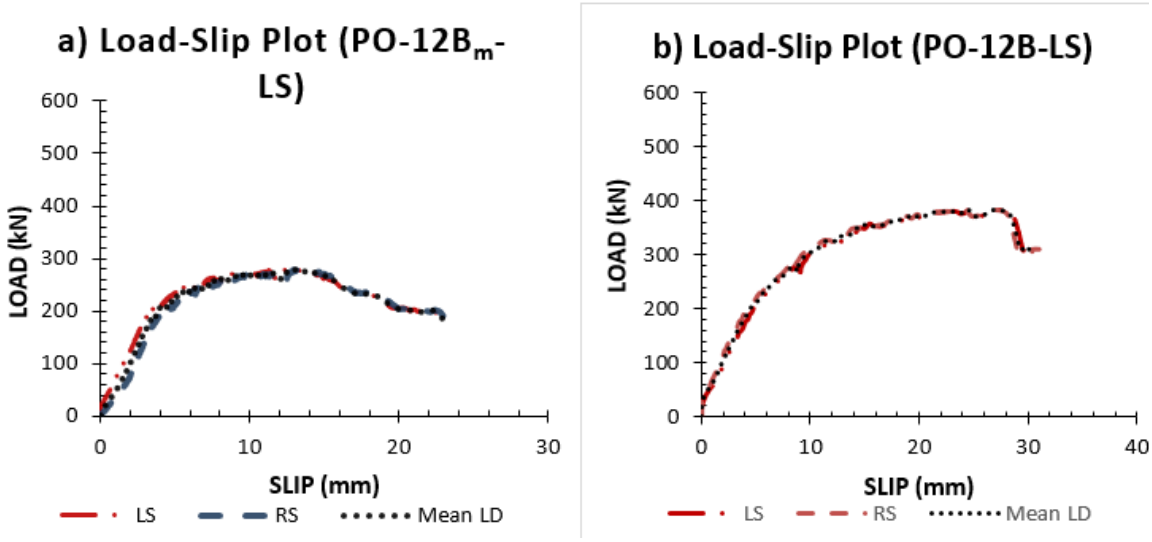

Figure 6.3: Load-slip plots for Phase III

6.2.2.4 Comparison of specimen PO-DR-S3, with 19 mm stud and specimen PO-16B-S6, with 16 mm stud

Presented in Figure 6.6 is the load-slip relationship of 16 mm and 19 mm diameter studs for comparative analysis. This comparison highlights the peculiarities between the 16 mm and 19 mm shear studs under the same stud arrangement.

The load-slip curve for PO-DR-S3 differs distinctively from PO-16B-S6 due to the sharp fall of the curve at the peak. The sudden drop from the peak represents the intensity of the failure observed in the 19 mm stud size specimen. The subsequent reduction observed on the curve after the sharp drop at the peak illustrates a fibre deformation due to bearing failure sustained throughout the connection during experimental testing. The curve for the 19 mm stud (PO-DR-S3) demonstrates a failure entirely dominated by bearing

deformation even though there was an appreciable bending of the stud represented by the nonlinear zone of the curve, but the sudden fall from the peak exhibits the bearing failure as an override to the stud deformation. Specimen PO-16B-S6 with 16 mm studs, on the other hand, produced an extended deformation to a relatively constant push-out load and

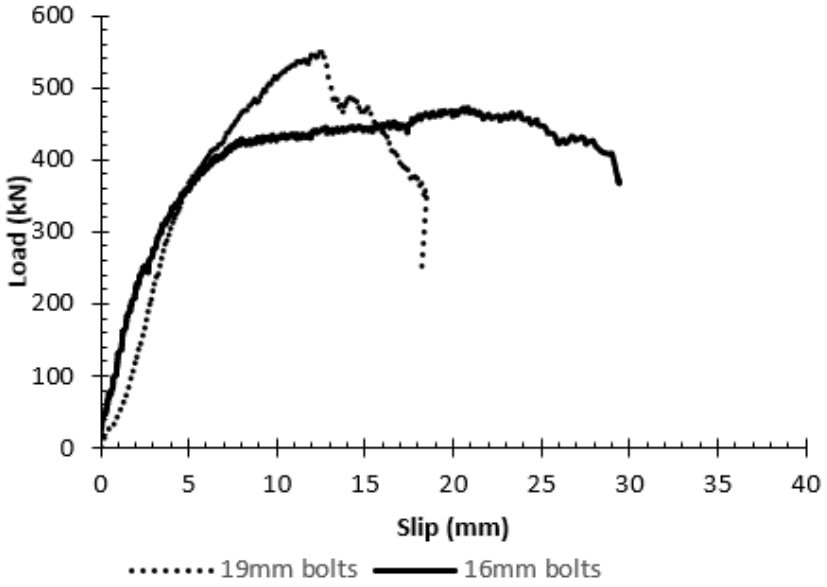

Figure 6.4: Load-slip plots (19 mm vs 16 mm)

illustrates ductility. The ductility is made possible by a combined interaction of the stud and flange panel failure. The ductility provided beyond the point of yield is not reliable and cannot be adopted for design as prescribed by EC 4. Specimen PO-DR-S3 with 19 mm studs exhibited a higher peak load of 552.7 kN, 22% greater than the specimen with 16 mm studs. However, the specimen with 19 mm studs may represent an unsafe upper boundary solution for PFRP-concrete composite connections in comparison with the specimen with 16 mm studs. The curve for 19mm bolt in figure 6.7 draws the observation that delamination occurred in stages as failure beyond yield is largely attributed to fibre bearing/delamination facilitated by fibre imperfections and material non-uniformity.

Non-uniformity of the material properties of FRP material on all eight areas of the bolt area may lead to temporary resistance produced from redistribution of stress during loading and further failures thereafter.

6.2.2.5 Comparison of LWAC specimen against NWC specimen

The load per stud obtained from LWAC specimen PO-12B-LS is within the same range with that obtained from the earlier experimental test (Phase I & II) for GFRP-NWC at a 41.6kN and 48.1kN for two consecutive specimens. The results reaffirm concrete compressive strength as a major parameter in the optimisation of shear strength as similar concrete compressive strengths were achieved for both specimens. However, the modified specimen PO-12Bm-LS shows a significant lower load strength per stud resulting from the limiting ability of the studs to deform in a ductile manner as required for full mobilisation of resistance against increased loading. The modified bolt has a characteristic load strength per stud of about 24.6% less than the unmodified studs in the both LWAC and NWC specimens. However, LWAC specimens; Po-12B-LS and PO-$12B_m$-LS were observed to have higher slips of 78.1% and 26.6% against the NWC specimens. The significant reduction in slip values between specimens PO-12B-LS and PO-12Bm-LS is due to the stud modification at the near surface of the concrete slabs limiting the deformation rate and subsequent ductility of the composite. At almost a constant rate of change, the maximum load obtained from test samples LS-12B and LS-12Bm was 300kN and 285kN with a corresponding slip of 10mm and 9mm respectively. Similar trend reported in earlier experiments conducted on GFRP-NWC composites (phase I & II) was also observed with GFRP-LWAC composites. Reasonable linear behaviour during loading is observed on the graph until the above ultimate loads were

attained. The curve maintains a near flat peak with a further distorted progression of tiny amplitude until the failure load is reached. This behaviour is not uncommon as it suggest possible inner fibre delamination from bearing against bolts as this was accompanied with fibre delamination sounds. The linear curve attains an estimated load of 300kN and 190kN for LS-12B and LS-12B$_m$ respectively then transitions into a nonlinear curve with corresponding drop in the load resistance. Possible redistribution of loads occurred at load intervals of 205kN and 272kN for LS-12B$_m$, 280kN and 350kN for LS-12B respectively. Both specimens exhibited a fairly sustained peak at ultimate loads of 300kN and 285kN with slope stiffness of 35kN/mm and 40kN/mm for LS-12B and LS-12Bm respectively. The load-slip plots for both NWC and LWAC specimens exhibits a similar trend of curve propagation with an almost steady peaks from yield up until failure occurs where a sharp drop in load is observed.

6.2.3 Strain responses

Strain responses were recorded to evaluate the effect of the load on the stud-concrete and stud-PFRP interactions. A knowledge of this is relevant in interpreting the overall performance and failure pattern exhibited in the composite connection. Phase 1 primarily captured only strain readings on PFRP flanges at 100 mm distances above studs. Early observations in Phase I informed the modifications to adopt the 25 mm placement height above clearance holes on PFRP flanges for strain readings and additional responses obtained from stud embedment in concrete.

6.2.3.1 Stud-strain response (Phase II)

Figure 6.7(a) illustrates the strain response of the studs for specimen PO-12B-S4 at a position near the stud cap. Strain readings became apparent on increase loading of 50 kN

due to the position of the strain gauges on the studs. The gauges were positioned towards the stud cap to study the compression and anchor effect of the stud in concrete to mobilise resistance against the shear loading. The negative strain results suggest a compression force on the strain gauges rather than tension due to the compressive action of the concrete. The strain curve produces a linear progression transitioning into a nonlinear curve until failure. The nonlinear strain curve propagates nonlinearly in respect of load increment, depicting mobilised resistance by the stud until failure. The strain measurements obtained are far lower in comparison to that obtained in PFRP strain responses. At a maximum strain of about 1000 micro-strain on the stud (percentage peak strain), the PFRP strain response transitions into the non-linear zone suggesting higher bearing interactions between the stud and the PFRP flange. The load-strain plot for the average strain at position near the concrete/flange interface is shown in Figure 6.7(b). It clearly shows the average behaviour of the connection at the concrete flange interface. The stud is under a tensile force that enhances the ductility of the connection. The steep profiles of the curve may suggest the sudden increase in loading due to the delamination failures of the PFRP flange fibres whereas, the near flat peaks may depict plastic hinging of studs at approximately 53% and 77% of the peak load. This reaffirms the combined failure mode of stud deformation and bearing failures. However, at ultimate load, another steep profile may conclude that the PFRP flange plate forms the dominant failure mode of the connection.

Figure 6.5: Stud strain response (PO-12B-S4) (Etim et al., 2020)

6.2.3.2 Stud-strain response (Phase III)

The modified studs were strain gauged to determine the collar effect on the stud strain distribution. The typical single curvature deformation model highlighted in a study by Hicks (2014) also reported by Nguyen (2014) suggest an ideal behaviour of shear studs embedded in flat concrete slabs. The model refers to the effect of concrete compressive forces around the stud cap providing anchorage for full tensile deformation allowing for the mobilization of resistance against shear forces. However, with the introduction of the collar at the concrete-flange interface, a limiting boundary setup increases the stud stiffness thereby, compromising the deformation behaviour. The strain distribution obtained from the plot illustrates that all studs embedded into the concrete slab (RHS) are in compression. This agrees with the model that concrete compressive forces act on the stud head to enable adequate anchorage for strength mobilization. The LHS stud embedment's strain plot shows the two studs in compression (SLS-TR and SLS-BL), with the plot for SLS-TR suggesting concrete cracking or sprawling around the embedded stud head. The other two studs also depict tensile strains due to increase tensile action caused by the deformed studs. Higher compressive strain of 10161με and tensile strain of 4074με was obtained for SLS-BL and SLS-BR (LHS concrete slabs). Significantly higher compressive strains characterized with sharp amplitudes fluctuating between the compressive and tensile zones of the plot (see Figure 6.8). Maximum compressive strain readings of 4609.7με and 3215.4με were obtained for SRS-BL and SRS-TL respectively. SRS (Right-hand) slabs provided consistent compressive strains which exemplified the ideal model suggesting the influence of compressive forces on the studs for strength mobility. The significant variance in the concrete slab is mainly due to the inhomogeneity of concrete and possible curing inconsistencies during the moulding process. Irrespective

of the improvised collar, the single stud deformation is an apparent feature for headed studs embedded in both LWAC and NWC. The strain distribution plot highlights the interaction of forces on the stud depicting concrete anchorage where concrete homogeneity and compressive strength are most influential and increased tensile forces where concrete homogeneity and compressive strengths are compromised.

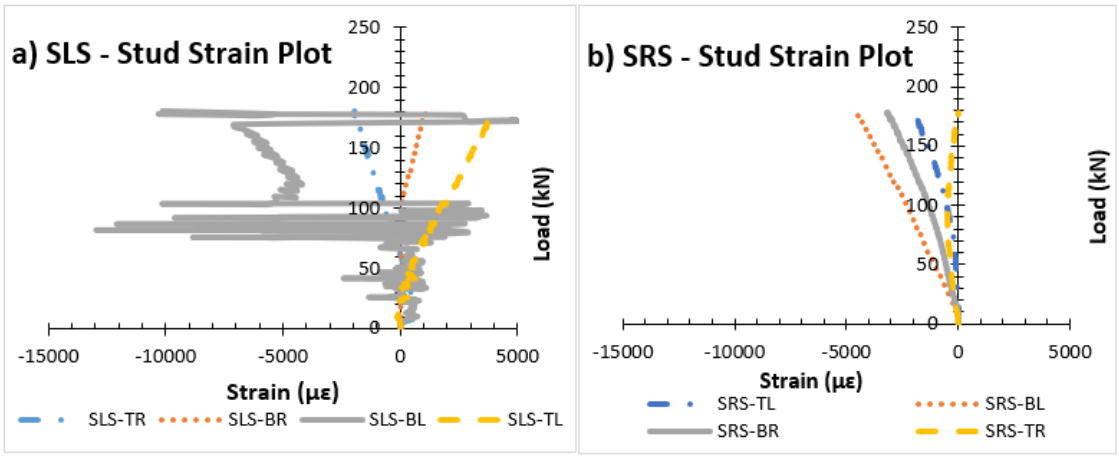

Figure 6.6: Stud response (Phase III)

6.2.3.3 Strain effect on FRP plates (Phase II)

The strain gauging for phase 1 included transverse and longitudinal gauges on the web and flanges of the FRP. However, strain readings from the transverse gauges were ignored since the strain recordings were too insignificant compared to the longitudinal strains. The most significant readings obtained on the flanges are reported here for analysis. The above observation and analysis informed the decision to omit web gauging and transverse gauging in phase 2. A detailed analysis was obtained from phase 2 testing with a reduction in the distance (from 100 mm) to 25 mm for strain gauging above stud clearance on FRP. Results for strain responses from Specimen PO-12B-S5 is presented

in Figure 6.9. The gauges were identified on the Right-hand side (RS) and Left-hand side (LS) of the slab; denoted as BL, BR, TL and TR for the bottom left, bottom right, top left and top right respectively. This was generally represented as RS-BL, LS-TR denoting right-hand side – bottom left clearance hole, left-hand side – top right, respectively as the case may be.

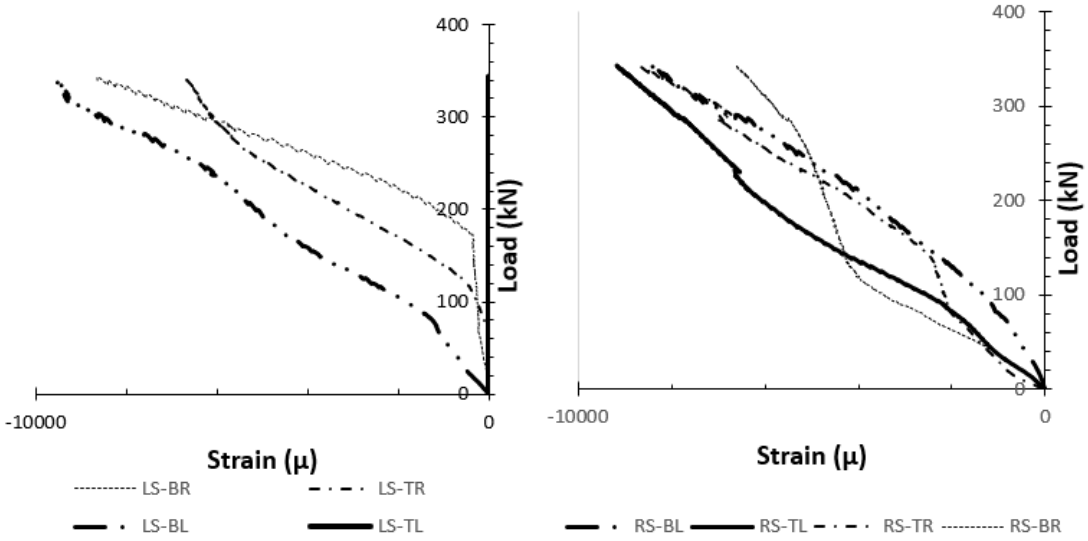

a) RHS Flange response (b) LHS Flange response

Figure 6.7: Flange strain response (PO-12B-S5)

The load-strain plots obtained showed negative reading depicting compression of FRP fibres due to the load resistance on the bearing surface of the clearance holes by the shear stud. The stud provides a boundary resistance against the compressive load on the fibres. The strain readings reflect the effect of the compressive forces on the fibres around the stud hole and the plotted lines are a little distorted (wavy) on the graph indicating de-bonding of the material fibres from the matrix. The early linearity of the plot for clearance holes around the stud indicates the proportional response of load against strain during

which the stud slips into bearing. Thereafter, increased loading resulted in higher resistance along with propagated failures of the GFRP flange fibres. The failure propagation on the fibre intensifies with a nonlinear curve (shown on Figure 6.11) until fibre delamination became visible. The nonlinear curve continues until failure, where further loading was not admissible. The final failure is represented on the graph at the peak of the plot in which case the fibres have been delaminated. The strain response of the various studs will differ as seen in the plots in Figure 6.11 because of the non-homogeneity of the FRP material.

The strain plot for the right-hand side slab showed higher strain readings at early loading in comparison to the left-hand side. This may be attributed to the difference in homogeneity between both flanges and a nonconsistency in the concrete mix between the slabs. However, this could be due to the load distribution on the studs caused by the difference in concrete resistances allowing for the early mobilisation of strength in the studs located on the left-hand side slab. This is reflected in the difference between average strains on the left-hand side against that on the right-hand side shown in Figure 6.9. Figure 6.10(a) is an output by Nguyen (2014) and illustrates the total average strain of all studs to the average strain at a distance 25 mm above the clearance holes. Nguyen (2014) observed higher strains obtained at 25 mm position above the stud holes while lower strains were obtained at 50 mm above the holes and insignificant strain readings were taken at 25 mm beneath the bolt holes. The resulting strain at 25 mm above stud hole is compared against the equivalent strain data reported by Nguyen (2014) at a similar position. The strain response reported by Nguyen (2014) was higher following the type of FRP material used, the size of the shear stud and concrete compressive strengths. The FRP material adopted was a hybrid polymer composed of carbon fibre for improved

strength along with the ultra-high performance fibre reinforced concrete (UHPFRC) connected using 16 mm high strength steel stud. The strength enhancement of the connection resulted in a likely higher strain response around the stud holes when compared to the performance of GFRP- normal weight concrete composite using 12 mm steel studs. The negative curve pattern provided by both graphs implies a systematic response of the FRP material to shear loading, in this case, provides consistency to validate the hypothesis that the FRP flange property influences the shear behaviour of FRP-Concrete composites.

Figure 6.8: Strain Comparison (Etim et al., 2020)

6.2.3.4 Strain effect on FRP plates (Phase III)

The strain response for LWAC specimen also follows a peculiar trajectory similar to the NWC push-out specimens. Previous research conducted by Nguyen had suggested that strain readings are most significant at heights of 25mm above the stud and this was

confirmed within the test result reported in phase II. The average strain response at 25mm height above the bolt perforations on the GFRP flanges shows a consistent trend in the behaviour of the composite irrespective of material composition. The strain reflects the corresponding distribution of compressive stresses bearing around the bolt area. The average strain values of 1460.1με at a load of 278.9kN are obtained for the LS-Mean plots of PO-12B-LS and 1460.1με at a load of 278.9kN for RS-Mean plots (Figure 6.12). The strain values significantly reflect an evenly distributed stress on both flanges. However, higher strain values of about 82% is reported in composites of NWC specimen although LWAC specimen have 78% higher slip values when compared against NWC counterparts. This important result reflects the relationship between slip and load capacities.

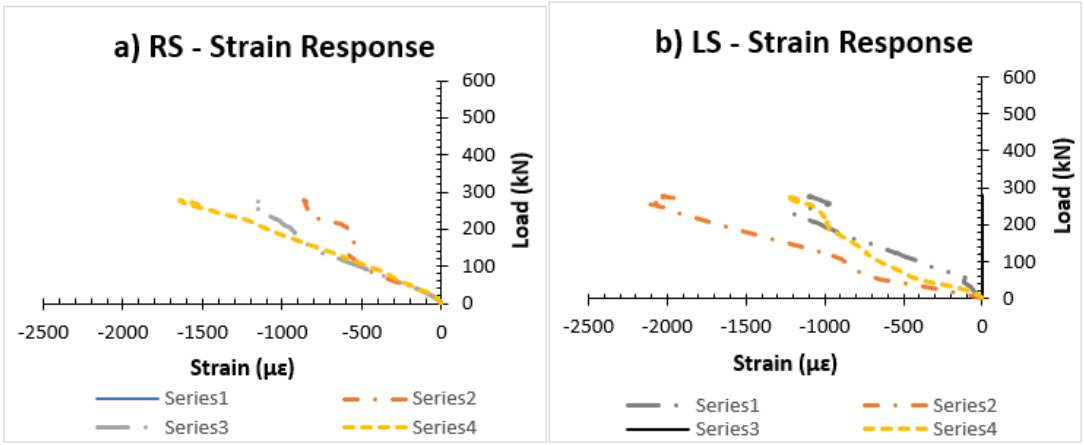

Figure 6.9: Strain response on FRP plates

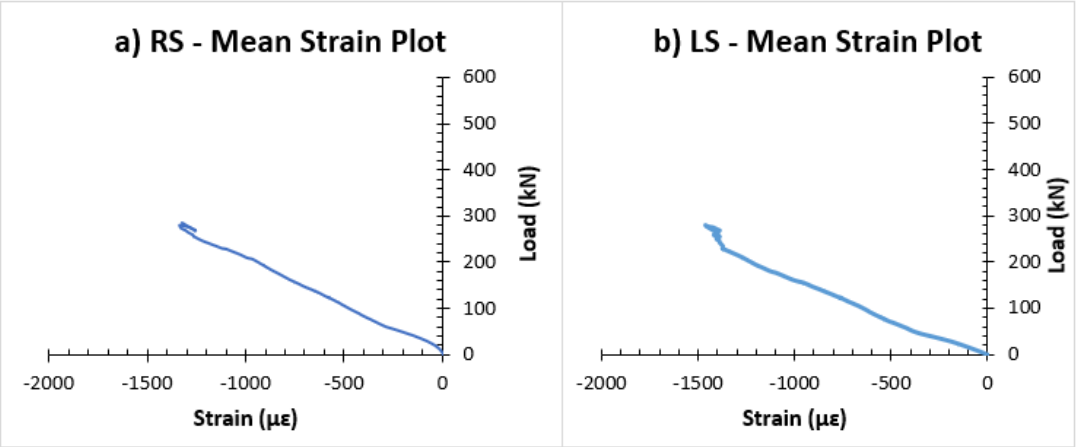

Figure 6.10: Mean strain response on FRP plates

The cumulative average strain obtained from the Left-hand-side (LHS) of the composite was 1011με which is about 32% higher than the strain obtained on the right-hand-side (RHS) of about 691.33με. However, the strains on the two opposite flanges reflected a nearly close trajectory with the two outstanding strain plots for RS-TL and LS-TL showing a similar trajectory (see Figure 6.13). The cumulative average strains were taken at load of 180.9kN. This is the load at which the load-strain curve transitions from a linear path into a nonlinear curve as shown in Figure 6.14. At this load, the strain values become distorted indicating fibre delamination or crack propagation on the Flange area around the stud clearance holes. At which point a combined stud deformation and fibre bearing failure slowly becomes visible in the experimental test.

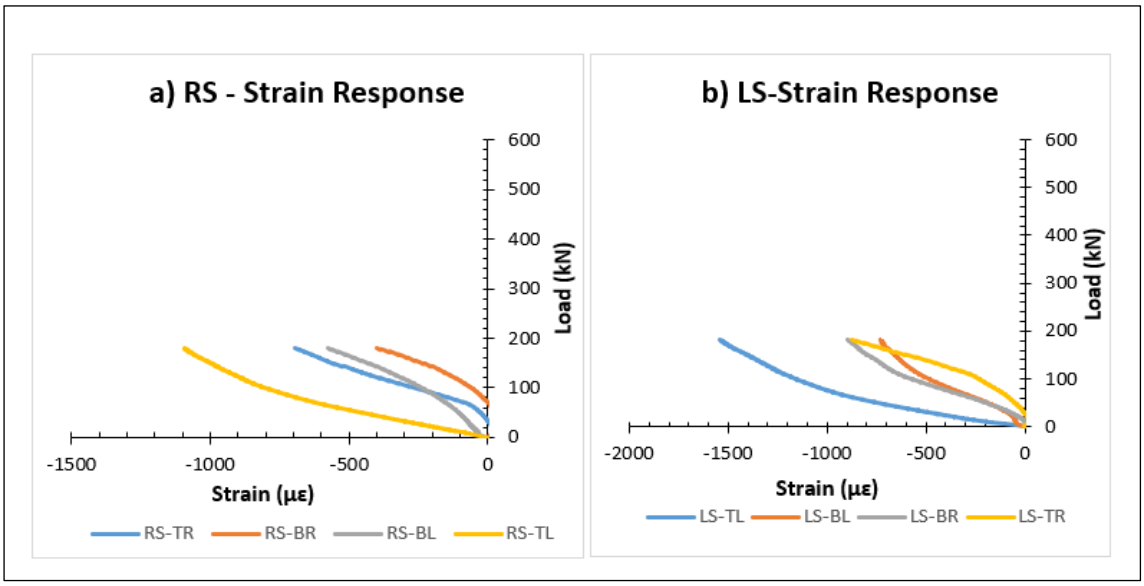

Figure 6.11:Strain plots on GFRP flanges

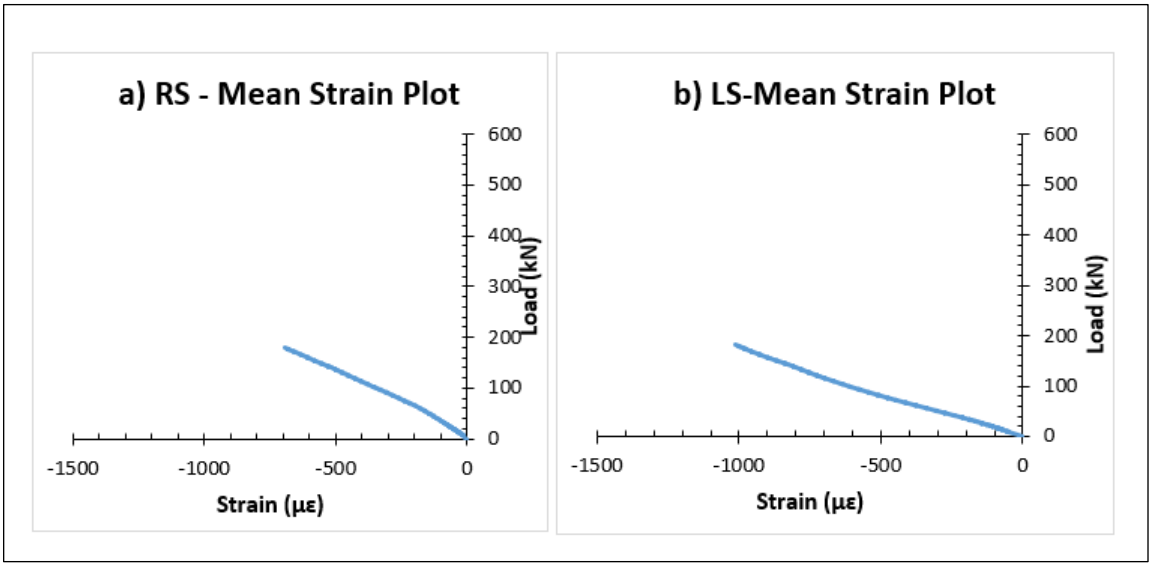

Figure 6.12: Average strain plot for FRP flanges

6.3 Flexural test results

6.3.1 Cyclic load test data

The results obtained from the cyclic load performance test is summarised below (see Table 6.3). The obtained peak load per cycle is reported as a percentage of the ultimate load at failure and the corresponding deflection capacity. The maximum deflection reported is taken from the data reading derived from the centrally positioned LVDT and subsequent deflection is recorded at 650mm to the LHS and RHS of the midspan. The load-deflection plots for all LVDTs is captured in a load-deflection plot reported in section 6.4.2. Associated crack development and propagation observed on composite beam is reported in section 6.5.5 with illustrated measurements of cracks and implication. Peak strain readings derived from experimental test is detailed in Table 6.4 & 6.5 respectively.

Table 6.3: Load-Deflection Results

Measurement Parameters	Cycle 1	Cycle 2	Cycle 3
Percentage capacity of load (%)	28.2	35.6	38.6
Peak load (kN)	97.7	123.5	133.5
Percentage capacity of deflection (%)	33.0	30.7	30.9
Peak Deflection (mm)	14.5	13.5	13.6
Final Deflection	5.2	2.3	2.9

Table 6.4: Peak Strain Response of GFRP Profile

Position	Cycle 1	Cycle 2	Cycle 3
Flange-concrete Interface (Outer Top Flange)			
Central strain	-327.5	-62.2	-59.5
LHS strain	-480.3	-149.8	-149.5
RHS strain	-32.9	71.8	61
Inner Top Flange			
Central strain	-99.0	219.8	258.4
LHS strain	-358.6	-3.6	13.2
RHS strain	-126.5	125.6	149.2
Mean Strain	-	-	-
Inner Bottom Flange			
Central strain	-	-	-
LHS strain	1336.3	1583.9	1695.2
RHS strain	1287.5	1534.0	1639.8
Mean strain	1311.9	-	-
Outer Bottom Flange			
Central strain	5143.6	6138.0	6578.8
LHS strain	1442.2	1693.1	1820.8
RHS strain	3923.6	4856.1	4870.2
Mean strain	-	-	-
Upper Web strains			
LHS strain	-	-	-
RHS strain	76.9	349.0	378.0
Centre strain	218.3	491.4	527.3
Mid-Web strains			
LHS strain	613.1	907.4	981.3

RHS strain	649.0	924.2	994.4
Centre strain	1394.6	1971.8	2097.7
Mean strain	631.1	915.8	987.9
Lower Web strains			
Bottom-Left strain	1343.5	1648.2	1775.6
Bottom-Right strain	1242.4	1539.1	1657.5
Mean strain	1293.0	1593.7	1716.6
Bottom-Centre strain	4165.0	5172.9	5563.8

Table 6.5:Concrete & Stud Strain Response at Peak Cyclic Loads

Position	C1	C2	C3
Outer Concrete strains			
LHS strain	-329.9	-401.4	-442.0
RHS strain	-354.4	-402.6	-430.4
Centre strain	-613.1	-715.1	-771.3
Central Stud strains			
R2 strain	191.7	103.8	103.8
R1 strain	0.9	-22.4	11.4
L2 strain	-582.6	226.1	327.2
L1 strain	-439.0	-97.5	-102.9

6.3.2 Ultimate load test data

Summary results obtained from the test exercise is presented in Table 6.6. Experimental values of flexural capacity, moment capacity and deflection are presented for load

capacities at 25%, 50%, 75% and 100% respectively. Further strain responses are given at ultimate load for GFRP profile, stud, and concrete subcomponents. Analysis and discussions of the result are presented in subsequent sections.

Table 6.6: Summary result of peak experimental load

Load Capacity (%)	***Moment Capacity (kNm)***	***Flexural capacity (kN)***	***Maximum deflection (mm)***	***Remarks***
25	47.6	86.5	11.08	No deformation or cracking
50	95.2	173	20.55	Crack development observed
75	142.7	259.5	29.07	Crack propagated alongside depth of the concrete
100	190.3	346	44.01	Cracking and splitting failure of concrete

Table 6.7: Ultimate peak strains for GFRP flange

Beam Arm	**Top Flange (TF)**		**Bottom Flange (BF)**	
	Outer/Interface	***Inner face***	***Outer face***	***Inner face***
Left Arm $(\mu\varepsilon)$	-1428.1	74.2	5561.4	4897.7
Mid-span $(\mu\varepsilon)$	-1353.9	142.4	18932.3	-
Right Arm $(\mu\varepsilon)$	-122.9	-3.9	15667.2	4662.6

Table 6.8: Web shear strains

Beam Arm	**Measurement Orientation**			**Remarks**
	0' deg.	***45' deg.***	***90' deg.***	
Left Arm $(\mu\varepsilon)$	-344.2	4242.4	-10.8	-
Mid-span $(\mu\varepsilon)$	-	4853.5	-	-

Right Arm $(\mu\varepsilon)$	3413.4	-	-391.5	-

Table 6.9: Concrete & stud strains

Strain position	Concrete strain	Stud Position	Stud strain
Left Arm $(\mu\varepsilon)$	-1066.5	***L1*** $(\boldsymbol{\mu\varepsilon})$	-931.7
Mid-span $(\mu\varepsilon)$	-2199.1	***L2*** $(\boldsymbol{\mu\varepsilon})$	-2173.1
Right Arm $(\mu\varepsilon)$	20.6	***R1*** $(\boldsymbol{\mu\varepsilon})$	120.2
-	-	***R2*** $(\boldsymbol{\mu\varepsilon})$	472.8

6.4 Hybrid Composite Beam

This section presents the analysis of the current research study. Results from experimental testing are presented under two broad subjects: serviceability and ultimate limits. Structural elements are often subjected to repeated cycles of loading throughout their service life hence, analysis of GFRP-concrete hybrid beams under serviceable loads is considered important in detailing the characteristic behaviour of the beam within an expected design life. The composite beam was subjected to three successive cycles of loading at a predetermined deflection of approximately 16mm which is estimated at 38% of the peak deflection of ultimate loading. On completion of cyclic loading, the composite beam was loaded until failure occurred under the ultimate limit state requirement for design. Ultimate loading is a requisite test for determining the characteristic performance of the composite hybrid beam under extreme loading circumstance, to understudy the failure development and overall effective response of the hybrid beam within a safe design criterion. The experimental procedure and specimen preparation are presented in chapter four detailing: the fabrication design, experimental test setup, instrumentation, and test procedures. Summary analysis are presented in subsections of this chapter for each broad subject with analytical findings on load-deflection and load-strain responses of the composite beam.

6.4.1 Load-deflection relationship

6.4.1.1 Cyclic test plots

The three cycles of loading are illustrated in the load-deflection cyclic plots using corresponding deflections of 3 centrally positioned LVDTs (see Figure 6.15). The first cycle was initiated until a mean deflection of approximately 13 mm corresponding to approximately 29% of the ultimate failure load at 97.7kN. The plot exhibits clear linear progressions from initial loading until the predetermined peak load at 29% of the ultimate at which point the hybrid is slowly unloaded under a load-step of 5kN back until zero (where unloading is fully achieved). At zero, the hybrid composite sustains a slight deformation of 5 mm (see Figure 6.15a). The curve from the first cycle shows an irregular increase at a load of approximately 40kN at 4 mm, also during unloading a sudden load drop approximately 25kN at a deflection-drop of 6 mm was observed. This behaviour may typically suggest initial slip resistance of the shear studs and debonding of the concrete from GFRP flange at interface. This was physically observed during testing with accompanied sounds suggesting elements of concrete debonding action and at a load of about 75 kN corresponding to approximately 9 mm deflection.

The second and third cycle of the load-deflection curve reflected the repeatability of the cyclic loading at which possible debonding may have fully occurred and the hybrid composite beam demonstrates an effective capacity under serviceability. The two cycles are closely represented on the plot with similar plot progressions and regressions on full cycles of loading (see Figure 6.15 b & c). Notable irregularities observed in the curve for the first cycle are not clearly visible in the second and third curves. This may clearly validate the assumptions on debonding actions achieved in the first cycle. The slopes of

the second and third cycle are closely similar but different from the curves from the first cycle also evidence that the composite action achieved in the first cycle was from the dominant influence of the concrete-GFRP flange bond. However, in the second and third cycles, the composite action is clearly defined by full-shear interactions achieved through the shear studs. Initial stud shear slips are observed on both curves for the second and third cycle at approximately 15 kN of loading and 1.2 mm deflection respectively. Both curves (for cycle 2 and 3) progress linearly until a peak load of approximately 125 kN and 135 kN corresponding to an estimated 12 mm deflection for cycle 2 and cycle 3 respectively. The regression of the curve on return of the cycles are similar, sustaining deflection of approximately 1 mm at the full unloading of the hybrid beam.

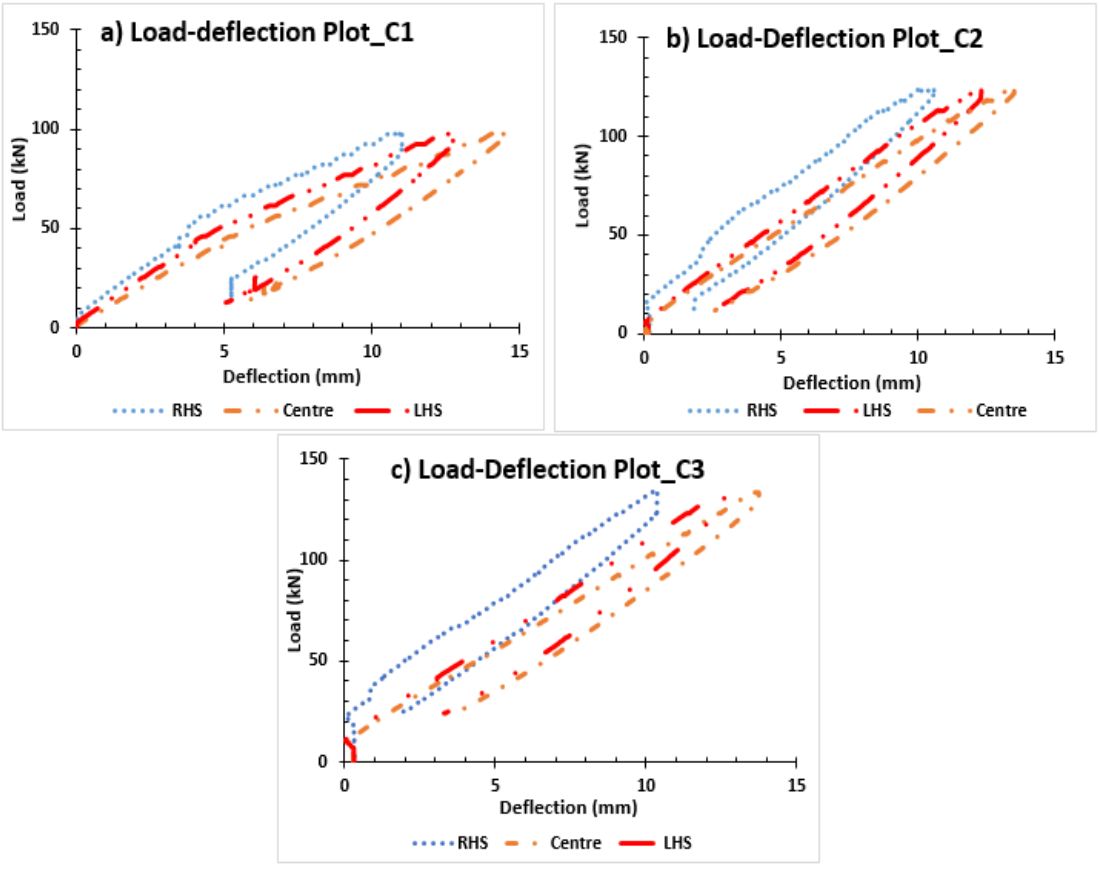

Figure 6.13: Load-deflection plots under cyclic loading

The plots for the left-hand-side (LHS) and right-hand-side (RHS) differ fairly in their deflection rates with a maximum difference of 0.03, 0.64 and 1.52 mm for cycles 1, 2 and 3 respectively (see Figure 6.15). Significant difference in deflection on the LHS in cycle 3 suggest development of failure cracks within the hybrid composite which eventually justifies the slab shear failures observed and reported in section 6.3.2. The higher deflection value of 3.3 mm was obtained on the LHS against 1.78 mm deflection values for RHS at a declining load of 24.1kN for cycle 3. The maximum deflections are derived from the centrally positioned LVDTs with a maximum deflection of 14.5 mm at a corresponding peak load of 97.7kN for Cycle 1, maximum deflection of 13.5 mm at a peak load of 123.3kN and maximum deflection of 13.63 mm at a peak load of 133.5kN for cycles 1, 2 and 3 respectively.

6.4.1.2 Ultimate load test plots

The load-slip curve is typical of a bilinear representation for FRP-concrete composites highlighted by Neagoe & Gil (2015). The plot curve for the LHS and RHS depicts a parallel propagation suggesting an evenly distributed load on the composite beam. The composite beam shows an initial response to loading at 4.4% and subsequently increases its stiffness at approximately 21% of the peak load respectively. The curve becomes wavy in a zig zag manner at approximately 75% of the peak load suggesting internal failures which became conspicuous shortly before peak failure at 346kN (see Figure 6.16).

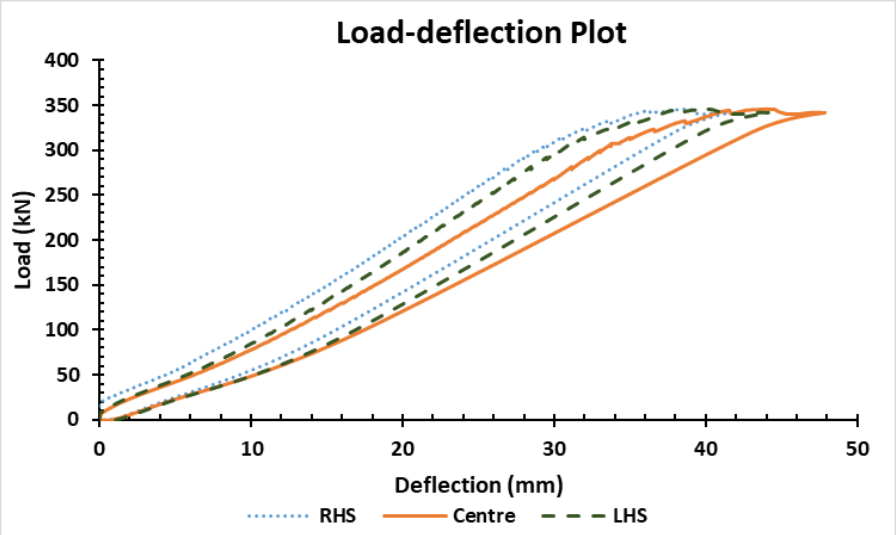

Figure 6.14: Load-deflection Curve

6.4.2 Load-Strain response of GFRP profile

6.4.2.1 Upper/Top Flange (TF)

The strain gauges were positioned centrally on the outer surface of the GFRP top flange interfacing with the concrete. The strain response was derived from the longitudinally placed strain gauge at mid-span of the section with two additional gauges placed at 600 mm to the left- and right-hand side of the of the centrally positioned gauge. In a similar fashion, strain gauges were positioned at the inner surface of the GFRP top flange to corroborate outer strain readings and determine the strain distribution at the top flange.

I) Outer/Interface TF strains:

a) Cyclic load test

The strain measurements obtained from the data loggers reflected similar curve plots for the midspan and LHS strains but an irregular plot on the RHS strain (see Figure 6.17).

The irregularity may be due to the debonding action of the concrete from the GFRP flange surface during unloading. The RHS strain values produced a highly irregular curve suggesting deformation or distortion due to debonding action. In cycle 1 (C1), the RHS strain curve showed a sharp drop in strain at declining cyclic loads and at peak cyclic load of 97.7kN (see Figure 6.17a) corroborating earlier observations of load-drop from the load-deflection plots in section 5.2.2. However, the RHS strain curve becomes more distorted during Cycle 2 (C2) suggesting inconsistent strain pattern or behaviour, which may be due to some damage to the outer flange (interface) area towards the RHS during debonding action (see Figure 6.17b). The suggestion of partial damage around the outer flange on the RHS may be due to observations on the contrasting strain readings of 32.9 (compressive strain) and 71.8 (tensile strain) at peak cyclic loads of cycle 1 and cycle 2 respectively. Also, the strain reading at C3 becomes more consistent with C2 indicating a tensile strain of 61 (see Figure 6.17 b & c). The other two strain plots established a consistent strain pattern beginning with a gradual increase in tensile strength progressing into compressive strains. This may be due to possible compression force transfer from the slab unto the flanges of the GFRP section. The difference in strain values indicate a drop in slab compression on the top flange at the centre due to early debonding action at C1 and subsequently variance in material curvature at C2 and C3 against the LHS strain. This may suggest practically, that debonding is initiated from the centre of the beam and therefore at peak loads, maximum strains may occur away from the centre.

The strain readings for LHS and midspan on all cycles are captured in Table 6.2 at peak cyclic loads. The difference in strain data obtained between the LHS and the centre is approximately 32%, 58% and 60% for C1, C2 and C3 respectively. However, the centre strain at peak cyclic load of C1 is 81% higher than C2 and 82% higher than C3. This also

emphasizes the combined effect of interface bond and shear connectors in providing shear resistance during loading in cycle 1 by which debonding occurs and at cycle 2, the effect of interface bond is diminished reducing the interface strain.

b) Ultimate load test

Strain response at ultimate loading deviates significantly from the strain plot under serviceability limit loading (see Figure 6.18). There is a consistent strain development on the LHS and centres of the composite but with a huge deviation in the reading obtained from the RHS. An irregular strain response earlier suggested from the cyclic loading to be due to possible debonding action may proliferate under intense loading hence compromising the strain readings obtained on the RHS. However, significant strain readings obtained from the midspan is highly consistent in its propagation with the LHS and records a maximum compressive strain value of 1353.9$\boldsymbol{\mu\varepsilon}$ approximately 5% less than the strain value recorded on the LHS at 1428.1$\boldsymbol{\mu\varepsilon}$**.** The strain curve is initiated slightly into tension from early loading and propagates linearly up to about 28% of the peak load where stiffness is increased suggesting increased mobilisation of stud shear capacity until 73% of the peak load at which strain curve transitions into the failure. Physical gaps are observed at 73% of the peak load towards the centre hence, the 5% difference in strain readings between the LHS and the midspan. Results show an estimated 89% increase in the compressive strain at the slip interface between the serviceable load and ultimate load at failure. At a load of about 260kN before the strain curve transitions nonlinearly into failure, the composite beam reserves a strain capacity of 77% at 660$\boldsymbol{\mu\varepsilon}$ above the serviceability load.

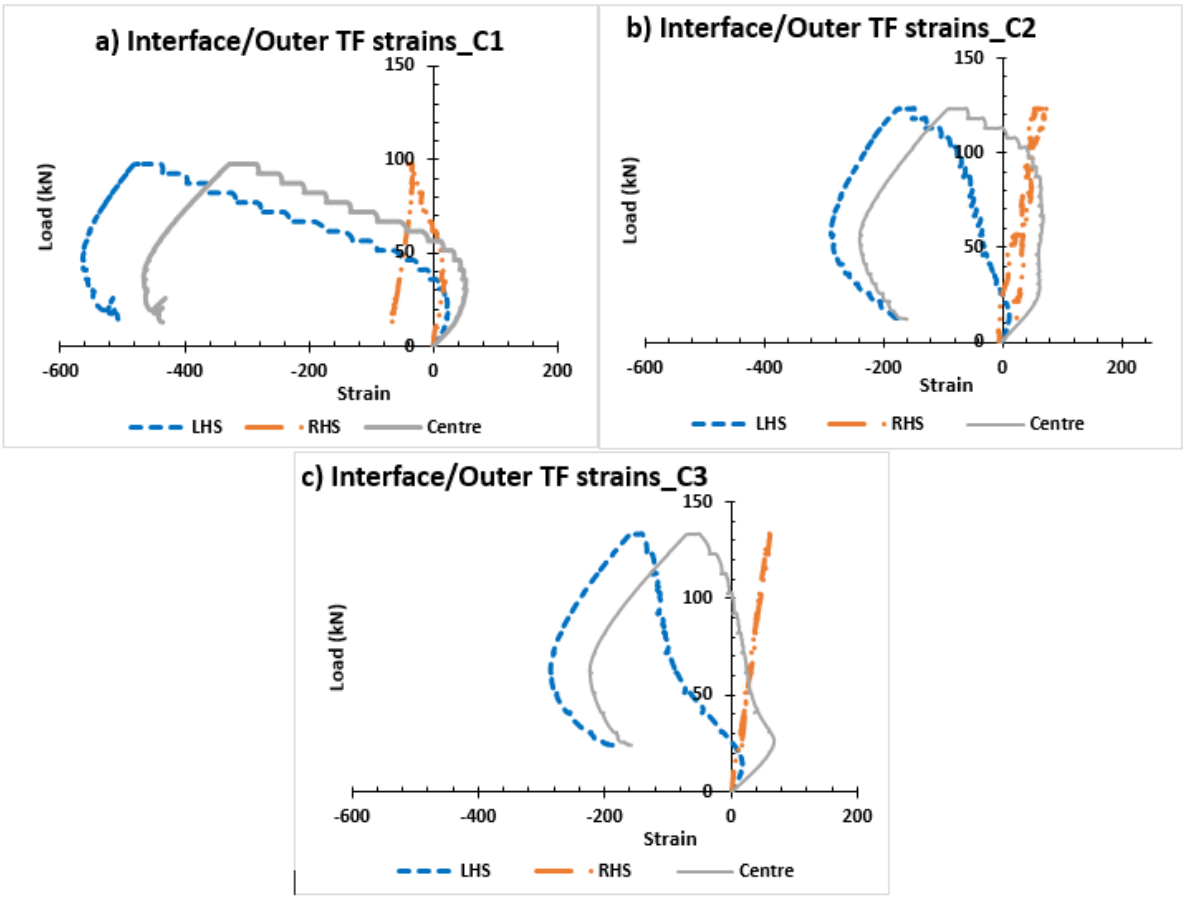

Figure 6.15: Interface Load-strain response at Cyclic Loading

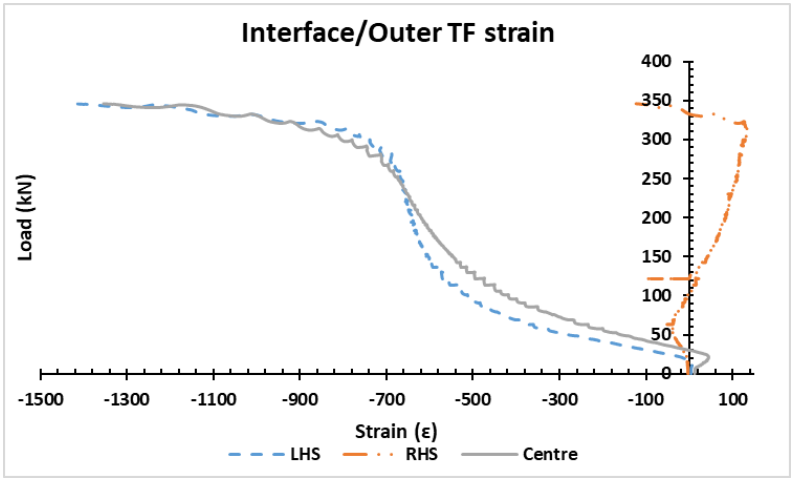

Figure 6.16:Interface Load-strain response at Ultimate Loading

II) Inner TF strains:

a) Cyclic load test

The inner face of the upper flange of the GFRP reflects a consistent trend in the development of strain plots against the interface plot. This corroborates the partial compression action on the flange suggesting that the GFRP flange was in partial compression. At initial cyclic loading, lower strain values were observed at midspan compared against its LHS and RHS counterparts indicating that debonding action may have been initiated earlier at the centre of section whereas, subsequent debonding actions may have followed through on the RHS and finally the LHS (see Figure 6.19a). At peak loading the maximum strains were 358.6, 126.5 and 99 at LHS, RHS and centre respectively for C1. The LHS and RHS produced 72.39% and 21.74% higher strains than the centre in compression. This demonstrates an ideal loading practice often encountered in construction such that loading distributions are hardly symmetric due to material non-linearities and geometric imperfections which can tilt the effect of the loading in higher amounts towards a singular support. The plot from C2 and C3 shows that the inner TF is in tension suggesting that the composite neutral axis may lie at the centre of the TF (see Figure 6.19 b & c). During unloading, the material proceeds to compression accounting for the self-weight effect of the concrete slab as earlier seen in C1. The strains at peak cyclic loads of 123.5kN are 3.6, 125.6 and 219.8 for LHS, RHS and centre respectively. The centre strain was 43% higher than the RHS strain and 98% higher than the LHS strain. However, the centre strain for C2 was 55% higher than its C1 counterpart at a 21% load difference and the strain for C3 was 62% higher than C1 at a 27% load capacity difference. The strain difference between C2 and C3 was insignificant, indicating the repeatability of the cycle and non-existing influence of slab compressive forces due to

bonding. The stain values for C2 and C3 at peak cyclic loads of 123.5kN and 133.5kN are 219.8 $\boldsymbol{\mu\varepsilon}$ and 258.4 $\boldsymbol{\mu\varepsilon}$ respectively.

b) Ultimate load test

The inner face of the top flange (TF) shows improved consistency in the behaviour also validating the suggestion of possible proliferation of the strain readings on the RHS due to debonding at slip interface (see Figure 6.20). The strain curve indicates early tensile strain propagation which slowly transitions into the compressive zone at about 14% of peak load and shortly transitions back into the tensile zone at 48% of the peak load. The LHS strain is significantly sustained in the compression zone at approximately 360$\boldsymbol{\mu\varepsilon}$ which is approximately 33% and 89% higher than the peak strain of the RHS and midspan strains respectively within the compression zone. However, within the tensile zone, the midspan strain is approximately 48% higher than the LHS strain at 74.2$\boldsymbol{\mu\varepsilon}$ and 99% higher than the RHS 3.9$\boldsymbol{\mu\varepsilon}$. The strain curve suggests that the GFRP flange was in tension at peak loading before failure hence, the neutral axis might be located at the flange area. Furthermore, the midspan strain curve is highly distorted in a wavy pattern suggest possible fibre failures which were not visible during the test although fibre noises were audible.

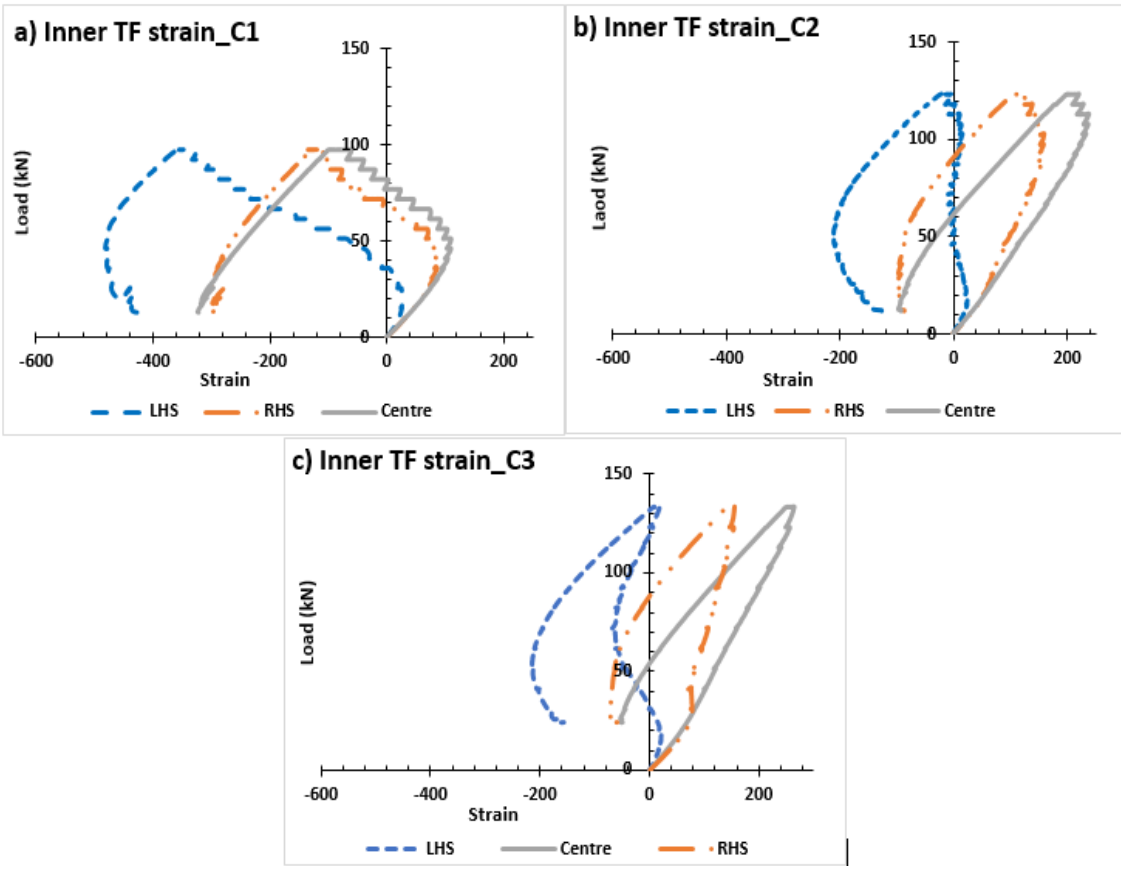

Figure 6.17:Top Flange (TF) Load-strain response at Cyclic Loading

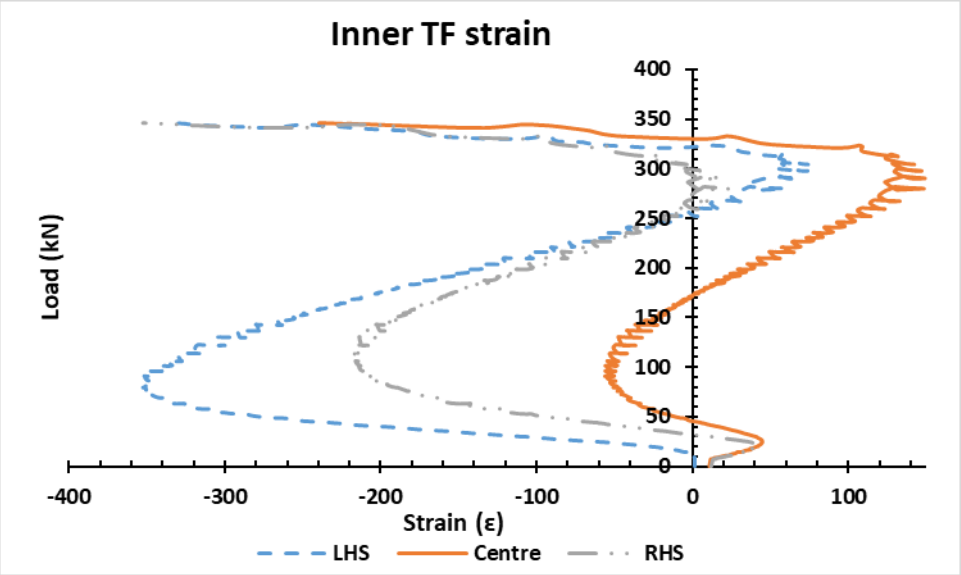

Figure 6.18: Top Flange (TF) Load-strain response at Ultimate Loading

6.4.2.2 Bottom Flange (BF)

At the bottom flange of the beam, the strain distribution exhibited similar trend in plot for all three positioned strains on both the inner and outer flange surfaces. The plot illustrates a linear strain progression against the load until peak with a similar linear regression of strain in similar fashion for the inner BF strains (see Figure 6.21 & 6.22).

I) Inner BF strains:

a) Cyclic load test

Both LHS and RHS strains progress and regress on a similar curve with 1336.3 and 1287.5 respectively implying a 0.4% difference in strain values at a mean strain value of 1311.9 for C1 (see Figure 6.21). 0.4% strain difference between the LHS and RHS is insignificant and suggest a near even distribution of stresses at the bottom flange at peak deflection. The strain difference of LHS and RHS for C2 and C3 are 3.2% and 3.3%

respectively. The inner and outer bottom flange recorded positive strain values, an indication of tensile stresses as anticipated of materials subjected to bending.

b) Ultimate load test

The strain response for the inner bottom flange (BF) is highly consistent between both arms; LHS and RHS of the composite beam. The strain response indicates a perfectly elastic tensile strain development from initial loading until failure. This behaviour is significantly consistent under the serviceability (cyclic) loading conditions and ultimate loading. The curve is perfectly linear with an initial distorted (zig zag) propagation at about 14% of the peak load corresponding to a strain value of 70$\boldsymbol{\mu\varepsilon}$ (see Figure 6.22). The distortion becomes more severe at about 72% of the peak load suggesting internal fibre failures at a strain of approximately 3300$\boldsymbol{\mu\varepsilon}$. The study observed an average strain increase of 65% between the serviceable loads at 1667.5$\boldsymbol{\mu\varepsilon}$ and ultimate loads at 4780.2$\boldsymbol{\mu\varepsilon}$ respectively. This implies that at 70% of the peak load, there will be an estimated 98% strain increase from the serviceable loads.

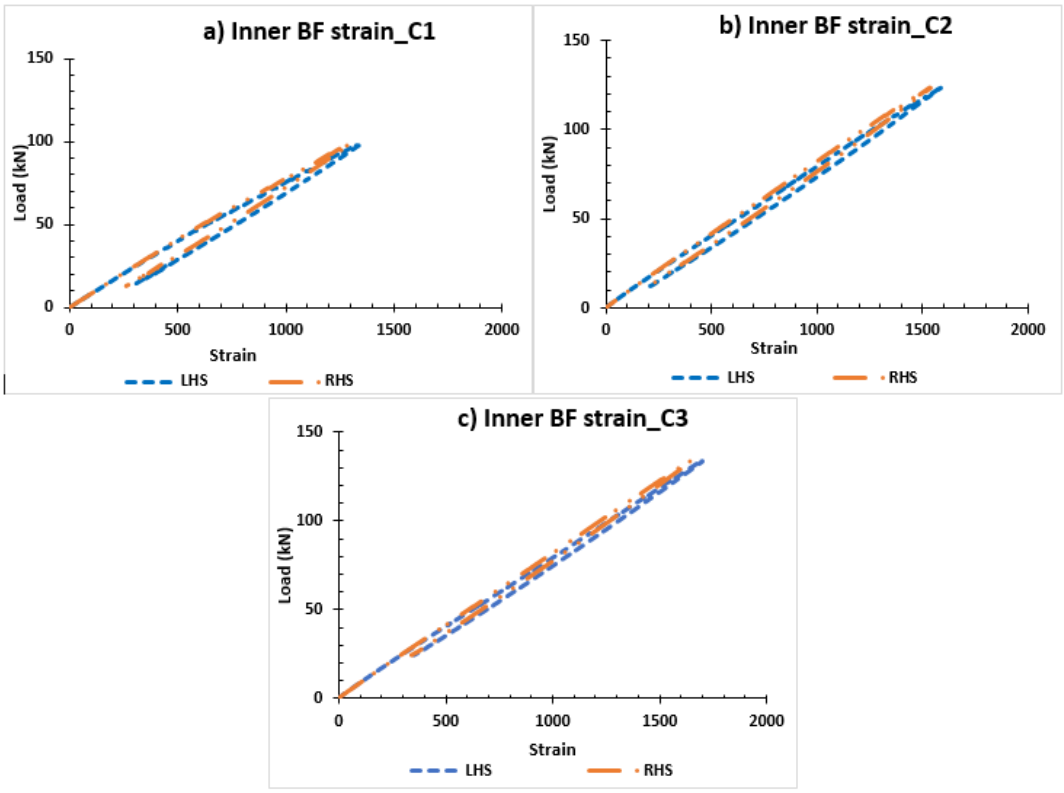

Figure 6.19: Bottom Flange (BF) Load-strain response at Cyclic Loading

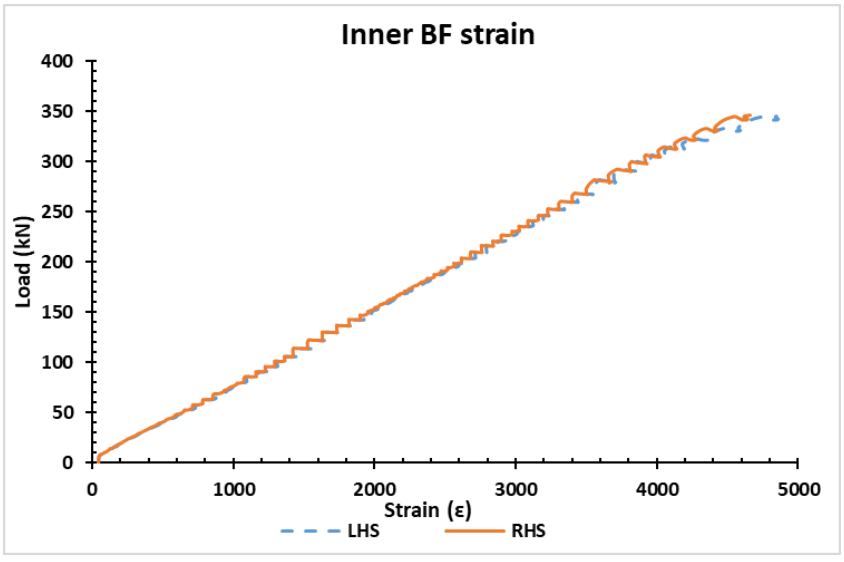

Figure 6.20: Bottom Flange (BF) Load-strain response at Ultimate Loading

II) Outer BF strains:

a) Cyclic load test

Significant variation in the outer layer of the bottom flange suggest peak strains of 5143.6 (for C1) at the mid-point with effects of extreme deflected curvature and varied differences in the strain distributions of 1442.2 and 3923.6 between the LHS and RHS of the outer bottom flange (see Figure 6.23). 37% differences in strain values between the LHS and RHS may be attributed to material non-homogeneity as it was equally non-consistent with the distribution at the top flange. 65% strain difference between LHS and RHS for C2 and 63% for C3. However, a consistent increase in the strains at the mid-span of the hybrid composite of 16.2% between C1 and C2 and 6.7% between C2 and C3 respectively. The large drop in strain difference at mid-span between the C1 and C2/C3 indicates the diminished influence of interface bond action due to cyclic loading. However, the plots exhibited similar progressions and patterns for strain propagations. Distorted strain curves suggest non-visible inner fibre failures as were characterised with cracking sounds during the test activity.

b) Ultimate load test

The midspan strain response of the outer bottom flange (BF) face is consistent with the inner face BF response above for the LHS and RHS illustrating a perfectly elastic linear behaviour. This is relevant in the analysis to satisfy the fundamental principle for flexural behaviour confirming a perfect tensile response of the bottom flange as would be for a steel profile section. However, the RHS strain response becomes highly distorted suggesting severe internal failures in the bottom flange whereas, the LHS strain is linearly consistent with the midspan strain. The response of the LHS strain suggest lower strain

response to increase loading against the midspan strain response which evidently suggest maximum tensile stresses at increased flexure (see Figure 6.24). An average linear strain difference of 770$\boldsymbol{\mu\varepsilon}$ is observed between the LHS and midspan strain response on increased flexure of beam. Midspan strain of 18952$\boldsymbol{\mu\varepsilon}$ is recorded at peak load corresponding to 198% (6358.4$\boldsymbol{\mu\varepsilon}$) of the average strain at serviceability limit.

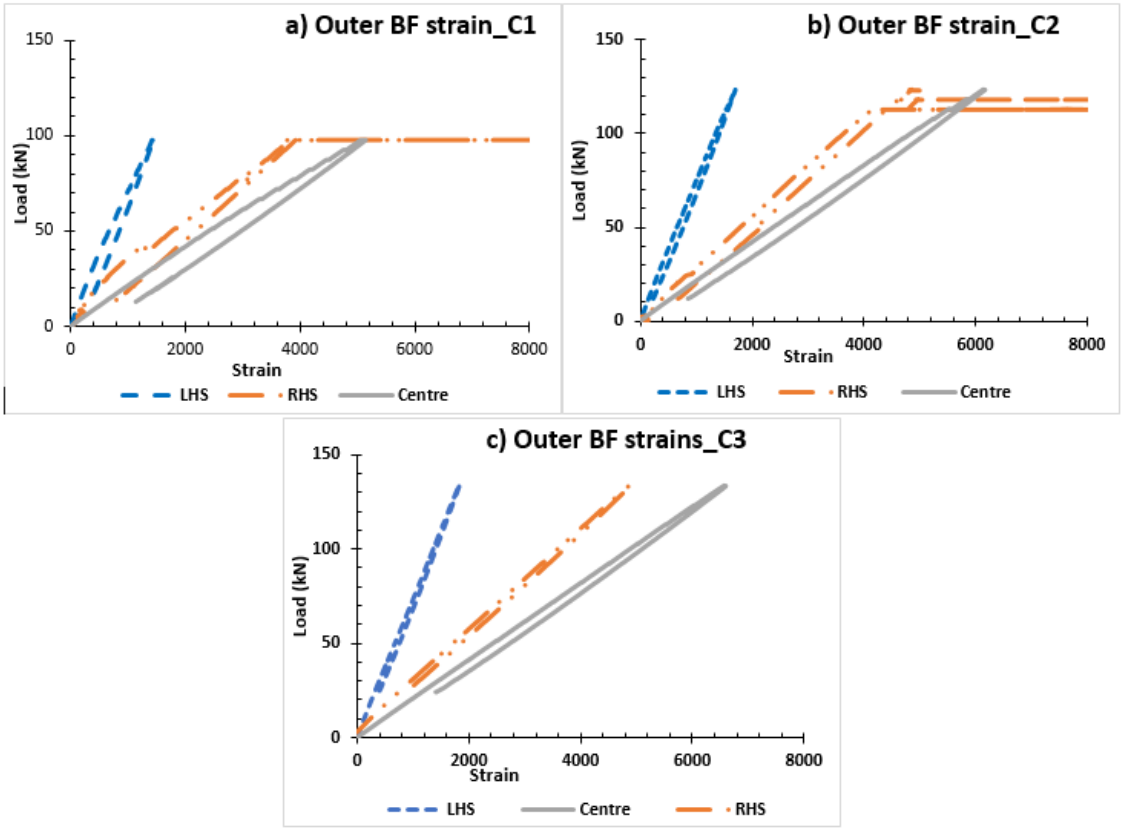

Figure 6.21: Bottom Flange (BF) Load-strain response at Cyclic Loading

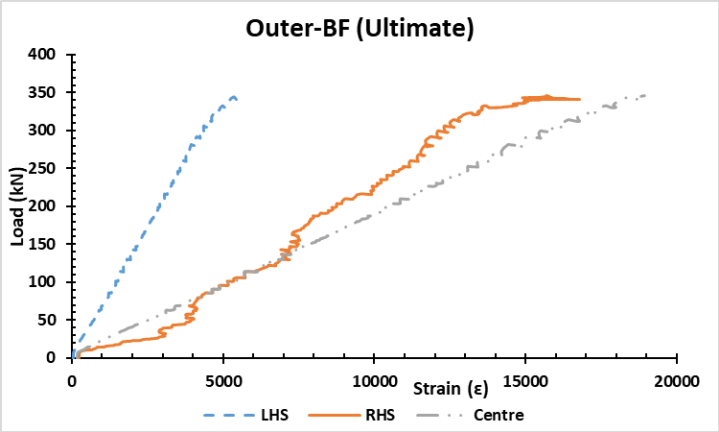

Figure 6.22: Bottom Flange (BF) Load-strain response at Ultimate Loading

6.4.2.3 Mid-span web

At 150mm Height:

Cyclic load test: The upper area of the web section closer to the top flange was in tension from the point of loading until the peak cyclic load for the hybrid composite. At a load of approximately 46kN for C1, strain readings become highly inconsistent due to yielding with strain values fluctuating between 204.3-209.7 for strains at centre and 159.7-166.6 for RHS strains. At peak cyclic loads, strain values of 218.3 and 76.9 are obtained for C1 corresponding to centre and LHS gauges, 491.4 and 349 for C2, 527. 3 and 378 for C3 respectively (see Figure 6.25). In the load return of the cycle, the centre strain values transitioned into compression at unloaded values of 55.7kN, 29kN and 29kN for C1, C2 and C3 respectively. The strains difference between RHS and centre for all three-load cycles are 65%, 29% and 28.3% for C1, C2 and C3 respectively. This shows a significant strain increase at the web mid-span of the hybrid composite. However, within the three

cycles of loading, there was significant difference in the values at the web mid-span between the three progressive loading cycles. C2 web mid-span strain values were 55.6% higher than C1 and C3 strain values were 6.8% higher than C2. Strain plot for both centre and RHS was very similar in the curve propagation and pattern. Similar pattern of plots reflects a significant consistency in the derived patterns as this was observed in almost all the load-strain plots reported in this study.

Ultimate load test: The RHS strain response is significantly lower than the midspan strain as deflection is maximum at the centre similarly to strain response at 30mm and 90mm vertical web strains. The strain response becomes significantly nonlinear but remains within the tensile zone suggesting that the entire web in addition to the bottom flange (BF) is in tension. The vertical mid-web tensile strain diminishes upwards from the bottom flange (BF) towards the top flange (TF). The tensile strain response at 150mm is 710.9 $\boldsymbol{\mu\varepsilon}$ which is approximately 91% and 95% less than the peak strain response at 90mm and 30mm vertical positions on the web. The vertical mid-web at midspan is approximately 54% higher than the RHS strain at 323.9$\boldsymbol{\mu\varepsilon}$ (see Figure 6.26). The vertical mid-web strain response suggests an early strain value of approximately 20$\boldsymbol{\mu\varepsilon}$ sustained from the cyclic loading and load response leap at about 30kN indicating possible redistribution of stress due to early fibre failures and a steady linear response until failure. The distorted strain propagation suggests again possible internal fibre failures on both midspan and RHS until failure occurs.

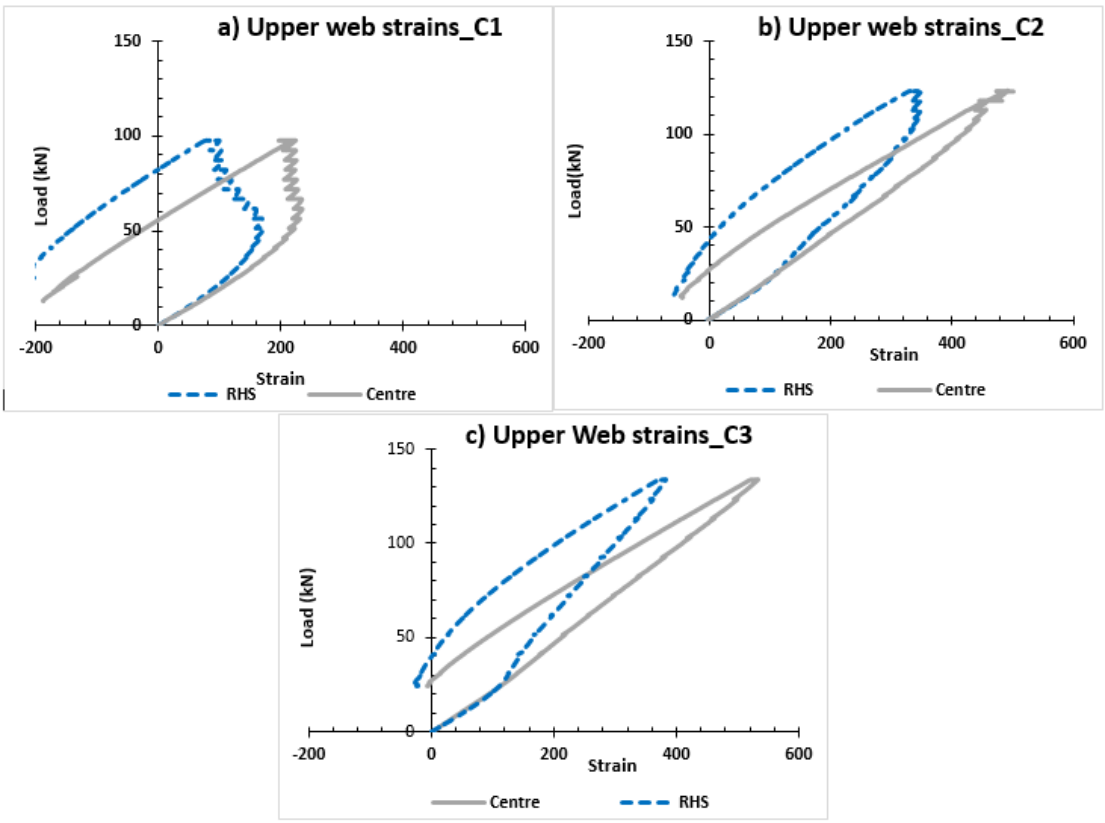

Figure 6.24:150 mm depth mid-web strain response at cyclic loading

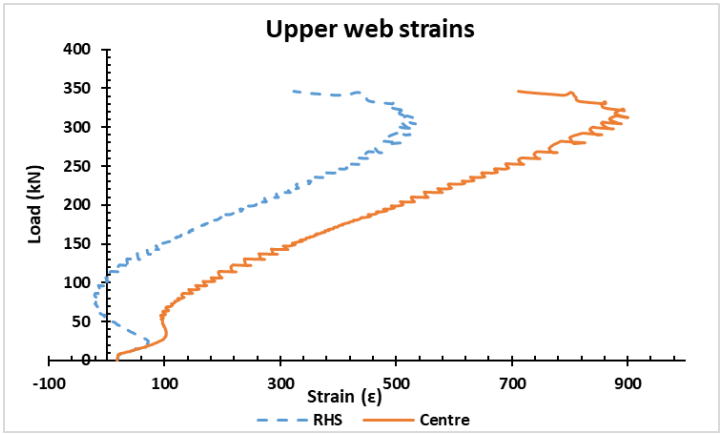

Figure 6.23: 150 mm depth mid-web strain response at ultimate loading

At 90mm mid-section height:

Cyclic load test: Similar to the strain measurement at the upper web, the mid-web strain values for LHS and RHS exhibit identical curves with strain differences of 5.5%, 1.8% and 1.3% for C1, C2 and C3 respectively at peak cyclic loads (see Figure 6.27). The strain readings show that the mid-web section was in tension during the cyclic loading. Significant difference in the strains between the LHS and RHS become visible on the curve at approximately loads of 34kN for C1. However, there are no significant visible differences between the strains for C2 and C3 as seen in the plots. At peak cyclic loads, the strains on the LHS and RHS are 613.1 and 649 for C1, 907.4 and 924.2 for C2, 981.3 and 994.4 for C3 respectively. The average significant strain difference between C1 and C2 is 31% with an average difference of 7.3% between C2 and C3. C2 and C3 values corroborate closely for experimental reliability and repeatability. The mid-span web strain readings for all three cycles are 1394.6, 1971.8 and 2097.7 for C1, C2 and C3 respectively. This corresponds to 29.3% strain increase in the second load cycle (C2) and 33.5% strain increase in the third load cycle (C3) from the first cycle (C1).

Ultimate load test: At 90mm vertical mid-web section, the strain values are only recorded for LHS and RHS however, central peak strains can be predicted as 30% increase of the average strains for LHS and RHS respectively. Hence, the predicted peak mid-section strain at midspan is 8222$\boldsymbol{\mu\varepsilon}$**.** The LHS and RHS strains are highly consistent with peak values of 2481.8$\boldsymbol{\mu\varepsilon}$ and 2451.5$\boldsymbol{\mu\varepsilon}$ showing an evenly distributed stress across the longitudinal length of the profile at mid-web section (see Figure 6.28). Strain response are linear elastic with distorted propagations suggesting possible internal fibre failures in the profile's web. The average mid-web strains LHS and RHS are approximately 50%

(2466.7$\boldsymbol{\mu\varepsilon}$) lower than the average mid-web strains at 30mm vertical height on the web. Generally, the ultimate strain responses are significantly consistent and about 30% higher than the serviceability strain response.

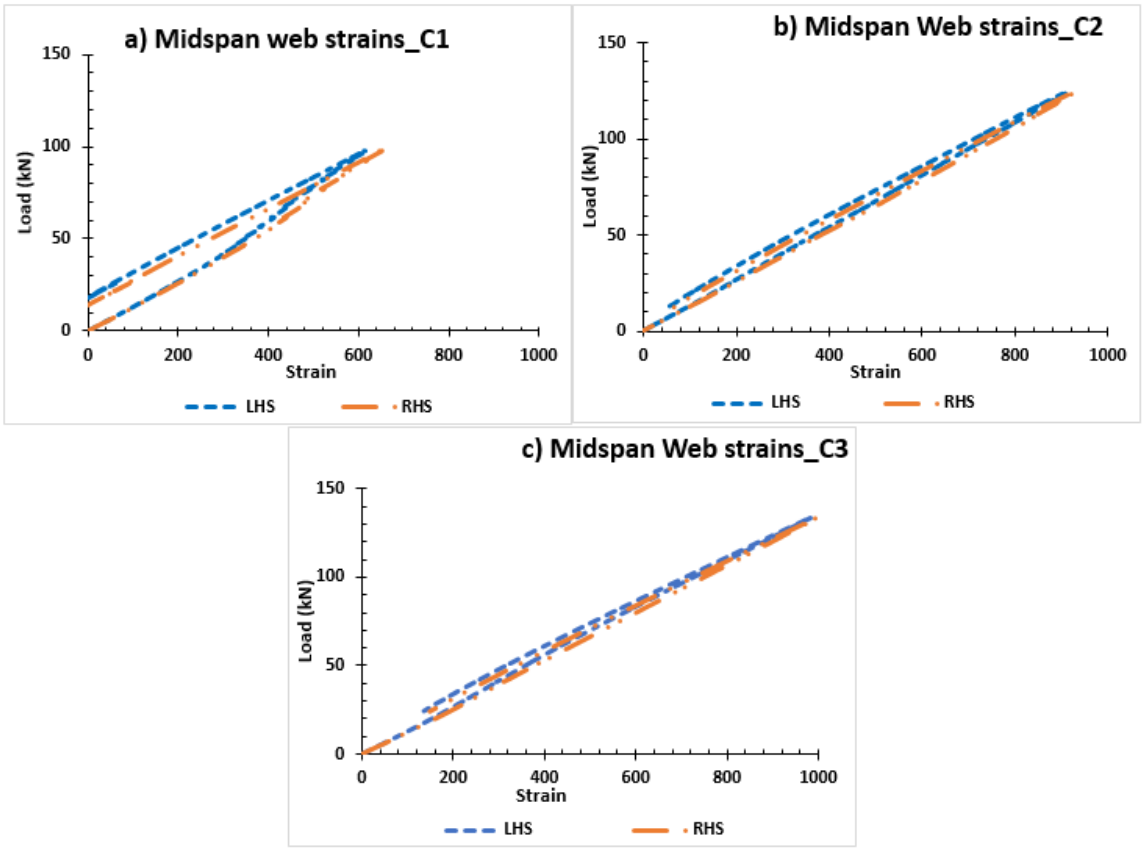

Figure 6.25: 90 mm depth mid-web strain response at cyclic loading

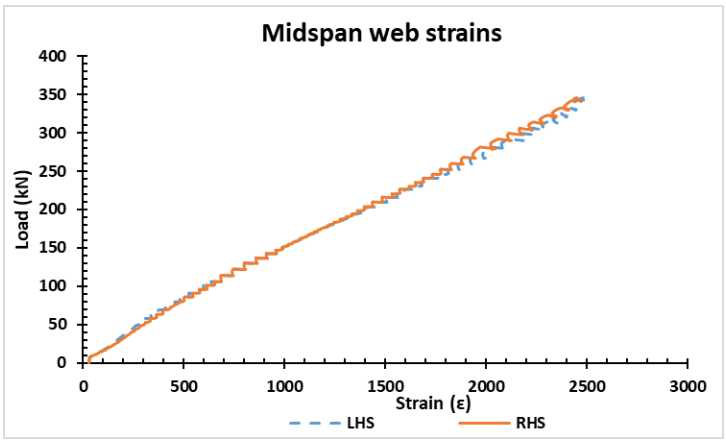

Figure 6.26: 90 mm depth mid-web strain response at ultimate loading

At 30mm height:

Cyclic load test: The lower web strain also exhibits significant increase in strain at the centre of the hybrid beam span at a strain of 4165 which is 68% higher than the LHS strain of 1343.5 and 70% higher than the RHS strain of 1242.4 (see Figure 6.29) for C1. The plot clearly reflects effects of bending forces causing the lower beam to be in tension with significant strain values obtained at the point of maximum deflection. The shear strains have shown consistent increase between the cycles with an increase of 19.5% at C2 from C1 and subsequently 7% increase from C2 to C3. The significant difference in strain values between the centre strain and average strain values for both LHS and RHS values is 69%, for all three loading cycles (C1, C2 and C3). Lower mid-span strain values for all three cycles at peak cyclic loads are 4165, 5172.9 and 5563.8 for C1, C2 and C3 respectively.

Ultimate load test: Linear elastic tensile strain behaviour is recorded at this position on the midspan and 600mm to the LHS and 600mm to the RHS respectively. Higher strain response is observed at the centre with a corresponding consistent tensile strain response on both LHS and RHS. The midspan strain response of 15283.8$\boldsymbol{\mu\varepsilon}$ is approximately 33% higher than the average strain response of both LHS (5321.2$\boldsymbol{\mu\varepsilon}$) and RHS (4707.2$\boldsymbol{\mu\varepsilon}$) respectively. This value is 24% less than the peak strain of the outer bottom flange. Also showing confirming that maximum peak stress occurs at the outer bottom flange according to bending stress principle. This value is expected to diminish at positions higher than 30mm and closer to the top flange where the possible neutral axis is located. Also, central strain curve shows a distorted propagation suggesting possible fibre failures

which are not evident on the LHS and RHS strain plots. At this point, LHS and RHS strains are approximately 70% lower than the peak strain and without suggestions of any

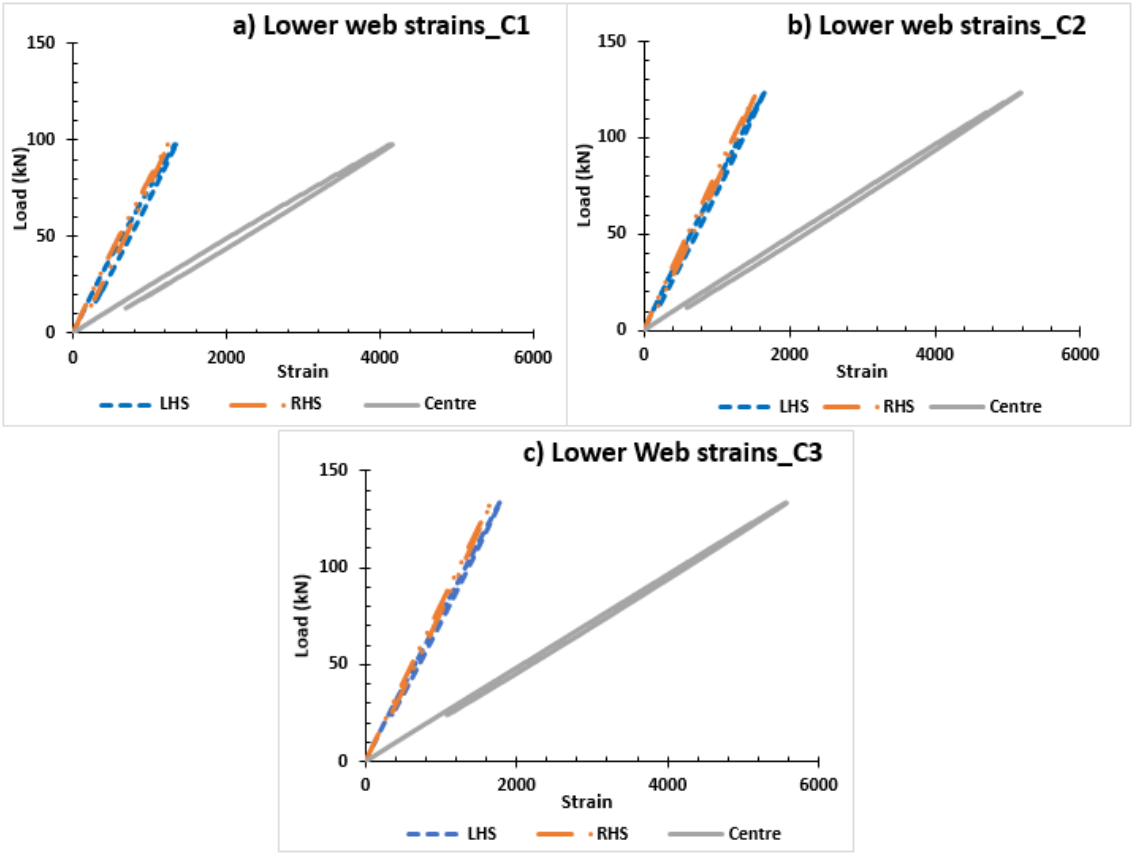

Figure 6.27: 30 mm depth mid-web strain response at cyclic loading

internal fibre failures (see Figure 6.30).

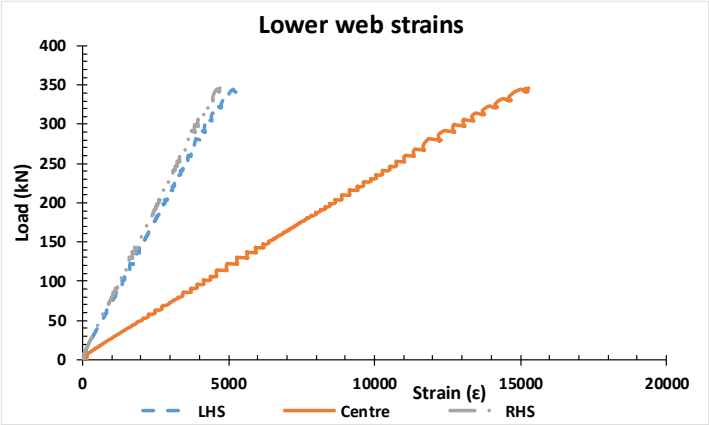

Figure 6.28: 30 mm depth mid-web strain response at ultimate loading

6.4.2.4 Concrete strain response

Cyclic load test: All three strain readings indicated compression stresses in the concrete as negative values were obtained for LHS, RHS and centre strains. In Figure 6.31, the centre strain recorded a maximum value of 613.1$\boldsymbol{\mu\varepsilon}$. However, the difference between the strain values on the LHS and RHS was not significant with a 0.07% difference but with significant 46% difference in strain values obtained at the centre. The strain values obtained at the LHS and RHS may suggest an even distribution of the applied load to the left and right span of the hybrid beam.

Ultimate load test: The entire concrete slab is in compression at a midspan maximum compression strain of 2199.1$\boldsymbol{\mu\varepsilon}$ to top layer of the concrete. The strain response is perfectly linear until failure but with a distorted curve suggesting concrete cracking which became visible at about 75% of the peak load (see Figure 6.32). The LHS peak strain is approximately 49% of the midspan peak strain. The peak midspan strain at ultimate is

about 66% higher than the average peak strains for C2 and C3. It is generally expected that peak strains will occur at midspan where the composite beam sustains its maximum deflection. It is possible to suggest that compressive modulus of the concrete slab contributes significantly to the flexural behaviour and capacity of the slab. However, further theoretical analysis will consider these contributions following the analytical approaches derived from literature.

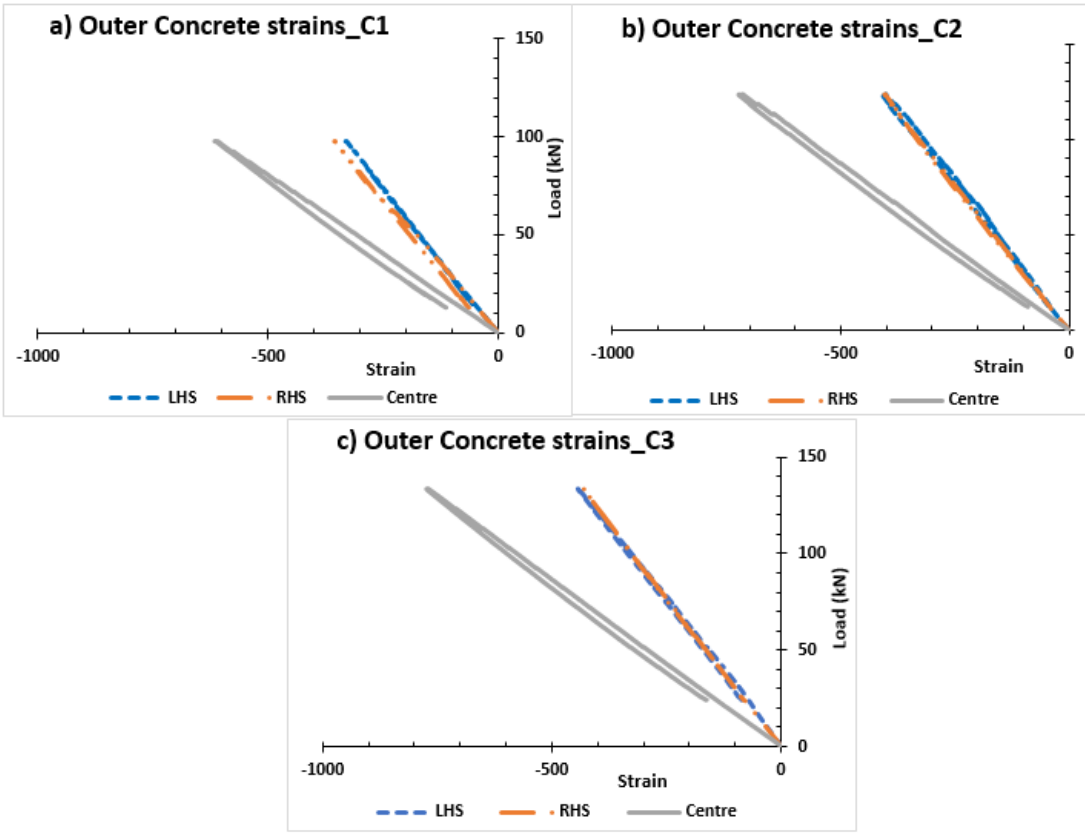

Figure 6.29: Concrete strain response at cyclic loading

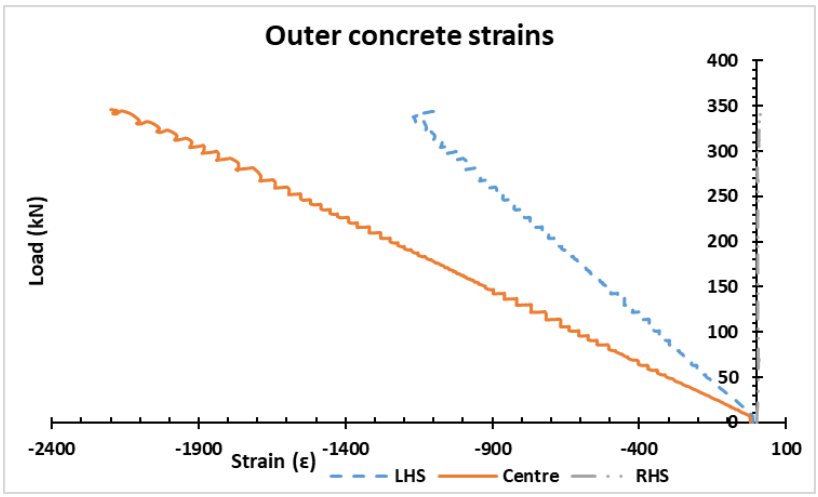

Figure 6.30:Concrete strain response at ultimate loading

6.4.2.5 Stud strain response

Cyclic load test: Initial strain response in the first cycle (C1) of loading shows significant higher strains in comparison the other cycles C2 and C3 for the LHS (see Figure 6.33). The compressive strains on the LHS suggest an uneven distribution of stress around the studs and the tensile strains on the RHS may be attributed to the dominant tensile influence of stud deformations. The peak values of stud strain L1 (582.6$\boldsymbol{\mu\varepsilon}$) and L2 (439$\boldsymbol{\mu\varepsilon}$) for C1 was about 61.2% and 78% higher than C2 strain values also, 44% and 77% higher than C3 strain values. The significant higher strains in the first cycle may be due mainly to the uneven debonding process occurring within the first cycle forces are redistributed within subsequent cycles to ensure an efficient performance of the beam. Hence, a significant drop in strain values showing possible redistribution of interfacial shear forces. The strain difference between L1 and L2 is consistent for all strain plots with C1 recording 25%. This illustrates the uneven influences concrete compressive forces on the pair of studs. Such uneven forces can develop localised stress concentrations around the stud which may compromise the integrity of the composite connection when the flexural loads are significantly increased. However, L1 strains for C2 and C3 appear to have been in tension suggesting a slip from compression strains to dominant tensile deformation strains.

The RHS strains for all three cycles titled towards the tensile zone of the strain plot suggesting some tensile deformations of the stud on the right arm of the composite beam. Stud R2 recorded significantly inconsistent lower strains indicating an almost negligible influence on the shear behaviour of the beam under serviceable loads. R1 strains were more consistent in C2 and C3 results respectively. R1 recorded a peak tensile strain of

191.7$\boldsymbol{\mu\varepsilon}$ which was approximately 46% higher than the strains for C2 and C3 at 103.8$\boldsymbol{\mu\varepsilon}$. Significant lower strains on the right arm of the composite beam are consistent with final failure observations as no longitudinal cracks were propagated on the RHS of the beam.

Ultimate load test: The load-strain plot for embedded studs shows a variation is response between the LHS and RHS suggesting possible concrete influences. The studs on the LHS of the midspan show compressive strains whereas the RHS studs show tensile deformations. Compressive strains on the studs reflect significant influences of concrete confinement forces on the stud necessitating full mobilisation of shear strength. Although there is a close resemblance in the pattern of strain propagation for the centrally configured studs, there is a significant variation in strain values (see Figure 6.34). L1 has a peak strain value of 931.7$\boldsymbol{\mu\varepsilon}$ approximately 57% of the strain value of L2 at 2173.1$\boldsymbol{\mu\varepsilon}$. R1 has a peak strain value of 120.2$\boldsymbol{\mu\varepsilon}$ which is approximately 75% of the peak strain of R2 at 472.8$\boldsymbol{\mu\varepsilon}$. LI and L2 have significantly higher compressive strains suggesting dominant compressive deformation of studs and increased compressive forces around the studs as observed from the compressive cracking of stud along the longitudinal row of studs. However, the values of L2 strains are consistent with parallel splitting failure observed on the beam where one of the longitudinal splitting crack was more severe than the other.

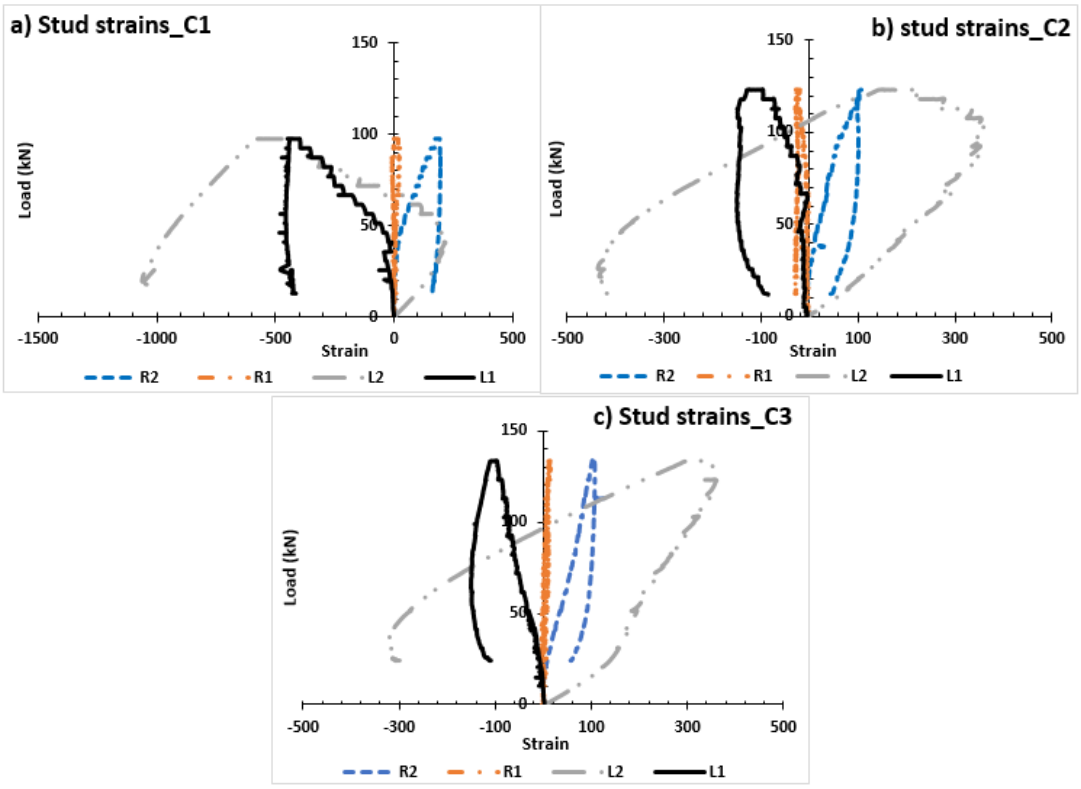

Figure 6.31: Stud strain response at cyclic loading

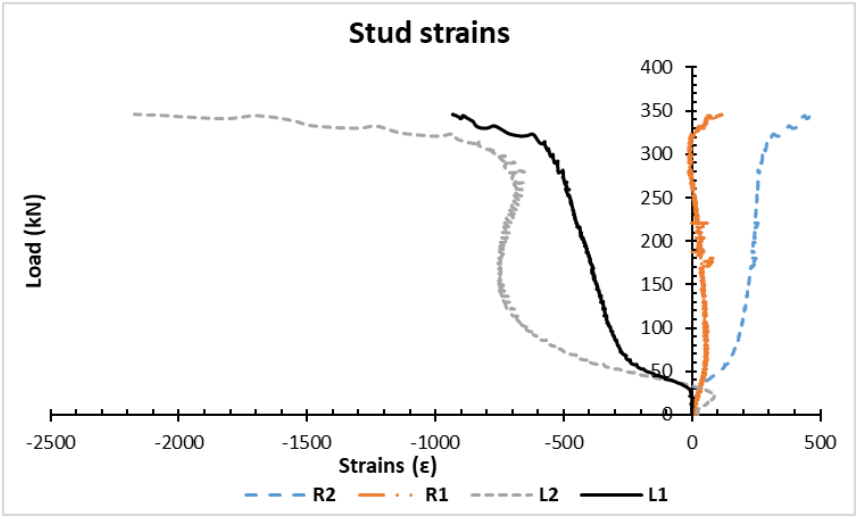

Figure 6.32:Stud strain response at ultimate loading

6.4.3 Crack Development & Failure of Hybrid Beam

The flexural deformation was characterised by concrete cracking and audible fibre failures. However, initial visible concrete cracking was observed during the second cycle of loading at about 65kN corresponding to approximately 8mm of deflection. This value is about 50% of the peak deflection value for the serviceable load. The initial cracks were less than 0.05mm in width and propagated from the bottom front elevation of the concrete slab vertically upwards to about one-third the height of the slab. The crack propagation was mostly visible on the left-hand-side (LHS) of the composite beam with subsequent cracks propagating mostly on the left at increasing loads 80kN, 100kN and 120kN respectively for the second and third cycles of loading (see Figure 6.35). Crack formations appear under control within the cyclic loading suggesting effective crack resistance from the square mesh formed from longitudinal and transverse reinforcement. The vertical crack development is observed at 38% of the peak load which is estimated as the serviceability limit. However, the cracks become more conspicuous with multiple cracks developing on both arms of the composite beam at approximately 60% of the peak load. Generally, the cracks recorded at the end of the test along the span of the beam do not appear significant as to compromise the integrity or behaviour of the composite beam even at ultimate loading.

Figure 6.33:Crack propagation on concrete slab

At 75% of the peak load parallel cracks are initiated longitudinally along the span of the composite beam at the top of the concrete slab (see Figure 6.36a). The longitudinal cracks are suggestive of increased localised stresses resulting from shear resistance interaction of the stud with concrete compressive forces. The parallel crack propagation is observed to occur along the length of the stud row arrangement (see Figure 6.36b). Due to the intensity of flexure, the interface between the concrete and GFRP subcomponents is subjected to severe longitudinal shear forces which are transferred to slabs. Hicks (2014) outlined the equilibrium model of the shear interaction between the subcomponents illustrating that the longitudinal shear, concrete compressive forces and transverse tensile forces from the rebar were at equilibrium during flexure. However, equilibrium will be

upturned if either force exceeded one another. Longitudinal splitting failure on the concrete suggest that effect of uneven localised stresses from concrete compressive forces, shear forces and possible transverse tensile forces. Such failures are further exacerbated if there are increased uplift forces over inclination forces of the shear stud. Hence, a combination of increased transfer of longitudinal shear forces and uplift reactions resulting from peak deflections of the beam. At ultimate design, the influence of these uplift reaction forces may be considered in addition to concrete compressive forces to effectively minimise the occurrence of such failures. Also, the observed failure mode suggests the modification of the standard push-out test in EC4 for conventional composite beams to account for the effect of concrete compressive forces against uplift reactions of stud from increased bending of the composite. Lowe et al. (2014) reported in his findings the longitudinal splitting of concrete along the line of studs observing a localised zone of transverse deformation around the stud in steel-concrete composite. Lowe suggested uneven stress distribution of concrete at the base of the stud combining large compressive stresses on one side of the stud and minor tensile stresses on the other. At a critical value of shear force transfer from the embedded studs in concrete, longitudinal concrete splitting begins to propagate along the line of studs throughout the span of the beam (Lowe et al., 2014 & 2020). Lowe et al. (2014) conclusions are somewhat in agreement with the current observation for GFRP-concrete composite suggesting uneven distribution of stresses around the stud and overturning of equilibrium conditions for the stud-concrete interactions for effective shear transfer between the subcomponents. Further examination of stud strain responses detailed in 6.5.2.5 suggest that unbalance influences of compression forces and tension forces at Midspan studs located to the left arm of the composite beam where the splitting failure occurred recorded

compressive strains while the left arm studs recorded tensile strains validating Lowe's hypothesis of uneven localised stresses around the stud. This can be validated from the peak strain value recorded at the top of the concrete at midspan corresponding to 2199$\boldsymbol{\mu\varepsilon}$ almost significantly equalling the peak strain recorded on the L2 of the stud at 2173.1$\boldsymbol{\mu\varepsilon}$.

Figure 6.34:Premature failure of slab

6.4.4 Strain Distribution Profile

A cross-sectional representation of the strain distribution shows a significant strain profile for a fully composite connection. The strain profile illustrates an approximate distribution of strain response for the composite beam under ultimate limit state at midspan (see Figure 6.37). The profile suggests a fully compressive behaviour (response) of the concrete slab and complete tensile response from the GFRP profile. The unified strain block diagram indicates practical composite action of the concrete and GFRP subcomponents in mobilising flexural strength. The concrete mobilises full compressive strength at a peak strain of 2199.1$\boldsymbol{\mu\varepsilon}$ and complete tensile strength at the bottom flange

(BF) with a peak strain of 18932.3$\boldsymbol{\mu\varepsilon}$. The peak strain of the bottom flange is approximately 88% higher than the peak compressive strain at the top of the concrete slab.

6.4.4.1 Cyclic strain profile

Strain responses from cyclic loading show significantly controlled strain behaviour emphasizing the stability of the composite beam under serviceable loads without any shear deterioration behaviour at the concrete-flange interface. Compressive strain values of 715 $\boldsymbol{\mu\varepsilon}$ and 771$\boldsymbol{\mu\varepsilon}$ are significantly sustained within the last two cycles. At the concrete-GFRP flange interface, a sudden drop in compressive strain from 327.5 $\boldsymbol{\mu\varepsilon}$ for C1 to 62.2 $\boldsymbol{\mu\varepsilon}$ and 59.5 $\boldsymbol{\mu\varepsilon}$ for C2 and C3 is observed respectively. This sudden drop in strain corresponds to approximately 20% decrease in strain for from C1 suggesting possible debonding of concrete from flange at the slip interface (see Table 6.3). In C2 and C3, the strains at the concrete-GFRP flange interface are significantly lower in comparison to the general strain distribution of the beam. Also, the strain at the interface during cyclic loading are significantly lower than the centrally measured strain confirming stud composite action. However, due to increase bending at midspan, the interfacial strain significantly increases due to higher concrete compression forces at ultimate loading. Generally, the strain increases laterally across all cycles including the ultimate loading and the reduces vertically from the top and bottom towards the neutral axis of the composite beam section (see Figure 6.38). Table 6.10 summarises the percentage strain difference of the three cycles against the peak strain to elaborate the significant strain changes along the depth of the composite beam section. Although, no physical cracks or failures were observed on the FRP; the strain distribution may suggest some internal fibre

failures at approximately 70% of the peak load. Ultimate design loads may be factored by an approximate value of 1.4 to establish a 25-30% reserve ultimate capacity against failure.

Table 6.10: Percentage strain distribution

Beam depth (mm)	Percentage strain (%)			Remarks
	C1	***C2***	***C3***	
320	27.9	32.5	35.1	Increased strain across load cycles
200	24.2	4.6	4.4	Initial higher strains at C1 suggesting interfacial concrete-GFRP flange debonding.
190	41.3	-	-	Transitional strain
160	10.1	22.8	24.5	Increased strain across load cycles
100	18.5	26.2	27.9	Increased strain across load cycles
40	27.3	33.8	36.4	Increased strain across load cycles
0	27.2	32.4	34.8	Increased strain across load cycles

6.4.4.2 Ultimate strain profile

The incremental strain distribution shown in Figure 6.38 illustrates the strain development from initial loading at ultimate until failure of the section. The strain propagation remains constant in its distribution throughout the depth of the composite section. The entire slap depth of 120mm remains in compression from initial loading until failure with peak yields at the top layer of the slab and bottom flange fibre of the GFRP section in corroboration with elastic theory of materials. The strain distribution profile for the composite section corresponding to a 20kN incremental loading until failure shows a nearly linear distribution within the tensile zone indicating that the entire tensile stress in borne by the

GFRP profile section. Due to some positioning difficulty of the strain gauges, the neutral axis appears to exist within the top flange of the GFRP section as concrete slab, as the interface (outer top flange) strain remains completely in compression. However, the inner face of the top flange transitions from compression to tension at a load beyond 160kN until failure. The profile web and bottom flange emerge in tension showing a nearly linear response to increased loading. A simplified illustration of the strain distribution profile at 25%, 50%, 75% and peak loading is represented in Figure 6.39 below.

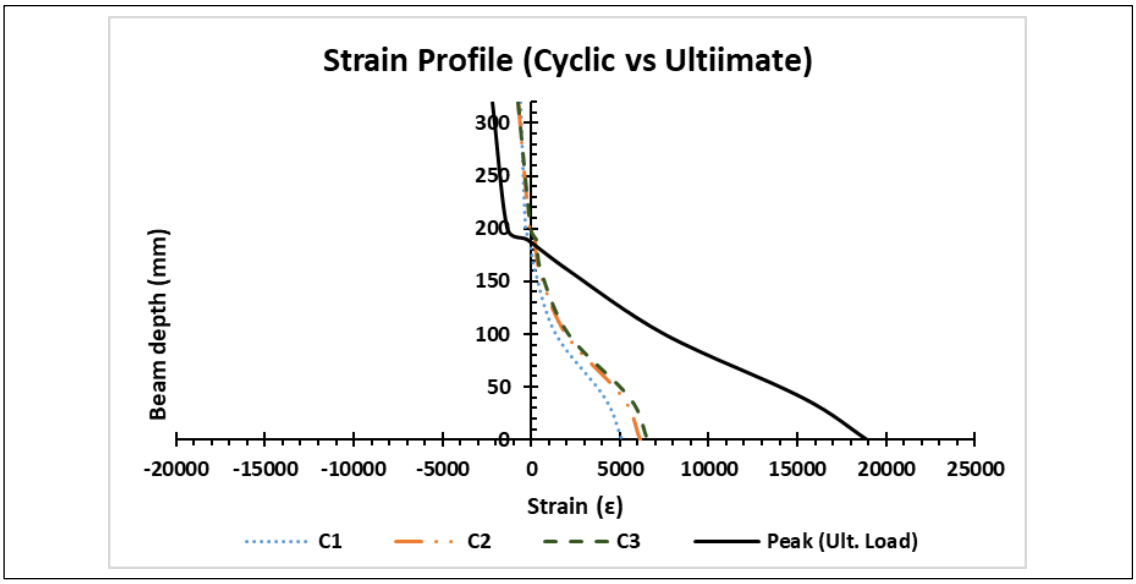

Figure 6.35: Cyclic vs ultimate strain distribution

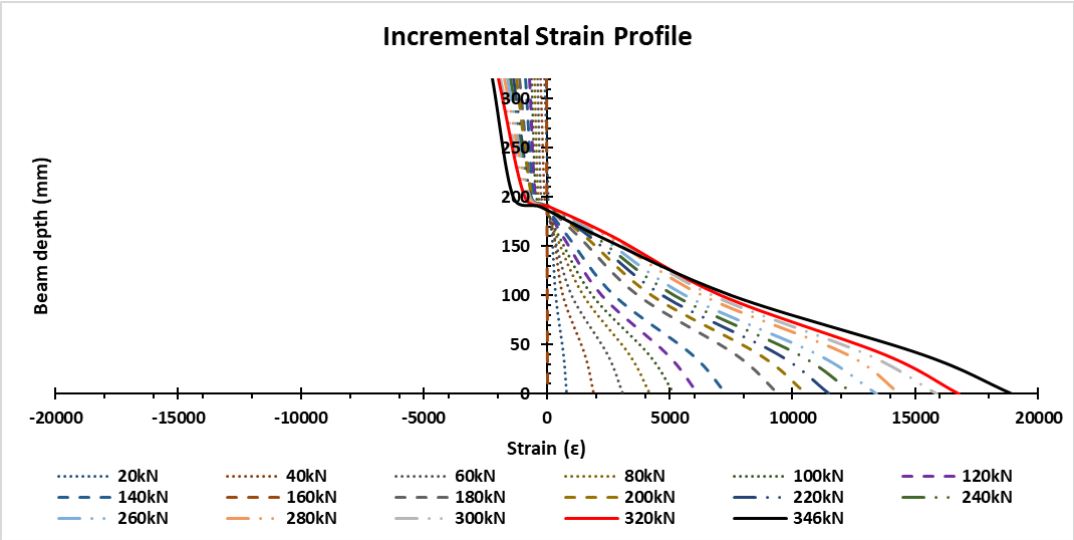

Figure 6.37:Incremental Strain Profile

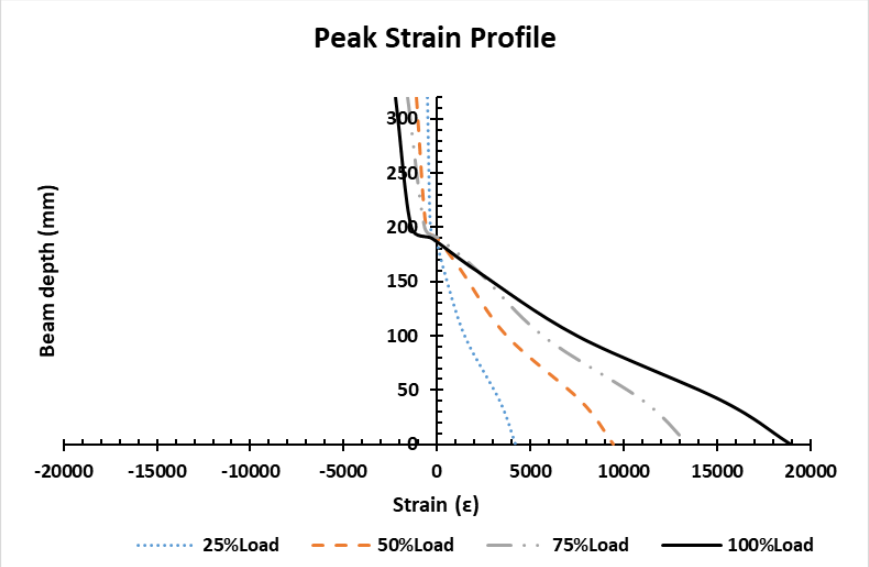

Figure 6.36:Strain distribution at ultimate loading

CHAPTER 7. DISCUSSION AND CALIBRATION OF RESULTS

7.1 Interfacial Shear Performance

Interfacial slip is a typical phenomenon in conventional composite members subjected to bending hence, shear studs are required to resist lateral shear forces which may induce out-of-plane behaviour in beams. Therefore, shear connections established in composites must be determined and tested to ensure satisfactory performance. Standard test methods informed by Eurocode 4 (EC4) are adopted for experimental characterisation of lateral shear performance (see previous sections 6.4) and to further explore numerical calibrations.

7.1.1 FE Calibration of Shear behaviour

The lateral slip characterised through push out experimental testing is observed in the FE model shown Figure 7.1. The lateral slip demonstrated by the beam is 2.16 mm at an ultimate lateral shear load of 30kN/stud. This slip value represents about 17 % of the peak slip for the LWAC specimen suggesting that no deformation has occurred as observed in both FE and experimental test. Although Figure 7.5 shows the initiation of curvature stresses however, the curvature deformation is not conspicuous both in experimental and FE beam. The push-out characterisation phases of experimental testing validates the FE results and corroborates the selection appropriateness of the stud arrangement for the hybrid composite beam modelling.

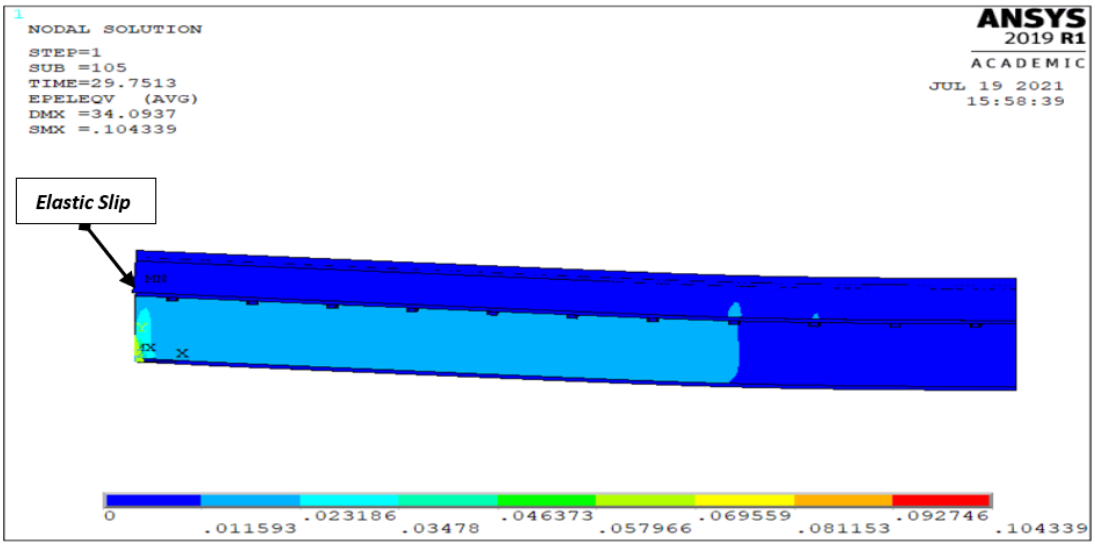

Figure 7.1:Lateral shear movement

7.1.2 Lateral shear strength

Experimental results show an increase in shear capacity following increase in stud sizes. This indicates that the shear stud size influences the shear capacity of the connection; therefore, larger sizes, with respect to the stud shank diameter will typically resist higher shear loads. The standard equation from EC4 for possible stud fracture can be supported based on experimental results. It therefore emphasizes the role of stud geometry in influencing shear capacity of composites. This forms a common composite behaviour for all types of composite connections including FRP-concrete composites. Influences on shear capacity for FRP-concrete composites go beyond stud geometrical factors as dominant flange bearing failures characterise the shear behaviour of these hybrid composites. However, an inconsistent peak capacity is observed between specimens 4 and 5, with 12 mm shear stud, this may be due to the uneven distribution of concrete within the slab also suggesting the concrete curing process as an influence on composite

behaviour. The shear strength of the connection can be derived from a critical value either due to concrete failure or stud fracture (where the concrete has sufficient strength to enhance the mobilization of stud capacity, Dai *et al*. (2015) for steel-concrete connection whereas, the critical value for shear resistance in an FRP-concrete may be assumed from a dominant bearing failure mode. At ultimate loading, the connection may have failed already due to the brittle nature of the FRP material. This clearly shows the influence of FRP mechanical properties in determining the shear resistance of FRP-concrete connections as suggested by Nguyen et al. (2014). Therefore, for an FRP material with higher strength properties, there will be a direct increase in shear capacity. The embedment depth of 100 mm was adopted to ensure an increase in shear capacity, as results are comparable to that reported by Nguyen (2014), which showed that high embedment depths up to 50 mm enhanced shear capacity when compared to lower depths of 35 mm.

Table 7.1: Theoretical comparison to experimental results (Double row or eight row configuration)

Specimen ID	**Experimental Strength per stud, P_{Exp} (kN)**	**Theoretical Strength per stud, P_{EC4} (kN)**	**Theoretical Strength per Stud, P_{OJ} (kN)**	**P_{Exp}/ P_{EC4}**	**P_{Exp}/ P_{OJ}**
PO-12B-S4	41.63	34.04	29.56	1.22	1.41
PO-12B-S5	48.13	33.68	29.34	1.42	1.64
PO-16B-S6	53.84	56.61	50.05	0.95	1.08
PO-19B-S7	69.0	92.10	98.43	0.75	0.70

In Table 7.1, the theoretical predictions, according to Eqs. (1), (2) and (3) are compared against experimental results. Theoretical predictions for 12 mm stud are between 22 - 42% lower than the experimental result according to Eq. (2) of EC4 which provided the smaller value compared to Eq. (1). Using Eq. (3), according to Oehlers & Johnson (1996) predicted between 41 – 64% lower values for shear strength against experimental results. Theoretical predictions for 16 mm bolt provided the closest of 5% higher value and an 8% lower value against experimental result for Eqs. (2) and (3), respectively. Lower values of 25% and 30% are predicted according to Eqs. (1) and (3) for 19 mm bolts. The consistent higher variability in results according to Eq. (3) is mostly due to the boundary conditions provided by the equation in which the girder influence is nullified and assumed rigid. This consideration does not, however, reflect the failure behaviour of our specimens and therefore suggest a stud fracture and concrete pull-out failure. The EC4 predictions were closest to experimental results and suggests a higher influence of concrete properties towards failure. This was observed in section 6.4.3 where the strain on the stud increased due to compression forces toward the stud cap. This behaviour suggested cracking failure in the concrete area around the stud cap. The 19 mm studs were observed to be more rigid during testing and provided little or no deformation with the dominant failure seen to be bearing and tensile tear out. The non-conformity of the equation obtained from EC4 towards the present study suggest the consideration of Nguyen's (2014) modified equation for strength prediction. Stud sizes of 12 mm and 16 mm showed higher levels of disparity from about 22% to 42% confirming the insufficiency of the equation to be adapted towards FRP-concrete composites.

The shear strength for the connections is quite significant in determining their capacity against horizontal interfacial slip. Experiments from all three phases has confirmed that

shear capacity is a function of cross-sectional sizes and configuration of studs. Studs embedded in LWAC can attain similar shear capacities as their NWC embedded counterparts. This reaffirms the reported findings on concrete compressive strength as the most important variable in enhancing shear capacities of concrete composites connections. When collar modifications are provided, shear capacity is reduced by about 25%. This strength reduction is similar the percentage reduction in strength observed in the use of welded steel studs for steel-concrete composites. For shear capacities to be fully mobilised, the shear studs should possess free shank areas (collarless shanks) in their embedment in concrete.

7.1.2.1 Steel-concrete Comparison

The obtained experimental test results on shear capacity from this study can be compared to results of steel-concrete push-outs reported in the literature. However, differences in shear capacity between results of this study and that reported by researchers in Table 4.4 may be further elaborated following the variations in the test conditions such as variations in concrete geometry, concrete properties, stud strength, test modifications and steel flanges. GFRP-concrete composites significantly provide a comparative performance with shear capacities of about 40-50 % that of steel-concrete counterparts.

Table 7.2: Shear strength per stud comparison.

Stud Dia.	***GFRP-concrete push-outs (kN)***		***Steel-concrete push-outs (kN)***				
(mm)	***Exp. test results***	***Nguyen et al. [2014]***	***Ollgaard et al. [1971]***	***Prakash et al., [2012]***	***Odenbreit & Nellinger [2017]***	***An and Cederwall [1996]***	***Rehman et al., [2016]***
16	54	103	89	-	-	-	80

19	69	-	137	-	52	120	-
20	-	-	-	132	-	-	66

7.1.3 Connection stiffness and ductility

The shear stiffness of the connection between Specimen PO-12B-S4 and PO-12B-S5 shows a 35% difference in stiffness with specimen PO-12B-S5 having higher stiffness. This may be due to an initial slip during loading on specimen one owing to the bearing of the stud against the clearance hole on the FRP flange. This early slip caused a major difference in stiffness and can be attributed to a difference in torque applied to the stud. Specimen 5 provides a closer stiffness to specimen 6 with a difference of 14% lower stiffness to specimen 6 of 110 kN/mm stiffness as both curve profiles are not smooth, showing a zigzag profile. However, this clearly shows that if concrete compressive strength is high with consistent curing, the stud stiffness for a 12 mm and 16 mm stud is almost insignificantly similar. Stud stiffness may be mobilised from proper concrete curing with high compressive strength. Specimen PO-SG-S2, phase I exhibited a significant shear stiffness (of about 117% and 39% for specimen PO-SG-S1 and PO-SG-S2, respectively) due to observed load redistribution among the studs during experimental testing. At peak loads, an average slip up to 8 mm can be achieved with 12 mm and 16 mm studs, which satisfy the ductility requirement specified in EC4. The measured longitudinal depth of 4.5 mm for bearing failure shows the contribution of the FRP flange delamination in forming a pseudo-ductile slip, which clearly distinguishes the ductility of GFRP-concrete from the typical ductile behaviour for a steel-concrete composite.

Shear stiffness of composite connections are required in determining the rate of slip response against shear forces. High values of shear stiffness reflect lower slip values as with bolted connections, stiffness values are dependent on a number of factor including stud size, spacing and material strengths. Shear stiffness values are considerably lower in LWAC specimens when compared to their NWC counterparts with estimated lower values up to 49%. However, research study on the comparative performance of NWC and LWAC for steel-concrete composites by Ollgaard et al. (1971) had reported that no significant changes in the load-slip pattern for LWAC and NWC specimens are observed. Stiffness of connections was inconsistent in all test experiments mostly owing to the nonlinearity of the GFRP material and the general variability in its properties across its geometry in all directions. The modified stud with collar recorded a significant strength increase of 39% over the unmodified stud (collarless stud).

The shear slips obtained from FRP-concrete interaction are characterised by combined stud deformations and fibre bearing failures. This sort of slip is recently reported to be pseudo-ductile (Etim et al., 2020). Therefore, slip values are obtained from linear transitional loads of PO-12B$_m$-LS (190kN) and PO-12B-LS (267kN) with corresponding values of 4 mm and 7.8 mm, respectively.

7.2 Flexural strength and deflection

7.2.1 FE Calibration of hybrid beam

Maximum principal stresses develop at the support due to reactions and proliferate towards the centre of the beam (see Figure 7.2 a & b). These stresses anticipated during the experimental testing were prevented using C-shaped steel stiffeners to avoid premature flange/web buckling. The maximum deflection conducted on FE was limited

to 34mm due to limitations of memory storage, computational time and physics. The associated maximum load recorded was 326kN corresponding to approximately 17% higher load value of the experimental result at similar deflection value. This percentage increase is expected following the intricacies of laboratory formulation of concrete which necessitates nonlinearities resulting from curing such as air void and particle distribution including reinforcement workmanship.

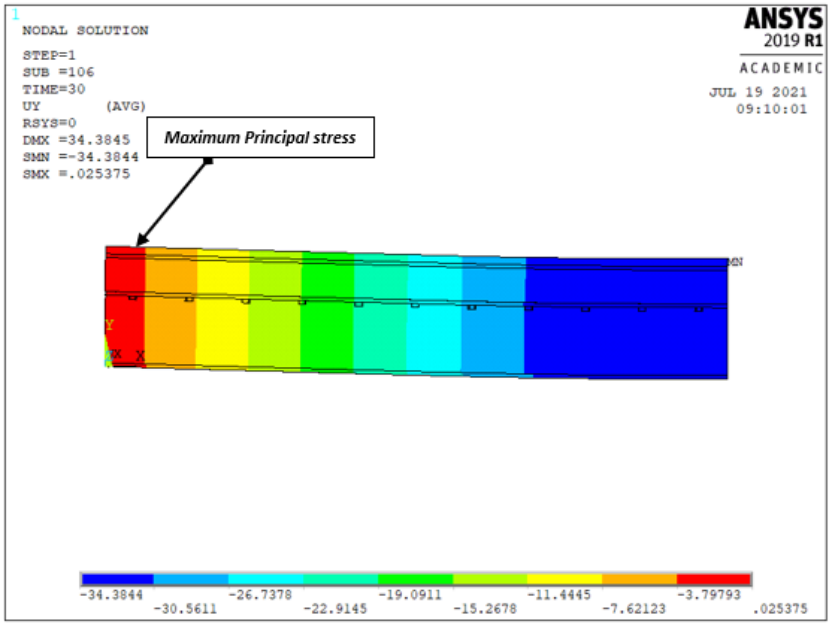

a) Principal stresses at Support

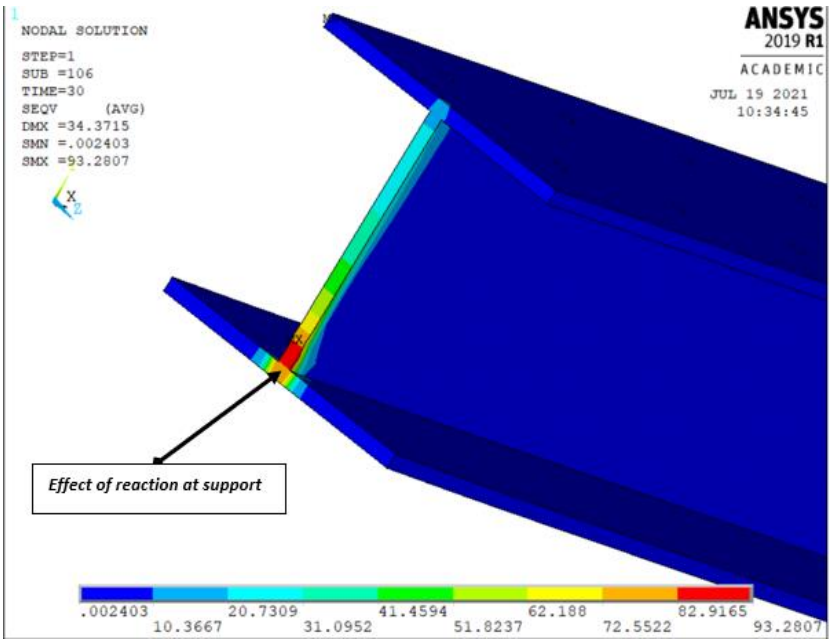

b) Effect of reaction at support

Figure 7.2:Loading effects at support

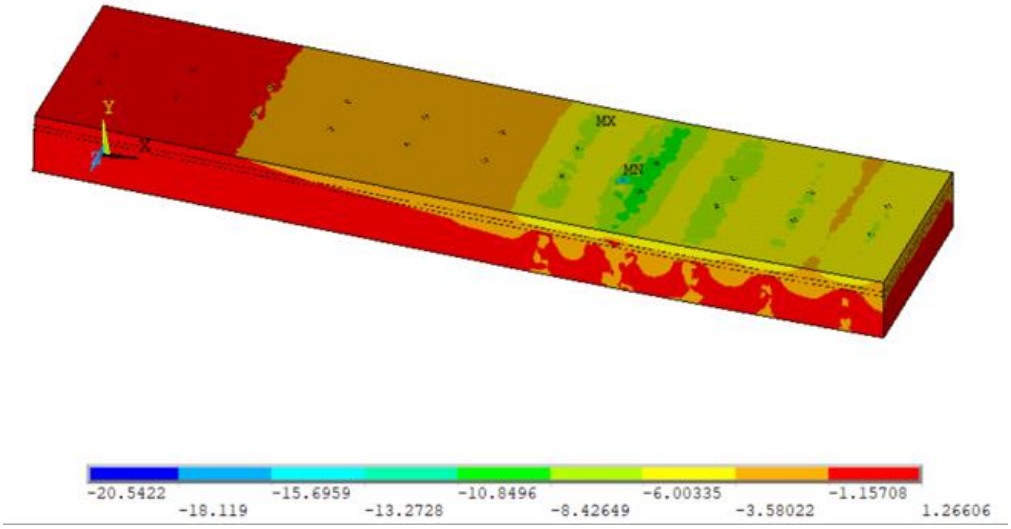

Figure 7.3:Stress distribution on the concrete slab

Compression stresses are observed in the concrete with minimum values observed towards the top area of the central bolts whereas significant stresses up to 1.157MPa are propagated at the shear interface of the bottom concrete upward towards the top corner at the support (see Figure 7.3). The maximum stress at 34mm deflection represent about 3% of the peak compressive stress of the concrete hence, suggesting no failures of concrete failures as observed in the experimental test. However, reported concrete failures where due to splitting tensile effect initiated by the studs (see section 6.5.5). Such premature failures are unlikely in the case of the FE model as it experimental testing was subject upon material formulation defects during concrete preparation and curing.

Concrete cracks observed in experimental testing earlier reported in section 6.4.3 are corroborated on the FE model (see Figure 7.4a). The cracks are significant towards the centre of the beam at area closely located under the point of load application and almost sparsely distributed from one another (see Figure 7.4b). Similarly, cracks were propagated from the bottom of the concrete slabs upwards due to the bending effect on the concrete slab as expected from theoretical principles of sections subjected to bending. These cracks may indicate possible tensile effects at the interface of the composite which are exacerbated by bending effects. These tension effects are more closely associated with the stud strength mobilisation resulting in cracks around the concrete area surrounding the centrally embedded bolts of the FE model whereas such was observed in the experimental specimen which later resulted in premature splitting tensile failures of the concrete slab.

No visible stud deformation was observed either from experimental specimen or numerical models (as shown in Figure 7.5). However, von mises stresses indicate possible hinge formation for single curvature deformation on the central bolts. These stresses become severe due to increase bending of the beam and strength mobilisation of the bolt around the concrete and such failures point towards improvement of concrete confinement strength. The entire hybrid beam illustrates a strain distribution profile similar to earlier profile reported in the experimental test in section 6.5.6. The FE strain profile was taken at peak FE load and 50% of the peak experimental loads respectively. The profile highlights full composite action of the FE model illustrating compression actions in concrete and tensile actions in GFRP with maximum values at top and bottom

fibres of concrete and GFRP respectively (see Figure 7.6). The FE strain distribution at 170kN (at 50% of experimental peak) compared against experimental profiles at 160kN and 180kN exhibit a propagation with values closely corroborating experimental test results. Figure 7.7 shows a significant correlation between the plots for FE and experimental results.

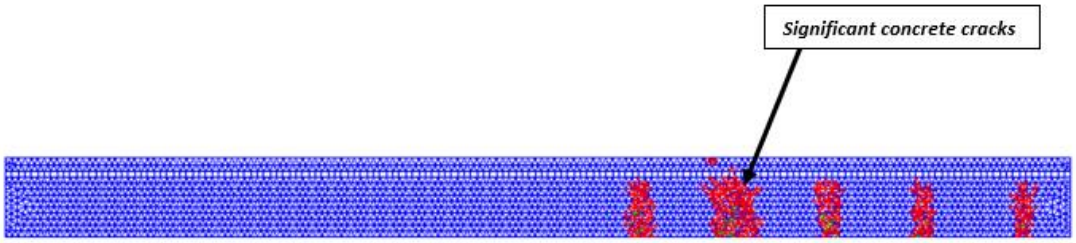

a) Crack failure on concrete (FE Model)

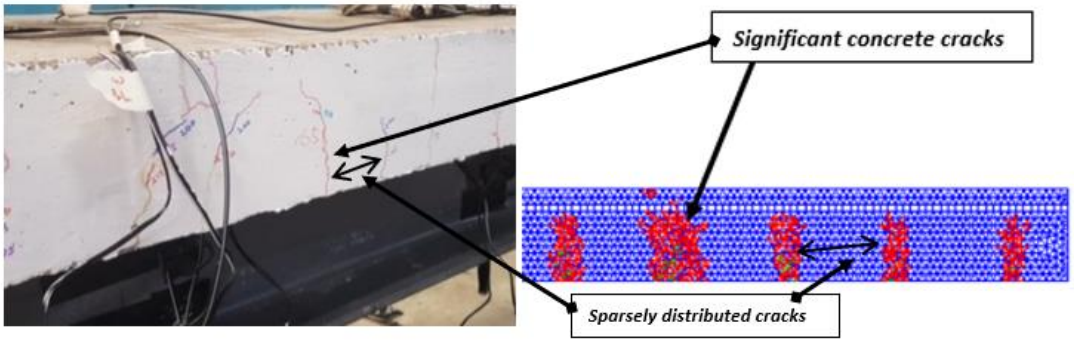

b) Crack comparison between FE & Experimental Models

Figure 7.4: Cracking failures in concrete

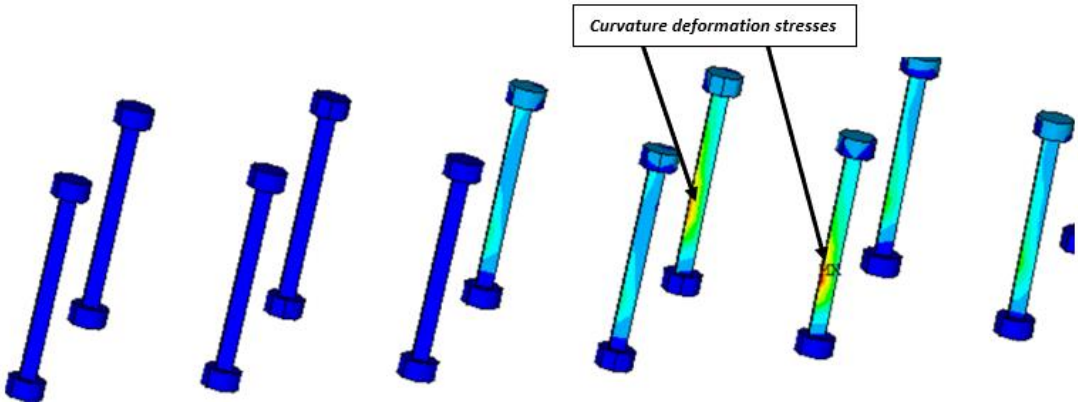

Figure 7.5: Stresses in studs

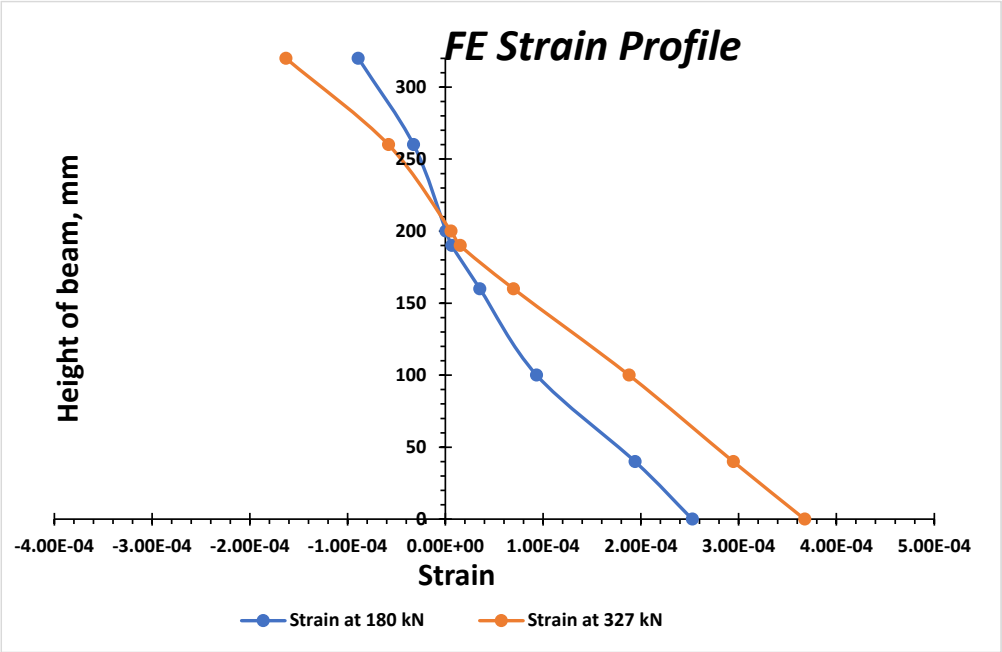

Figure 7.6: Strain distribution profile

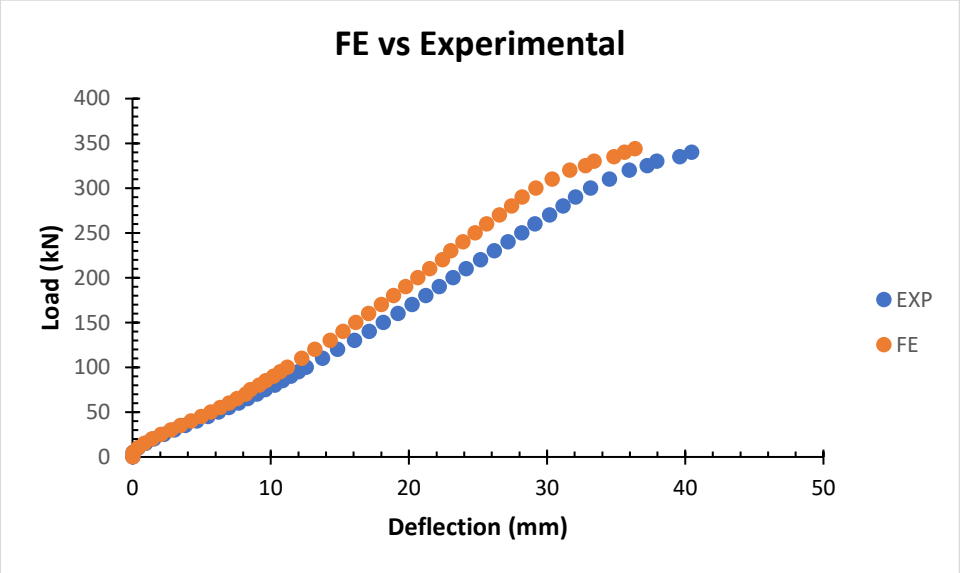

Figure 7.7: Comparative plot (FE vs Experimental)

7.2.2 Experimental Overview of flexural behaviour

The flexural capacity of the beam slowly increases over the cycles at a similar measured deflection. Flexural capacity is a requirement for horizontal members and even a major component of improvement for composite beams. The flexural behaviour is a characteristic feature determined by the associated deflection of a member in response to loading. This performance characteristic is required under serviceability and ultimate limit design of structures. The characteristic flexural strength of the beam at three cycles were 97.7kN, 123.5kN and 133.5kN respectively. The percentage load capacities against the ultimate strength of the beam was 28.2%, 35.6% and 38.5% corresponding to C1, C2 and C3 respectively. A significant increase between the various cycles are; 20.9% increase between C1 and C2. A corresponding smaller difference of 7.5% between C2 and C3 load capacities. This was also observed for deflections within cycles, the

maximum serviceable deflection within the cycles obtained are 14.5mm, 13.5mm and 13.6mm for C1, C2 and C3 respectively. The deflection values corresponded to the 33%, 30.7% and 30.9% of the deflection capacity at ultimate load. There was a corresponding relationship between flexural capacity and deflection. Within various cycles, there was an increase in flexural capacity under the same range of deflection values. However, the significant differences were only observed in cycle 1 (C1) against the other two cycles (C2 & C3). C1 produced approximately 2% higher deflection capacity than C2 and C3, which had no significant difference in their corresponding deflections. The results obtained reaffirms the suggestion that shear action in cycle 1 (C1) was mostly achieved through concrete-GFRP interface bond action which was eventually lost from the cyclic loading process. Consistency in the results between C2 and C3 also emphasizes the full influence of the shear studs in ensuring shear resistance of the composite while mobilizing full composite action for flexural performance. Data consistency is an important feature of repeatability emphasizing the close estimations of possible behaviours of system(s). The cyclic repetition of load-deflection curves obtained in C2 and C3 represent closely the serviceability behaviour of the system, which is an important component in its design consideration. At a pre-determined deflection value of approximately 14mm, the load capacity of the material may increase due to the mobilisation of flexural stiffness by the composite section, which defines the ability of the section to attain the safety requirement for structures under deflection. Strain development in concrete-GFRP hybrid beams are progressively linear depicting general tensile strain response to flexural loading (see Figure 7.7). Deflection-strain response suggests early fibre tensile weakening within the cyclic loading at 10 – 15 mm deflection and possible redistribution of strain easing inner fibre failures at 20 – 25mm deflection. Beyond 25mm deflection, possible inner fibre

failures are repeated and progressively increased at higher micro-strains above 10000$\boldsymbol{\mu\varepsilon}$ until failure of the hybrid composite section.

At ultimate loading, the peak flexural load was recorded as 346kN corresponding to approximately 60-65% significant increase from the serviceable loads. For safe practice, the design load factored load is estimated to be about 75% of the ultimate load providing 25% flexural reserve capacity for the composite beam. The designed load at 75% of the peak flexural load will correspond to a deflection of 29.16mm, about 66% of the peak deflection at failure. The values recorded from the experimental testing corroborates with reported values from literature on GFRP-concrete hybrid beams and compares significantly against their steel-concrete counterparts. It is quite challenging to make parallel comparisons with reported values from literature due to multivariate parameters that influence the strength performance of the beam such as beam span-depth ratio, concrete compressive strength, concrete reinforcement, stud sizes and arrangements, material linearity and geometric imperfections etc. However, comparisons can be drawn

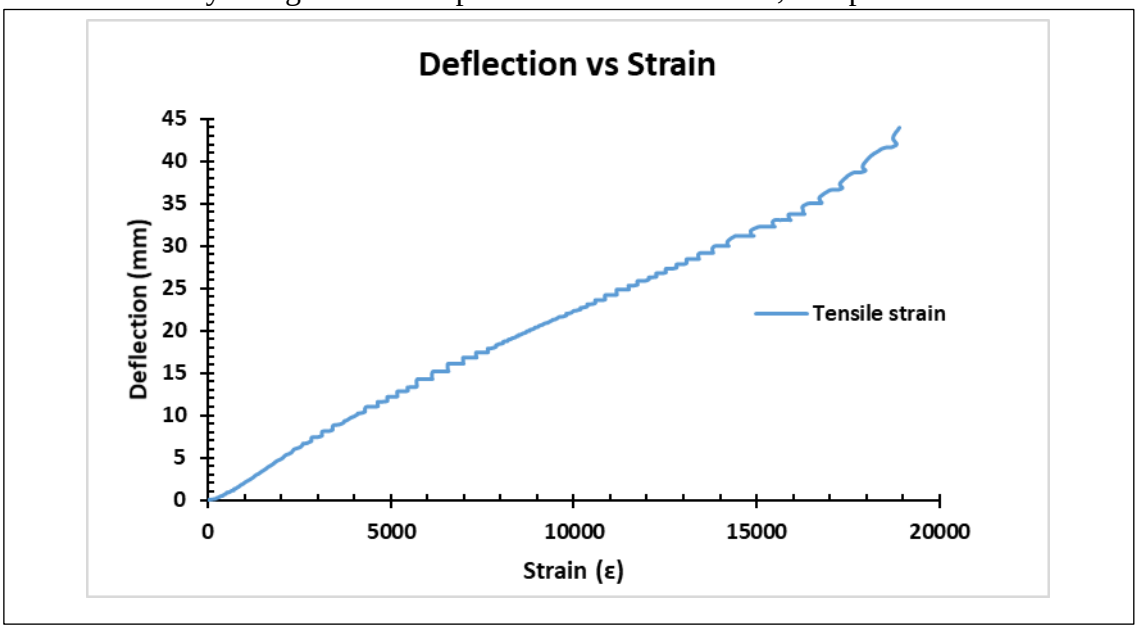

Figure 7.8: Deflection-strain plot

from simplified variables outlining the deviation of reported experimental test of composites from literature. Such variables include span/depth (L/d) ratio, width/span (b/L) ratio, width/depth ratio (b/d) and flange thickness/flange width (h_p/b_f) ratio respectively. Hence, the current study compares significantly with reported experimental values; about 1.9 times higher flexural capacity than the value reported by Correia et al. (2007) for GFRP-concrete hybrid beams (see Table 7.3). Variations in reported values can be attributed to the increase composite beam span resulting in higher deflection of about 54% and corresponding reduced flexural capacity of 47%. It may be observed that flexural capacity of GFRP-concrete beams compares significantly with reported values of steel-concrete composites however results vary due to major influences of span/depth ratio and width/depth ratio respectively. Similar span/depth ratio of steel-concrete composites may result closely in deflections within similar limit for GFRP-concrete beams provided their width/depth ratios are kept low. At a span/depth ratio of 11.11 and width/depth ratio of 3.3 for steel-concrete composite reported by Zhang et al. (2020), the flexural capacity difference is approximately 12.6%.

Table 7.3: Result comparison with Literature findings

Authors	***Span Length (mm)***	***L/d***	***b/L***	***b/d***	h_p/b_f	***Load (kN)***	***Moment Capacity (kNm)***	***Deflection (mm)***	***Failure mode***
Current study	3300	10.3	0.12	1.25	-	346*	190.3	44.01*	Longitudinal splitting of concrete
Chapman & Balakrishnan (1964)	5490	12	0.22	2.67	-	468	-	70mm	Slab crushing and stud failure
Correia et al. (2007)	4000	13.3	0.1	1.33	-	182*	120	95*	Compressive cracking of concrete layer and intralaminar shear of the FRP profile.
Suwaed & Karavasilis (2020)	8500	14	0.14	2.06	-	999	1259	275	-
Nie et al. (2014)	4000	12.9	0.2	2.58	-	208.1	145.7	65	Longitudinal cracking of concrete
Zhang et al. (2020)	4000	11.11	0.3	3.33	-	396.1	257.43	43.04	Longitudinal shear failure of concrete
Nguyen et al. (2013)	3000	10	0.05	0.45	-	438*	-	72*	-

7.2.3 Moment capacity and Stiffness

The moment capacity of the beam was determined from the transposed flexural load applied on the beam. The moment capacity is plotted against the bottom flange strain of the hybrid beam to illustrate the fibre deformation derived from the composite section's capacity. The peak midspan moment of 190kNm for the composite section is comparable to the value reported by Correia et al. (2007) for similar GFRP-concrete hybrid beam of higher span to depth ratio. The value is 37% higher than the value of 120kNm reported by Correia (2007). However, a comparison of the moment capacity of the presently developed hybrid beam against their steel-concrete counterpart shows that GFRP-concrete hybrid sections can attain up to 70% of their steel-concrete counterpart under the similar geometrical size and tolerance. The behaviour of composite beams are similar to steel-concrete composites providing linear compressive and tensile strains at the top and bottom of the composite respectively. The study observes a proportional linear strain development between the outer layers of the concrete slab and GFRP bottom flange in response to incremental moment until failure (see Figure 7.9). The top concrete slab records approximately 12% proportional strain of the peak bottom strain as the moment of the composite section increases. Such proportional relationship confirms the independent influence of the subcomponent's elastic modulus on their collective flexural rigidity. Hence, this suggest mathematically that the combined flexural stiffness of the hybrid composite section can be expressed as a ratio of the elastic modulus of one component to the other as applicable for all composite sections and demonstrated in chapter 6.

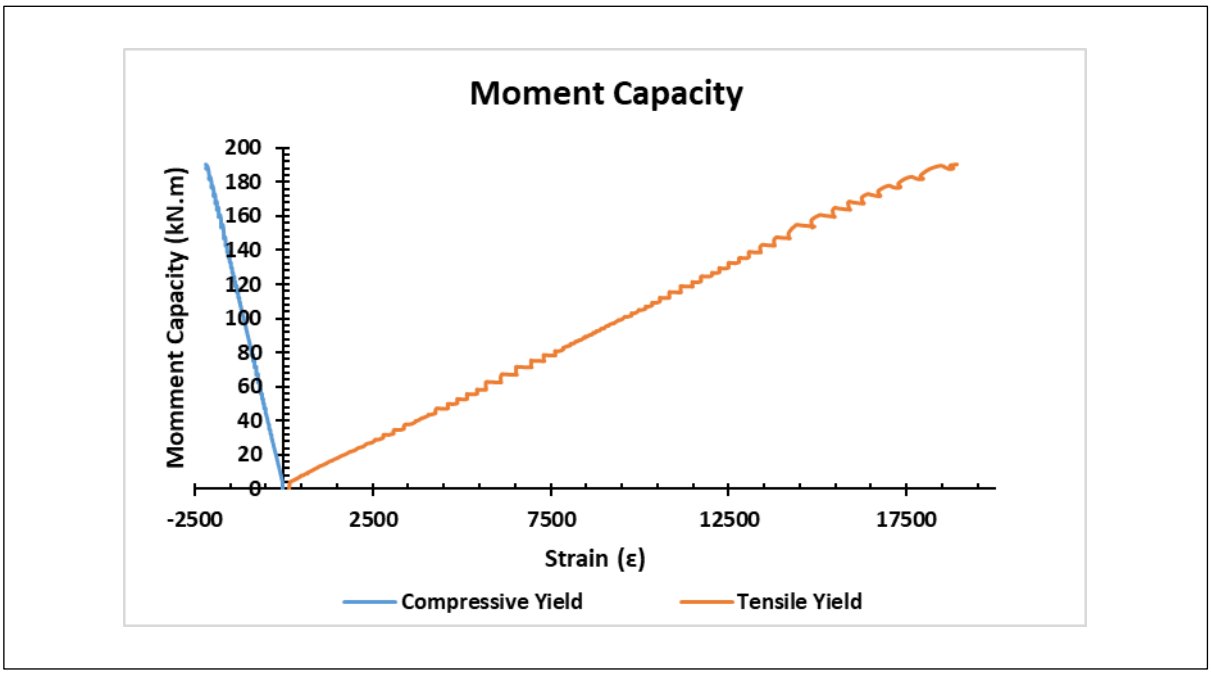

Figure 7.9:Moment capacity of components

CHAPTER 8. CONCLUSION, LIMITATION & RECOMMENDATION

8.1 General

GFRP structural sections offer sustainable solutions to challenging construction problems therefore, become relevant as alternative materials for structural composite frameworks including novel composite beams owing to their significant characteristics which can compensate for the weight challenges of conventional steel while sustaining the required mechanical performance of the novel structural composites. This section provides a summary of the study approach in determining the potential benefits of GFRP-concrete composites in providing sustainable solution to traditional construction practices.

8.1.1 Literature Findings

This research study began exploring relevant literature to build understanding on the nature of the traditional composite beams involving concrete and steel with further development of the novel composite connections to determine appropriate modelling for the novel composite beam. Literature findings provided the underpinning principle for the design and fabrication of the novel composite connection between GFRP and LWAC with emphasis on the characterisation for its interfacial shear connection. Findings were not limited to GFRP but considered structural steel as its counterpart to formulate knowledge and establish guiding principles for experimental development of the study.

8.1.2 Experimental Fabrications

Pilot test conducted on GFRP-NWC composite outlined the preliminary results on which the basic principles governing shear behaviour was established. Further test on GFRP-

LWAC composites were characterised to establish reliability of propounded findings and compared against baseline results for consistency in line with the limited research publications on GFRP structural composites. Hence, shear characterisation of the GFRP-LWAC composite connection informed the development of the fully fabricated novel GFRP-LWAC composite beam.

8.1.3 Numerical Modelling:

To promote material conservation and curb waste in experimental testing, numerical models for the novel hybrid beam were developed. Advantages of adopting numerical methods in carrying out research investigations are highlighted in sections 5.1 hence, cannot be overemphasized. The FE model reported on concrete cracking, elastic slip, deflection, and overall moment capacity of the novel hybrid beams. Some of the conclusions accounted from results, analysis and discussions are presented in sections below.

8.2 Interfacial Shear Performance

Pilot test results and analysis established a trend of influences consistent with traditional composite connections involving demountable shear studs though with deviations in the interfacial shear failure propagations. Load capacity curves for interfacial shear connections in GFRP are generally similar in propagation to that of steel-concrete counterparts despite the clear differences in material behaviour for both profiles (i.e. steel and GFRP). Initial elastic behaviour observed in the composite connection indicates dominant influences of the shear stud in resisting the applied shear loads as observed in steel composite counterparts clearly upholding the equations outlined in EC4 for determining shear capacity of composite connections. Conspicuous transitioning from the

elastic response of the stud into yielding observed on the load-slip plot may resemble that which is obtainable in steel-concrete counterparts but becomes distorted evidencing combined plastic yielding of stud and fibre delamination failures of GFRP flange around the clearance holes as observed from experimental testing. Further experimental testing on novel GFRP-LWAC shear composite connection provides reliability on the results earlier obtained from pilot test results involving GFRP-NWC composite without any deviations from the load-slip curve propagations without any significant changes in the load-slip responses relationship. However, earlier studies reported from literature suggested some influences on the shear/slip capacities and ultimately interfacial shear behaviour of steel-concrete composites while some of these influences remain true for GFRP-LWAC composites, there are limited differences as summarised in subsections below.

8.2.1 Stud Influences on GFRP-LWAC Composite Configurations

Stud sizing contributes significantly to the shear capacity of the composite and ultimately to the failure mechanism impacting the interfacial shear connections significantly. Results from pilot experimental test in phases I & II involving three sizes of studs showed significant increase in their corresponding shear capacities with 19 mm stud having 22% higher capacity to 16 mm studs whereas 16 mm studs reported approximately 17% average capacities over their 12 mm counterparts. Strain results obtained from the test suggested that strength mobilisation of shear studs begin initiating from the embedded stud cap due to anchor effects thereby supporting the Hicks (2014) theory of single curvature formation of studs in solid slabs derived from plastic hinging. The research concludes that this singular phenomenon characterises steel stud behaviours in GFRP-

LWAC composites, therefore becomes significant in theoretical equations for the determination of shear capacities of GFRP-Concrete composites. Hence, equations for the determination of GFRP-concrete shear capacities must take into account the cross-sectional area of shear studs and their yielding capacities in corroboration to EC4 standard equation for steel-concrete composites.

Apart from the stud cross-sections and mechanical properties, the stud configuration contributes significantly to the shear capacities and subsequent performance of the interfacial connections. The results reported in table 4.1 evidently outlines the increase in shear capacities obtained under various stud arrangements. PO-SR-S1 only accounted for transverse spacing between the studs, PO-DR-S3 accounted for both transverse and longitudinal spacing between studs. Hence, single-row arrangement (PO-SR-S1) earlier put forward in BS 5400-5 (2005) shows lower shear capacities due to the lack of longitudinal spacing between studs in comparison to the revised test arrangement outlined in EC 4 (PO-DR-S3) which reported 45% higher shear capacity. The staggered stud arrangement deployed to replicate possible industry practice did show considerable 32% higher shear capacity to the single row arrangement but with approximately 20% lower values to the double row configurations. No significant changes were observed for slip values although stiffness values were significant with higher stiffness values of 28% (between the staggered and double row arrangements) and 36% (between double and single row arrangements) respectively. In addition, modified collar studs adopted in one of the samples of the phase III provided consistency to support the plastic hinge theory for stud strength mobilisation. The modified studs reported significantly lower shear capacities in in comparison to their non-collared counterpart suggesting that strength improvement of studs are limited to their cross-sectional efficiency and yield strength

whereas geometrical modifications of studs contribute to their shear capacities either enhancing the resistance or limiting single curvature formation. The research study suggest that for an efficient setup to characterise interfacial shear connections, the proposed model should account for both longitudinal and transverse stud arrangements. Experimental shear strengths for GFRP-LWAC composites reported between 22 – 42% higher strength capacities against predicted values using equations from EC4 (P_{EC4}) and 40 – 60% higher values against Oehler and Johnson's (P_{OJ}) proposed equations for 12 mm stud sizes. However, values became comparatively close for 16 mm studs at $\pm$10% with at 5 % lower experimental values against P_{EC4} predicted values and 8 % higher values against P_{OJ} values. Due to severe delamination failures for specimen of 19 mm studs, experimental values become 20 -25 % less than theoretically predicted values from P_{EC4} and P_{OJ}. Experimental shear strength of GFRP-LWAC composites have provided between 40 – 50% shear capacities of published results generated from steel-concrete counterparts. This is consistent with literature findings on the strength to weight benefit of structural GFRP materials to provide up to 40 – 50 % strength at significantly lower densities in comparison to structural steel.

8.2.2 Concrete Influences on GFRP-LWAC Composite Configurations

Although literature findings suggest the influence of concrete mechanical properties in interfacial shear performance of structural composites, the methods of assessment and testing required for determination are quite laborious and often consuming high volumes of concrete materials. However, such crucial findings were subject of parametric and sensitivity investigations involving numerical modelling of the composites. Result findings were consistent with literature reports for both traditional steel-concrete and

GFRP-concrete indicating that concrete compressive strengths were dominant in enabling the mobilisation of stud resistance against shear failure. Experimental results showed correlated shear capacity values at the close range of compressive strengths for both LWAC and NWC specimens irrespective of their concrete densities. Slip values are higher in LWAC compared to their NWC counterparts.

8.2.3 GFRP Flange Influences on GFRP-LWAC Composite Configurations

Strain responses of GFRP flange discontinuities show dominant bearing failures resulting from increased resistance of fibres against compressive forces bearing around the steel studs. Average compressive strains up to 6000 um can be attained on GFRP flanges with bolted discontinuities. The research study also corroborates Nguyen (2014) findings on strain gauge positioning for measurements of GFRP flange strain under bearing failure. Strain measurement for GFRP plates undergoing shear loading are practical at vertical distances of 25 mm above the clearance hole. The research study thus conclude that GFRP flange properties contribute dominantly to interfacial shear resistance as against their corresponding web properties.

8.3 Flexural Behaviour

Fabrication techniques integrating GFRP profiles as part of the concrete curing setup does promote interface bonding which contributes significantly to the rigidity of interfacial shear connection thus establishing full interaction of subcomponents. This can be beneficial to sustain the full composite strength of the beam at the early-life of post construction. Compressive strain propagates in a decreasing order from the mid-span

towards the supports of the composite section under flexure for both limit states. The mid-span compressive strain at debonding is 327.5 $\mu\varepsilon$ which is approximately 76% less than the measured strain at ultimate flexure of 1353 $\mu\varepsilon$. However, after concrete debonding from GFRP flange occurs, the corresponding mid-span strain under serviceable loading is 95% significantly lower than the compressive strain at failure. The experimental values for interfacial strain of cycles two and three correlates closely between 0.2 - 4% thus reinforcing reliability in the obtained results. The study concludes that in addition to the normal force in the composite beam, interfacial shear resistance contributes to the strain development on concrete and GFRP flanges.

Longitudinal shear failure of the concrete slab at ultimate loading is observed in the study against expected tensile yielding of GFRP bottom flange. This type of failure earlier reported in the studies conducted by Lowe et al. (2014) on steel-concrete composites. This outlines the peculiar similarities between conventional steel-concrete composites and the novel GFRP-LWAC composite citing possible uneven distribution of forces around the stud at the interfacial shear zone. The equilibrium of forces maintained by the embedded stud shear to mobilise resistance during increased interfacial shearing is upturned enabling an uncontrolled transfer of shear forces in the concrete slab at maximum flexure. This finding generates some concern in the design of GFRP-LWAC beam with particular attention to be given to the concrete formulation with the provision of reinforcement bars to counter the longitudinal shear stresses that may propagate through the concrete slab leading to premature failure of the beam.

The strain profile for the cyclic loading shows a consistent distribution of strain within both compressive and tensile zones with a significant strain capacity reserve of

approximately 66% to the peak for both compressive and tensile strains. Analytical findings thus conclude, that if a partial safety factor of 1.2 were applied on the ultimate compressive stress, an upper boundary may be established to provide a 50% reserve capacity to the beam ultimate limits.

i. The proposition that hybrid beams possess inherent general linear behaviour until failure is valid and therefore, evaluation of deflection for PFRP-concrete hybrid beams can be considered under the elastic region.
ii. Interfacial shear resistance contributes significantly to strain developments in concrete and GFRP upper flanges in flexure. Strain plots for upper flanges of GFRP indicate sensitivity to shear resistances unlike their lower (bottom flange) counterparts. Evidently, strain readings at the bottom flange are tensile as consequence of the normal force which develop during flexural behaviour.
iii. Strains obtained from the cycle 1 are significantly lower than strains reported in Cycle 2 due to initial debonding action between the GFRP-concrete interface. It can be assumed that composite action is mainly achieved initially by interface bond with lesser connector influence.
iv. The observed failure mode suggests the modification of the standard push-out test in EC4 for conventional composite beams to account for the effect of concrete compressive forces against uplift reactions of stud from increased bending of the composite.
v. When multiple influencing variables such as slab geometry, stud arrangement, profile properties are adjusted and modified, GFRP-concrete composite beams can compare significantly with their steel-concrete counterparts producing low density structural elements with remarkable strength capacity.

8.4 Limitations of the Current Study

The current research study is pioneer investigation on GFRP profiles as structural elements carried out at Coventry University hence, several challenges were encountered with many successes and a few limitations. This section provides a detail account some of these challenges and their corresponding limitations.

8.4.1 Experimental Test Limitations

There were many challenges associated with the experimental test setups and fabrication of specimens. Fabrication challenges were mainly centred on the adoption of appropriate techniques for geometrical sizing of GFRP with minimal impact to the material fibre. The light structures laboratory did not possess the desired cutting machine suited for GFRP or relevant to manage health & safety concerns emanating from cutting process. Hence, size fabrication and drilling for all GFRP materials were managed remotely increasing the overall cost of the research. The first phase of experimental testing for shear performance adopted manual load cells which posed concerns on the consistency of generated results although utmost attention was given to ensure that load application was reliable holistically. Subsequent testing was efficiently managed using automated loading programmed into data loggers for high reliability. The main limitation for experimental testing was centred on characterisation of GFRP strips as the existing tensile testing machine lacked the capability to accommodate GFRP strips due to shape variability of the clamp heads. Further experimental limitations are elaborated below.

i. **GFRP Profile Characterisation:** It is good practice to calibrate the mechanical properties of GFRP test specimens as research findings have reported that material properties specified by manufacturers are generally lower than calibrated test properties from experimental testing for GFRP profiles. Therefore, material characterisation is a crucial aspect of GFRP research standardisation. However, being a pioneer research investigation at Coventry University, the test machines available at the light structures laboratory did not meet the tolerance specification for characterising the required GFRP coupons thus, creating an early challenge in the research study. Mechanical properties data of the profile was required to further numerical analysis and contribute to the theoretical evaluation of the novel beam performance. The research profiles used for the GFRP-LWAC composites were sourced from a batch of profiles recently studied and characterised at Warwick University with results published by Matharu (2018). The secondary data derived is practicable as it correlates effectively within the property range for GFRP profiles manufactured by the pultrusion process.

ii. **Shear Characterisation:** Although eight fabricated specimens are developed for GFRP-Concrete shear characterisation under three phases of testing, parametric studies remain limited at the experimental stage due to potential large consumption of materials and excessive waste resulting from large geometric sizes of specimens. Experimental characterisation focused largely on GFRP and stud deformations whereas studies can be extended to concrete parameters contributing to the mobilisation of shear resistance in the novel composite. This provides some limitations for the conclusions on concrete influences to the

mechanical behaviour of the composite although the numerical analysis attempts to address the challenge.

8.4.2 FE Numerical Limitations

The FE simulations were mostly impacted by the COVID-19 pandemic following limited access to the FE software; ANSYS APDL. FE simulations relied on remote connections to the University's software hence, significant impact due to limited capacity of personal laptop to run the heavily loaded programme. Simulation run time was increasingly high in most cases, programmes were disconnected following delays in sustaining connections. Further problems were encountered with data storage as each single-operated-run for the hybrid beam generated data up to 750 Gigabyte and exceeded the university's storage allocation for research.

8.5 Recommendations

The following recommendations are proposed based upon current findings from this research.

- Further investigation be carried out on lytag lightweight concrete formulation to address concrete confinement strength development and associated hardened properties which will enable effective strength mobilisation of studs and tensile stress distribution to prevent premature failure of composite concrete slabs.
- The compression effect of concrete slabs on GFRP composite formulation should be accounted for in lateral shear characterisation hence, proposed experimental test setups inculcating these forces should be developed and investigated to

determine the most appropriate methods for lateral shear characterisation of conventional concrete-GFRP composites.

- Comparative response of GFRP-concrete composites to four-point and three-point bending test be conducted on shorter spans to determine vertical shear performance of novel hybrid beam. Such research can be supported with numerical simulations using ANSYS APDL or related FE softwares.

Reference

ACI 211. 2-98. Standard practice for selecting proportions for lightweight concrete. *American Concrete Institute, Farmington Hills, MI*.

ACI Committee 213R, 2014. Guide for structural lightweight-aggregate concrete. *American Concrete Institute, Farmington Hills, MI*.

Allwood, J. M., Cullen, R.L. Milford, Options for achieving a 50% cut in industrial carbon emissions by 2050, Environmental Science & Technology44 (March (6)) (2010) 1888 – 1894

An, L., and Cederwall, L., 1996. Push-out tests on studs in high strength and normal strength concrete. *Journal of Constructional Steel Research*. 36, No. 1, pp 15-29.

ASCE, 2010. *Pre-standard for load and resistance factor design (LRFD) of pultruded fiber reinforced polymer (FRP) structures.* American Society of Civil Engineers (2010)

ASTM C330/330M, 2014. Standard specification for lightweight aggregates for structural concrete. *ASTM International, West Conshohocken, PA. US*.

Ataei A., Zeynalian M., Yazdi Y., 2019. *Cyclic behaviour of bolted shear connectors in steel-concrete composite beams.* Eng. Struct., 198 (2019), Article 109455

Ayati, B., Ferrándiz-Mas, V., Newport, D., & Cheeseman, C. (2018). Use of clay in the manufacture of lightweight aggregate. *Construction and Building Materials*, 162, 124–131. doi:10.1016/j.conbuildmat.2017.12.018

Bank, I. C., 2006. Composites for construction: Structural Design with FRP Materials. *John Wiley and Sons.*

Bardhan-Roy B. K., Crozier W. F. G., 1983. FIP manual of lightweight aggregate concrete. *Glasgow: Surrey University Press*.

BIS, Estimating the amount of CO2emissions that the construction industry can influence – supporting material for the Low Carbon Construction IGT Report, 2010, Available: https://assets.publishing.service.gov.uk/government/uploads/system/uploads/attachment_data/file/31737/10-1316-estimating-co2-emissions-supporting-low-carbon-igt-report.pdf

Bouwers, H., Radix, H., 2005. Self-compacting concrete: theoretical and experimental study. *Cem. Conc. Res.* 35:2116-36

BS EN 12390-3, 2019. Testing hardened concrete – compressive strength of test specimens. *British Standards Institution*.

BS EN 1994-1-1, 2004. Design of Composite Steel and Concrete Structures. London: *British Standards Institution*.

Chamis, C.C. and Sinclair, J.H., 1976. 10° Off-Axis Tensile Test for Intralaminar Shear Characterization of Fiber Composites. *Contract*, *506*, p.17.

Chandra, S., & Berntsson, L. (2002). Historical Background of Lightweight Aggregate Concrete. Lightweight Aggregate Concrete, 5–19. doi:10.1016/b978-081551486-2.50004-3

Chen, X. and Liu, Y., 2015. Finite Element Modelling and Simulation with ANSYS Workbench. London: CRC Press

Correia J., Branco J. and Ferreira J., 2005. Structural behaviour of GFRP-concrete hybrid beams. Composites in Construction. *3rd International Conference*, Lyon, France.

Correia J., Branco J. and Ferreira J., 2007. Flexural behaviour of GFRP-concrete hybrid beams with interconnection slip. *Composite structures*, 77, pp. 66-78

Costa, H., Julio, E. and Lourenco, J., 2010. A new mixture design method for structural lightweight aggregate concrete. *8th Fib PhD Symposium in Kgs. Lyngby, Denmark*.

Cui, H., Lo, T., Memon, S. and Xu, W., 2012. Effect of lightweight aggregates on the mechanical properties and brittleness of lightweight aggregate concrete. *Construction and Building Materials*, 35, pp.149-158.

Dai, X., Lam, D. and Saveri, E., 2015. Effect of concrete strength and stud collar size to a shear capacity of demountable shear connectors. *Journal of Structural Engineering*. 141 (11), 04015025.

D'Amico, B., & Pomponi, F. (2018). Sustainability Tool to Optimise Material Quantities of Steel in the Construction Industry. Procedia CIRP, 69, 184–188. doi:10.1016/j.procir.2017.10.006

DEFRA, UK Waste Data, UK Waste Data and Waste Management Statistics, 2011, Available: https://www.gov.uk/government/uploads/system/uploads/attachment data/file/141979/UK Waste data.pdf

Dilli, M., Atahan, H. and Şengül, C., 2015. A comparison of strength and elastic properties between conventional and lightweight structural concretes designed with expanded clay aggregates. *Construction and Building Materials*, 101, pp.260-267.

Driscoll, G. C. and Stutter, R. G. Research on Composite Design at Lehigh University Proceedings, National Engineering Conference, AISC, May, 1961

Emad, H., Shahrizan, B., Wan H., Badaruzzaman, W. and Ahmed, W., 2018. Push-out test on the web opening shear connector for a slim-floor steel beam: Experimental and analytical study. *Engineering Structures*. 163, pp 137-152.

Engen, M., Hendriks, M., Øverli, J. and Åldstedt, E., 2015. Solution strategy for non-linear finite element analyses of large reinforced concrete structures. *Structural Concrete*, 16(3), pp.389-397.

Etim, O., Gand, A., Saidani, M., Fom, P., Ganjian, E., & Okon, E., 2020. Shear characterization of pultruded superstructural FRP-Concrete push-outs. Structures, Vol 23, pp 254 – 266.

Ferreira, F., Martins, C. and De Nardin, S., 2020. Advances in composite beams with web openings and composite cellular beams. *Journal of Constructional Steel Research*, 172, p.106182.

Gai, X., Darby, A., Ibell, T. and Evernden, M., 2013. Experimental investigation into a ductile FRP stay-in-place formwork system for concrete slabs. *Construction and Building Materials*. Volume 49, pp 1013 – 1023.

Gibson, R. F., 2001. Principles of composite material mechanics. *CRC Press.*

Giesekam, J., Barrett, J., Taylor, P., & Owen, A. (2014). The greenhouse gas emissions and mitigation options for materials used in UK construction. Energy and Buildings, 78, 202–214. doi:10.1016/j.enbuild.2014.04.035

Girhammar, U. and Gopu, V., 1993. Composite Beam-Columns with Interlayer Slip—Exact Analysis. *Journal of Structural Engineering*, 119(4), pp.1265-1282.

He, H., Guo, Z., Stroeven, P., Stroeven, M. and Sluys, L., 2009. Characterization of the packing of aggregate in concrete by a discrete element approach. *Materials Characterization*, 60(10), pp.1082-1087.

He, Y., Zhang, X., Zhang, Y. and Zhou, Y., 2014. Effects of particle characteristics of lightweight aggregate on mechanical properties of lightweight aggregate concrete. *Construction and Building Materials*, 72, pp270-282.

Hicks, S.J. and Smith, A.L., 2014. Stud shear connectors in composite beams that support slabs with profiled steel sheeting. Structural Engineering International: *Journal of the International Association for Bridge and Structural Engineering (LABSE)*. 24 (2), pp 246-253.

Hosseini S.M., Mamun M.S., Mirza O., Mashiri F., 2020. *Behaviour of blind bolt shear connectors subjected to static and fatigue loading*. Eng. Struct., 214 (2020), Article 110584

Hwang, C. and Hung, M., 2005. Durability design and performance of self-consolidating lightweight concrete. *Construction and Building Materials*, 19(8), pp.619-626.

IS 10262, 2019. Indian standard concrete mix proportioning. Bureau of Indian Standards, New Delhi.

Jalal, M., Mansouri, E., Sharifipour, M. and Pouladkhan, A., 2012. Mechanical, rheological, durability and microstructural properties of high performance self-

compacting concrete containing SiO2 micro and nanoparticles. *Materials & Design*, 34, pp.389-400.

Jayajothi, P., Kumutha, R. and Vijai, K., 2013. finite element analysis of FRP strengthened RC beams using ANSYS. Asian Journal of Civil Engineering (BHRC) Vol. 14, No. 4 (2013) pp 631-642

Johnson, R. P., May, I. M., 1975. Partial-interaction design of composite beams. *The Structural Engineer*. 53(8) pp 305-311.

Jin, D., Yang, Z., Xuhong, Z., Fengjiang Q. and Xi P., 2018. Push-out test of large perfobond connectors in steel-concrete joints of hybrid bridges. *Journal of Constructional Steel Research*. 150, pp 415-429.

Kachlakev, D. & Miller, T., 2001. Finite Element Modelling of Reinforced Concrete Structures Strengthened with FRP Laminates. Final report (SPR316), Oregon Department of Transportation.

Kanadasan, J. and Razak, H., 2014. Mix design for self-compacting palm oil clinker concrete based on particle packing. *Materials & Design (1980-2015)*, 56, pp.9-19.

Kim, J., Kwark, J., Joh, C., Yoo, S. and Lee, K., 2015. Headed Stud Shear Connector for thin ultrahigh-performance concrete bridge deck. *Journal of Constructional Steel Research*. Volume 108, pp 23 – 30.

Kotsovos, MD., Pavlovic, MN., 1995. Structural concrete: finite-element analysis for limit-state design. *London: Thomas Telford Ltd*.

Kozma, A., Odenbreit, C., Braun, M. V., Veljkovic, M., & Nijgh, M. P. (2019). Push-out tests on demountable shear connectors of steel-concrete composite structures. Structures. doi:10.1016/j.istruc.2019.05.011

Kwan, A. and Fung, W., 2009. Packing density measurement and modelling of fine aggregate and mortar. *Cement and Concrete Composites*, 31(6), pp.349-357.

Li, J., Chen, Y. and Wan, C., 2017. A mix-design method for lightweight aggregate self-compacting concrete based on packing and mortar film thickness theories. *Construction and Building Materials*, 157, pp.621-634.

Lowe, D., Das, R. and Clifton, C., 2014. Characterisation of the splitting behaviour of steel concrete composite beams with shear stud connection. *Procedia Materials Science*. Vol 3. Pp 2174 – 2179.

Lowe, D., Roy, K., Das, R., Clifton, C. and Lim, J., 2020. Full scale experiments on splitting behaviour of concrete slabs in steel concrete composite beams with shear stud connection. *Structures*. Vol 23, pp 126-138.

Luo, Y., Li, A., & Kang, Z. (2012). Parametric study of bonded steel–concrete composite beams by using finite element analysis. *Engineering Structures*, 34, 40– 51.

Matharu, N. and Mottram, J., 2017. Plain and threaded bearing strengths for the design of bolted connections with pultruded FRP material. *Engineering Structures, 152, pp 878-887.*

Middleton, B. (2016). Composites: Manufacture and Application. Design and Manufacture of Plastic Components for Multifunctionality, 53–101. doi:10.1016/b978-0-323-34061-8.00003-x

Mirza, O. and Uy, B., 2010. Effects of the combination of axial and shear loading on the behaviour of headed stud steel anchors. *Engineering Structures*. 32(1), 93-105.

Molkens, T., Dobric, J. and Rossi, B., 2019. Shear resistance of headed shear studs welded on welded plates in composite floors. *Engineering Structures*. Volume 197. Article 109412

Mottram, J. T., 2009. Determination of pin-bearing strength for the design of bolted connections with standard pultruded profiles. *4th International Conference on Advanced Composites in Construction. Net Composites Ltd, Chesterfield*, pp 483-495.

Mottram, J. and Turvey, G., 2003. Physical test data for appraisal of design procedures for bolted joints in pultruded FRP structural shapes and systems. *Prog. Struct. Eng. Mat.*, 5(4), pp 195 – 222

Moynihan, M. and Allwood, J., 2012. The flow of steel into the construction sector. *Resources, Conservation and Recycling*, 68, pp.88-95.

Neagoe C., Gil L. and Pérez, M., 2015. Experimental study of GFRP-concrete hybrid beams with a low degree of shear connection. *Construction and Building Materials*. 101, pp.141-151.

Neagoe, C. A., & Gil, L. (2015). Analytical procedure for the design of PFRP-RC hybrid beams including shear interaction effects. Composite Structures, 132, 122–135. doi:10.1016/j.compstruct.2015.04.054

Nellinger, S., 2015. On the behaviour of shear stud connections in composite beams with deep decking. *PhD thesis, University of Luxembourg*. https://orbilu.uni.lu/handle/10993/24468

Neville, A. M., 2000. Properties of concrete. *4th Edition, Prentice Hall*.

Nguyen, H. and Kim, S., 2009. Finite element modelling of push-out tests for large stud shear connectors. *Journal of Constructional Steel Research.* 65(10-11), pp 1909-1920.

Nguyen, H., Mutsuyoshi, H. and Zatar, W., 2013. Flexural behaviour of hybrid composite beams. *Transportation Research Record: Journal of Transportation Research Board. No 2332, Transportation Research Board of the National Academies, Washington DC*. Pp 53-63. doi:10.3141/2332-06

Nguyen, H., Mutsuyoshi, H., and Zatar, W., 2014. Push-out tests for shear connections between UHPFRC slabs and FRP girder. *Composite Structures*. 118 (1), pp 528-547.

Nie, J., Fan, J., & Cai, C. S. (2004). Stiffness and Deflection of Steel–Concrete Composite Beams under Negative Bending. Journal of Structural Engineering, 130(11), 1842–1851. doi:10.1061/(asce)0733-9445(2004)130:11(1842)

Odenbreit, C. and Nellinger, S., 2017. Mechanical model to predict the resistance of the shear connection in composite beams with deep steel decking. *Steel Construction*. 10 (3), pp 248-253.

Oehlers, D. J. and Johnson, R. P., 1987. The strength of stud shear connections in composite beams. *Structural Engineer*. 6(2), pp 44-48.

Ollgaard, J., Slutter, R., and Fisher, J., 1971. Shear strength of stud connectors in lightweight and normal-weight concrete. *AISC Engineering Journal*. pp 55-64.

Øverli, J., 2017. Towards a better understanding of the ultimate behaviour of LWAC in compression and bending. *Engineering Structures*, 151, pp.821-838.

Prakash, A., Anandavalli, N., Madheswaran, C. and Lakshmanan, N., 2012. Modified push-out tests for determining shear strength and stiffness of HSS stud connector: Experimental study. *International Journal of Composite Materials*. 2(3), pp 22-31.

Priyanka, M., Kaythikeyanm, M., Chand, M., 2020. Development of mix proportions of geopolymer lightweight aggregate concrete with LECA. *Materials Today: Proceedings 27*, pp958-962

Queiroz, F. D., Vellasco, P. C. G. S., & Nethercot, D. A. (2007). Finite element modelling of composite beams with full and partial shear connection. *Journal of Constructional Steel Research*, 63(4), 505–521. doi:10.1016/j.jcsr.2006.06.003

Qureshi, J., Lam, D. and Ye, J., 2011a. Effect of shear connector spacing and layout on the shear connector capacity in composite beams. *J. Constr. Steel Res.*, 67 (4), 706 – 719.

Qureshi, J., Lam, D. and Ye, J., 2011b. The influence of profiled sheeting thickness and shear connectors position on strength and ductility of headed shear connector. *Eng. Struct.*, 33 (5), 1643 – 1656.

Rehman, N., Lam, D., Dai, X. and Ashour, A., 2016. Experimental study on demountable shear connectors in composite slabs with profiled decking, *Journal of Constructional Steel Research*. 122, pp 178-189.

Selver, E., et al., 2015. Healing potential of hybrid materials for structural composites. Compos. Structures 122, 57–66.

Shen, M., Chung, K., Elghazouli, A. and Tong, J., 2020. Structural behaviour of stud shear connections in composite floors with various connector arrangements and profiled deck configurations. *Engineering Structures*, 210.

Shetty, M. S., 2006. Concrete technology theory and practice. *S. Chand & Co. Ltd., England*.

Subramani, T., Manivannan, R. and Kavitha, M. 2014a. Finite Element Modelling on Behaviour of Reinforced Concrete Beam Column Joints Retrofitted with CFRP sheets Using Ansys. Journal of Engineering Research and Applications 4 (12), 69-76.

Subramani, T., Manivannan, R. and Kavitha, M. 2014b. Crack Identification in Reinforced Concrete Beams Using ANSYS Software. Journal of Engineering Research and Applications 4 (6), 133-141.

Suwaed, A. and Karavasilis, T., 2020. Demountable steel-concrete composite beam with full-interaction and low degree of shear connection. *Journal of Constructional Steel Research*, 171, p.106152.

Swamy, R. N., & Lambert, G. H. (1981). The microstructure of Lytag aggregate. International *Journal of Cement Composites and Lightweight Concrete*, 3(4), 273–282. doi:10.1016/0262-5075(81)90038-5

Swolfs, Y., Gorbatikh, L., Verpoest, I., 2014. Fibre hybridisation in polymer composites: a review. Compos. Part A 67, 181–200.

Thienel, K.-C., Haller, T., & Beuntner, N. (2020). *Lightweight Concrete—From Basics to Innovations. Materials, 13(5), 1120.* doi:10.3390/ma13051120

Turvey, G. J. (2013). Testing of pultruded glass fibre-reinforced polymer (GFRP) composite materials and structures. *Advanced Fibre-Reinforced Polymer (FRP) Composites for Structural Applications*, 440–508. doi:10.1533/9780857098641.3.440

Turvey, G. J. and Zhang, Y., 2018. Mechanical properties of pultruded GFRP WF, channel and angle profiles for limit state/permissible stress design. Composites Part B (148). 260-271.

Turvey, G. J. (2011). Bolted joints in pultruded glass fibre reinforced polymer (GFRP) composites. . Lancaster University, UK. Woodhead Publishing Limited.

Vacev, T., Bonic, Z., Prolovic, V., Davidovic, N. and Lukic, D. 2015. Testing and Finite Element Analysis of Reinforced Concrete Column Footings Failing by Punching Shear. Engineering Structures 92, 1 – 14.

Vidosa, F., Kotsovos, M. and Pavlović, M., 1991. Nonlinear finite-element analysis of concrete structures: Performance of a fully three-dimensional brittle model. *Computers & Structures*, 40(5), pp.1287-1306.

Wang, X., Wang, K., Taylor, P., & Morcous, G. (2014). Assessing particle packing based self-consolidating concrete mix design method. *Construction and Building Materials, 70, 439–452.* doi:10.1016/j.conbuildmat.2014.08.002

Wang, T. and Müller, D. B. G. T. E., 2007. Forging the anthropogenic iron cycle. Environmental science & technology, vol. 41, No. 14, pp. 5120-5129.

Xu, C., Sugiura, K., Wu, C., & Su, Q. (2012). Parametrical static analysis on group studs with typical push-out tests. Journal of Constructional Steel Research, 72, 84–96. doi:10.1016/j.jcsr.2011.10.029

Yang, F., Yuqing, L., Zhibo, J., and Haohui, X., 2018. Shear performance of a novel demountable steel-concrete stud connector under static push-out tests. *Engineering Structures*. 160, pp 133-146.

Yang, K., Kim, G. and Choi, Y., 2014. An initial trial mixture proportioning procedure for structural lightweight aggregate concrete. *Construction and Building Materials*, 55, pp.431-439.

Zhang, S., Caprani, C., & Heidarpour, A. (2018). Influence of fibre orientation on pultruded GFRP material properties. *Composite Structures*, 204, 368–377. doi:10.1016/j.compstruct.2018.07.104

Zhang, J., Hu, X., Fu, W., Du, H., Sun, Q., & Zhang, Q. (2020). Experimental and theoretical study on longitudinal shear behavior of steel-concrete composite beams. Journal of Constructional Steel Research, 171, 106144. doi:10.1016/j.jcsr.2020.106144

Zhang, C. (2014). Life cycle assessment (LCA) of fibre reinforced polymer (FRP) composites in civil applications. Eco-Efficient Construction and Building Materials, 565–591. doi:10.1533/9780857097729.3.565

Zoghi, M., 2014. *The International Handbook Of FRP Composites In Civil Engineering*. Boca Raton, Fl: Taylor & Francis.

Zou, X., Feng, P., Wang, J., Wu, Y. and Feng, Y., 2018. FRP stay-in-place form and shear key connection for FRP-concrete hybrid beams/decks. *Composite Structures*, 192, pp.489-499.

Zou, X., Feng, P., Bao, Y., Wang, J., & Xin, H. (2020). Experimental and analytical studies on shear behaviors of FRP-concrete composite sections. *Engineering Structures, 215, 110649*. doi:10.1016/j.engstruct.2020.110649

Appendix A

A1: Concrete Mix Design

Normal Weight Concrete (NWC) mix design using the BRE design method

- **Design Parameters:**

Cement class: EN class 52.5

Target compressive strength fc= 40 N/mm^2 at 28 days curing.

5% proportion defective (Standard)

Target slump = 50mm

Coarse aggregates = 10mm uncrushed river gravel

Fine aggregate = 40% passing through 600 μm sieve

Aggregate saturated surface dry density = 2650kg/mm^3 (known)

Standard deviation, S = 8N/mm^2 …… (Assumed from table)(ref)
5% defective; k = 1.64

Margin = 1.64 x 8 = 13 N/mm^2

Target mean strength fm = fc + k

fm = 40 N/mm^2 + 13 N/mm^2 = 53 N/mm^2

Water/cement ratio = 0.46 (interpolated from figure 4 of BRE guide)

Workability (table 3)

Free water content, w = 205 kg/mm^3

Cement content, c = $\frac{w}{w\backslash c}$ = $\frac{205}{0.46}$ = 445 $kg/mm3$

Concrete density

Estimated wet density of concrete = 2370 kg/mm^3 (using figure 5)

Total aggregate content = density – cement – water

TAC = 2370 – 445 – 205 = 1720 kg/mm^3

Proportion of fine aggregate

Maximum aggregate size = 10mm

Target slump = 50mm

w/c ratio = 0.46

Therefore for 40% passing through 600 μm sieve, proportion of fine aggregates = 48%

Fine aggregate content

% fine aggregate x total aggregate content

= 0.48 x 1720 = 825 kg/mm^3

Coarse aggregate content

Total aggregate content – fine aggregate content = 895 kg/mm^3

Volume of concrete: $0.094m^3$

Table A1. 1 Mix proportions for NWC

	Cement (kg)	Water (litre)	Fine aggregate (kg)	Coarse aggregate (kg)
/m^3	445	205	825	895
/0.094m^3	46.28	21.32	85.8	93.08

NWC Mechanical Properties

The compressive test results for NWC samples are presented in Figure and table below.

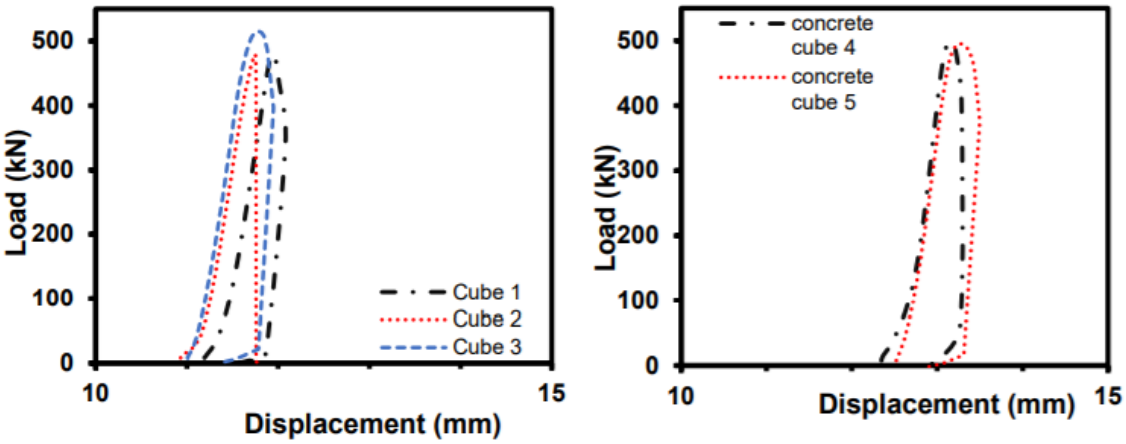

A1. 0.1: Cube compressive plot (NWC)

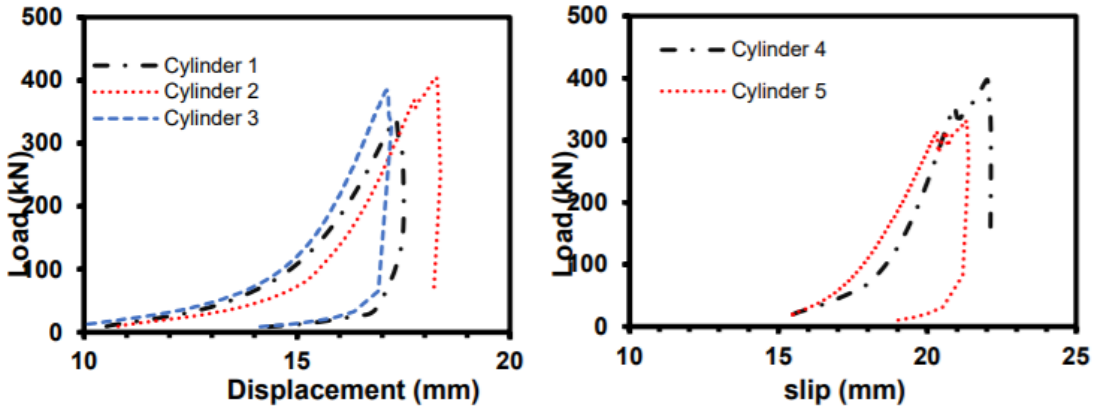

A1. 0.2: Cylinder compressive plot (NWC)

Table A1.2: Cube compressive test data

	Cube 1	Cube 2	Cube 3	Cube 4	Cube 5	Mean Value
f_{ck} (kN)	479.13	507.45	514.95	497.92	495	498.89
f_c (MPa)	47.913	50.745	51.495	49.792	49.500	49.889
E_{cm} (MPa)	818.57	758.82	860.86	883.53	968.47	858.05

Table A1.3: Cylinder compressive test data

	Cylinder 1	Cylinder 2	Cylinder 3	Cylinder 4	Cylinder 5	Mean Value
f_{ck} (kN)	337.59	404.11	397.71	384.4	330.81	370.924
f_c (MPa)	43	51.5	50.64	48.94	42.12	47.24
E_{cm} (MPa)	65.27	77.49	140.23	63.61	127.67	94.854

A2: Trial Mix Data for Lytag Concrete

This section presents information on mix design and proportions for Lytag concrete

Table A2.1: Mix Design for Lytag Concrete

S/N	Mix Design							
	Specimen ID	Description	Total weight of Concrete (kg)	W/C ratio	C/A ratio		Aggregate ratio	
				water	cement	aggregate	Fine	Coarse
1	M1-01	37% CEMENT CONTENT	12	0.4	2	3	2	4
2	M1-02	37% CEMENT CONTENT	12	0.4	2	3	2	4
3	M2-01	30.3% CEMENT CONTENT	12.5	0.45	1.5	3	2	4
4	M2-01		12.5	0.45	1.5	3	2	4
5	M3-01	30.3% CEMENT CONTENT	12.5	0.45	1.5	3	2	4
6	M4-01	22.7% CEMENT CONTENT	12.5	0.4	1	3	2	4
7	M4-02	22.7% CEMENT CONTENT	12.5	0.4	1	3	2	4
8	M5-01	16% CEMENT CONTENT	13.29	0.4	0.75	3.5	2	4
9	M5-02	26% CEMENT CONTENT	13.29	0.46			2	5
10	M6-01	26% CEMENT CONTENT	13.29	0.43			2	5
11				0.45				

Table A2.2: Mix proportions for Lytag Concrete

S/N	Specimen ID	Mass of aggregate (kg)	Water content (kg)	Cementitious Material (kg)		Fine aggregate (kg)		Lytag aggregate (kg)		Air entrainment (0.6% by wt. of cement)	Fibres (% by volume)
				Cement	Fly ash	Sand	Other	5mm	10mm		
1		6.67	1.66	4.44	-	2.22		4.44	-	-	-
2	M1-01	6.67	1.66	4.44	-	2.22		-	4.44	-	-
3	M1-02	7.58	1.63	3.79	-	2.53		5.05		-	-
4	M2-01	7.58	1.63	3.79	-	2.53		-	5.05	-	-

			June, 2019	Fresh Properties						Hardened Properties			
	Batch ID	Specimen		Slump	Weight	Curing Period	Weight	Density	Compressive strength (Mpa)	Curing Period	Density	Compressive strength (Mpa)
S/N				mm	kg		kg	kg/m3			kg/m3	
1	M1-01	1	6/13/2019	-	1968	7 days	1920.0	1953.8	48.26	28 days	2009.00	52.91
2	M1-01	2	6/13/2019	-	1968		1922.9	1926.7	49.49		2010.00	52.53
3	M1-01	3	6/13/2019		1968		1973.2	1925.8	48.44		2009.00	53.08
4	M1-02	1	6/13/2019		1883		1851.6	1924.5	41.12		2003.00	47.38
5	M1-02	2	6/13/2019		1883		1832.3	1918.7	39.96		2008.00	44.8
6	M1-02	3	6/13/2019		1883		1871.6	1950.1	39.45		2012.00	41.5
7	M2-01	1	6/16/2019					1902	35.54	28 days		35.32
8	M2-01	2	6/16/2019					1887	26.09			35.32
9	M2-01	3	6/16/2019					1911	36.1			35.32
10	M3-01	1	6/16/2019					1893	35.04			37.31
11	M3-01	2	6/16/2019					1888	-			
12	M3-01	3	6/16/2019					1889	-			
13	M5-02	1		45	1871.2							
13	M5-02	2		45	1909.3							
13	M5-02	3		45	1918.6							
13	M6-01			110	2032.1							
13	M6-01			110	2038.2							
13	M6-01			110	2005.8							

5	M2-01	7.58	1.63	3.79	-	2.53		5.05		0.023	-
6	M3-01	8.52	1.14	2.84	-	2.84		5.68		-	-
7	M4-01	8.52	1.14	2.84	-	2.84		5.68		0.017	-
8	M4-02	10.00	0.88	2.14		3.33		6.67		-	-
9	M5-01	8.34	1.61	3.54		2.357		4.19	1.79	-	-
10	M5-02	8.34	1.51	3.54		2.357		3.59	2.39	-	-
11	M6-01	8.34	1.414	3.14		2.75				-	-

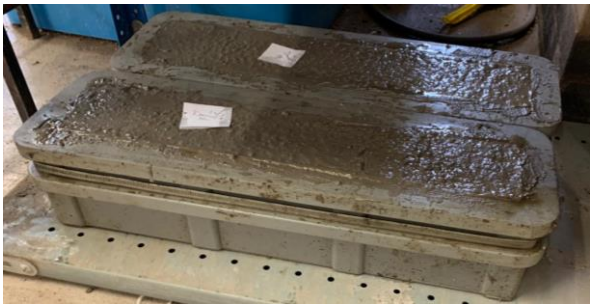

A1. 0.3: LWAC sample specimens

Appendix B

Glass Fibre Reinforced Polymer (GFRP) Characteristics

Table B 1: Compressive strength properties for GFRP web

Specimen (1)	Thickness (mm) (2)	Width (mm) (3)	Area (mm^2) (4)	Maximum Amsler Load (t) (5)	Maximum Specimen Load (kN) (6)	Compressive Strength (N/mm^2) (7)
Longitudinal (0°)						
W/0-01	9.56	50.0	478	15.1	149	311
W/0-02	9.60	50.0	480	14.2	140	291
W/0-03	9.54	50.0	477	13.8	136	285
W/0-04	9.54	50.0	477	14.8	145	304
W/0-05	9.56	50.0	478	13.6	134	280
W/0-06	9.52	50.0	476	16.1	158	333
W/0-07	9.58	50.0	479	16.0	157	328
W/0-08	9.59	50.0	480	13.7	135	281
W/0-09	9.58	50.0	479	15.8	155	323
W/0-10	9.56	50.0	478	15.9	157	327
Transverse (90°)						
W/90-01	9.57	50.0	479	4.80	47.3	98.8
W/90-02	9.56	50.0	478	6.85	67.4	141
W/90-03	9.54	50.0	477	6.83	67.2	141
W/90-04	9.56	50.0	478	7.44	73.2	153
W/90-05	9.57	50.0	479	6.30	62.0	130
W/90-06	9.55	50.0	478	6.42	63.1	132
W/90-07	9.57	50.0	479	6.36	62.6	131
W/90-08	9.56	50.0	478	6.90	67.9	142
W/90-09	9.58	50.0	479	6.65	65.4	137
W/90-10	9.59	50.0	480	6.25	61.5	128

Table B 2: Compressive strength properties for GFRP flanges

Specimen (1)	Thickness (mm) (2)	Width (mm) (3)	Area (mm^2) (4)	Maximum Amsler Load (t) (5)	Maximum Specimen Load (kN) (6)	Compressive Strength (N/mm^2) (7)
Longitudinal (0°)						
F/0-01	9.55	50.0	478	18.5	181	380
F/0-02	9.79	50.0	490	17.2	169	345
F/0-03	10.3	50.0	514	19.7	193	377
F/0-04	9.86	50.0	493	14.6	143	291
F/0-05	9.59	50.0	480	17.0	167	349
F/0-06	9.57	50.0	479	17.8	175	366
F/0-07	9.61	50.0	481	17.5	171	357
F/0-08	9.60	50.0	480	16.6	163	340
F/0-09	9.59	50.0	480	17.8	175	365
F/0-10	9.57	50.0	479	18.4	180	377
Transverse (90°)						
F/90-01	10.2	50.0	511	5.24	51.6	101
F/90-02	9.57	50.0	479	3.65	36.0	75.2
F/90-03	9.82	50.0	491	5.22	51.4	105
F/90-04	9.58	50.0	479	5.13	50.5	105
F/90-05	9.59	50.0	480	5.38	52.9	110
F/90-06	10.3	50.0	514	4.84	47.7	92.8
F/90-07	9.60	50.0	480	5.35	52.7	110
F/90-08	10.2	50.0	512	5.56	54.7	107
F/90-09	9.58	50.0	479	5.29	52.1	109
F/90-10	9.81	50.0	491	5.33	52.5	107

Table B 3: Summary of compressive strength properties for GFRP specimen

Specimen Batch (1)	Thickness (mm) (2)	Width (mm) (3)	Specimen Load (kN) (4)	Compressive Strength (N/mm^2) (5)	SD (N/mm^2) (6)	CoV (%) (7)	EN 1990 Char. Value (N/mm^2) (8)	ASTM D2970 Char. Value (N/mm^2) (9)
Web 0°	9.56	50.0	146	306	21.0	6.86	270	249
Web 90°	9.57	50.0	63.7	133	14.3	10.7	109	100
Flange 0°	9.70	50.0	172	355	26.3	7.43	309	298
Flange 90°	9.83	50.0	50.2	102	10.8	10.6	84	83

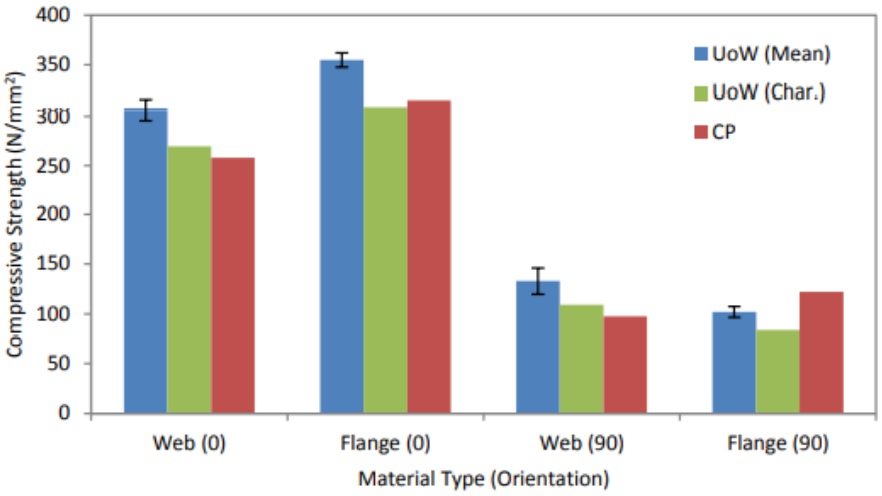

Figure B 1: Compressive strength comparison against Manufacturers

Table B 4: Tensile strength properties for GFRP

Specimen	Thickness (mm)	Width (mm)	Area (mm^2)	Maximum Amsler Load (t)	Maximum Specimen Load (kN)	Tensile Strength (N/mm^2)
(1)	(2)	(3)	(4)	(5)	(6)	(7)
Web Material						
W/0-01	9.60	25.1	241	6.94	68.1	282
W/0-02	9.60	25.1	241	6.23	61.1	254
W/0-03	9.59	25.1	241	7.22	70.9	294
W/0-04	9.64	25.1	242	7.32	71.8	297
W/0-05	9.66	25.1	243	7.50	73.6	303
Flange Material						
F/0-01	9.59	24.8	237	7.65	75.1	316
F/0-02	9.58	25.2	241	8.87	87.0	361
F/0-03	10.3	25.2	259	9.45	92.7	358
F/0-04	10.3	25.2	260	8.25	80.9	311
F/0-05	9.59	25.1	241	7.98	78.3	325

Table B 5: Tensile strength properties for GFRP web

Specimen	Thickness (mm)	Width (mm)	Area (mm^2)	Maximum Amsler Load (t)	Maximum Specimen Load (kN)	Tensile Strength (N/mm^2)
(1)	(2)	(3)	(4)	(5)	(6)	(7)
W/90-01	9.63	25.0	241	2.40	23.5	97.8
W/90-02	9.63	25.0	241	2.19	21.5	89.2
W/90-03	9.61	25.0	240	2.18	21.4	89.0
W/90-04	9.66	25.0	242	2.19	21.5	89.0
W/90-05	9.64	25.0	241	2.23	21.9	90.8
W/90-06	9.61	25.0	240	1.97	19.3	80.4
W/90-07	9.71	25.0	243	1.99	19.5	80.4
W/90-08	9.68	25.0	242	1.95	19.1	79.1
W/90-09	9.63	25.0	241	2.12	20.8	86.4
W/90-11	9.64	25.0	241	1.88	18.4	76.5

Table B 6: Summary of tensile strength properties for GFRP specimen

Specimen Batch	Thickness (mm)	Width (mm)	Specimen Load (kN)	Tensile Strength (N/mm^2)	SD (N/mm^2)	CoV (%)	EN 1990 Char. Value (N/mm^2)
(1)	(2)	(3)	(4)	(5)	(6)	(7)	(8)
Web 0°	9.62	25.1	69.1	294	7.6	2.6	280
Web 90°	9.64	25.0	20.3	84	8.6	10	69
Flange 0°	9.87	25.1	82.8	334	23.6	7.1	294

Table B 7: Material properties for 1525 Superstructural Pultruded WF sections

(Creative Pultrusions, 2010)

Mechanical Property	Units (ASTM Test Method)	Longitudinal (LengthWise - LW)	Transverse (CrossWise – CW)
Flange Section			
Tensile Strength	N/mm^2 (D638)	275	-
Tensile Modulus	kN/mm^2 (D638)	28.6	-
Compressive Strength	N/mm^2 (D695)	316	122
Compressive Modulus	kN/mm^2 (D695)	26.5	13.1
Shear Strength (by Punch)	N/mm^2 (D732)	37.8	-
Inter-laminar Shear	N/mm^2 (D2344)	27.5	-
Maximum Bearing Strength	N/mm^2 (D953)	227	158
Poisson Ratio	- (D3039)	0.35	0.12
Web Section			
Tensile Strength	N/mm^2 (D638)	208	72.2
Tensile Modulus	kN/mm^2 (D638)	21.3	9.6
Compressive Strength	N/mm^2 (D695)	258	97.6
Compressive Modulus	kN/mm^2 (D695)	19.2	13.1
Shear Strength (by Punch)	N/mm^2 (D732)	37.8	-
Inter-laminar Shear	N/mm^2 (D2344)	23.4	-
Maximum Bearing Strength	N/mm^2 (D953)	234	206
Poisson Ratio	- (D3039)	0.35	0.12